MICROSTRUCTURE AND MECHANICAL PROPERTIES OF NITRIDED STEELS

A thesis submitted for the degree of

Doctor of Philosophy

of the University of Newcastle upon Tyne

by

David Stafford Rickerby

Crystallography Laboratory

Department of Metallurgy and Engineering Materials

University of Newcastle upon Tyne

July 1982

PREFACE

This thesis describes original work which has not been submitted for a degree at any other University.

The investigations were carried out in the Crystallography Laboratory, Department of Metallurgy and Engineering Materials of the University of Newcastle upon Tyne, during the period October 1978 to September 1981 under the supervision of Professor K.H. Jack and Dr. A. Hendry.

A study of the relationship between the structure and mechanical properties of nitrided iron-titanium alloys is described as part of a wider investigation at Newcastle on the effect of substitutional alloying elements on the behaviour of nitrogen in iron.

D.S. Ricketby

July 1982.

ACKNOWLEDGEMENTS

I am indebted to Professor K.H. Jack and Dr. A. Hendry for advice, encouragement and the general supervision of the work.

I also wish to thank:

the Science Research Council for the award of a maintenance grant;

members of the electron optical group, Department of Metallurgy and Engineering Materials, for their technical assistance with the scanning electron microscope;

Mr. M. Naylor of Cambridge University, for his assistance with the hot-hardness tester;

many colleagues, past and present, in the Crystallography Laboratory for their stimulating company over the past three years;

the technical staff of the Crystallography Laboratory for their assistance;

Mrs. M. Bennett for typing the script;

Pam for her help in the preparation of this thesis.

July 1982.

ABSTRACT

As shown by hardness, lattice parameter and electron microscopy observations, constant activity nitriding of iron-titanium alloys in the temperature range 400-650°C leads to the formation of mixed substitutional-interstitial clusters. A model for the zone structure of Fe-Ti alloys containing < 0.3 a/o Ti, deduced from internal friction and weight-change measurements, is proposed in which nitrogen atoms occupy four kinds of octahedral site, two of which give rise to internal friction. The distribution of nitrogen atoms between these sites depends on nitriding temperature, rate of quench, titanium content and the nitrogen potential.

Low-temperature aging of nitrided Fe-Ti alloys leads to transfer of nitrogen between these octahedral sites with nitrogen atoms condensing onto the Ti-N zones formed at nitriding temperature. The transformations which take place are analogous to those in quench-aged nitrogen-ferrite except the stabilities of the "Fe-N" clusters and the α''-$Fe_{16}N_2$ are enhanced by the Ti-N clusters on which they form.

High increases in strength result on nitriding but the product is brittle, with further strength increases occurring on aging at temperatures > 580°C. These increases in strength on aging are correlated with changes in zone

structure and distribution inferred from internal friction measurements and electron microscopy observations. The maximum strength increases are proportional to the square root of the titanium concentration and are highly temperature dependent, suggesting chemical strengthening as the major hardening mechanism in nitrided Fe-Ti alloys. A grain size analysis shows that clustering increases the temperature dependent component of the friction stress and also the Hall-Petch slope. Aging at high temperatures causes the substitutional-interstitial zones gradually to transform to the equilibrium precipitate, TiN, with deformation by glide dislocations changing from a cutting to a looping or Orowan mechanism with a corresponding increase in work-hardening rate and reductions in friction stress and Hall-Petch slope.

By cold-working Fe-Ti alloys prior to nitriding, large strength increases are produced and the product is more ductile than annealed and nitrided material. This is attributed to replacement of grain boundaries, onto which titanium nitride precipitates causing embrittlement, by a fine dislocation sub-cell structure. However, nitriding cold-worked iron-titanium alloys at temperatures where only recovery processes occur results in a brittle product, the origins of which are discussed. Although the mechanism of strengthening in annealed and nitrided alloys has been established the complex microstructure of cold-worked and nitrided material prevents detailed analysis of the strengthening process.

CONTENTS

			page
Chapter I		INTRODUCTION	1
Chapter II		PREVIOUS WORK	3
	II.1	The Iron-Nitrogen Phase Diagram	3
	II.2	The Quench-Aging of Nitrogen-Ferrite	4
	II.3	Fe-X-N Systems	5
		(i) Introduction	5
		(ii) Conditions for zone formation	7
	II.4	The Iron-Titanium-Nitrogen System	10
		(i) The structure of nitrided Fe-Ti alloys	10
		(ii) Proposed structural models for nitrided Fe-Ti alloys	12
		(iii) The nitriding kinetics of Fe-Ti alloys	15
		(iv) Mechanical properties of Fe-Ti-N alloys	15
Chapter III		ALLOY MATERIALS	18
	III.1	The Preparation of Alloy Samples	18
	III.2	The Lattice Parameters of Fe-Ti Alloys	20

			page
Chapter IV		EXPERIMENTAL METHODS	24
	IV.1	Ammonia-Hydrogen Nitriding	24
	IV.2	Nitriding Apparatus	26
	IV.3	Nitriding Procedure	27
	IV.4	Optical Metallography	28
	IV.5	Hardness Measurements	28
	IV.6	Preparation of Specimens for Transmission Electron Microscopy	30
	IV.7	Electron Microscopy	30
	IV.8	X-Ray Diffraction	30
	IV.9	Internal Friction Equipment	31
	IV.10	Mechanical Testing	33
Chapter V		THE SCOPE OF THE PRESENT INVESTIGATION	34
Chapter VI		THEORETICAL AND PRACTICAL ASPECTS OF INTERNAL FRICTION	36
	VI.1	Formal Theory of Anelasticity	36
	VI.2	Measures of Internal Friction	42
	VI.3	Dynamic Properties of the Standard Anelastic Solid as a Function of Temperature	43
	VI.4	Internal Friction Arising from Interstitial Atoms - the Snoek Relaxation	45
	VI.5	Factors Affecting the Measurement of the Snoek Peak	47

			page
Chapter VII		THERMOCHEMISTRY AND ZONE STRUCTURE OF Fe-Ti-N ALLOYS	50
	VII.1	Introduction	50
	VII.2	Internal Friction of Nitrided Fe-Ti Alloys	51
	VII.3	Resolution of Internal Friction Damping Spectra	60
	VII.4	Nitrogen Absorption Isotherms for Nitrided Fe-Ti Alloys	64
	VII.5	Discussion	70
Chapter VIII		QUENCH-AGING OF NITRIDED Fe-Ti ALLOYS	74
	VIII.1	Introduction	74
	VIII.2	Results and Discussion	75
	VIII.3	Conclusions	86
Chapter IX		STRENGTHENING MECHANISMS IN Fe-Ti-N ALLOYS	87
	IX.1	Introduction	87
	IX.2	The Effect of Nitriding Potential and Time on Mechanical Properties	94
	IX.3	Grain Size Dependence of Mechanical Properties for Fe-0.18 w/o Ti	97
	IX.4	The Mechanical Properties of Aged Fe-Ti-N Alloys	105
	IX.5	Temperature Dependence of Yield Strength in Fe-Ti-N Alloys	112

			page
	IX.6	Strengthening Mechanisms - General Discussion	116
	IX.7	Electron Metallography of Deformed Alloys	123
	IX.8	Conclusions	126
Chapter X		THE INFLUENCE OF COLD WORK ON THE MECHANICAL PROPERTIES OF Fe-Ti-N ALLOYS	128
	X.1	Introduction	128
	X.2	The Effect of Nitriding Potential on Mechanical Properties	128
	X.3	The Influence of Nitriding Temperature on the Properties of Cold-Worked Fe-Ti Alloys	132
	X.4	The Variation of Mechanical Properties of Nitrided Fe-Ti Alloys with Percentage Cold-Work	137
	X.5	High-Temperature Aging of Cold-Worked and Nitrided Fe-Ti Alloys	140
	X.6	General Discussion	141
	X.7	Conclusions	143
Chapter XI		CLUSTERING IN A COMMERCIAL STEEL	144
	XI.1	Introduction	144
	XI.2	Results and Discussion	144

page

Chapter XII GENERAL DISCUSSION 150

REFERENCES 154

LINE DRAWINGS NEGATIVE NUMBER INDEX

Figure	Negative Number	Figure	Negative Number
II.1	C14307	VII.1	D34772
II.2	C13364	VII.2	D34764
II.3	C13374	VII.3	D34776
II.6	D34755	VII.4	D34775
II.7	D34758	VII.5	D34773
II.9	D29252	VII.6	D34774
II.10	D34753	VII.8	D35195
II.11	D34748	VII.9	D34749
		VII.10	D34750
III.1	D34740	VII.11	D35198
III.2	D34763	VII.12	D35197
IV.1	D28513	VIII.1	D31630
IV.2	D34756	VIII.2	D31634
IV.3	D25076	VIII.4	D31631
IV.4	C67456	VIII.6	D35194
IV.5	D24897	VIII.7	D35200
IV.6	D34759	VIII.8	D35193
IV.7	C2017		
IV.8	D25077		
VI.1	D25078		
VI.2	D26203		
VI.3	D24898		
VI.4	D27615		

LINE DRAWINGS NEGATIVE NUMBER INDEX

Figure	Negative Number	Figure	Negative Number
IX.1	D34751	X.1	D39441
IX.2	D34754	X.2	D34768
IX.3	D39442	X.4	D34767
IX.4	D39443	X.8	D34766
IX.7	D34743	X.9	D34769
IX.8	D34738	X.14	D34765
IX.9	D34744		
IX.10	D34760	XI.1	D35199
IX.11	D34396	XI.2	D35196
IX.14	D34739		
IX.15	D34747		
IX.16	D34742		
IX.17	D34745		
IX.18	D34741		
IX.19	D34761		

Chapter I

INTRODUCTION

For many years, steels were strengthened only by grain refinement or by application of the austenite-martensite transformation. In neither of these do second-phase particles contribute directly to the strength of the steel although they may play an important secondary role. As the need for high strength materials developed it was realised that carbon alone could not give satisfactory strength-toughness relationships at these high strength levels and this led to a reduction in carbon concentrations and the use of intermetallic particles to achieve high strength with satisfactory toughness.

Work at Newcastle has shown that "constant activity" nitriding provides a novel method of introducing a high volume fraction of very small precipitates that are analogues of the GP zones in face-centred cubic alloys. These zones or clusters are deformable and lead to a high specific strengthening of the ferritic matrix. The products are extremely hard and, because the zones are stable, the hardness is retained even after heat-treatment in a non-nitriding atmosphere above 700°C. The strength of these alloys is thought to lie in the strength of the interaction between the alloying element and nitrogen, although other factors have been proposed. In order to extend the knowledge already accumulated on these

systems an investigation into one system, namely iron-titanium, seemed worthwhile with particular emphasis on the strengthening processes that occur at different stages of precipitation.

Experimental techniques used in the present investigation include controlled metal-gas equilibration, X-ray diffraction, electron metallography, internal friction and mechanical testing, together with the standard metallographic techniques.

Chapter II

PREVIOUS WORK

II.1 The Iron-Nitrogen Phase Diagram

Figure II.1 shows the iron-nitrogen phase diagram. There are five major phases formed with increasing nitrogen potential: α-nitrogen-ferrite, γ-nitrogen-austenite, γ'-Fe_4N, ϵ-$Fe_{3-2}N$ and ζ-Fe_2N. There are two additional phases: α'-nitrogen-martensite obtained by quenching γ-nitrogen-austenite, and α''-$Fe_{16}N_2$ formed during the tempering of nitrogen-martensite or the aging of nitrogen-ferrite. At the eutectoid temperature of 590°C nitrogen-austenite contains 9.4 a/o nitrogen and the maximum solubility of nitrogen in ferrite is $\simeq$ 0.4 a/o. The γ'-phase has a face-centred cubic arrangement of iron atoms, like austenite, but the nitrogen atoms occupy one-quarter of the number of available octahedral interstices in a completely ordered manner.

The structure of body-centred tetragonal α''-$Fe_{16}N_2$ can be regarded as a fully ordered supersaturated solid solution of nitrogen in body-centred cubic iron, i.e. a fully ordered martensite. Alternatively, it is a distorted "Fe_4N" in which alternate nitrogen atoms are missing and which fits with the ferrite matrix with a Bain orientation relationship, (Jack, 1951a). α''-$Fe_{16}N_2$ is therefore

Figure II.1

The iron-nitrogen phase diagram

(after Jack, 1951)

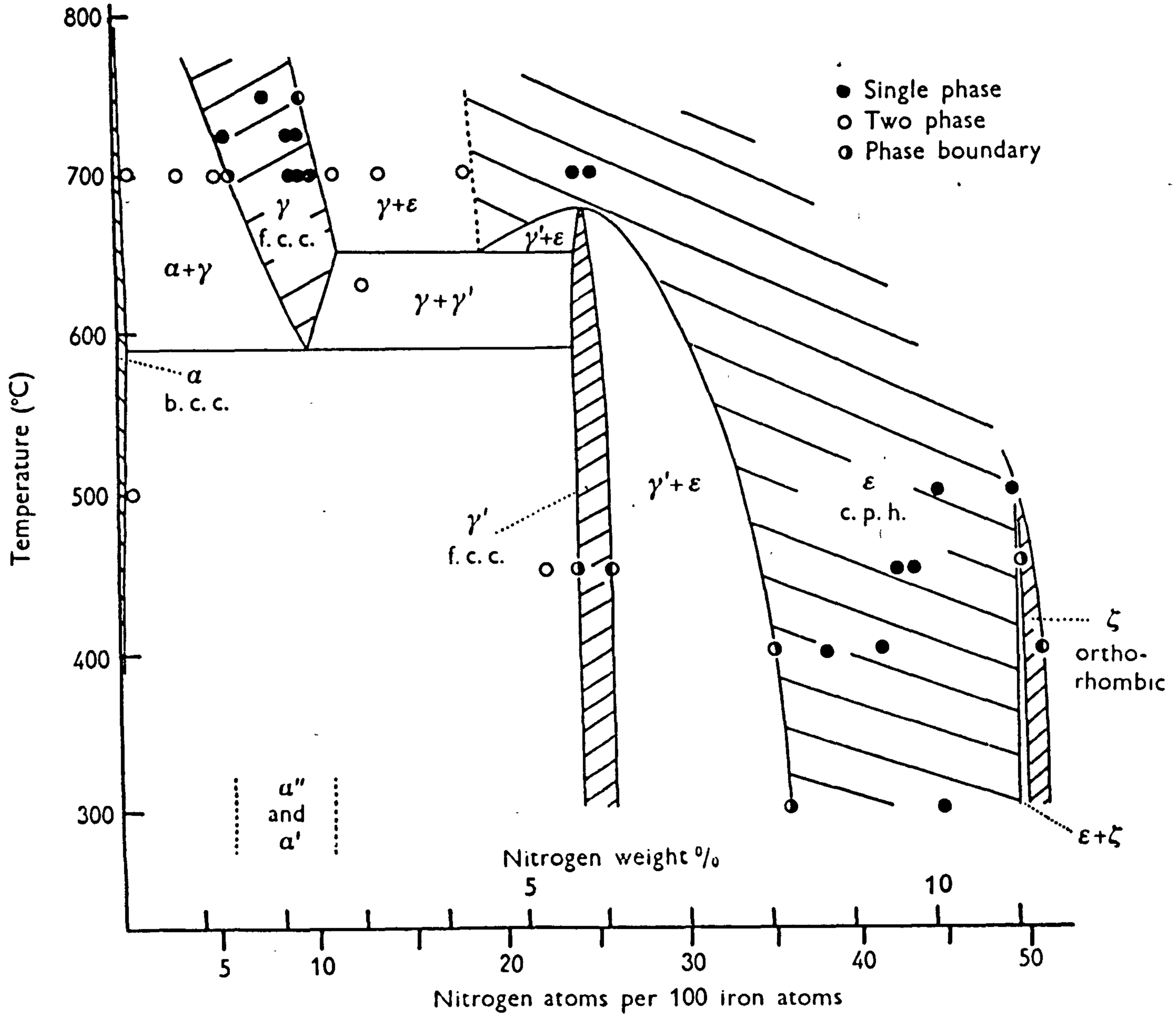
800
700
600
500
400
300
Temperature (°C)
Single phase
Two phase
Phase boundary
γ
f. c. c.
γ+ε
γ'+ε
α+γ
γ+γ'
α
b. c. c.
γ'
f. c. c.
γ'+ε
ε
c. p. h.
ζ
ortho-
rhombic
ε+ζ
α"
and
α'
Nitrogen weight %
5
10
5
10
20
30
40
50
Nitrogen atoms per 100 iron atoms

intermediate both in structure and in composition between b.c.c. N-ferrite and f.c.c. γ'-Fe_4N.

II.2 The Quench-Aging of Nitrogen-Ferrite

An investigation into the solubility of Fe_4N in α-iron at various temperatures (Dijkstra, 1949) showed nitrogen in excess of that in equilibrium with Fe_4N precipitated by a two-stage process. A new phase formed which preceded the formation of Fe_4N at temperatures between 100° and 300°C, being later identified as α''-$Fe_{16}N_2$ (Jack & Maxwell, 1952a) a phase which occurred during low-temperature decomposition of nitrogen-martensite (Jack, 1951b). Its structure (Figure II.2) is that of a fully ordered tetragonal martensite i.e. a b.c.c. arrangement of iron atoms anisotropically expanded in the c dimension because one in twenty-four octahedral interstices are occupied in an ordered manner. There is a consequent small contraction of the lattice in a directions (see Figure II.3). The structure is in fact ferrite with a nitrogen superlattice which causes some tetragonal strain. The α'' structure fits perfectly coherently with the ferrite matrix in "a" directions but there is a misfit in the "c" dimension. Therefore α''-$Fe_{16}N_2$ grows as plates, thin in the c direction, by diffusion, clustering and ordering of nitrogen atoms; no major movement of iron atoms is involved.

Figure II.2

The structure of α''-$Fe_{16}N_2$

(after Jack, 1951a)

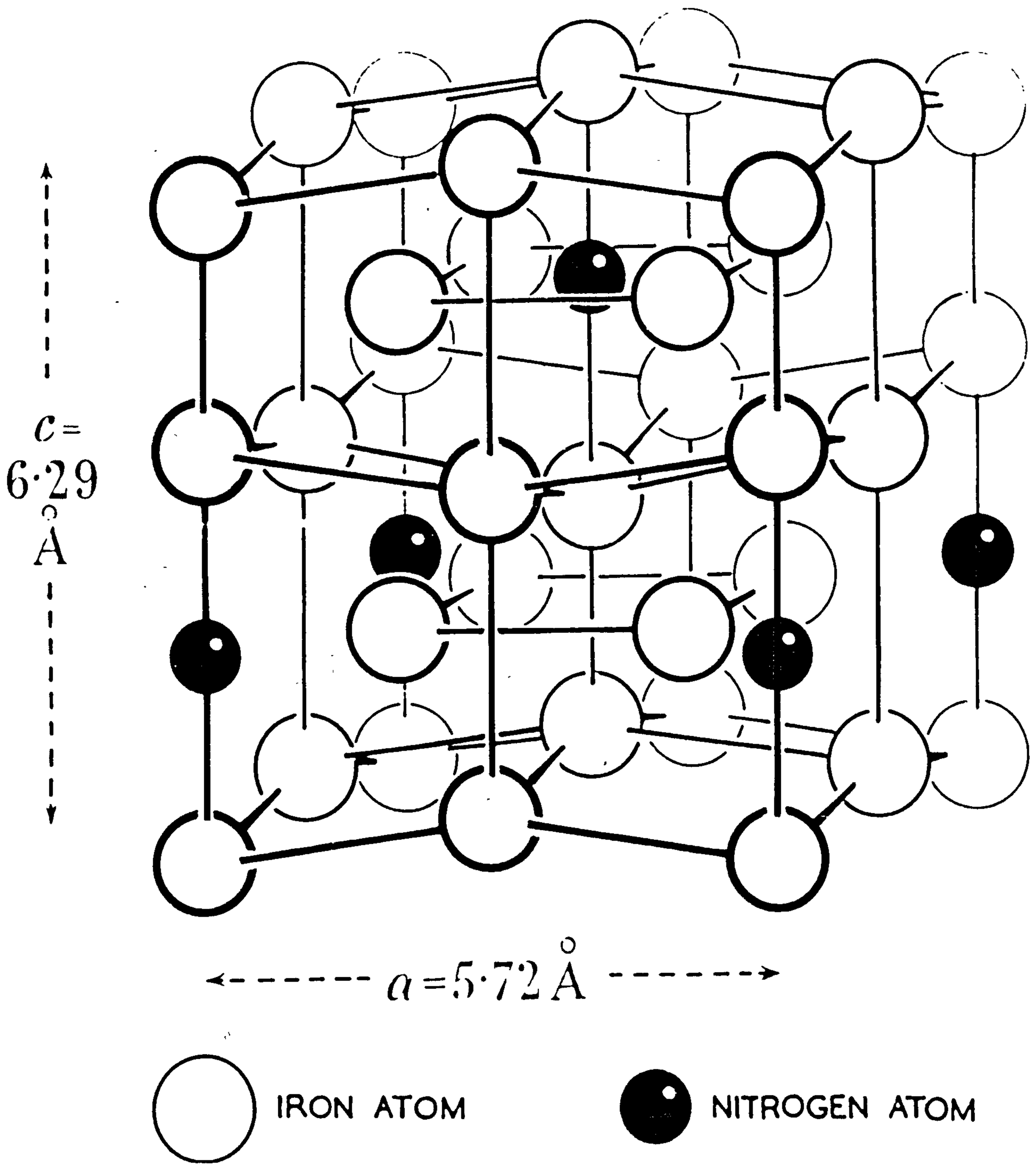
c = 6·29 Å
a = 5·72 Å
IRON ATOM
NITROGEN ATOM

Figure II.3

Unfilled and filled octahedra in b.c.c. α-iron

(after Jack, 1951b)

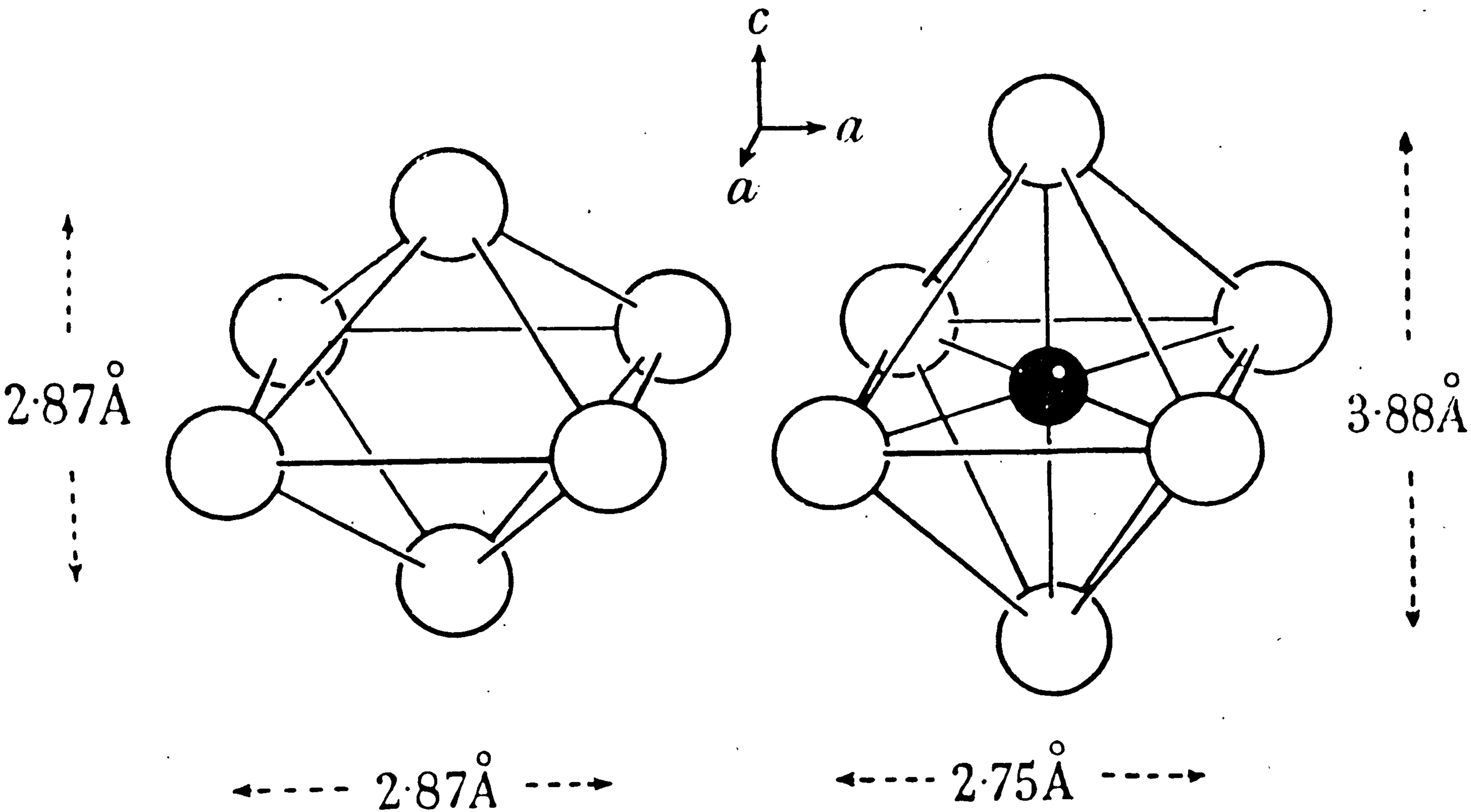
c
a
a
2·87Å
3·88Å
2·87Å
2·75Å

It was observed by Roberts (1970) that at high supersaturations and low temperatures (~20°C) precipitation of α''-$Fe_{16}N_2$ was homogeneous and preceded by Guinier-Preston zone formation (see Figure II.4). However, at low supersaturations and high temperatures precipitation was found to be heterogeneous (see Figure II.5). Subsequent work by Ferguson (1981) confirmed these observations and further showed at intermediate nitrogen levels ($\simeq$ 0.16 a/o N) nitrogen-atom cluster formation takes place only after an incubation period and these clusters rapidly coarsen to form α''-$Fe_{16}N_2$.

The precipitation of γ'-Fe_4N occurs at the expense of α''-$Fe_{16}N_2$ after long aging times above about 200°C, and also forms as a grain boundary precipitate during the early stages of aging at these temperatures (Roberts, 1970). γ'-Fe_4N grows as plates such that (112)γ' is parallel to the plate surface (Mehl et al., 1934; Brooker et al., 1957).

II.3 Fe-X-N Systems

(i) Introduction

The substitutional-interstitial solute interactions occurring in nitrogen ferrites can be classified as taking place in three distinct ranges of temperature: high, medium, and low defined by the relative mobilities of the

Figure II.4

Fe-0.07 w/o N quench aged 5.5 h at 23°C. Bright field and diffraction pattern (after Ferguson, 1981)

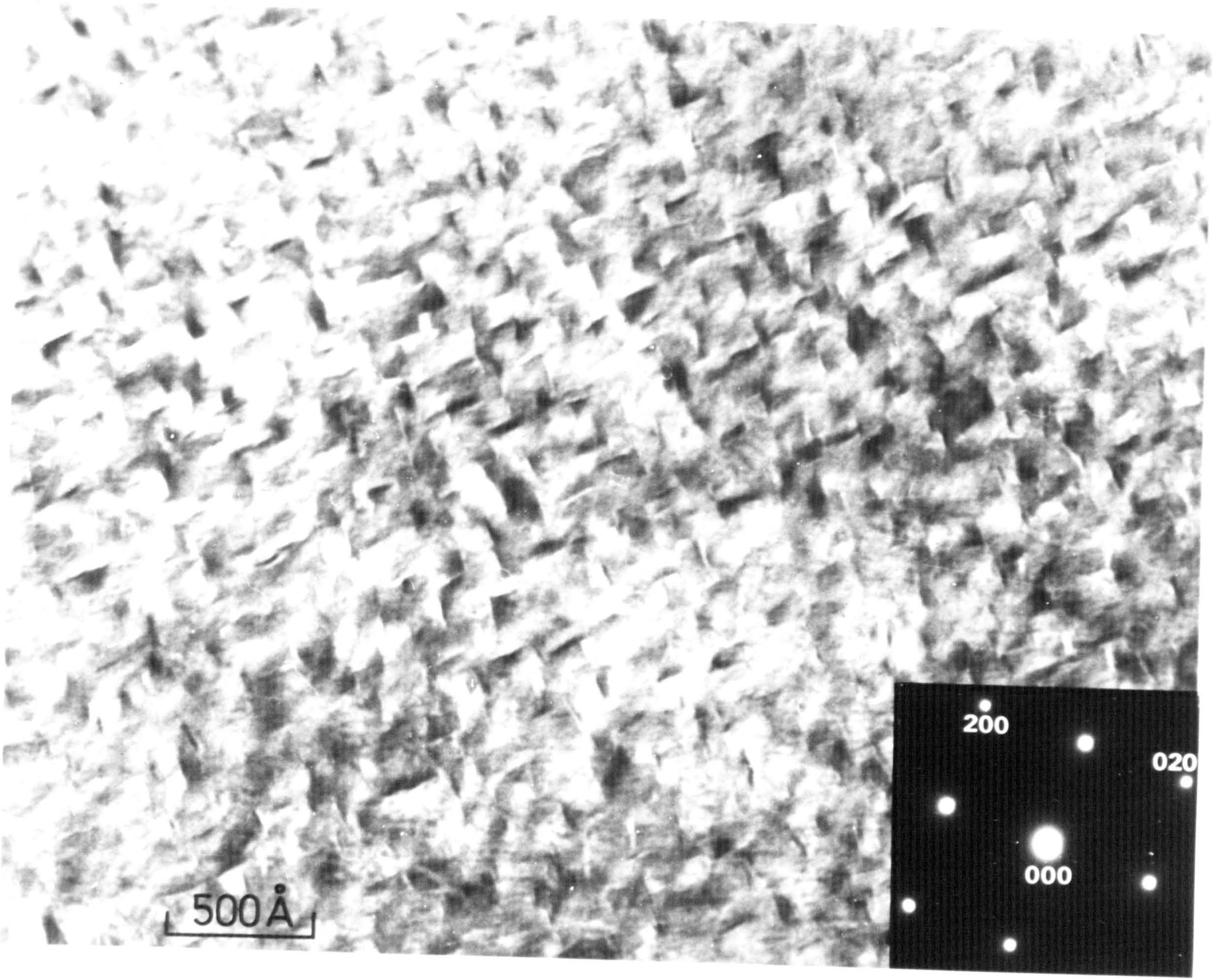
500 Å
200
020
000

Figure II.5

Fe-0.013 w/o N quench aged 664 d at 23°C

(a) Bright field.

(b) Centred dark field using an α''-$Fe_{16}N_2$ diffraction spot.

(after Ferguson, 1981)

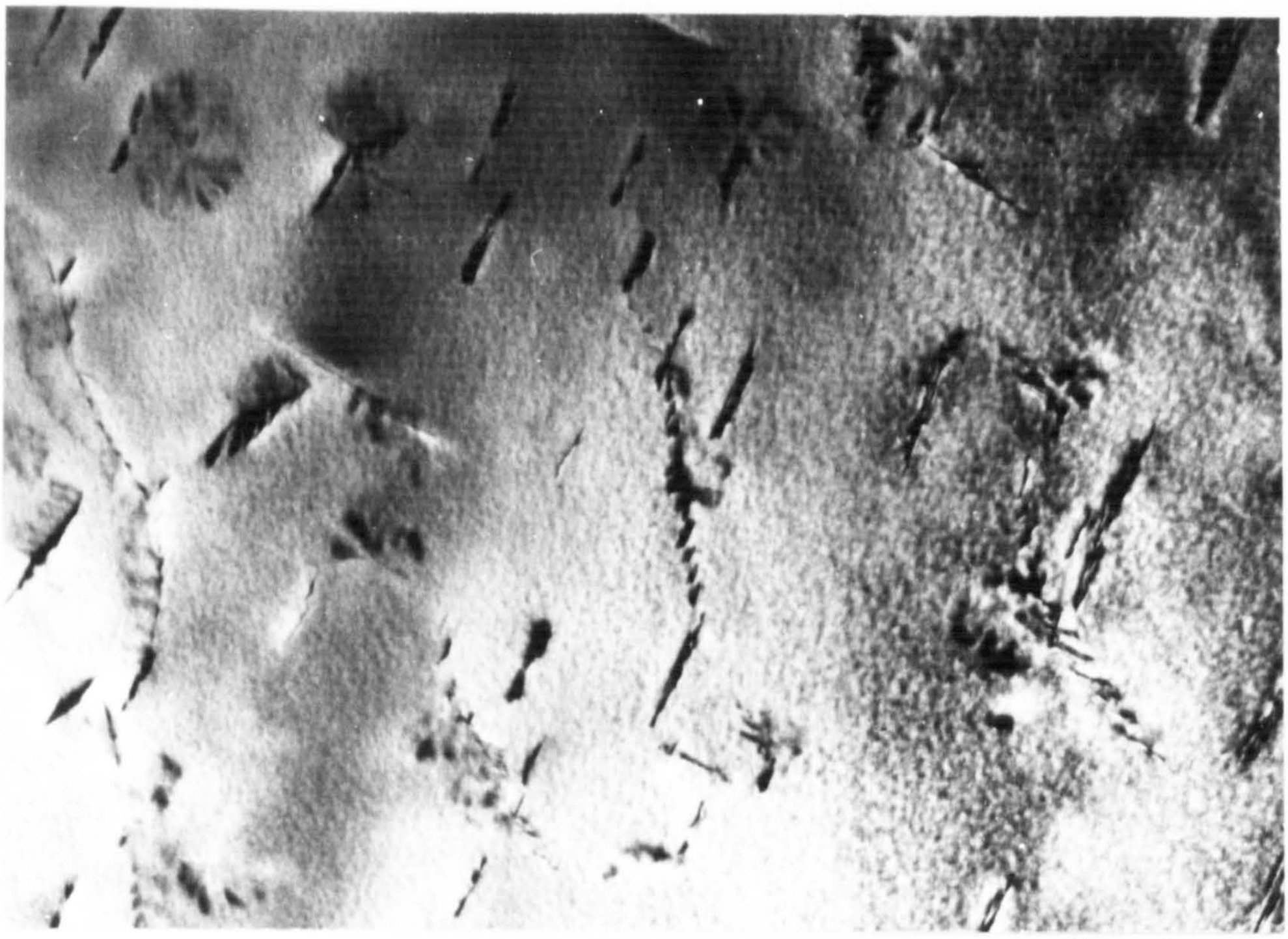

(a)

0·4μ

[200]

(001)

[020]

(b)

substitutional and interstitial solutes. At high temperatures substitutional solutes such as Ti, V, Cr, Mn, Nb, Mo, Ta, and W move readily through the ferrite matrix to precipitate alloy nitrides by reaction with nitrogen. At low temperatures where these solutes are unable to move they still affect the precipitation of iron nitrides because they change the activity coefficients of interstitial elements (Pipkin, 1968; Speirs, 1969; Mortimer et al., 1972).

During conventional quench-aging of Fe-X-N alloys the precipitation reaction depletes the matrix nitrogen concentration and rapidly decreases the driving force for continued precipitation making interpretation of the resulting microstructures difficult. However, by maintaining an appropriate nitrogen activity at the specimen surface precipitation takes place continuously at a rate controlled by the slowly diffusing substitutional solute. By using this technique of "constant activity aging" at intermediate temperatures (350-650°C), where substitutional atoms can move only over short distances compared with interstitial nitrogen, then mixed substitutional-interstitial clusters or GP zones are formed (Speirs et al., 1970). The clustered non-random solid solution is a pre-precipitation stage in a continuous series of transformations and results in pronounced strengthening of the ferritic matrix. Prolonged overaging shows that clustering is the first of a sequence of homogeneous precipitation stages

analogous to those observed in the classical work on Al-Cu alloys (Speirs et al., 1970). These changes are similar to those observed during quench-aging of Fe-N alloys at 0-200°C except the presence of the substitutional solute raises the transformation reaction to higher temperatures.

The precipitation sequence can be represented as:

$$\underset{\text{I}}{\text{zones}} \xrightarrow{(1)} \underset{\text{IIa}}{\alpha''\text{-type intermediate}} \xrightarrow{(2)} \underset{\text{IIb}}{\gamma'\text{-type intermediate}} \xrightarrow{(3)} \underset{\text{III}}{\text{equilibrium precipitate}}$$

where homogeneous precipitation occurs by continuous clustering and subsequent ordering within the clusters of both interstitial and substitutional solutes. The designations α'' and γ' are not meant to imply rigid structure types but suggest respectively distorted b.c.c. and f.c.c.-metal-atom arrangements accommodating nitrogen with or without ordering of either the substitutional or the interstitial solute atoms. Each particular system is different in detail; for example, in Fe-Mo-N each stage is clearly recognised whereas in Fe-W-N transformation (1) is rapid compared with (3) and so stage II is the first to be observed (Stephenson, 1973a).

(ii) Conditions for zone formation

The general conditions for zone formation in Fe-X-N alloys can be summarised as:

(a) the nitrogen potential must exceed that of the zone solvus;

(b) there must be a strong interaction between the substitutional solute and nitrogen and the most effective solutes are those which decrease the activity coefficient f_n^x of nitrogen in iron (see Figure II.6), that is, they increase the solubility of nitrogen prior to precipitation;

(c) the substitutional solute must have a high affinity for nitrogen (see Figure II.7);

(d) the temperature should be high enough for movement of substitutional atoms over short distances but not so high as to allow large-scale metal atom movement and thus the ready nucleation and growth of the equilibrium alloy nitride.

Since the GP zones observed in these alloys are very small and only a few atom layers thick it might be argued that they are in fact very small coherent precipitates. However, the evidence that they are true GP zones formed by solute-atom clustering is based on the following observations:

(a) the abnormal N/X ratios in the alloys are higher than can be accounted for by equilibrium

Figure II.6

The effect of alloying elements on the activity coefficient of nitrogen in liquid iron.

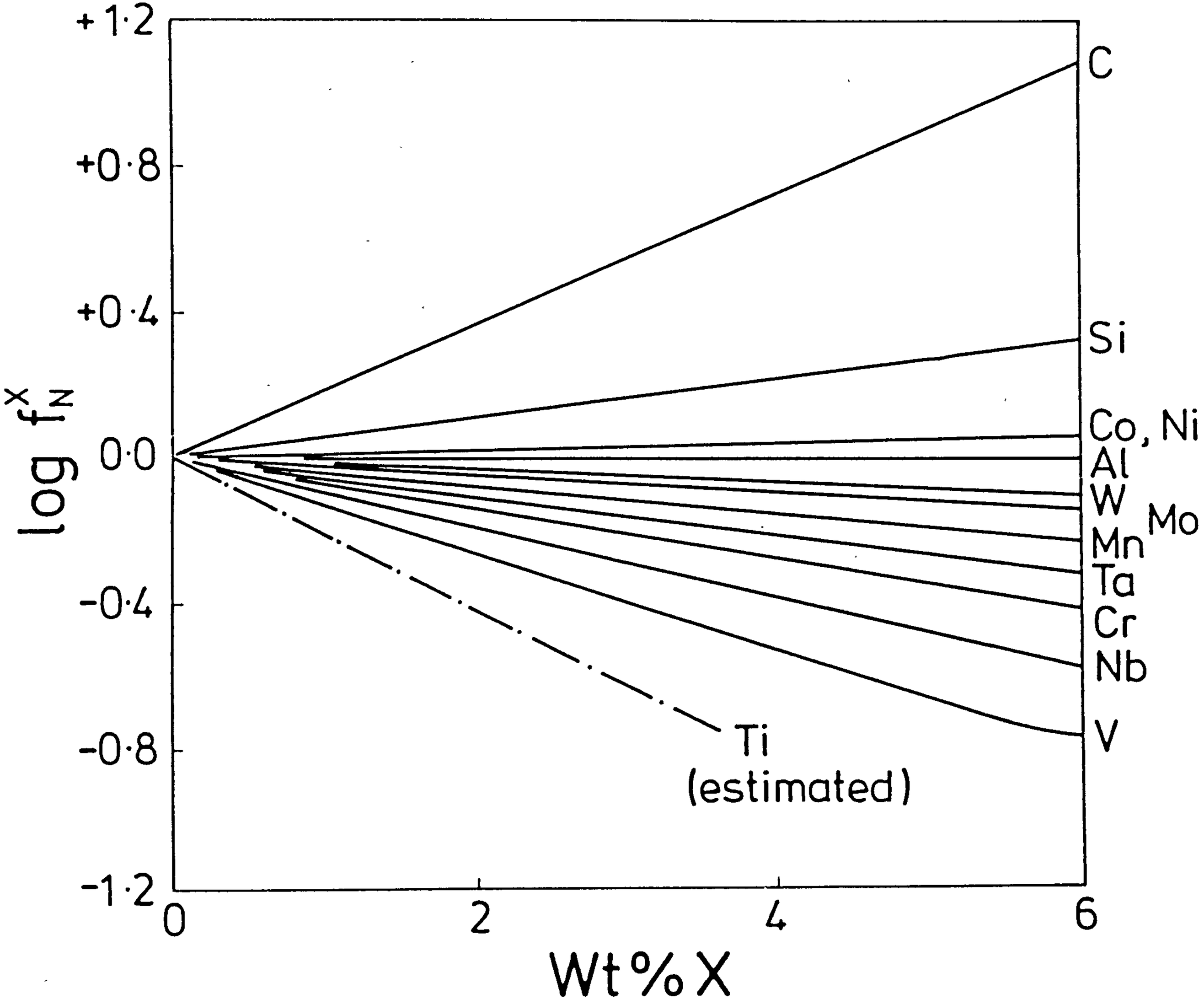
+1·2
+0·8
+0·4
0·0
-0·4
-0·8
-1·2
log f X N
0
2
4
6
Wt% X
C
Si
Co, Ni
Al
W
Mo
Mn
Ta
Cr
Nb
V
Ti
(estimated)

Figure II.7

The standard free energy of formation of some nitrides.

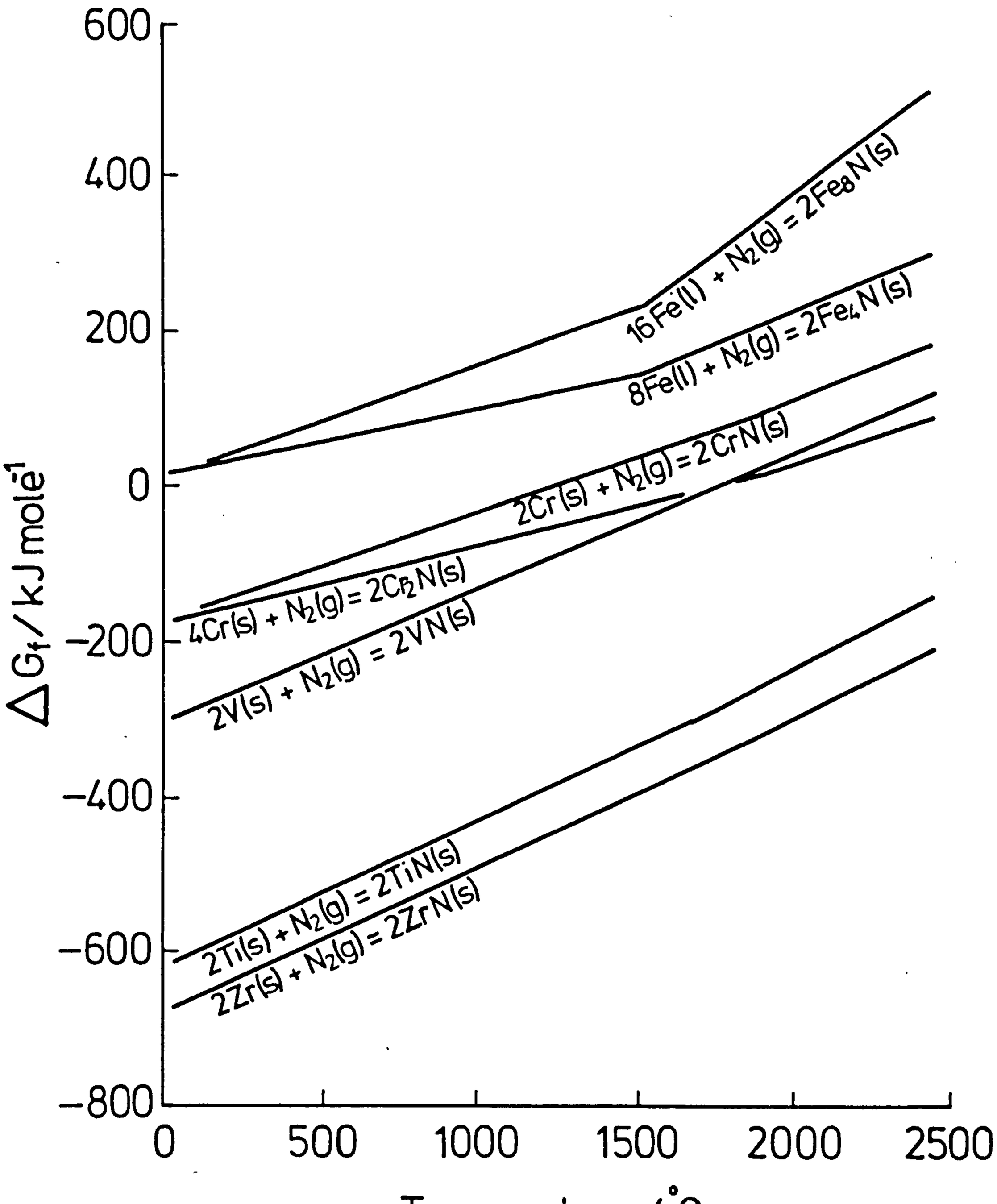

The reference states are pure phases which are stable at one atmosphere pressure and the designated temperature.

nitride precipitates (Jack, 1975);

(b) very high nitrogen potentials are required to form the zones compared with those necessary to precipitate the equilibrium nitride;

(c) a zone solvus which is different from the solvus for the equilibrium nitride is observed (Roberts, 1970; Stephenson, 1973a);

(d) continuous streaking of matrix reflections with no maxima characteristic of the precipitate structure occurs on electron diffraction patterns of nitrided Fe-X alloys;

(e) the interstitial content of clusters in nitrided Fe-3 a/o Mo can be continuously changed and reduced to zero by aging in hydrogen at 580°C to leave Mo atom clusters on {100} matrix planes. These Mo clusters cannot be produced in Fe-3 a/o Mo without the introduction of nitrogen nor can they be obtained by decomposition of the equilibrium nitride precipitate (Driver et al., 1972).

Additional evidence for clustering is obtained from matrix unit-cell dimensions because a matrix containing GP zones is a non-random solid solution but its unit-cell dimensions are the same as for a random solid solution of

the same solute concentration (Krawitz & Sinclair, 1975). Only when precipitation occurs is the lattice parameter reduced to that of the depleted solid solution. The unit-cell edge length of a substituted nitrogen ferrite is given by:

$$a_o = a_{Fe} + \Delta a_X \text{ (a/o X)} + \Delta a_N \text{ (a/o N)}$$

where a_{Fe} is the cell dimension of pure α-iron (2.8664 Å), and Δa_X and Δa_N are the increases caused by solution of 1 a/o of metal (X) and nitrogen (N) respectively. Δa_N is considerably larger than Δa_X due to the large dilation that occurs when an octahedral interstice is occupied by C or N (see Figure II.3) and so small concentrations of N can be determined precisely by simple measurement of X-ray powder patterns. The unit-cell dimensions of constant activity nitrided Fe-Mo, Fe-V (Pope et al., 1975) and Fe-Ti alloys (Henderson, 1976) are in close agreement with those expected for iron containing the same amount of solute in random solution, but electron microscopy, field ion microscopy and electron diffraction patterns indicate that the solute atom distribution cannot be random. The solute atoms must therefore be clustered in a non-random solid solution.

II.4 The Iron-Titanium-Nitrogen System

(i) The structure of nitrided Fe-Ti alloys

Electron microscopy of Fe-Ti alloys nitrided in the

range 350-650°C shows irresolvable random dot contrast under general imaging conditions (Phillips & Seybolt, 1968; Jack, 1976; Henderson, 1976). However, contrast under two-beam dynamical conditions is similar to that observed in Cu-2 w/o Be alloys (Tanner, 1966; Phillips & Tanner, 1971). A chequered "tweed" pattern is observed when $\bar{g} = \langle 200 \rangle$ in a $[001]_\alpha$ zone with orthogonal basket-weave texture whose weave directions are parallel to $\langle 110 \rangle$ directions (Figure II.8). The diffraction patterns from as-nitrided specimens are characterised by extensive streaking in $\langle 100 \rangle$ ferrite directions as shown in Figure II.8. These two observations led D.H. Jack to propose that nitrided iron-titanium alloys consist of closely spaced thin plates which form on the $\{100\}$ matrix planes (Jack, 1976). And by analogy with ordered nuclei in CoPt alloys, where the elastic interaction between precipitate plates which cause tetragonal distortions lead to a pseudo-periodic array to maximise the number of edge-face configurations, the author further suggested the arrangement of plates to be as shown in Figure II.9. This pseudo-periodic array of tetragonal centres leads to diffuse scattering on X-ray diffraction patterns (Kirkwood et al., 1974; Henderson, 1976). This diffuse scattering was wrongly interpreted by Kirkwood et al. (1974) as being due to tetragonal distortions of the matrix, but this implied that precipitate plates only occur on one set of $\{100\}$ matrix planes which is not the case. Later work by Henderson (1976) showed that all observations could be better interpreted as

Figure II.8

Fe-2 w/o Ti nitrided in $30NH_3:70H_2$ at $400^{\circ}C$.

(a) Bright field micrograph showing tweed contrast.

(b) Diffraction pattern.

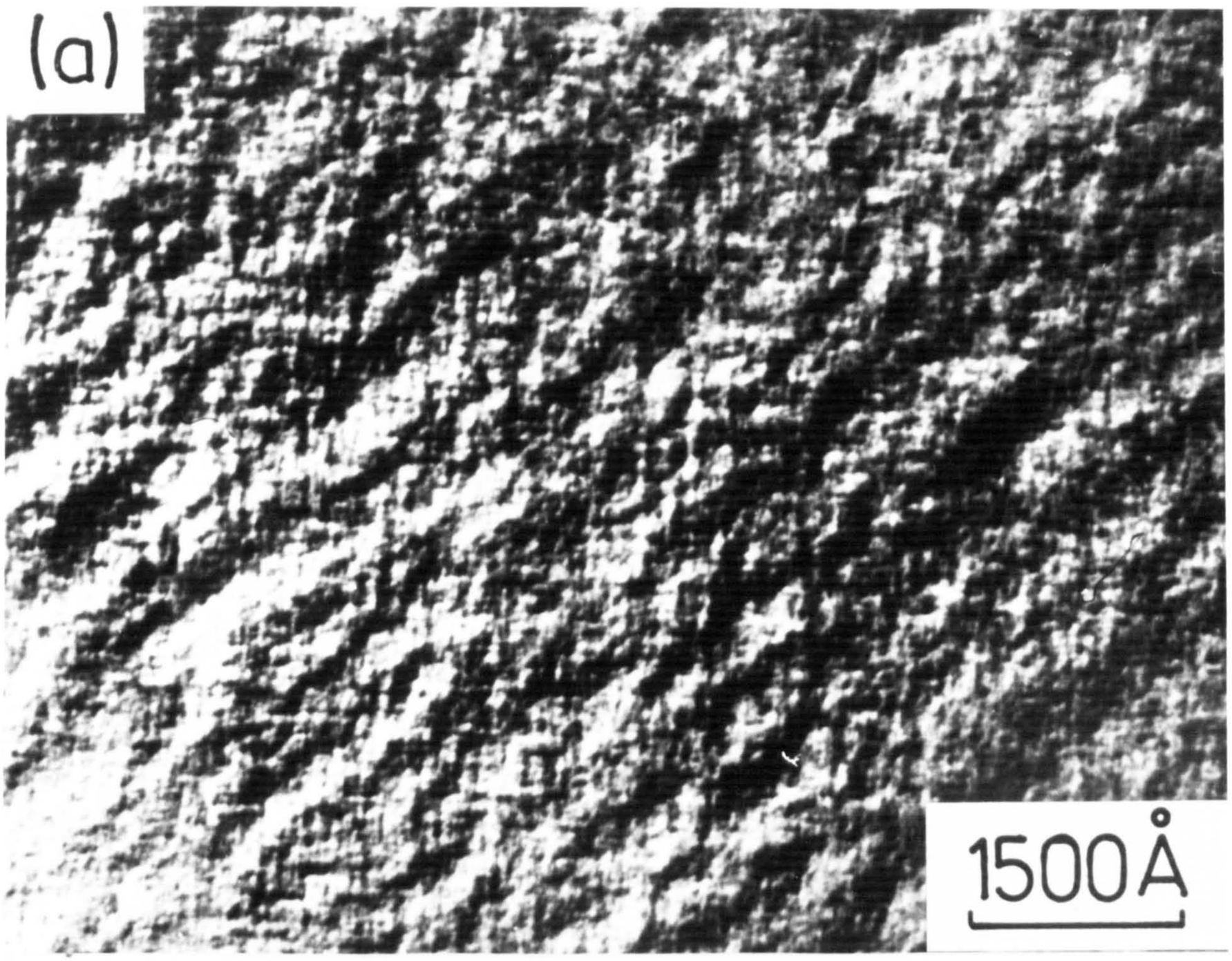
(a)
1500Å

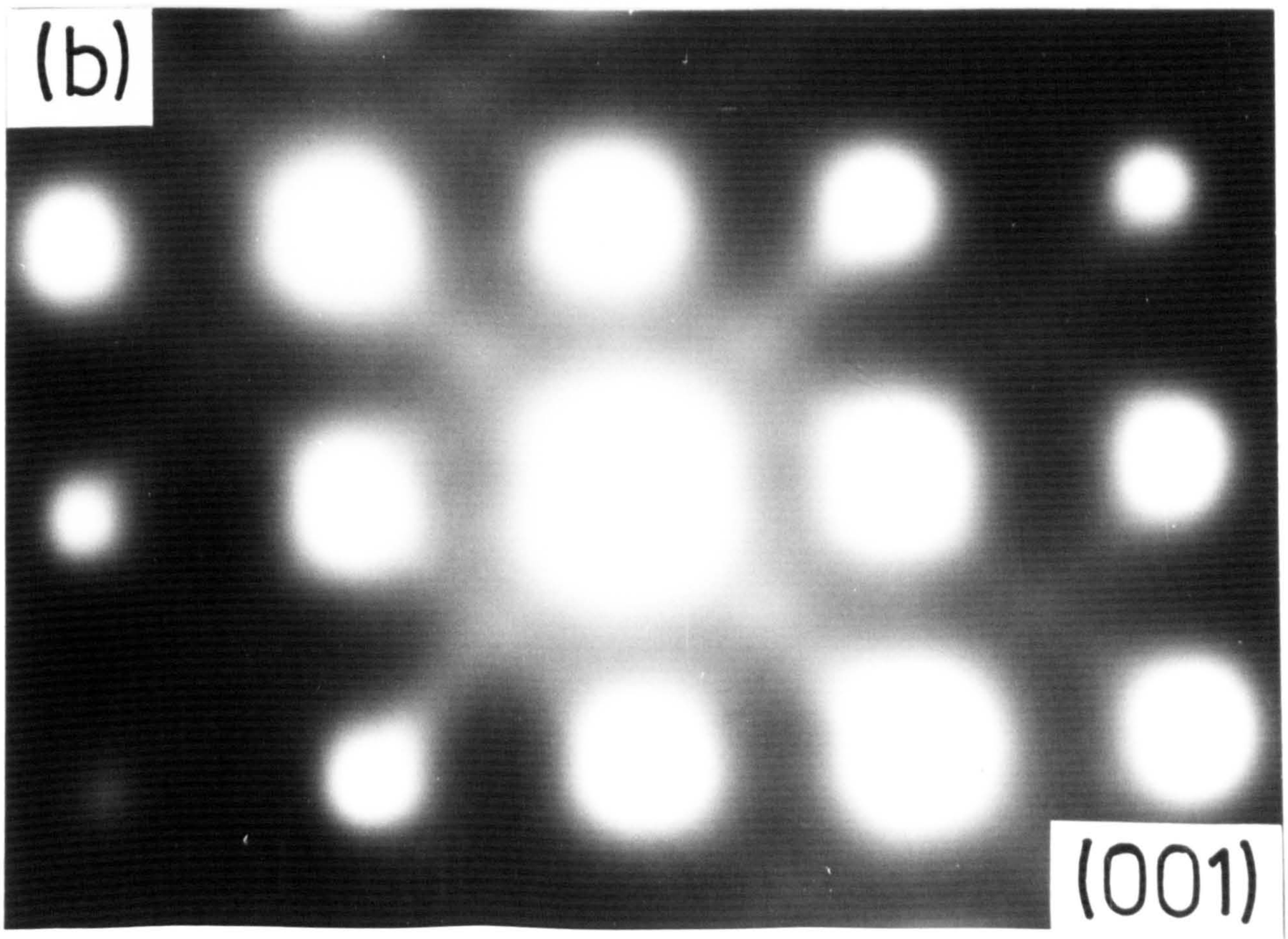
(b)
(001)

Figure II.9

Disposition of disc-shaped zones in b.c.c. α-Fe (after Jack, 1976).

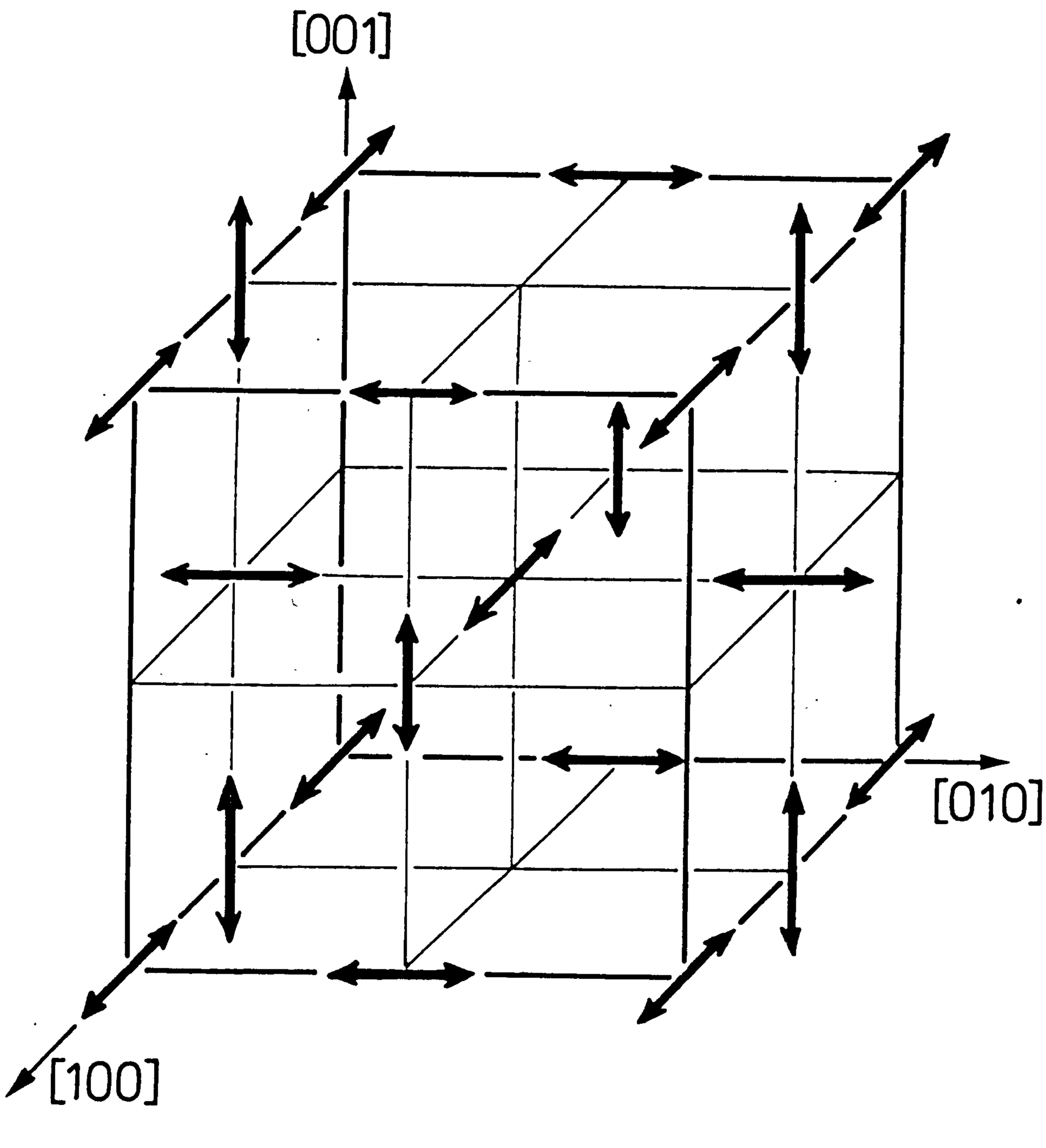
[001]
[010]
[100]

side-bands occurring predominantly on the high-angle side of matrix reflections since the volume fraction of lower d-spacing matrix is much greater than that of the larger d-spacing cluster. The metastable zones overage slowly when aged at high temperatures (800 and 850°C) to give the equilibrium precipitate, f.c.c. TiN, in a Bain orientation relationship with the matrix (see for example Kirkwood et al., 1974).

The nitriding of Fe-Ti alloys leads to nitrogen uptakes which exceed that required for the formation of stoichiometric TiN plus the amount corresponding to the equilibration of the ferrite matrix with the nitriding atmosphere (Jack, 1976; Henderson, 1976; Podgurski & Davis, 1981). The initial N:Ti atom ratio reaches a maximum of about 3:1 at low temperatures and high nitriding potentials and hydrogen reduction reduces this to 1:1. Measurement of matrix unit-cell dimensions of nitrided Fe-Ti alloys are consistent with both Ti and N being effectively in solution, that is, present as substitutional-interstitial GP zones, the Ti and N atoms occupying the same type of crystallographic site as they would in a random solid solution (Jack, 1976; Henderson, 1976).

(ii) Proposed structural models for nitrided Fe-Ti alloys

To explain the observations outlined above the following

models have been proposed for the structure of nitrided Fe-Ti alloys, an additional constraint being that the strong chemical affinity between Ti and N implies that the mutual co-ordination of N and Ti should be a maximum.

(a) Due to D.H. Jack (1976) and K.H. Jack (1978)

The fact that hydrogen reduction removes two-thirds of the total clustered nitrogen shows the remaining one-third to be in a more stable chemical environment. At the 1:1 composition, as suggested by D.H. Jack (1976), the Ti and N are clustered in a monolayer confined to one cube plane of the ferrite matrix (see Figure II.10). Each nitrogen is co-ordinated by 4Ti and 2Fe and the cluster can be regarded as a Fe_2TiN plate. Unlike D.H. Jack (1976) who states that the "excess" nitrogen is accommodated in the tensile-strained region at the periphery of the TiN monolayers, K.H. Jack (1978) believes that it occupies octahedral interstices in the next metal-atom layers above and below the central disc (Figure II.10). The additional nitrogens are thus co-ordinated by 5Fe and 1Ti; the zone composition is then Fe_4TiN_3. This model accounts for two-thirds of the nitrogen being in a less stable chemical environment and also for the N:Ti atom ratios of 1:1 and 3:1.

There exists therefore three sites for nitrogen atoms:

Figure II.10

Nitrogen atom environments in nitrided Fe-Ti alloys (after Jack, 1978).

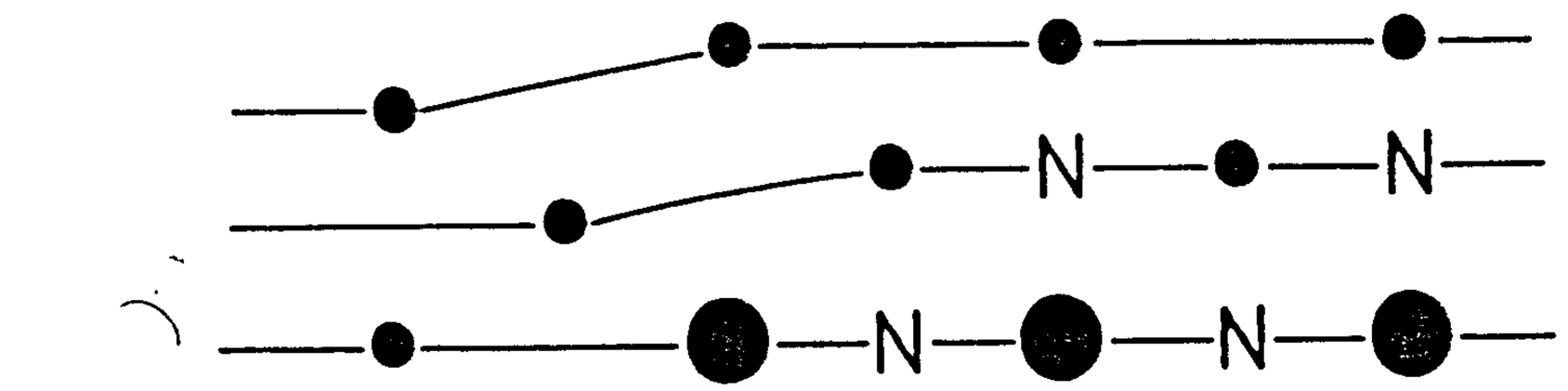

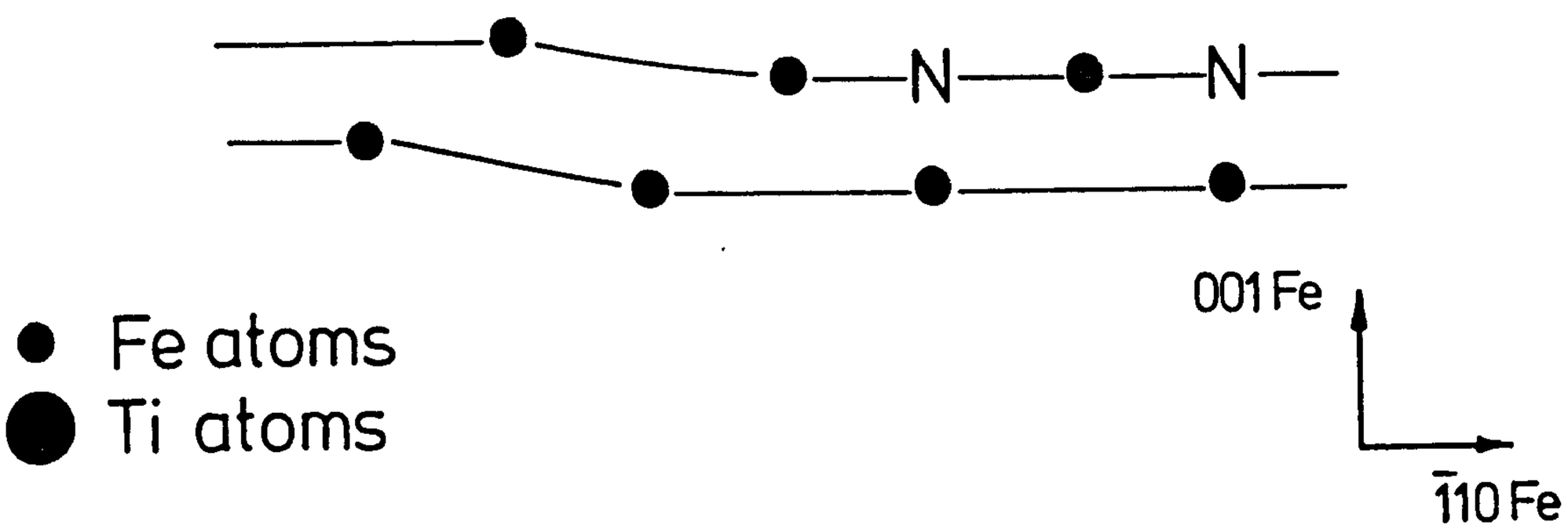

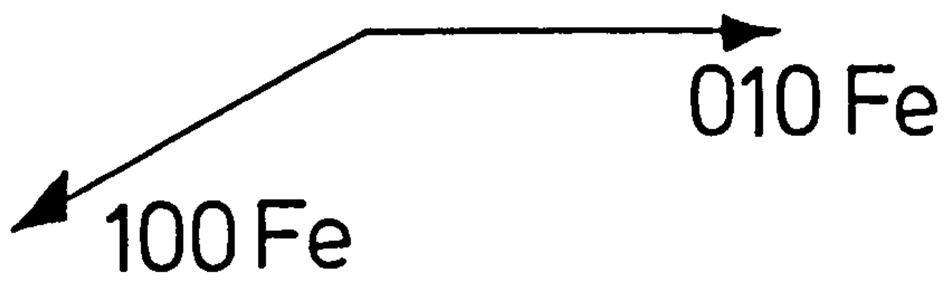

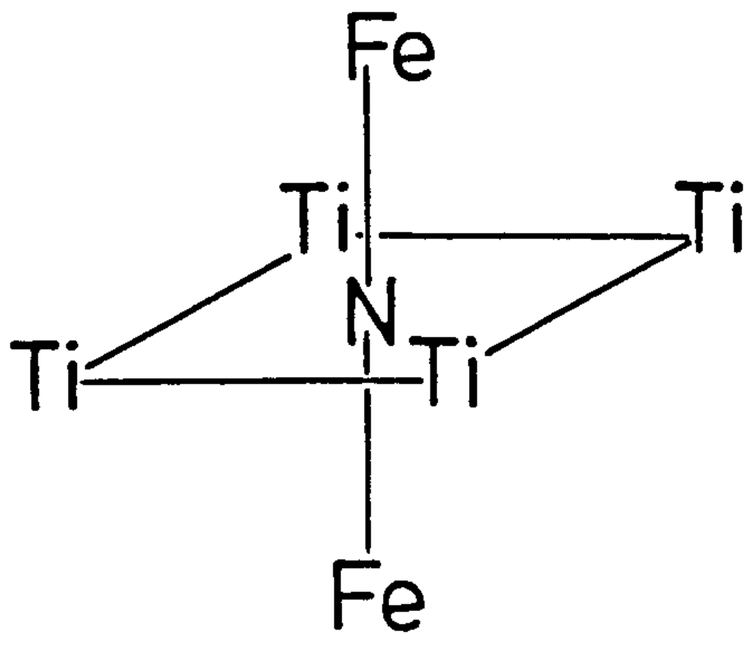

monolayer site

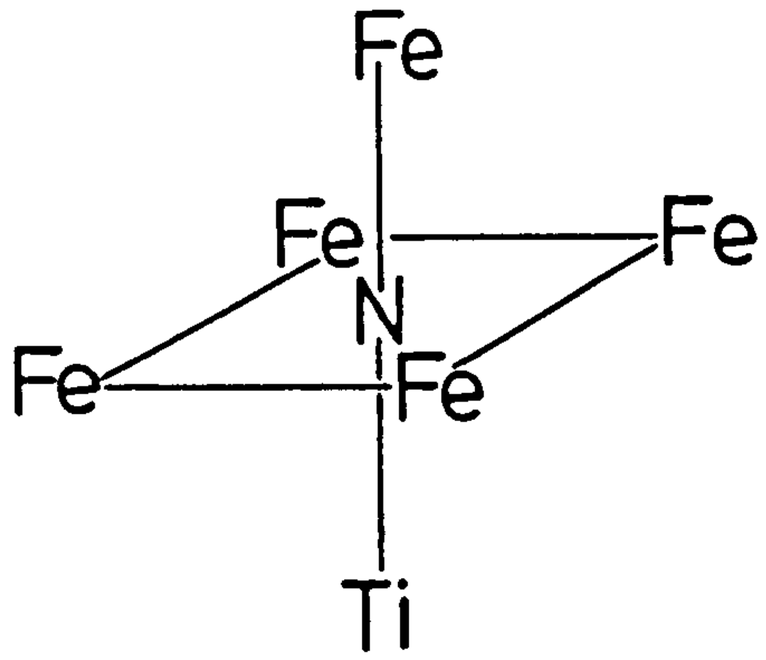

"excess nitrogen" site

(1) nitrogen bonded to Ti as a TiN monolayer;

(2) nitrogen dissolved in the ferrite matrix;

(3) "excess" nitrogen, which according to K.H. Jack (1978) occupies the flat faces of the monolayer to produce TiN_x where x can take any value between 1 and 3.

(b) Due to Podgurski & Davis (1981).

Nitrogen absorption studies, transmission electron microscopy and Mossbauer investigations showed nitrogen to exist as three distinct species:

(1) nitrogen bonded to Ti as TiN;

(2) nitrogen dissolved in the ferrite matrix;

(3) "interface" nitrogen, that absorbed at the ferrite-TiN interface to produce TiN_x where x can take any value between 1 and 2.

The additional or loosely bound nitrogen in TiN_2 occupies every fourth interstitial site in the two ferrite planes immediately above and below the TiN platelet (see Figure II.11 a,b). Using linear elasticity theory the authors predicted that a homogeneously dilated ferrite matrix could result from a dispersion of small coherent particles, and thereby suggested the solubility of nitrogen to be uniform throughout the ferrite matrix.

Figure II.11

Nitrogen atom environments in nitrided Fe-Ti alloys (after Podgurski & Davis, 1981).

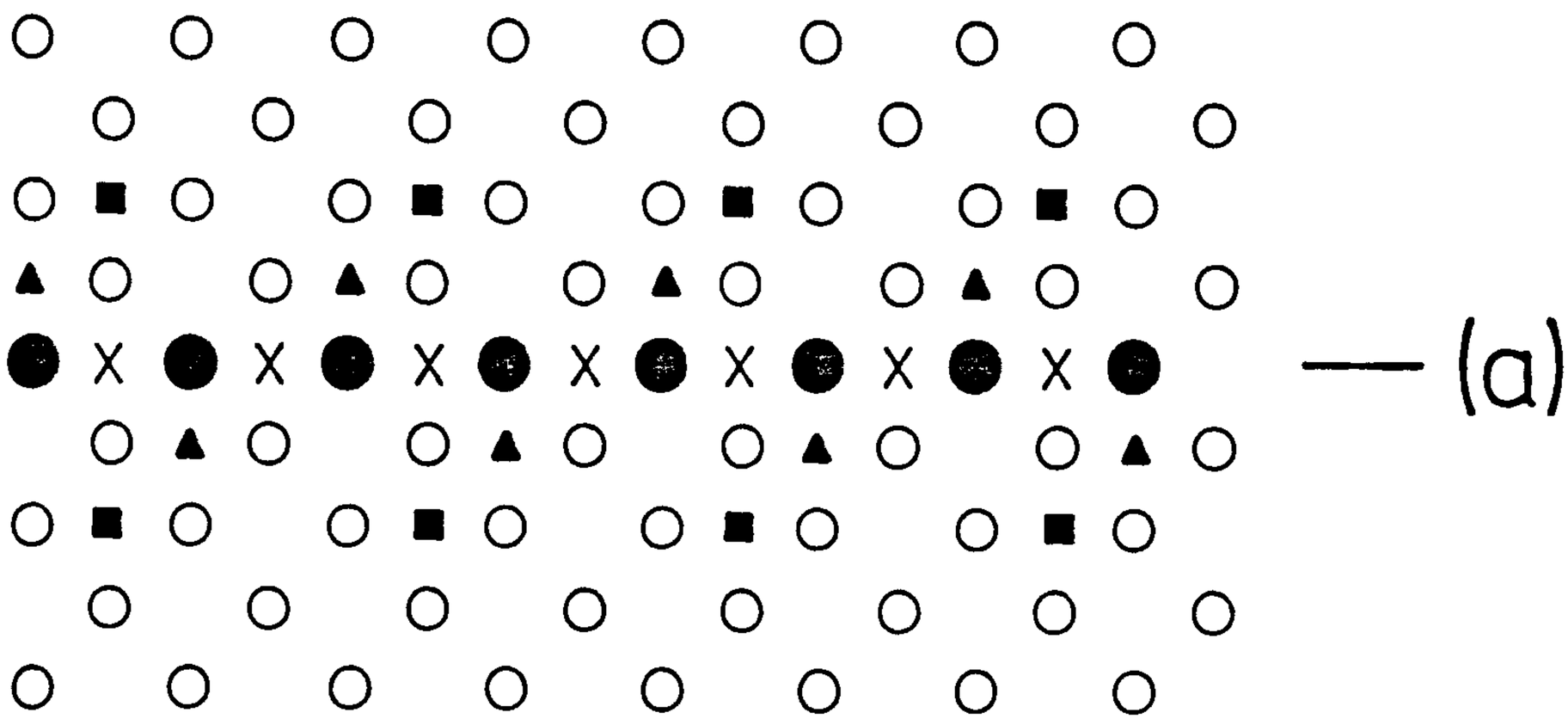

— (a)

○-Fe X — N in TiN plane

●-Ti ▲— N in first planes above & below TiN plate

■ — N in second planes above & below TiN plate

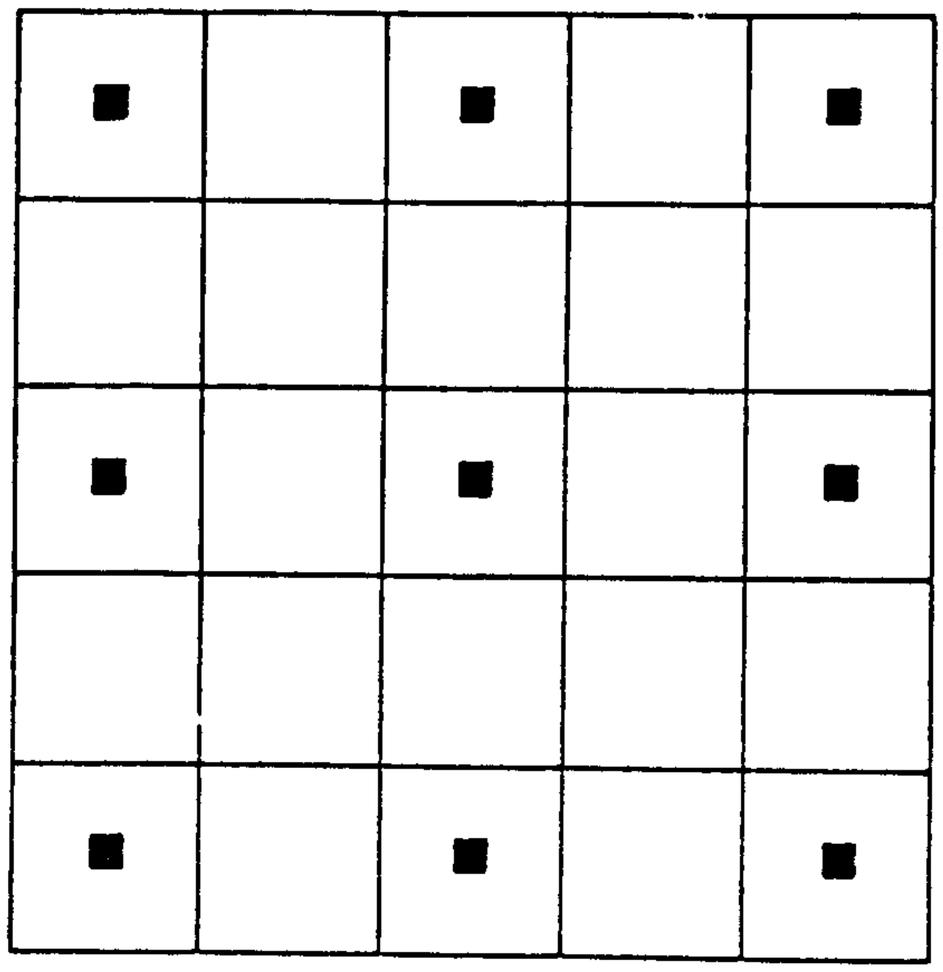

— (b)

Comparison of the models shows similarities but quite different views regarding, in particular, the sites occupied by the nitrogen in excess of a N:Ti atom ratio of 1:1. These models will be discussed further in Chapter VII of the present work.

(iii) The nitriding kinetics of Fe-Ti alloys.

The nitriding of Fe-Ti alloys containing 0.35-2.3 a/o Ti occurs by the formation of a hard, sharply defined subscale which advances progressively into the bulk of the material (Chen 1965; Jack et al., 1971). The kinetics of subscale advancement are consistent with the internal nitriding equation (see Hepworth et al., 1966):

$$X^2 = \frac{2}{r} \cdot \frac{\{N\}}{\{X\}} \cdot Dt \qquad \ldots \text{ II.1}$$

where X = the subscale depth at time t

r = N/X atom ratio in the "compound" formed

D = the diffusivity of nitrogen in iron at the reaction temperature

$\{N\}$ = a/o nitrogen concentration at the surface

$\{X\}$ = a/o of alloying element X.

(iv) Mechanical properties of Fe-Ti-N alloys.

Chen (1965) first observed that the strengthening

of nitrided Fe-Ti alloys, which were subsequently aged at high temperatures (>800°C), was due to the formation of plate-like particles of incoherent titanium nitride. These precipitates acted as non-deformable barriers to dislocation motion and forced the glide dislocation to bow-out and by-pass them by an Orowan mechanism. These observations were later confirmed by Hamano & Tsuya (1979), and in both investigations electron microscopy showed dislocation loops left around the particles after deformation.

Work on as-nitrided materials is made difficult due to their brittle nature but despite this Jack et al. (1971) and Kirkwood et al. (1974) observed increases in hardness on nitriding which were proportional to the square root of the titanium concentration. In addition to this Henderson (1976) using a dilute Fe-Ti alloy, showed the as-nitrided material to be characterised by a work-hardening rate typical of as-annealed material. These two observations led Henderson (1976) to suggest that "chemical strengthening" was the dominating hardening mechanism in nitrided Fe-Ti alloys, the increased resistance to dislocation movement being the additional work needed to create new interface as the dislocation cuts the particle. Work by Jones (1976), on nitrided Fe-V alloys, confirmed these observations and further showed the yield stress of nitrided material to be strongly temperature dependent. However, recent work by

Spitzig (1981) proposes that the increases in flow stress of nitrided Fe-Ti alloys are due to the summation of two effects. There is a contribution arising from the differences between the elastic moduli of matrix and particle, modulus hardening, and an effect from the elastic coherency stresses surrounding the particle, coherency hardening.

These models will be discussed further in Chapter IX of the present work which presents the results of a detailed analysis of the strengthening processes which occur on nitriding Fe-Ti alloys.

Chapter III

ALLOY MATERIALS

III.1 The Preparation of Alloy Samples

The chemical analyses of the alloys used in the present investigation are listed in Table III.1, the code for supplier and source of analysis are given in Table III.2.

Internal friction and X-ray specimens were prepared by cold drawing to 0.06 mm diameter wire. Sheet specimens, about 0.1 mm thick, for electron microscopy were prepared by cold rolling. For nitriding experiments the as-rolled strip or as-drawn wires were abraded, cleaned, degreased and either:

(a) sealed in transparent vitreous silica capsules, evacuated and back flushed with argon to ensure one atmosphere pressure at annealing temperature.

(b) annealed in the nitriding furnace in flowing hydrogen.

Samples for mechanical testing were stamped from 0.6 mm plate obtained from alloy stock. Annealed samples were prepared by hot-rolling to 2 mm followed by cold-rolling and

Table III.1

Cast Code	Fe	Nominal Composition, w/o							Analysis Code
		Ti	Mn	Nb	Al	C	N	Ni	
A/4244-1	Balance	0.07	<0.01	<0.01	<0.01	0.007	ND	0.01	F
B/Z83	Balance	0.15	0.005	ND	ND	0.002	ND	ND	B
C/K2732	Balance	0.15	ND	ND	ND	<0.02	ND	ND	C
A/4142-2	Balance	0.18	<0.01	<0.01	<0.01	0.009	ND	0.01	F
A/4244-2	Balance	0.32	<0.01	<0.01	<0.01	0.007	ND	0.02	F
A/4244-3	Balance	0.58	<0.01	<0.01	<0.01	0.004	ND	0.025	F
C/K2734	Balance	1.00	ND	ND	ND	<0.02	ND	ND	C
C/K2722	Balance	2.20	ND	ND	ND	<0.02	ND	ND	C
D/FS	Balance	0.12	0.29	0.06	0.05	0.008	ND	ND	D
D/FS	Balance	0.11*	ND	ND	0.05*	0.012	0.06	ND	G
E/Battelle 126	Balance	← All < 0.0002 →							E

N.D. - not determined.

*Acid soluble.

Table III.2

Code	Supplier/Source of Analysis
A	International Nickel (INCO)
B	United States Steel Corporation
C	British Iron and Steel Research Institute
D	Armco Iron
E	Battelle Institute
F	Foster Wheeler Power Products Limited
G	Surahammars, Sweden

then annealing in flowing hydrogen to give a uniform grain size of ASTM 7-8. Cold-worked samples were prepared from hot-rolled plate by rolling to a thickness of approximately 6 mm, 2.4 mm or 1 mm and then annealing in vacuum before final cold-rolling to 0.6 mm, equivalent to about 90%, 70% and 40% cold reduction respectively.

III.2 The Lattice Parameters of Fe-Ti Alloys

The lattice parameters obtained from the Fe-Ti alloys are shown in Figure III.1 along with the available data from the literature. At titanium contents < 0.2 a/o Ti the lattice parameter is virtually independent of titanium concentration, and in alloys with > 1 a/o Ti the lattice

Figure III.1

Variation of lattice parameter with titanium content for annealed Fe-Ti alloys. Solid line represents best variation of lattice parameter to fit all reported experimental observations.

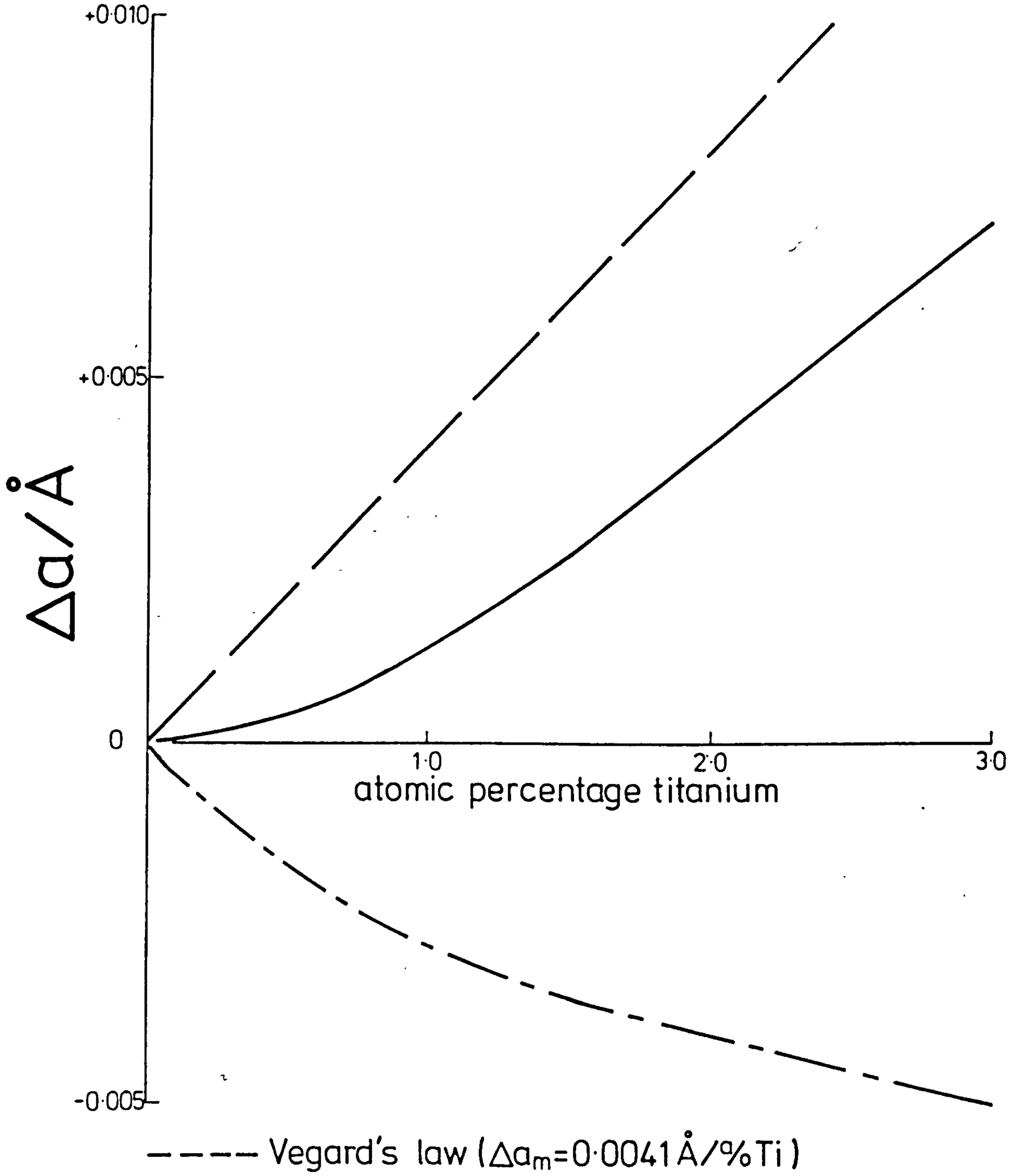
+0·010
+0·005
0
-0·005
Δa/Å
1·0
2·0
3·0
atomic percentage titanium
----- Vegard's law (Δa_m=0·0041 Å/%Ti)
——— Experimental data (Δa=a_obs-a_Fe)
- —— - Electronic constitution factor (Δa_e=a_obs-a_m)

parameter varies linearly with concentration. The slope of the linear part of the curve is in agreement with Abrahamson & Lopata (1966) and Zwell & Wriedt (1972), with a dilation coefficient of 0.0027 Å/ a/o Ti. To explain the behaviour shown in Figure III.1 Arrott & Noakes (1963) suggested that titanium was removed from solid solution by internal oxidation during sample preparation. This is not true for the present alloys which were prepared for subsequent nitriding. As shown in Chapter II, for nitrided Fe-Ti alloys the N:Ti atom ratio is always much higher than required for the formation of TiN, but this ratio can be reduced to 1:1 by hydrogen reduction. Therefore by hydrogen reduction the concentration of titanium available to form clusters during nitriding can be determined. The titanium concentration so-obtained is identical, within experimental error, to that of the starting composition of the alloy showing that no removal or titanium occurs by internal oxidation prior to nitriding. In addition, Bozorth (1959) and Arrott & Noakes (1963) show a linear relationship between magnetic moment and titanium concentration over the entire range of solid solubility. The slope of the plot is greater than that expected merely by magnetic dilution by titanium and again suggests that the titanium is all in solid solution. It is proposed that a more reasonable explanation for the anomalous behaviour of lattice parameter shown in Figure III.1 is that in addition to an atomic size effect (Vegard's Law) there is also an electronic constitution effect as described

in transition-metal alloys systems by Raynor (1975).

Following Raynor (1975), the lattice parameter of a solid solution (a_m) as given by Vegard's Law (1921) can be expressed:

$$100 \cdot a_m = n_{Ti} a_{Ti(\beta)} + (100-n_{Ti}) a_{Fe} \quad \ldots \text{III.1}$$

where a_{Fe} and $a_{Ti(\beta)}$ are, respectively, the lattice parameters of iron and titanium and n_{Ti} is the atomic concentration of titanium. The deviation from Vegard's Law (1921) is given by:

$$\Delta a_e = a_{obs} - a_m \quad \ldots \text{III.2}$$

where a_{obs} is the observed lattice parameter, and Δa_e is an electronic constitution factor.

Using accepted values for a_{Fe} and $a_{Ti(\beta)}$ (Raynor, 1975) the variations of atomic size and electronic constitution effects with atomic percentage titanium are given in Figure III.2. The negative deviation of the electronic constitution factor is in accordance with the general rules put forward by Raynor (1975), that is, if the group number of the solute metal (Ti, 4) is less than that of the solvent (Fe, 8), then the lattice spacings of the solid solution tend to be less than those due to the effects from atomic size alone, i.e. there is a negative deviation from Vegard's Law.

Figure III.2

$\Delta a(\text{Å})$ plotted against atomic percentage titanium.

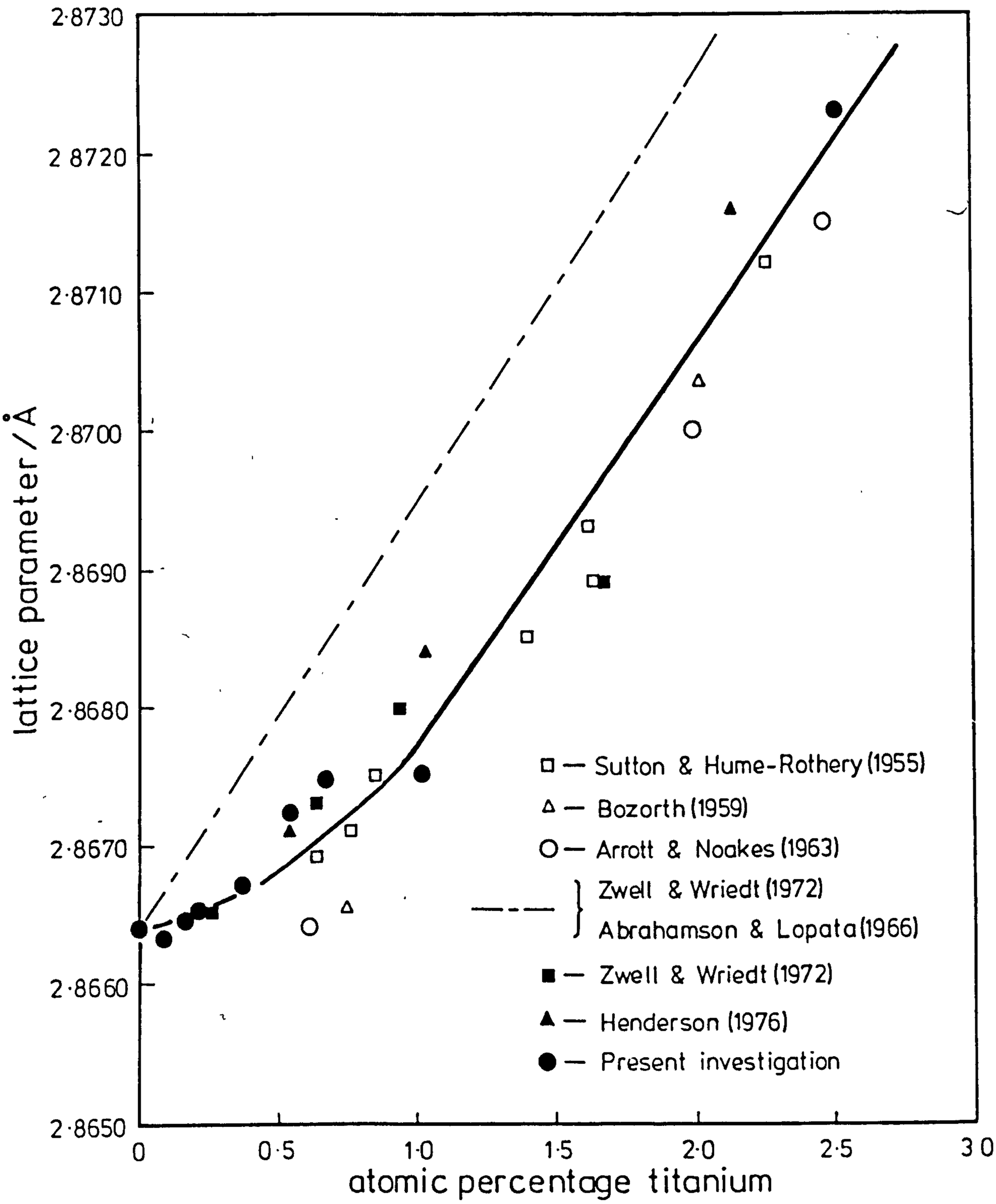
2·8730
2 8720
2·8710
2·8700
2·8690
2·8680
2·8670
2·8660
2·8650
lattice parameter / Å
0
0·5
1·0
1·5
2·0
2·5
3 0
atomic percentage titanium
□ — Sutton & Hume-Rothery (1955)
△ — Bozorth (1959)
○ — Arrott & Noakes (1963)
Zwell & Wriedt (1972)
Abrahamson & Lopata (1966)
■ — Zwell & Wriedt (1972)
▲ — Henderson (1976)
● — Present investigation

It is therefore proposed that the observed deviation from Vegard's Law in solid solutions of titanium in iron is due to an electronic constitution factor and not, as previously suggested, to removal of titanium from solid solution by internal oxidation.

Chapter IV

EXPERIMENTAL METHODS

IV.1 Ammonia-Hydrogen Nitriding

Nitriding was carried out between 400° and 650°C, the nitrogen activity at a particular temperature being dictated by the relative proportions of ammonia and hydrogen in the gas mixture. The nitriding reaction can be written as:

$$NH_3\ (g) \rightleftharpoons \underline{N} + {}^{3}/_{2}\ H_2\ (g) \qquad \ldots\ IV.1$$

for which, at T°K, the equilibrium constant is:

$$K_p = a_N \cdot pH_2^{3/2}/pNH_3 \qquad \ldots\ IV.2$$

where a_N is the activity of nitrogen in the nitride phase or solid solution and pNH_3 and pH_2 are the partial pressures of ammonia and hydrogen respectively. A system can therefore be brought to equilibrium under a predetermined nitrogen activity by controlling both the proportions of ammonia and hydrogen in the gas atmosphere and the nitriding temperature. For the iron-nitrogen system the phases in equilibrium with various ammonia-hydrogen gas mixtures at any particular temperature have been determined by

Lehrer (1930), see Figure IV.1. In the present investigation only nitriding conditions within the α-nitrogen-ferrite phase field of Figure IV.1 were employed.

The standard state for nitrogen dissolved in iron is defined such that, in dilute solutions

$$a_N = \text{w/o N} \qquad \ldots \text{IV.3}$$

Combining equations IV.2 and IV.3 and re-arranging, the weight percentage nitrogen in equilibrium with ferrite at any particular temperature and ammonia-hydrogen ratio can be expressed as:

$$\text{w/o N} = K_p \, pNH_3/pH_2^{3/2} \qquad \ldots \text{IV.4}$$

The variation of K_p with temperature has been determined by Podgurski & Knechtel (1969) as:

$$\ell n \, K_p = -9270/T + 10.27 \qquad \ldots \text{IV.5}$$

The diagram shown in Figure IV.2, derived from equation IV.4, proved useful in determining suitable nitriding conditions within the α-nitrogen-ferrite phase field whose limit is given by the dotted line.

A complicating reaction which may occur in addition to equation IV.1 is the dissociation of ammonia. However, work by Roberts (1970) showed that with the flow rates

Figure IV.1

Equilibrium between NH_3-H_2 mixtures (1 atm) and solid phases of the iron-nitrogen system (after Lehrer, 1930).

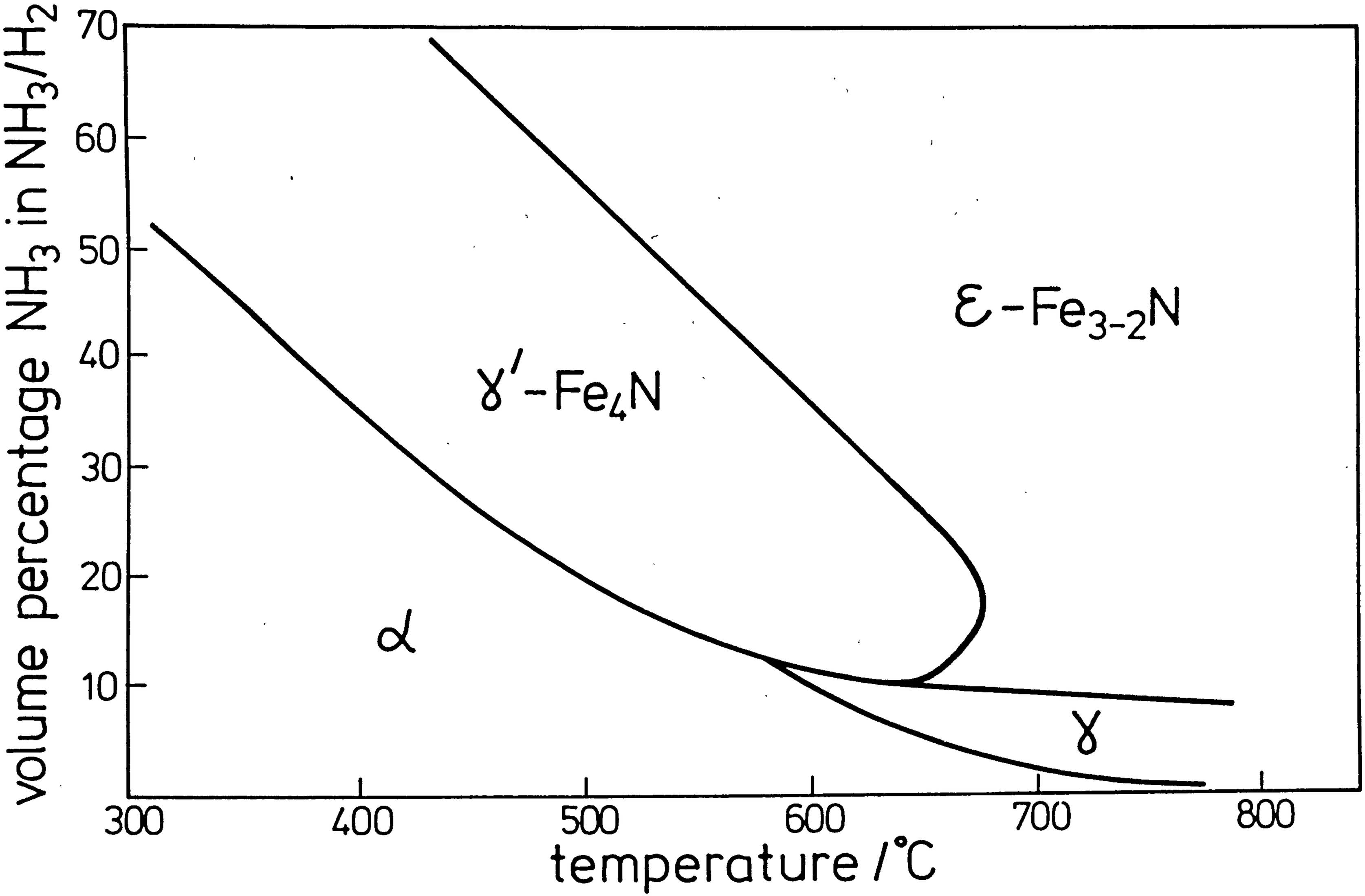
volume percentage NH_3 in NH_3/H_2
70
60
50
40
30
20
10
300
400
500
600
700
800
temperature /°C
ε-$Fe_{3-2}N$
γ'-Fe_4N
α
γ

Figure IV.2

Nitrogen concentration in pure iron in equilibrium with NH_3:H_2 gas mixtures.

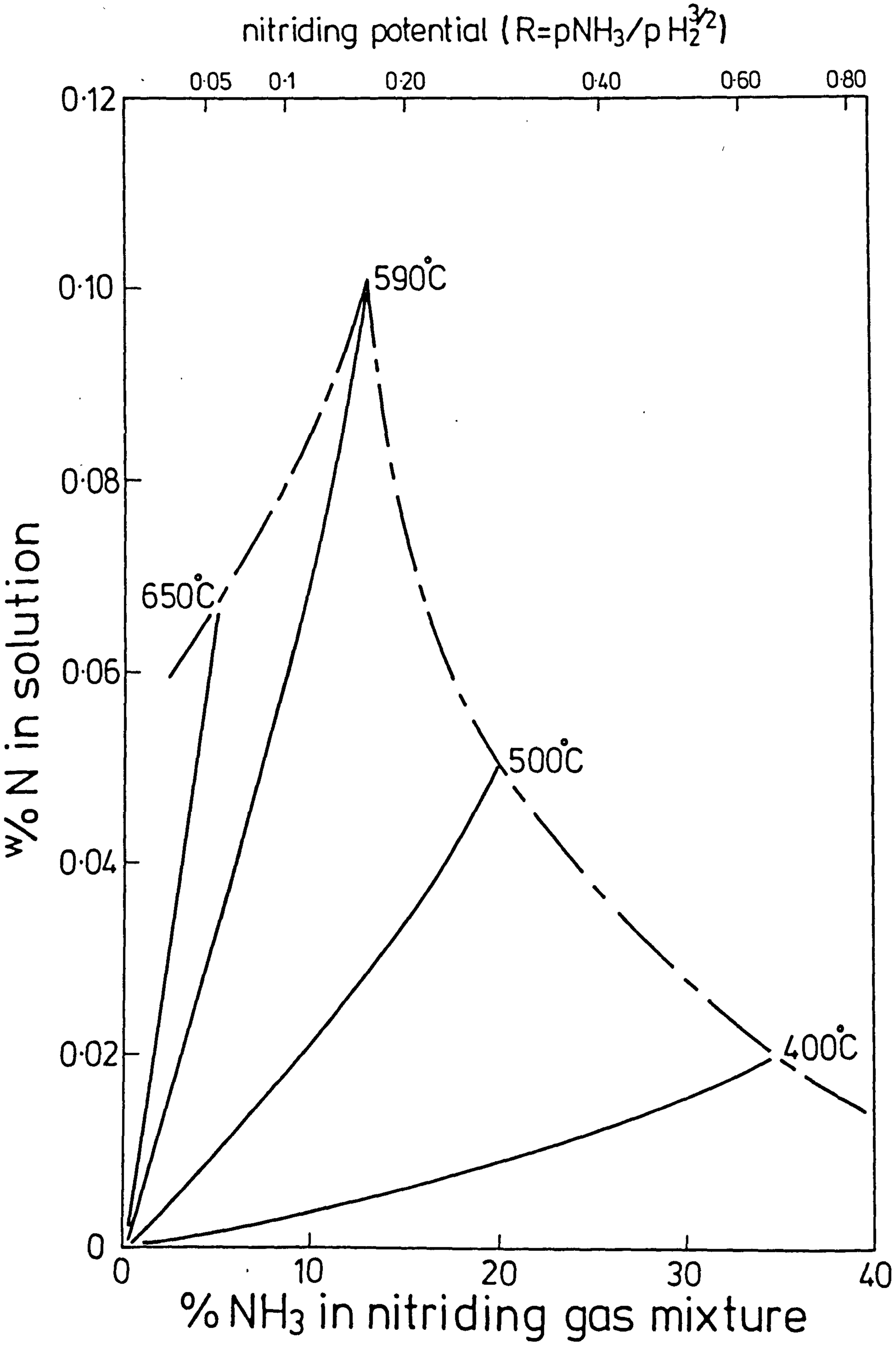
nitriding potential (R=pNH3/p H2 3/2)
0·05
0·1
0·20
0·40
0·60
0·80
0·12
0·10
0·08
0·06
0·04
0·02
0
w/o N in solution
590°C
650°C
500°C
400°C
0
10
20
30
40
% NH3 in nitriding gas mixture

used in the present investigation there is no detectable dissociation of ammonia below 650°C and hence no reduction in the effective nitriding potential expected for a particular set of nitriding conditions below this temperature.

IV.2 Nitriding Apparatus

A schematic diagram of the nitriding apparatus is shown in Figure IV.3 with a vertical reaction tube (25 mm i.d.) of recrystallised alumina. Commercial hydrogen, nitrogen and ammonia were purified by standard methods (Schwerdtfeger & Turkdogen, 1970) as illustrated in Figure IV.4. The activated copper was pre-reduced in hydrogen for several days at 160°C and maintained at 120°C during use. Gas flows were measured by capillary flow meters (see Figure IV.5) calibrated by a bubble displacement technique (Darken & Gurry, 1945). Total gas flow rates of 200 ml min^{-1} were used during nitriding runs.

The temperature of the furnace hot zone was controlled to $\pm$ 5°C by an "Ether" controller using a Pt/Pt-13% Rh thermocouple positioned between the reaction tube and the furnace winding. The specimen temperature was monitored by a chromel/alumel thermocouple in an alumina sheath adjacent to the specimen.

The total gas pressure was maintained at slightly greater than atmospheric by 10-20 mm of oil in an exit bubbler.

Figure IV.3

Ammonia-hydrogen gas equilibration apparatus.

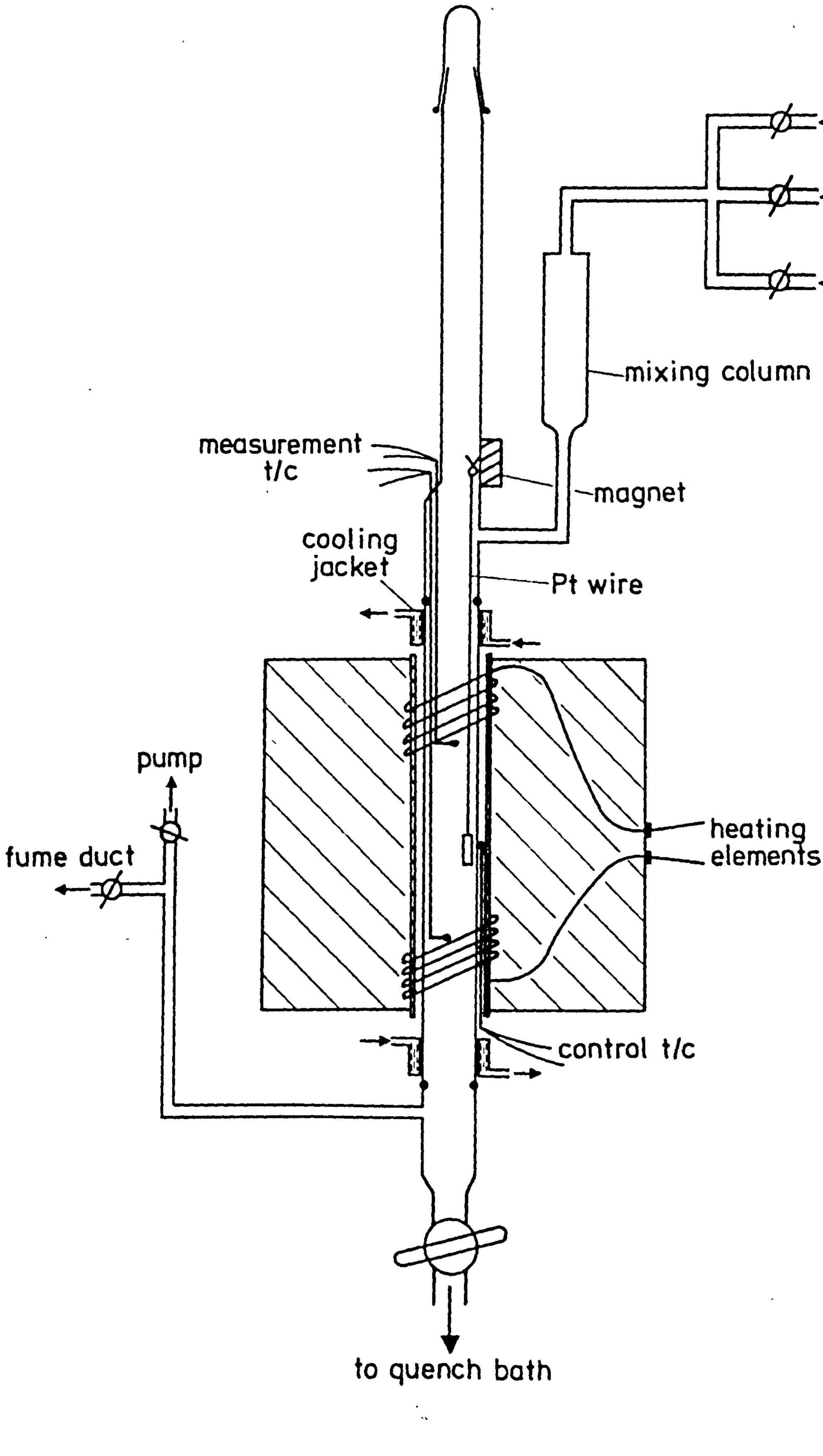
H_2
NH_3
N_2
mixing column
measurement t/c
magnet
cooling jacket
Pt wire
pump
fume duct
heating elements
control t/c
to quench bath

Figure IV.4

Gas flow system for ammonia-hydrogen gas equilibrations.

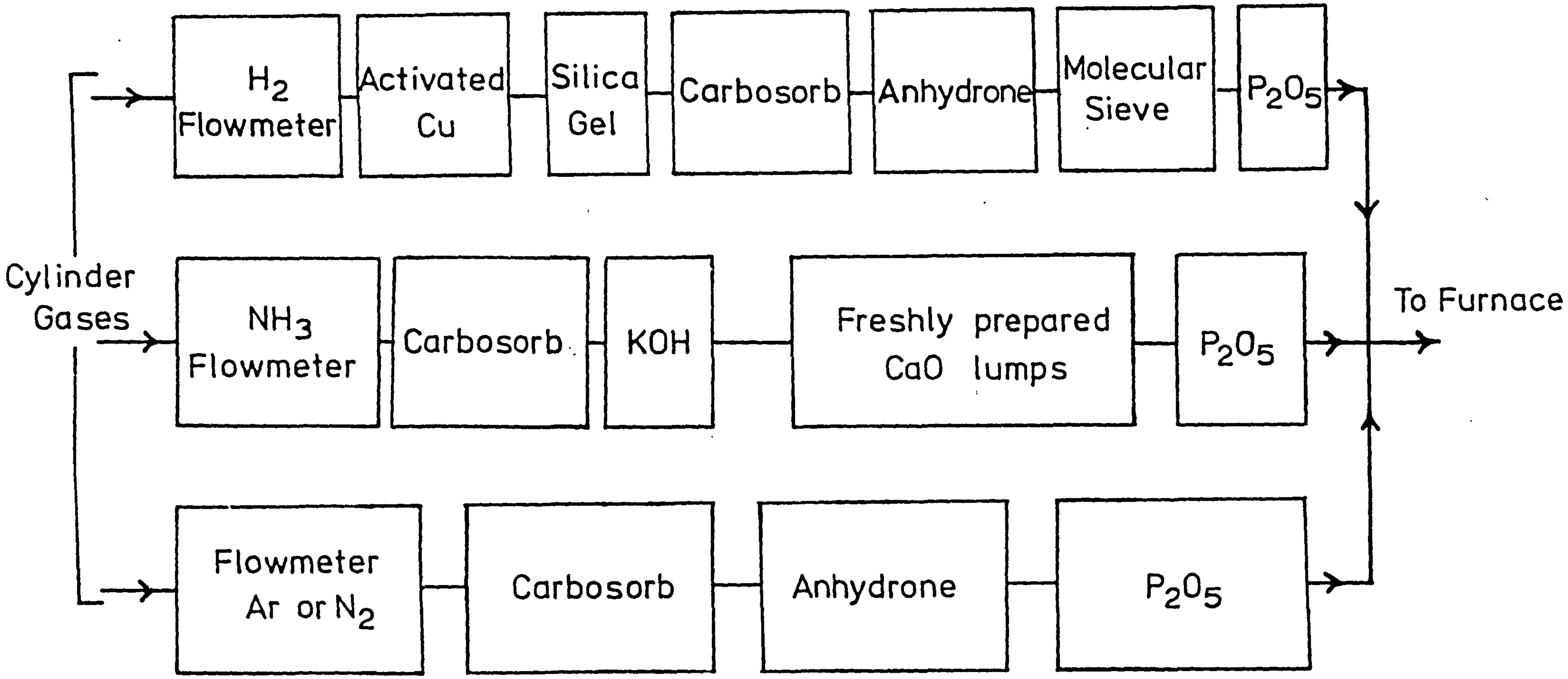
H_2 Flowmeter
Activated Cu
Silica Gel
Carbosorb
Anhydrone
Molecular Sieve
P_2O_5
Cylinder Gases
NH_3 Flowmeter
Carbosorb
KOH
Freshly prepared CaO lumps
P_2O_5
To Furnace
Flowmeter Ar or N_2
Carbosorb
Anhydrone
P_2O_5

Figure IV.5

A capillary flowmeter.

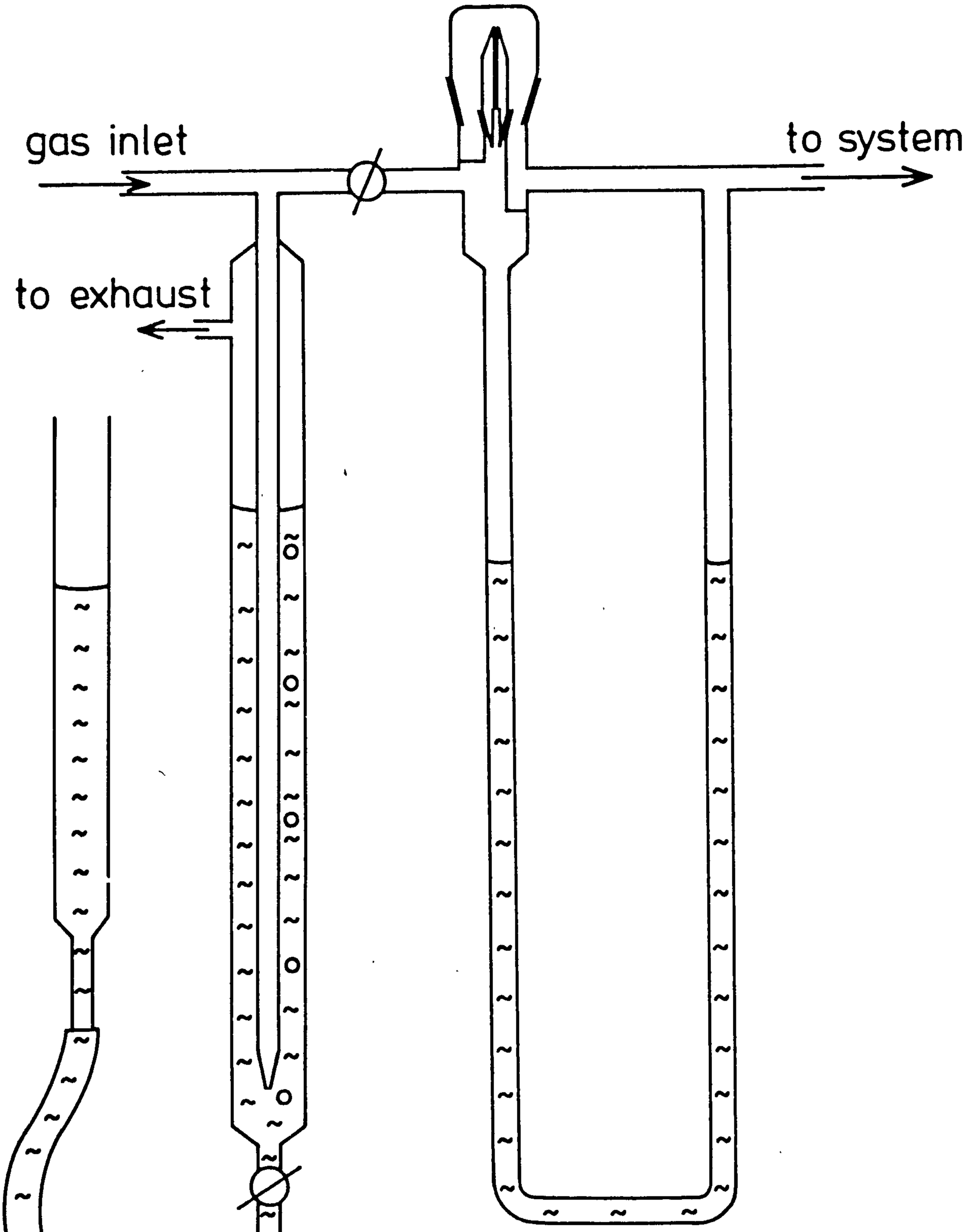
gas inlet
to system
to exhaust

IV.3 Nitriding Procedure

Specimens were abraded and given a light electro-polish. After weighing they were degreased in chemiclene, suspended on a platinum wire, inserted into the cold (upper) end of the furnace and supported there by attachment to a soft iron bob held by a magnet. The top of the reaction tube was then sealed, the system evacuated, checked for leaks and flushed with nitrogen. The appropriate ammonia-hydrogen gas mixtures were then passed through the furnace for about one hour before lowering the specimen into the furnace hot zone.

After nitriding, the specimens were removed from the hot zone by one of two methods dependent on the severity of quench required. The first method involved raising the specimens quickly out of the hot zone so that they were cooled in the incoming gas stream in the cold zone of the furnace. They were left there for 15 min before the furnace was evacuated, flushed with nitrogen, and the specimens removed and weighed. The second method involved opening the quench tap at the bottom of the furnace and dropping the specimens rapidly from the hot zone into a quench bath of de-gassed iced brine. The specimens were then removed, washed and dried. Specimens were weighed before and after nitriding to $\pm$ 0.00005 g on an analytical balance, taking an average of at least three readings.

IV.4 Optical Metallography

Specimens were mounted either in bakelite (pressure cured at 120°C) or Serrifix cold mounting resin. Serrifix was used to prevent premature aging of the specimens containing nitrogen, the maximum temperature reached during setting being about 30°C. Mounted specimens were abraded through various grades of silicon carbide paper down to 800 grit and then polished with diamond paste down to 1 μm size on polishing wheels using a "Selvyt" cloth lap. Specimens were etched in 2% Nital for 5-20 seconds.

A Reichart projection microscope was used for optical metallography and photomicrography at a direct magnification of up to x 1200. The grain size of mechanical testing and internal friction specimens was measured using a mean linear intercept method (De Hoff & Rhines, 1968).

IV.5 Hardness Measurements

Room-temperature hardness measurements were made on metallographic specimens using a standard micro-hardness tester fitted to the Reichart microscope with loads of 20 or 50 g on the diamond indenter.

Hot-hardness experiments were carried out in a Wilberforce Scientific Developments high-temperature

micro-hardness tester in the Department of Metallurgy, Cambridge University; the equipment is shown schematically in Figure IV.6 a,b. The instrument consists of specimen and indenter assemblies together with heating furnaces and water cooling systems contained in a sealed stainless steel vessel capable of evacuation to $\sim 2 \times 10^{-7}$ torr to 1×10^{-6} torr (with the furnaces outgassed and at temperature).

Specimens were spot-welded onto metal stubs and polished as for optical metallography. The stub, to which a chromel/alumel thermocouple was spot-welded, was then screwed onto a pedestal in the bottom of the specimen furnace assembly within the instrument (see Figure IV.6 b). The whole specimen furnace unit could be translated to a position directly underneath the indenter assembly, which comprised a mechanically-retained sapphire (Vicker's profile) on a stainless steel shank contained in its own separately-controlled furnace, and loaded by a series of weights stacked in a stepped cylinder. The descent of the indenter was controlled by an external oil dashpot and a constant loading time of 15 secs was used for each indent at a load of 50 g. By moving the specimen furnace to a "view" position the indent could be measured at temperature using a Zeiss Epignost II microscope fitted with a Leitz long working distance objective lens and a screw micrometer measuring device.

Figure IV.6

High-temperature micro-hardness tester.

(a)

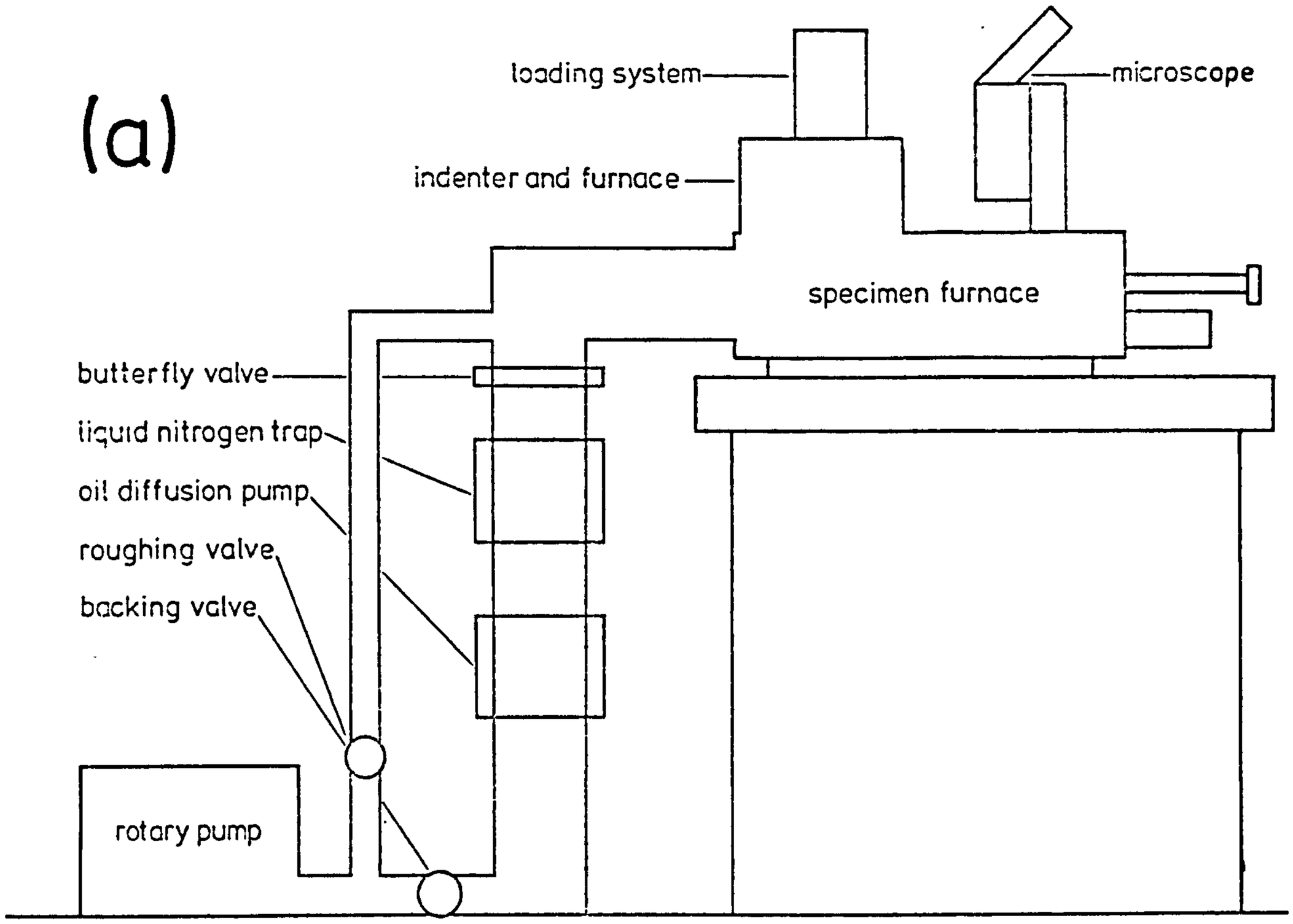
loading system
microscope
indenter and furnace
specimen furnace
butterfly valve
liquid nitrogen trap
oil diffusion pump
roughing valve
backing valve
rotary pump

(b)

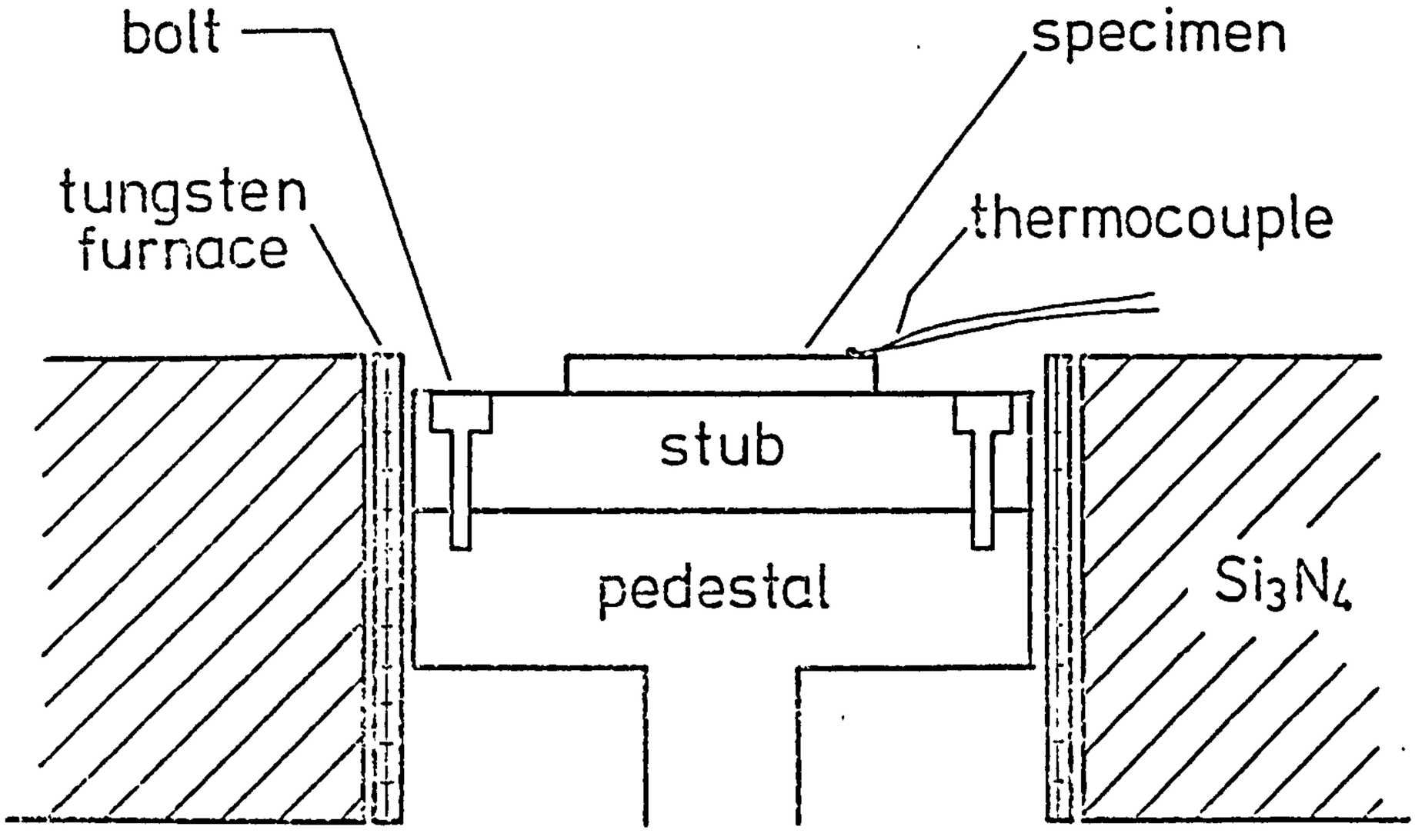
bolt
specimen
tungsten furnace
thermocouple
stub
pedestal
Si_3N_4

IV.6 Preparation of Specimens for Transmission Electron Microscopy

Thin foils of nitrided alloy specimens were prepared from strip material. 0.6 mm thick specimens were first mechanically thinned to 0.2 mm (the remaining specimens had a starting thickness between 0.1-0.2 mm) and thin foils were then prepared by electropolishing using a standard "window" technique and a "Shandon" potentiostat at 18 V and 0°C in a solution of 68 v/o glacial acetic acid:16 v/o perchloric acid:16 v/o 2-butoxyethanol.

IV.7 Electron Microscopy

Transmission electron microscopy was carried out on Philips EM300 and JEOL 100 CX instruments. Scanning electron microscopy was carried out on metallographically prepared specimens and on fracture faces using a Cambridge Stereoscan S600 or JEOL T20 instruments.

IV.8 X-ray Diffraction

Specimens examined by X-ray powder photography were prepared from wire (0.3-0.6 mm diameter) or narrow strip cut from sheet, which were electropolished and washed in methanol prior to exposure.

X-ray powder photographs for determination of ferrite

lattice parameter were obtained using a Unicam 190 mm diameter camera with iron filtered Co-Kα radiation and the lattice parameters were determined by Nelson-Riley extrapolation (Nelson & Riley, 1945). For identification of second phases a Unicam 90 mm diameter camera was used with LiF crystal monochromated Fe-Kα radiation.

The intensity of reflections were measured on a manual direct-reading X-ray microdensitometer designed by Taylor (1951); see Figure IV.7. This compares the optical density of reflections on the film with that of a pair of linear density optical wedges. The two light beams fall alternately onto a selenium photocell connected to a sensitive galvanometer the deflection of which is adjusted to be the same for both beams by varying the position of the wedges. The intensity profile of reflections, recorded at successive 0.1 mm intervals, were plotted on large scale graph paper and from these a value of integral breadth calculated (Rachinger, 1948).

IV.9 Internal Friction Equipment

Internal friction measurements as a function of temperature were made on 150 mm long wire specimens in an inverted torsion pendulum assembly, see Figure IV.8, equipped with a non-inductively wound furnace. Any damping of magnetic origin was suppressed by application

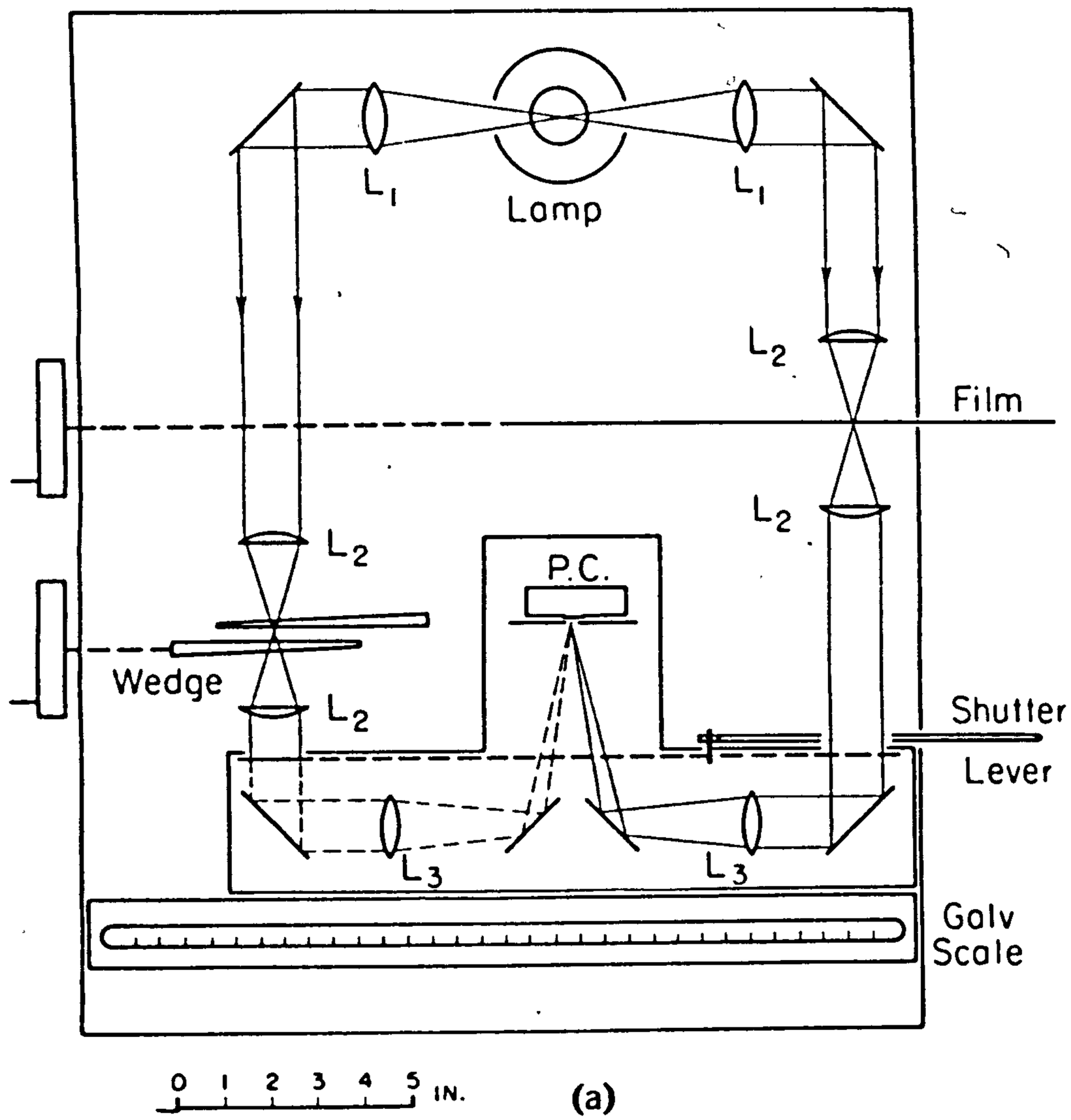

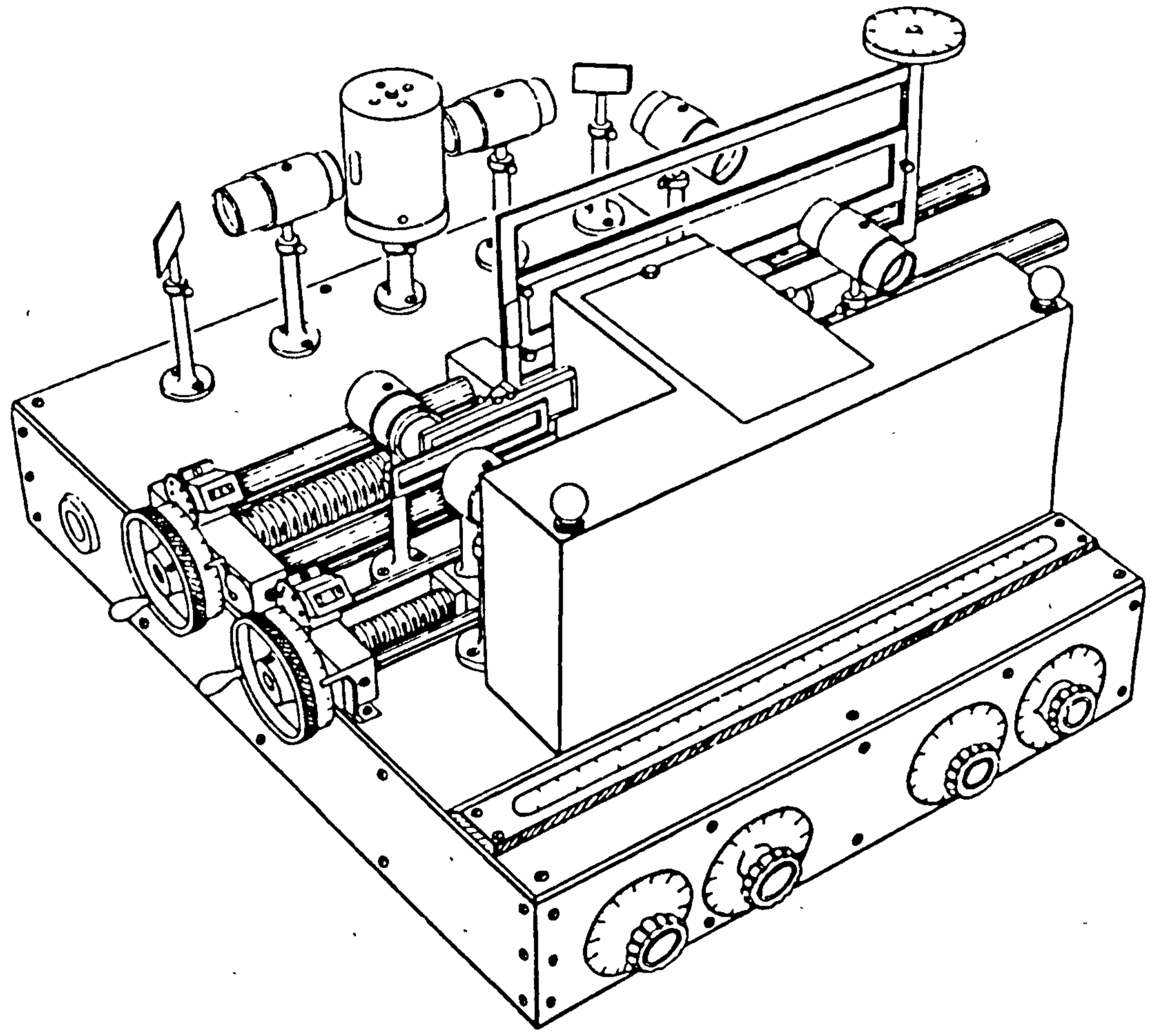

(*a*) Plan of microdensitometer. (*b*) General view of instrument.

Figure IV.8

Internal friction apparatus, pendulum and furnace assemblies.

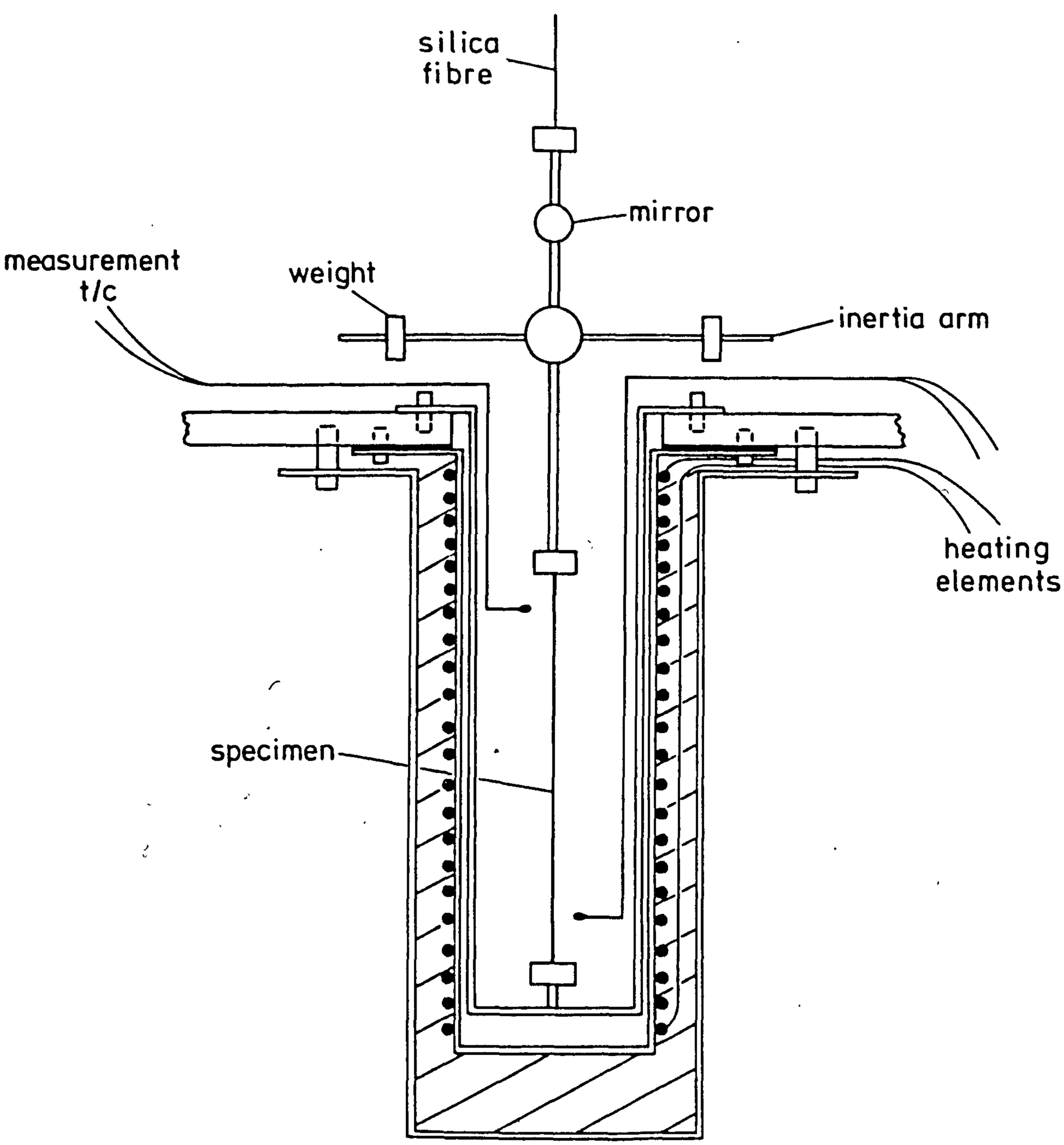
silica
fibre
mirror
measurement
t/c
weight
inertia arm
heating
elements
specimen

of a 100 Oe magnetic field. A torsionally rigid knife-edge balance arm and counterweight, used in conjunction with a fine silica fibre as the suspension element, enabled a small constant load to be maintained on the specimen. This suspension system, together with an operating vacuum of 2×10^{-5} torr, results in a very low level of background damping. Electromagnets acting upon the bar start the oscillation, the frequency of which can be adjusted in the range 0.2-1.6 Hz by varying the inertia of the system. An automatic Sefram photodyne records the rate of decay by following a light beam reflected from a mirror mounted on the inertia assembly and the internal friction was evaluated by calculation of the logarithmic decrement (see Chapter VI).

Damping was measured at appropriate intervals in the temperature range -60 to 250°C by using a liquid nitrogen cooling jacket and furnace assembly situated around the specimen. The temperature of the specimen was recorded by copper-constantan thermocouples situated near the top and bottom of the specimen, and could be maintained to $\pm$ 1°C by varying the power supplied to three parallel heating coils using external rheostats. A variable heating rate was used in order to investigate parts of the damping spectrum in more detail, but was always followed by a period of thermal equilibrium under reduced power for three minutes in all measurements.

IV.10 Mechanical Testing

Tensile tests on flat 20 mm gauge length specimens were made at a nominal strain rate ($\dot{\epsilon}$) of 4.2×10^{-4} sec^{-1} on an Instron 1115 machine equipped with automatic chart control and stepped zero suppression facilities. Low temperature testing was carried out in cooled liquid baths, the temperature of which was measured by a copper-constantan thermocouple situated close to the specimen. To test specimens up to 600°C a nitrogen-atmosphere furnace was used, consisting of a vertical furnace having three windings controlled by three thyristor units. Thermocouples to these windings were arranged so that the upper and lower furnace zones were controlled by the difference in e.m.f. produced by each of the two "end-zone" thermocouples and the one in the centre, this enabled control to within $\pm$ 2°C. The capsule containing the specimen, grips and pull rods was evacuated and filled with nitrogen to give one atmosphere pressure at the testing temperature which was measured by a thermocouple placed directly alongside the specimen.

Chapter V

THE SCOPE OF THE PRESENT INVESTIGATION

Previous work at Newcastle has shown that mixed substitutional-interstitial solute atom clusters are formed when both ferritic and austenitic Fe-X alloys are constant-activity nitrided in ammonia:hydrogen gas mixtures at 350-700°C. Large increases in strength accompany zone formation and the strength of the alloys stems from the interaction between the alloying element and the nitrogen, that is, it is chemical in origin. In the present work similar experimental methods, including electron microscopy, X-ray diffraction, internal friction, observation of weight changes, mechanical properties measurements, are all used with nitrided Fe-Ti alloys to provide further insight into the structure and properties of mixed substitutional-interstitial solute atom clusters.

In Chapter VII the particles responsible for the strengthening of dilute iron-titanium alloys are shown to be Ti-N clusters; and a combination of internal friction and measurements of nitrogen absorption isotherms are used to propose a model for the zone structure in Fe-Ti alloys containing < 0.3 w/o Ti. The model suggests that a range of metal-atom octahedral environments exist whose potential energy varies with the proximity and

distribution of titanium atoms. In Chapter VIII it is shown that low-temperature aging further modifies the distribution of nitrogen in these sites causing changes in the breadth and peak positions of X-ray reflections. These low-temperature transformations are analogous to those observed in the quench-aging of nitrogen-ferrite.

In Chapter IX a detailed analysis of the strengthening mechanisms operating in Fe-Ti alloys at different particle dispersions is presented. Initially the zones are cut by glide dislocations and the hardening is strongly temperature dependent, suggesting that strengthening is due to chemical factors arising from the creation of new interfaces as the TiN zones are sheared. As the zones overage to the equilibrium precipitate the particles are looped by glide dislocations according to an Orowan condition. Chapter X extends these ideas into cold-worked and nitrided Fe-Ti alloys where the strengthening is shown to be a complex balance between a decrease in strength due to recovery and recrystallisation of the material at nitriding temperature, and strength increases brought about by homogeneous and heterogeneous precipitation of Ti-N zones or TiN precipitates.

Finally in Chapter XI it is shown that the ideas presented in Chapters IX and X can be applied to a commercial steel.

Chapter VI

THEORETICAL AND PRACTICAL ASPECTS OF INTERNAL FRICTION

VI.1 Formal Theory of Anelasticity

Within the framework of classical linear theory of elasticity a rigorous proportionality is assumed between the stresses and strains in a solid. This means that the strains in a perfectly elastic solid are a unique function of the applied stress, and that the time dependence of the strain is completely determined by the time dependence of the stress. For a harmonic variation of the stress, the strain also varies harmonically, and in such a way that stress and strain are always in phase. As a consequence, there is no energy dissipation within the specimen and if no energy were lost from the system the amplitude of oscillation of a solid body, driven at its resonance frequency with even an infinitely small driving force, would become infinite. Even when energy losses to the surroundings can be neglected, considerable energy dissipation usually occurs, that is, real solids do not obey Hooke's law. Therefore the strain is not uniquely determined by the stress, but lags behind by an amount φ. The resulting dissipation of energy in the solid is called internal friction.

The behaviour of real materials can be satisfactorily described by using anelastic theory and a standard linear solid model for which Zener (1948) proposes the equation:

$$a_o\sigma + a_1\dot{\sigma} = b_o\epsilon + b_1\dot{\epsilon} \qquad \ldots \text{ VI.1}$$

where stress and strain are linked with their first time derivatives. Materials obeying this equation are termed 'standard linear solids', and their behaviour can be represented schematically as shown in Figure VI.1(b), a_o, a_1, b_o and b_1 are constants, σ is the stress and ϵ the strain. The system shown in Figure VI.1(a) will undergo an instantaneous displacement when a stress is suddenly applied, whose magnitude is determined solely by the spring constants. As the stress is maintained, the dashpot deforms relaxing the stress and causing a gradual increase in overall deformation. Conversely, when the stress is suddenly removed, the springs will suddenly release some of their stored energy, resulting in a partial instantaneous recovery. The complete release of all the energy must await the gradual relaxation of stress across the dashpot. Such a system therefore shows the general features of elastic aftereffects in real solids, illustrated in Figure VI.1(b).

In order to illustrate the physical interpretation attached to the parameters a_o, a_1, b_o and b_1 it is necessary to consider a few special cases. First, suppose that both ϵ and $\dot{\epsilon}$ are zero then equation VI.1 reduces to:

$$a_o\sigma + a_1\dot{\sigma} = 0 \qquad \ldots \text{ VI.2}$$

Figure VI.1

Standard linear solid (after Zener, 1948).

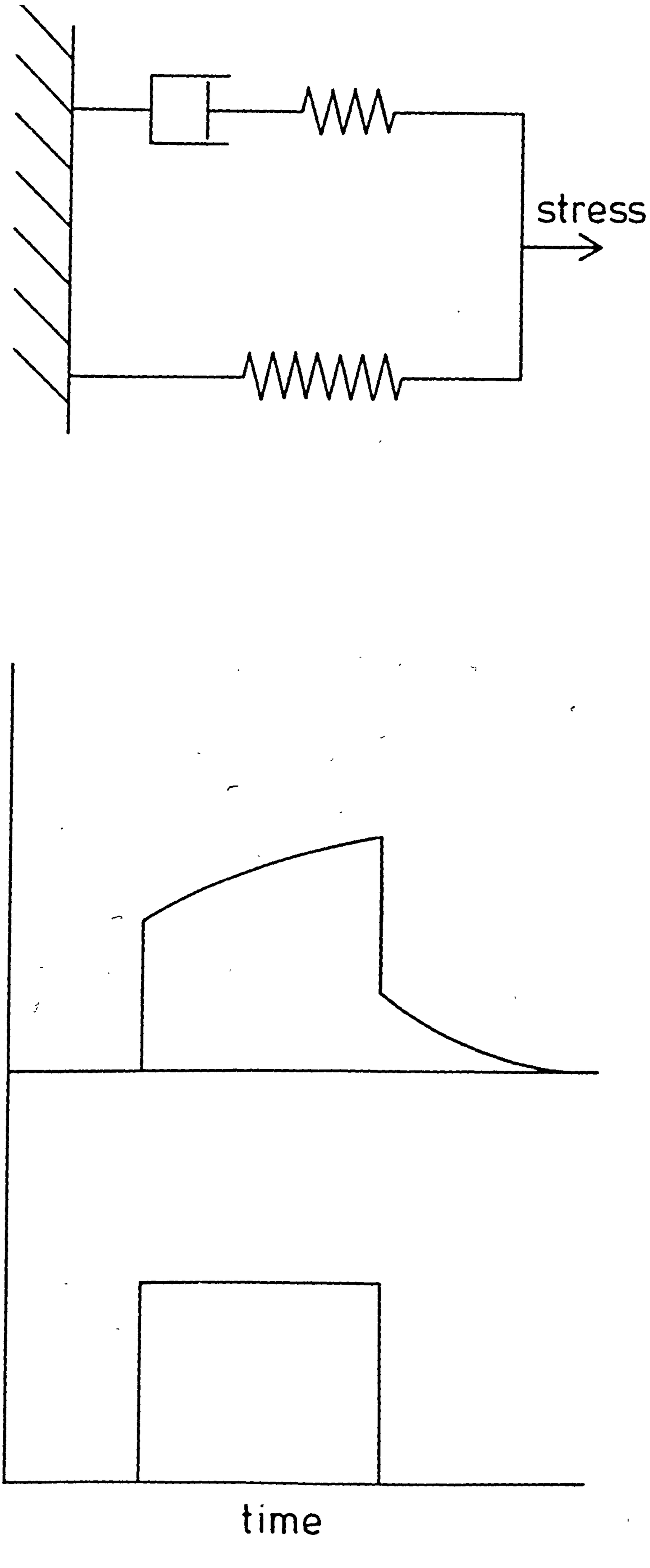

(a)

(b)

which has the solution:

$$\sigma = \sigma_o \exp(-a_o t/a_1) \qquad \ldots \text{VI.3}$$

where σ_o is the stress at t = 0. Thus a_o/a_1 represents the decay constant for constant strain λ_ϵ or as its inverse of a relaxation time for a constant strain τ_ϵ.

In the second case suppose that at t = 0 a constant strain ϵ_o is applied, so equation VI.1 can be written as:

$$a_o\sigma + a_1\dot{\sigma} = b_o\epsilon_o \qquad \ldots \text{VI.4}$$

which has the solution

$$\sigma = \frac{b_o}{a_o}\epsilon_o + \left(\sigma_o - \frac{b_o}{a_o}\epsilon_o\right) \exp(-\lambda_\epsilon t) \qquad \ldots \text{VI.5}$$

In equation VI.5 the stress tends to its equilibrium value of $\frac{b_o\epsilon_o}{a_o}$ with a relaxation time τ_ϵ. Therefore b_o/a_o is the ratio of stress to strain for complete relaxation; it is known as the 'relaxed elastic modulus' M_R.

Finally consider the case when σ and $\dot{\sigma}$ are zero so equation VI.1 reduces to:

$$b_o\epsilon + b_1\dot{\epsilon} = 0 \qquad \ldots \text{VI.6}$$

which has the solution:

$$\epsilon = \epsilon_o \exp(-b_o t/b_1) \qquad \ldots \text{VI.7}$$

where ϵ_o is the strain at t = 0. Thus b_o/b_1 can be

regarded as the decay constant for constant stress λ_σ or the inverse of the relaxation constant τ_σ.

These three quantities enable equation VI.1 to be rewritten as:

$$\sigma + \tau_\epsilon \dot{\sigma} = M_R \left\{ \epsilon + \tau_\sigma \dot{\epsilon} \right\} \quad \ldots \text{VI.8}$$

New constants, which have physical significance may be derived from τ_σ, τ_ϵ and M_R. If in a time δt the stress receives a finite increment $\Delta\sigma$, then from equation VI.8:

$$\tau_\epsilon \Delta\sigma = M_R \tau_\sigma \Delta\epsilon \quad \ldots \text{VI.9}$$

The ratio $\Delta\sigma / \Delta\epsilon$ is the unrelaxed modulus, M_u, which correlates changes in stress and strain occurring so rapidly that no relaxation has time to take effect. The relaxed modulus, M_R, is the modulus for the condition when relaxation is complete; consequently $M_u > M_R$ and from equation VI.9:

$$M_u = M_R \tau_\sigma / \tau_\epsilon \quad \ldots \text{VI.10}$$

Internal friction measurements are carried out under dynamic conditions of periodic stress and strain illustrated by the following equations:

$$\sigma = \sigma_o \exp(i\omega t) \; ; \; \epsilon = \epsilon_o \exp(i\omega t)$$

Using these equations in equation VI.8 leads to:

$$(1 + i\omega\tau_\epsilon)\sigma_o = M_R (1 + i\omega\tau_\sigma)\epsilon_o \qquad \ldots \text{VI.11}$$

or $$\sigma_o = \mathcal{M} \epsilon_o \qquad \ldots \text{VI.12}$$

where $\mathcal{M}$ is the complex modulus given by:

$$\mathcal{M} = \left\{ \frac{1 + i\omega\tau_\sigma}{1 + i\omega\tau_\epsilon} \right\} M_R$$

Under conditions of alternating stress, the lag between stress and strain gives rise to damping. The phase angle, φ, by which strain lags stress is used as a measure of internal friction and can be derived from the complex modulus:

$$\tan\varphi = \frac{\text{imaginary part of } \mathcal{M}}{\text{real part of } \mathcal{M}}$$

$$= \frac{\omega(\tau_\sigma - \tau_\epsilon)}{1 + \omega^2(\tau_\sigma \tau_\epsilon)} \qquad \ldots \text{VI.13}$$

If the geometric mean of the relaxation times, $\bar{\tau}$ and the moduli, $\bar{M}$, areintroduced into equation VI.13 and making use of equation VI.10 then:

$$\tan \varphi = \frac{M_u - M_R}{\bar{M}} \cdot \frac{\omega \bar{\tau}}{1 + (\omega \bar{\tau})^2} \qquad \ldots \text{ VI.14}$$

The maximum value of $\tan \varphi$ occurs when $\omega \bar{\tau} = 1$, therefore,

$$\tan \varphi_{max} = \frac{M_u - M_R}{2\bar{M}} \qquad \ldots \text{ VI.15}$$

Substituting equation VI.15 into equation VI.14 gives:

$$\tan \varphi = 2 \tan \varphi_{max} \cdot \frac{\omega \bar{\tau}}{1 + (\omega \bar{\tau})^2} \qquad \ldots \text{ VI.16}$$

Zener (1948) showed equation VI.14 could be rewritten in terms of a quantity known as the relaxation strength, Δ ,

$$\tan \varphi = \frac{\Delta}{(1 + \Delta)^{\frac{1}{2}}} \cdot \frac{\omega \bar{\tau}}{1 + (\omega \bar{\tau})^2} \qquad \ldots \text{ VI.17}$$

which is a Debye peak whose maximum occurs at $\omega \bar{\tau} = 1$. The relationship between peak height and relaxation strength can be obtained by combining equations VI.16 and VI.17.

$$\tan \varphi_{max} = \frac{\Delta}{(1 + \Delta)^{\frac{1}{2}}} \qquad \ldots \text{ VI.18}$$

From VI.18 it can be seen that the relaxation strength may be found from the height of the peak, while the mean relaxation time $\bar{\tau}$ is obtained from the frequency at which the peak occurs. The relaxation strength depends on which

modulus governs the relaxation between stress and strain; since the elastic constants of a material are anisotropic properties the relaxation strength itself is dependent on crystallographic orientation.

VI.2 Measures of Internal Friction

A number of relationships exist between the various measures of internal friction and these are given below:

$$\tan \varphi = \varphi = Q^{-1} \qquad \ldots \text{VI.19}$$

equation VI.19 resulting from analogy with electrical circuit theory and is only valid for $\varphi << 1$. If the internal friction, Q^{-1}, is determined by the free decay method it is usually calculated from the logarithmic decrement, δ, of the decaying amplitudes with the formula:

$$Q^{-1} = \delta/\pi \qquad \ldots \text{VI.20}$$

where

$$\delta = \text{In } (A_n/A_{n+1}) \qquad \ldots \text{VI.21}$$

However, since a damped oscillation is not precisely a harmonic one equation VI.20 is only an approximation (Zener, 1947). The true relationship between the peak value of the loss angle φ_m, Q_m^{-1}, and the peak value of

δ_m is:

$$\tan \varphi_m \approx \varphi_m = Q_m^{-1} = (\delta m/\pi)\left[1 - (\frac{\delta m}{2\pi}) + \ldots\right] \qquad \ldots \text{VI.22}$$

which is an important result since the correction is of the first order in δ_m and the error in using equation VI.20 instead of equation VI.22 can be large; for example, for $Q^{-1} = 0.01$ the error is about 0.5%.

VI.3 Dynamic Properties of the Standard Anelastic Solid as a Function of Temperature

The variation of φ or Q^{-1} has been expressed as a function of $\omega\tau$. This means the relaxation peak can be traced out either by varying ω at constant τ, or by varying τ at constant ω. If the peak is to be measured by frequency variations changes of several orders of magnitude are required, and this is experimentally very difficult. In practice one capitalizes upon the fact that τ is very often an exponential function of temperature, T, the relaxation time obeying an Arrhenius equation:

$$\tau = \tau_o \exp \Delta H/RT \qquad \ldots \text{VI.23}$$

where ΔH is the activation enthalpy for the reaction, and R is the gas constant. From equations VI.16, VI.19 and VI.23 then:

$$Q^{-1} = 2Q^{-1}_{max} \cdot \frac{\omega\tau_o \exp(\Delta H/RT)}{1 + \omega^2 \tau_o^2 \exp(2\Delta H/RT)} \quad \ldots \text{VI.24}$$

and since at constant ω, Q^{-1}_{max} occurs at T_p and $\omega\tau = 1$, then equation VI.24 becomes:

$$Q^{-1} = Q^{-1}_{max} \operatorname{sech}\left[\frac{\Delta H}{R}\left(\frac{1}{T} - \frac{1}{T_p}\right)\right] \quad \ldots \text{VI.25}$$

where T_p is taken to be the peak temperature, and hence damping can be measured at constant frequency by varying the temperature. Although equation VI.25 defines the ideal internal friction characteristics of a single relaxation process it must be remembered that ω (measured frequency) varies with temperature, because of the variation of the modulus, and also that the relaxation strength, Δ, is slightly temperature dependent.

There is a large volume of literature on the subject of internal friction in metals which can be explained in terms of certain physical processes occurring within the material. The work in this thesis is concerned with investigating the internal friction arising from interstitial atom movement in body-centred cubic iron containing a dispersion of second-phase particles. The remaining part of this chapter discusses this damping process and the various factors which influence its measurement.

VI.4 Internal Friction Arising from Interstitial Atoms - the Snoek Relaxation

An interstitial atom in body-centred cubic iron occupies the octahedral interstices, thereby producing a tetragonal distortion of the lattice in the direction of the two closest iron atoms (i.e. along ⟨100⟩ directions). If the directions are designated x, y, z, the interstitial sites may also be termed x, y, z, according to the direction in which the maximum distortion is produced, see Figure VI.2(a). In an unstressed specimen all octahedral sites are equivalent, and are randomly occupied, each containing one-third of the total interstitial content. If a tensile stress is applied, for example in the z direction (see Figure VI.2(b)), then a redistribution of interstitials will take place so that the z sites will contain more than one-third of the total interstitial concentration. The movement of interstitials from x and y sites to z sites will be at a rate dependent on D, the diffusivity of the interstitial atoms in iron, and the application of the applied stress will produce a strain varying with time, resulting in anelasticity.

At the equilibrium value of anelastic strain the relaxation strength Δ, is proportional to the solute concentration, c, and is given by:

$$\Delta = \frac{2V_c E}{9RT} \cdot \left\{ \frac{\epsilon_{zz} - \epsilon_{xx}}{C_z} \right\}^2 \qquad \ldots \text{ VI.26}$$

Figure VI.2

Interstitial sites and diffusion path in a b.c.c. alloy for (a) no applied stress and (b) with an applied stress.

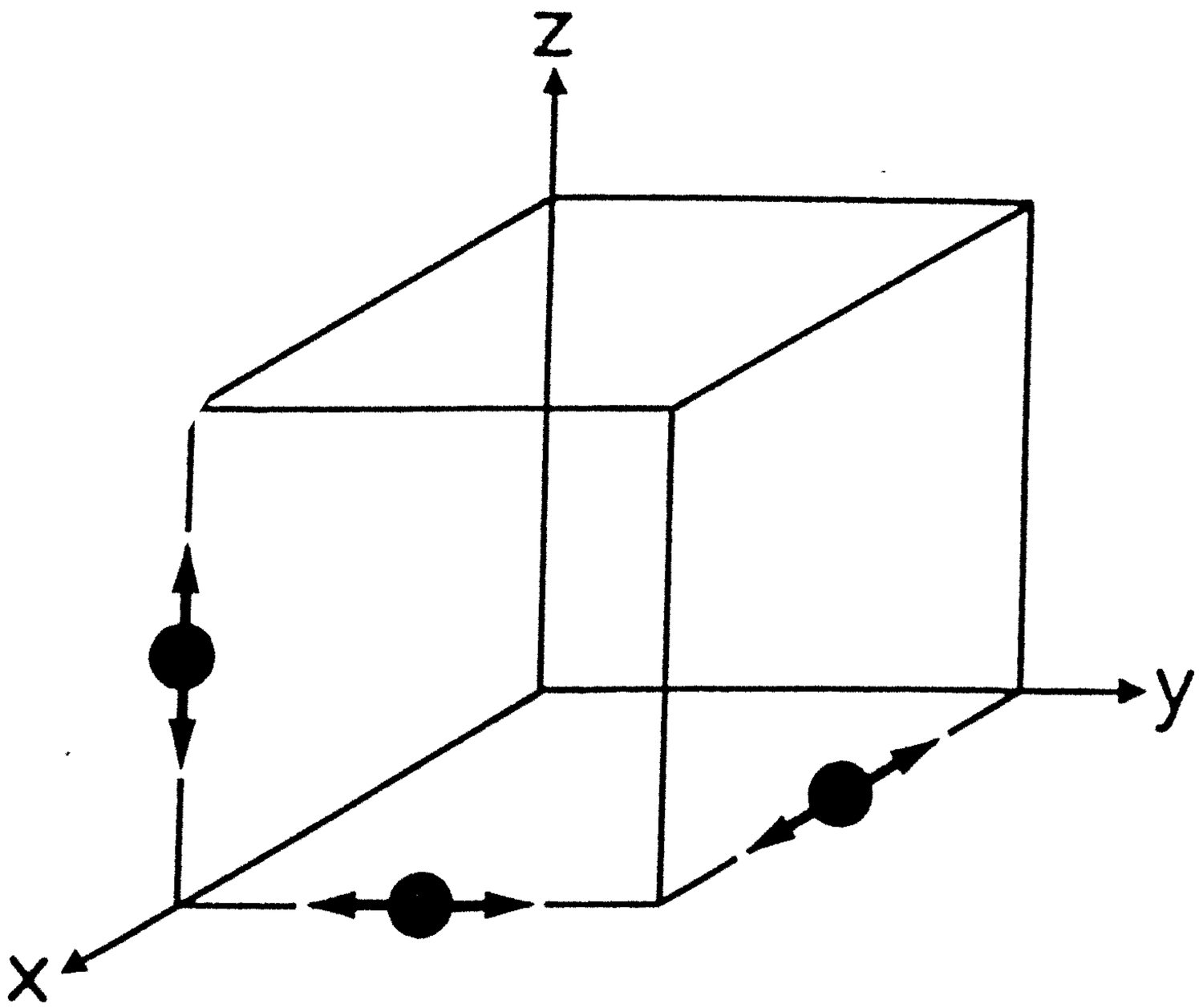

(a)

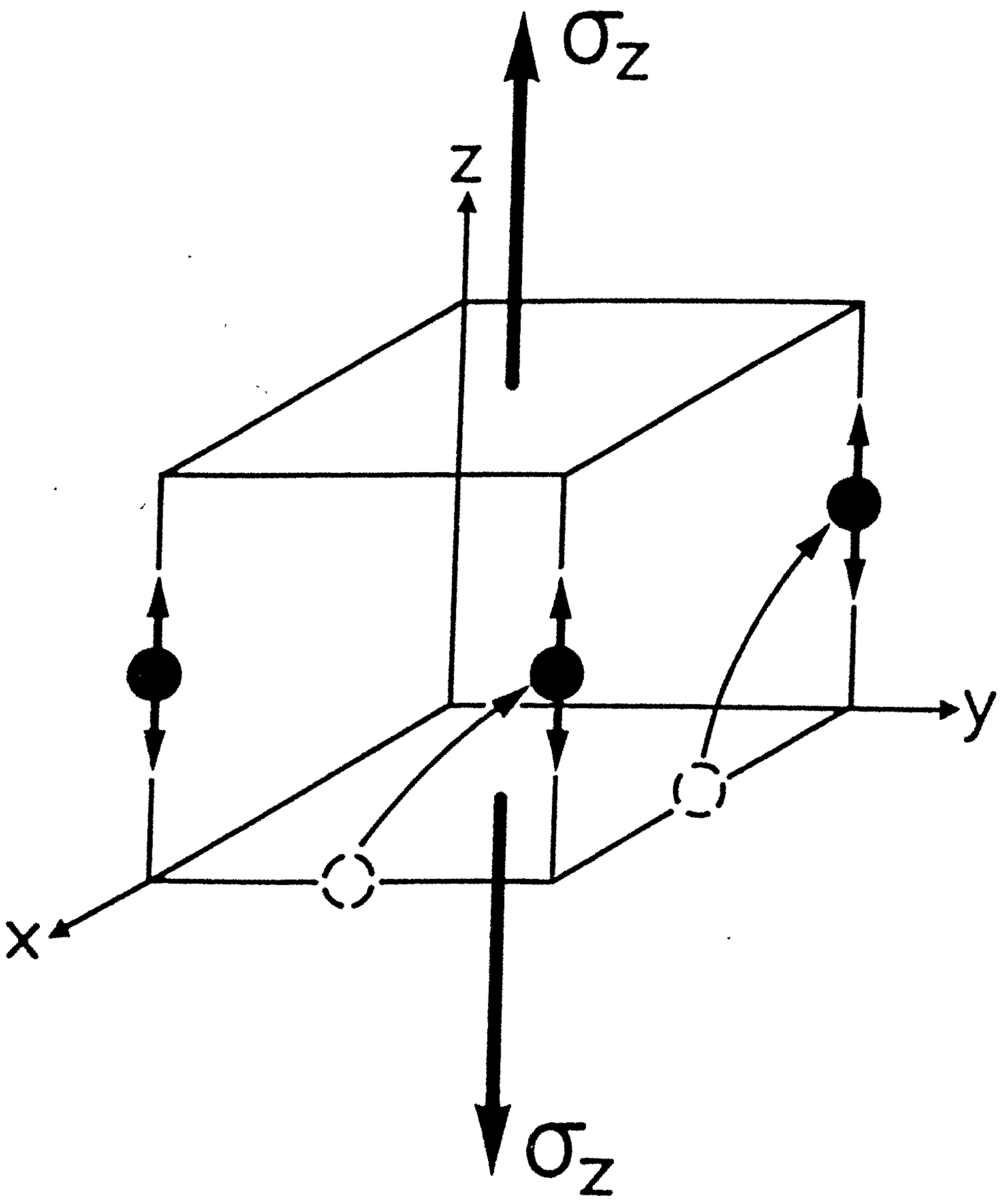

(b)

where E represents the unrelaxed modulus of elasticity in a ⟨100⟩ direction, C_z is the increased interstitial content in z sites at the expense of that in x and y sites, ϵ_{zz}, ϵ_{xx} are the values of strain in z and x directions, and V is the molar volume of iron.

If the tensile stress is not applied in a ⟨100⟩ direction of a single crystal but in some arbitrary direction then equation VI.26 becomes:

$$\Delta = \frac{2VcE}{9RT} \cdot \left\{ \frac{\epsilon_{zz} - \epsilon_{xx}}{C_z} \right\}^2 \cdot \left[1 - 3 \left(\alpha_1^2 \alpha_2^2 + \alpha_2^2 \alpha_3^2 + \alpha_3^2 \alpha_1^2 \right) \right] \quad \ldots \text{VI.27}$$

Here α_1, α_2 and α_3 are the direction cosines of the applied stress with respect to the ⟨100⟩ axes of the crystal, E is the value of Young's modulus in the direction α_1, α_2, α_3.

It should be noted that equation VI.27 predicts that the Snoek effect must be absent when the tensile stress is applied in a ⟨111⟩ direction and this was confirmed experimentally by Dijkstra (1947). In general:

$$\text{w/o (interstitial)} = k \cdot Q_{max}^{-1} \quad \ldots \text{VI.28}$$

where the proportionality constant, k, can be calculated on a theoretical basis for single crystals of known orientation. For polycrystalline wires no exact theoretical calculation of the internal friction magnitude is possible; this problem is discussed in the next section.

VI.5 Factors Affecting the Measurement of the Snoek Peak

In order that internal friction measurements can be used to accurately determine small concentrations of interstitially dissolved elements in body-centred cubic iron a value of k in equation VI.28 is needed. As previously mentioned for single crystals of known orientation this presents little problem, but in general no theoretical calculation of the magnitude of k is possible for polycrystalline materials.

In polycrystalline samples the value of k is influenced by the grain size of the material and the existence of preferred orientation within the specimen. By ignoring the effect of texture Smit & Van Bueren (1954) used an averaging procedure based on the observed relation between the elastic constants of single crystals and polycrystalline specimens to predict the linear variation between peak damping and nitrogen concentration for polycrystalline iron-nitrogen alloys and the theoretical results were in good agreement with the experimental work of Fast & Verrijp (1955). For iron containing C or N in solid solution Lagerberg & Josefoson (1955) showed that peak damping varied with grain size for constant interstitial concentration. These observations were later confirmed by Ferguson (1981) using iron-nitrogen alloys; the deviation from the straight line at high interstitial contents, see Figure VI.3, being due to the clustering of nitrogen atoms before the internal friction peak can be measured. However, work by Swartz (1969) failed to show any correlation between peak damping and

Figure VI.3

Dependence of internal friction on nitrogen concentration, for different grain sized materials (after Ferguson, 1981).

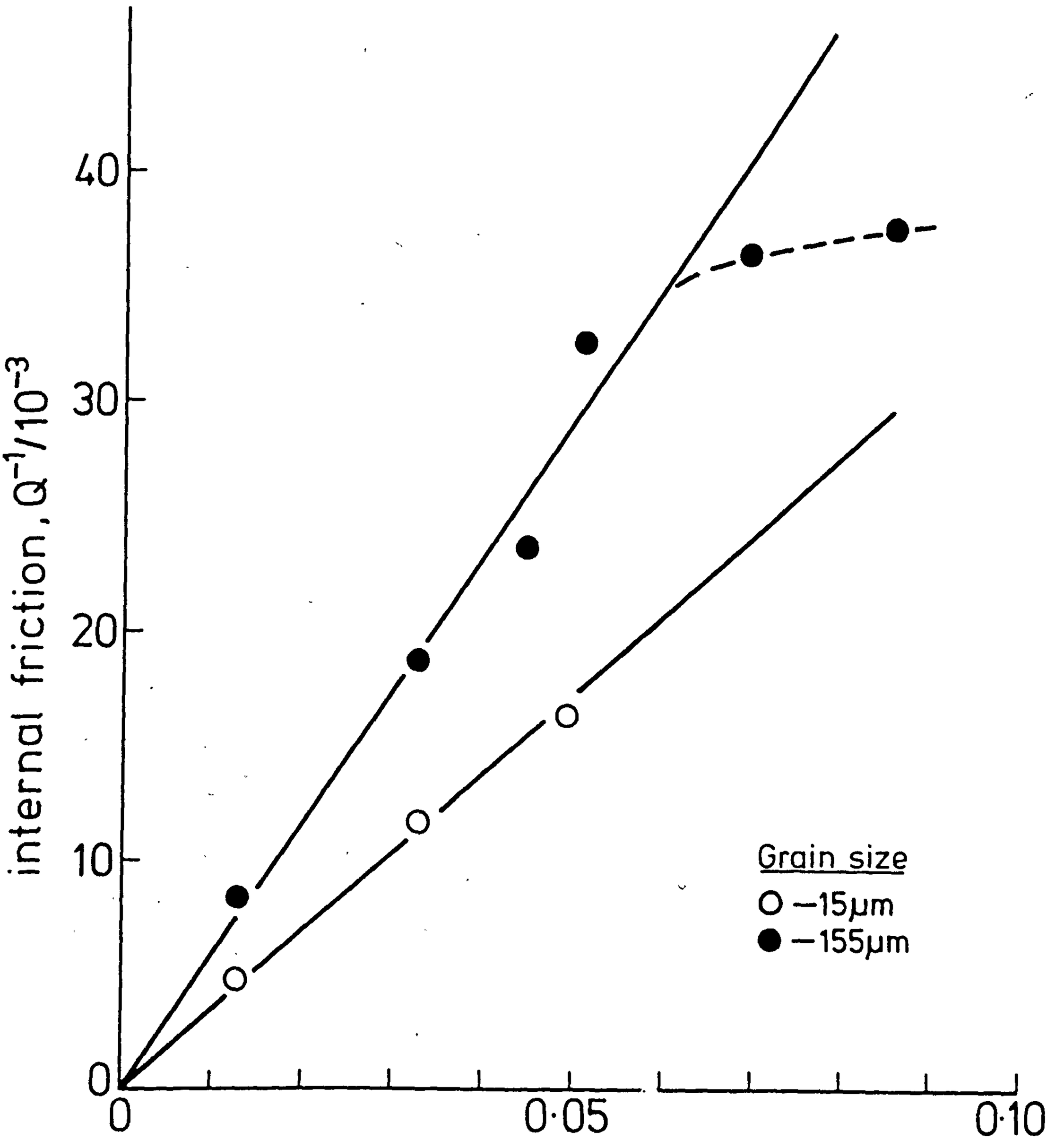
internal friction, $Q^{-1}/10^{-3}$
40
30
20
10
0
0
0·05
0·10
nitrogen concentration in solution/wt%
Grain size
○ −15μm
● −155μm

grain size, suggesting all variations in peak damping could be ascribed to variations in polycrystalline texture. It is therefore important to derive the relationship between internal friction and solute content for polycrystalline specimens experimentally, using samples of truly random texture in order to obtain reliable and reproducible results.

In addition to the damping caused by stress-induced diffusion of interstitial atoms in solid solution, damping due to the ferromagnetic nature of iron is also possible. This additional source of damping is important since it may interfere with the resolution of the damping spectra caused by interstitial atoms in iron and iron-alloys. In the demagnetised conditions, Figure VI.4; curve 1, the internal friction spectrum of an iron-nitrogen alloy shows a Snoek peak at about 20°C which is accompanied by additional damping below and above the Snoek peak temperature. By applying a saturated magnetic field of 85 Oe this additional damping is suppressed and the Snoek peak is easily resolved; see Figure VI.4, curve 2. This additional magnetic damping has many origins but the most important contributions result from:

(i) Magneto elastic static hysteresis loss; domain walls through magnetostrictive coupling move under an applied stress. Because part of this motion is irreversible, such movement gives rise to an energy loss in damping experiments. This type of damping is strongly amplitude dependent.

(ii) Magneto elastic phase lag loss results from

Figure VI.4

The influence of a magnetic field on the internal friction damping of a Fe-N alloy (after Forguson, 1931).

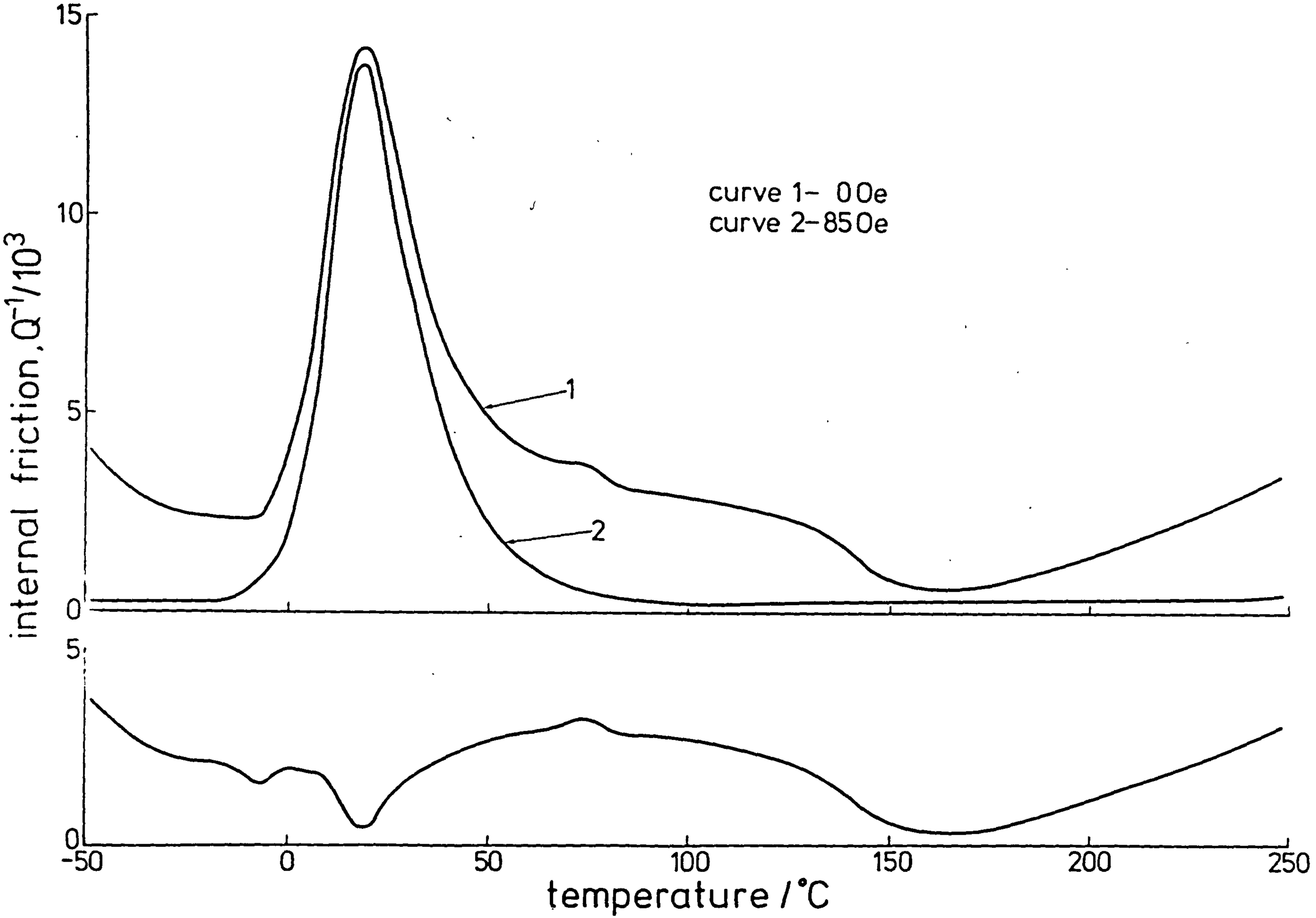
curve 1– 0Oe
curve 2–85Oe
internal friction, $Q^{-1}/10^3$
15
10
5
0
1
2
5
0
-50
0
50
100
150
200
250
temperature / °C

a phase lag between the applied stress and domain wall movement, and is accompanied by directional ordering of the interstitial solute.

It is therefore important when carrying out damping experiments on iron and iron alloys to apply a saturating magnetic field to suppress magnetic contributions to the damping spectra.

Chapter VII

THERMOCHEMISTRY AND ZONE STRUCTURE OF Fe-Ti-N ALLOYS

VII.1 Introduction

It is possible to characterise completely the structures produced by gaseous nitriding of ferritic alloys by a combination of internal friction, electron microscopy, X-ray determination of matrix unit-cell dimensions and weight change measurements. Internal friction provides useful information concerning the metal-atom environments around a nitrogen atom as it occupies an octahedral interstice in the body-centred cubic lattice and changes produced by nitriding and aging treatments are reflected in the internal friction spectra. Chapter II has shown that measurement of unit-cell dimensions, in conjunction with electron microscopy and strength measurements, provides a means of identifying mixed substitutional-interstitial solute-atom clusters in nitrided materials and the transformation of Ti-N clusters to the equilibrium precipitate, TiN, is followed by measuring the decrease in the ferrite lattice parameter with aging time.

In the present investigation this combination of techniques has been particularly useful in determining a model for the substitutional-interstitial zones formed by nitriding Fe-Ti alloys with less than 0.30 w/o Ti, and as

a means of investigating the thermodynamics of nitrogen absorption in nitrided Fe-Ti alloys.

VII.2 Internal Friction of Nitrided Fe-Ti Alloys

Figure VII.1 shows the internal friction spectra of iron and dilute Fe-Ti alloys nitrided at 500°C with a nitrogen activity (a_N) of 0.035. These show a normal Snoek peak at about 20°C that decreases in height with increasing titanium content, and also a "high-temperature" peak, now designated and described in the present thesis as a "substitutional-interstitial peak", (s-i), the position of which moves to higher temperatures as the titanium increases. The matrix unit-cell dimensions of the nitrided alloys are much higher than that of pure iron (2.8664 Å) and are consistent with all of the nitrogen absorbed during nitriding being in solid solution - either random or clustered. The observed expansions in unit-cell dimensions above that of pure iron are in good agreement with the theoretical expansion derived from equation II.1; see Figure VII.2. And since the nitriding of these alloys was accompanied by large increases in strength (see Chapter IX) the solute-atom distribution cannot be random, a fact confirmed by transmission electron microscopy. These observations taken together indicate the presence of solute-atom clusters or GP zones in the ferrite matrix.

In Chapter VI it was shown that the Snoek peak height

Figure VII.1

Internal friction scans of iron and Fe-Ti alloys nitrided in $16NH_3:84H_2$ at 500°C for 18 h and brine quenched.

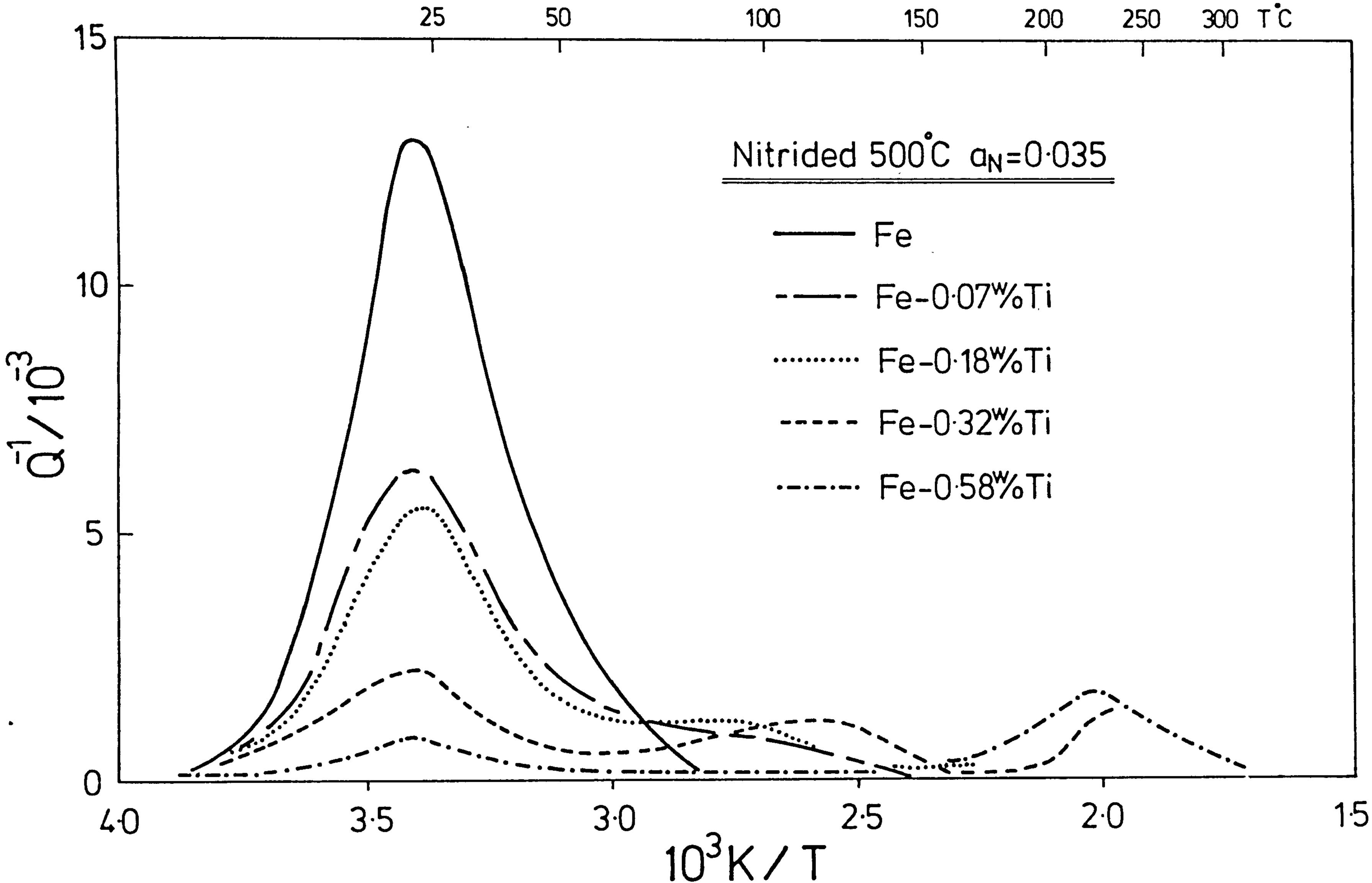
25
50
100
150
200
250
300 T°C
15
10
5
0
$Q^{-1}/10^{-3}$
Nitrided 500°C a_N=0·035
Fe
Fe-0·07w%Ti
Fe-0·18w%Ti
Fe-0·32w%Ti
Fe-0·58w%Ti
4·0
3·5
3·0
2·5
2·0
1·5
10^3K / T

Figure VII.2

Calculated and observed lattice expansions in nitrided Fe-Ti alloys.

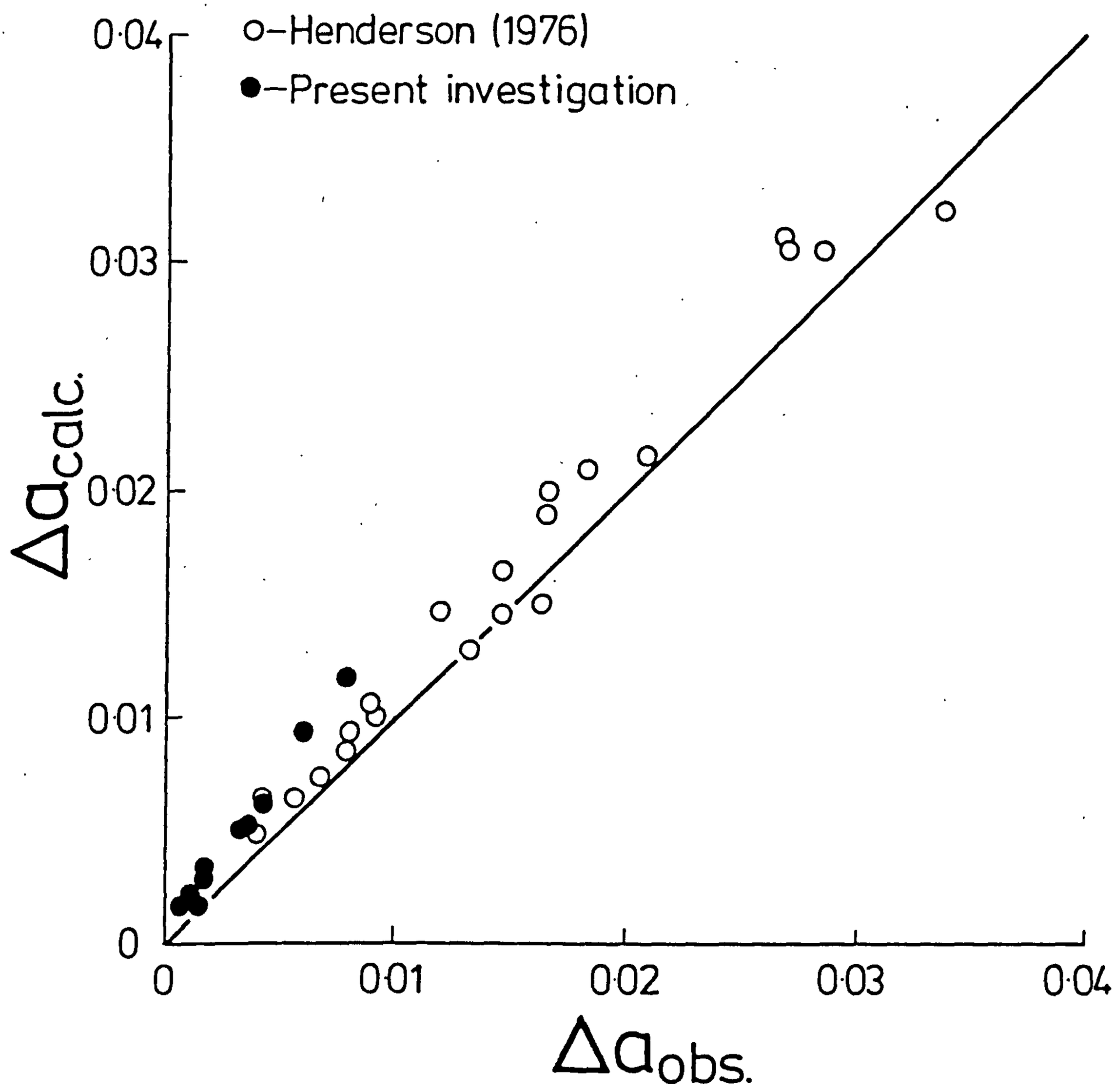
o–Henderson (1976)
●–Present investigation
0·04
0·03
0·02
0·01
0
0
0·01
0·02
0·03
0·04
$\Delta a_{calc.}$
$\Delta a_{obs.}$

varies linearly with nitrogen content. The amount of nitrogen in equilibrium with ferrite at nitriding temperature being determined by the equilibrium constant for the nitriding reaction, K_p, and the nitriding potential, $R(= pNH_3/pH_2^{3/2})$. In general:

$$a_N = K_p \cdot R$$

that is $$w/o\ N = K_p \cdot R/f_N$$

or $$w/o\ N = K_p' \cdot R \qquad \ldots \text{ VII.1}$$

where f_N is the activity coefficient, and K_p' is a pseudo equilibrium constant which refers to the nitriding of Fe-Ti alloys. Figure VII.3 shows in nitrided Fe-0.18 w/o Ti a linear dependence exists between internal friction damping and R, indicating that the activity coefficient for nitrogen is constant for a given titanium concentration at fixed nitriding temperature. At high nitriding potentials the experimental points deviate from the straight line as nitrogen atoms are removed from random solid solution before measurement of the Snoek peak can be completed, indicating at high supersaturations clusters of nitrogen can form readily even at room temperature. The open circles in Figure VII.3 for Fe-0.18 w/o Ti represent the Snoek peak heights obtained from samples initially nitrided at 585°C with R = 0.13 but then re-equilibrated at the nitriding potential indicated. Within experimental

Figure VII.3

Peak damping against nitriding potential (R) for Fe and Fe-0.18 w/o Ti alloys nitrided at 585°C.

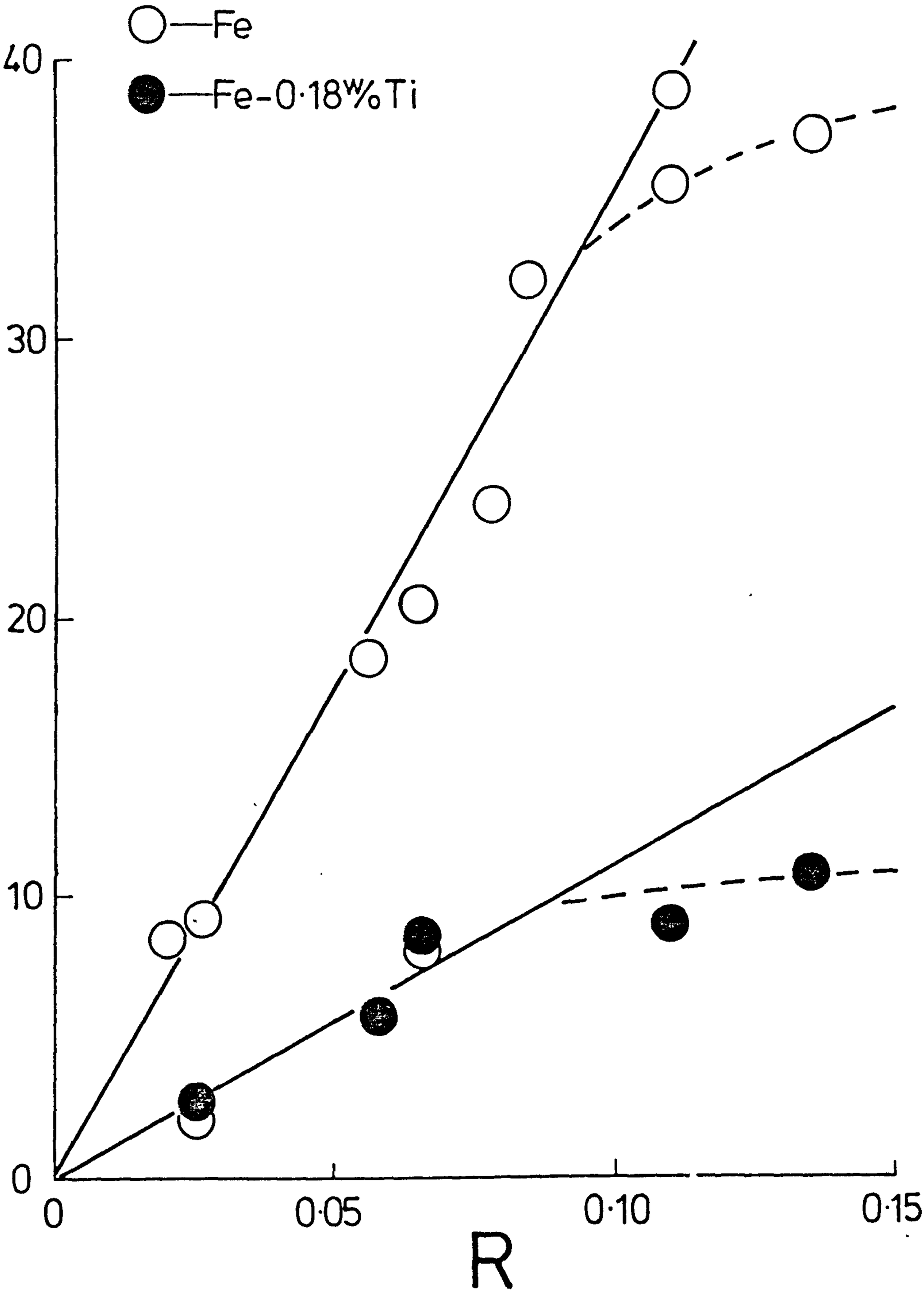
○—Fe
●—Fe-0·18w% Ti
40
30
20
10
0
$Q^{-1}/10^{-3}$
0
0·05
0·10
0·15
R

error the internal friction scans of alloys nitrided directly or renitrided are identical, showing the nitrogen atoms absorbed on nitriding to be in equilibrium with the nitriding gas mixture although they occupy a number of different environments.

It has been reported that on nitriding Fe-Ti alloys under similar conditions to those used in the present investigation there exists no unstrained ferrite lattice sites - Snoek sites (Podgurski & Davis, 1981). However, the Snoek peak in nitrided Fe-Ti alloys occurs at the same temperature as that in Fe-N alloys confirming the existence of unstrained ferrite sites. If the octahedral sites occupied by nitrogen were influenced by strain the peak temperature would not occur at around 20°C for a frequency of approximately 1 Hz. Both Figures VII.1 and VII.3 show the Snoek peaks in nitrided Fe-Ti alloys to be lower than those observed in the corresponding Fe-N alloy although in both cases the samples are in equilibrium with the same nitriding gas mixture. It is unlikely that the number of iron-atom octahedra available for Snoek peak relaxations could be changed greatly by physical exclusion of sites due to the presence of the substitutional-interstitial clusters. However the dashed curve in Figure VII.4, which represents the ratio of the Snoek peak heights obtained for nitrided Fe-Ti and pure iron alloys over a range of nitriding temperatures and potentials, clearly shows the number of Snoek sites falls appreciably with increasing

Figure VII.4

Ratio of peak damping Fe-Ti-N/Fe-N against atomic percentage titanium for various nitriding conditions.

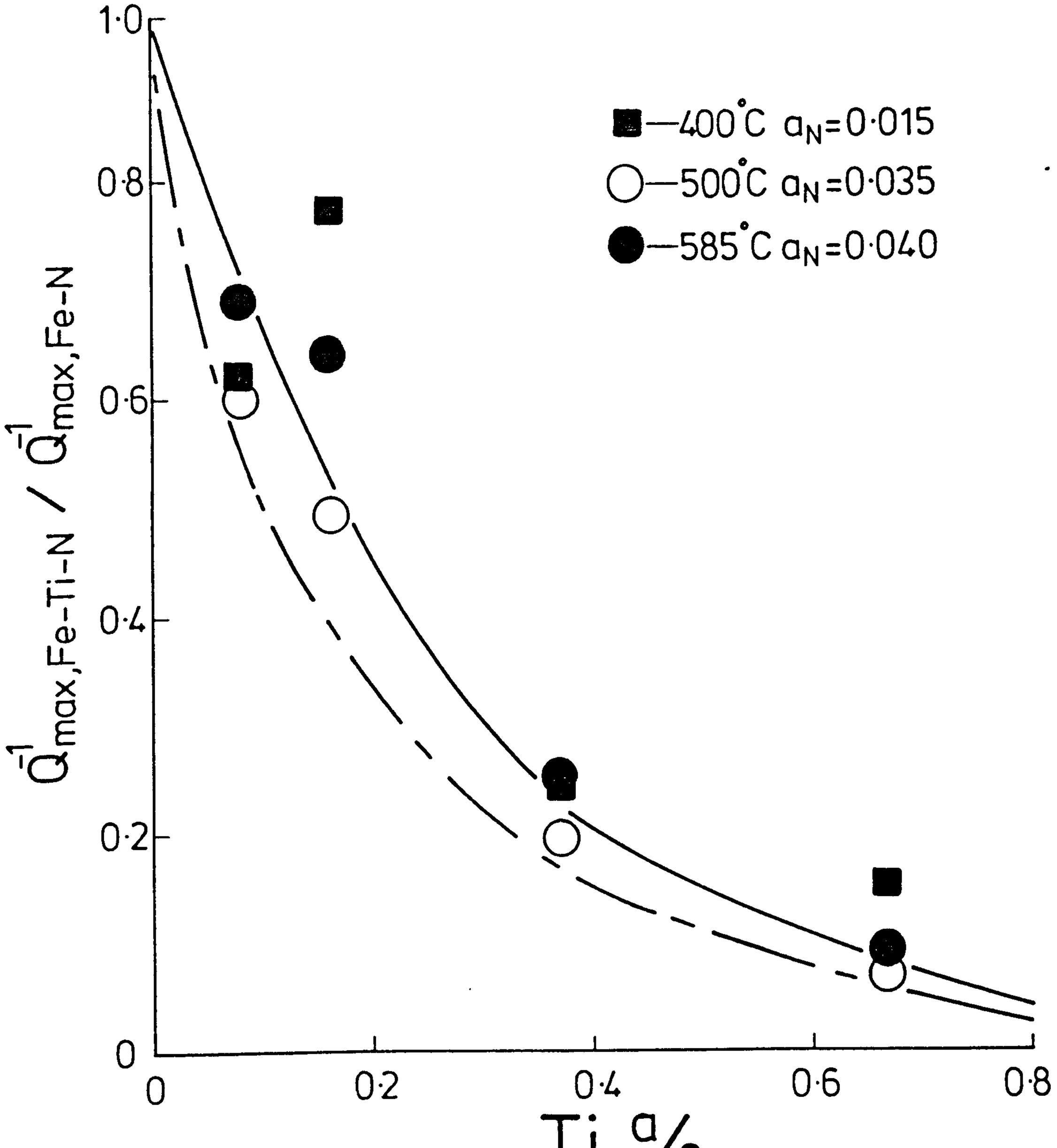
■—400°C a_N=0·015
○—500°C a_N=0·035
●—585°C a_N=0·040
$Q^{-1}_{max,Fe-N}$ / $Q^{-1}_{max,Fe-Ti-N}$
1·0
0·8
0·6
0·4
0·2
0
0
0·2
0·4
0·6
0·8
Ti, %

volume fraction of Ti-N clusters in the ferrite matrix. This marked reduction in Snoek sites with increasing titanium concentration is still apparent even when allowance is made for the difference in grain size which exists between the iron-titanium alloys; full curve in Figure VII.4. By using a modified version of the model already proposed for the zone structure of nitrided Fe-Ti alloys (Jack, 1978) it is possible to explain the data given in Figure VII.4. The existing model is based on experimental work which used Fe-Ti alloys with > 0.5 w/o Ti and represents the zones formed on nitriding as discs of Ti and N atoms parallel to the three cube planes of the ferrite matrix. These discs are essentially monolayer clusters of titanium and nitrogen atoms with each nitrogen coordinated by four Ti atoms in the layer and an Fe atom above and below it giving a zone composition of Fe_2TiN; see Chapter II. In nitrided alloys containing less than about 0.3 w/o Ti it is considered that the clusters are different in composition and structure from the idealised monolayer model that is approached at high titanium concentrations. It is likely that the cluster will contain increasing concentration of iron with decreasing titanium in the alloy and there will be a variety of iron-atom octahedral environments the potential energies of which will vary with the proximity and distribution of Ti atoms. On this modified model the stress induced diffusion of nitrogen atoms around a Ti-N cluster will have a range of activation energies since the Ti-N clusters influence

nitrogen atoms which are several atom-jumps away. As the volume fraction of clusters is increased the amount of ferrite which will be influenced by titanium atoms which are themselves part of a cluster or in random solid solution will also increase. In addition, during the quench from nitriding temperature the high diffusivity of nitrogen means that condensation of nitrogen onto existing Ti-N clusters can occur. The proportion of nitrogen atoms originally occupying normal Snoek sites which segregate to the Ti-N clusters on cooling increases with the volume fraction of clusters. Therefore with increased titanium concentration the Snoek peak height will decrease in nitrided Fe-Ti alloys as shown in Figure VII.4.

The proposed model for the zone structure of dilute Fe-Ti alloy therefore allows for a range of stress induced nitrogen-atom jumps during internal friction measurements whose energy depends on the distribution of Ti atoms in adjacent sites. The high-temperature peak being attributed to nitrogen atom jumps between iron-atom octahedra which are influenced by neighbouring Ti atoms, these sites are now designated "modified" octahedra. On this model, varying the nitriding temperature should result in variations in cluster composition with corresponding changes in the high-temperature peak reflecting a change in the distribution of nitrogen-atom environments. This prediction is confirmed for Fe-0.18 w/o Ti nitrided between

400-650°C with approximately the same activity of nitrogen ($a_N \simeq 0.015$), Figure VII.5, in which the Snoek peak heights are approximately constant. At low nitriding temperatures substitutional atom diffusivity is low, the titanium atoms are more widely dispersed than depicted in the idealised monolayer model (Jack, 1978) and hence a larger proportion of nitrogen atoms occupy "modified" iron-atom octahedra giving rise to a high-temperature peak. As the nitriding temperature is increased and more titanium atoms are accommodated in the monolayer, the proportion of nitrogen atoms which occupy octahedral sites with energies characteristic of those which make up the high-temperature peak decreases and so this peak declines. Eventually by nitriding at 650°C the approximation of the Ti-N clusters to a monolayer of titanium atoms is more realistic and the high-temperature peak cannot be detected within the temperature investigated. These differences in high-temperature damping will be discussed further.

Approximate activation energies can be calculated for positions along the temperature axis of an internal friction scan by using the law of Wert & Marx (1953) which may be expressed as:

$$\frac{T_1}{\Delta H_1} = \frac{T_2}{\Delta H_2} \qquad \ldots \text{ VII.2}$$

where T_1 and T_2 are the absolute temperatures of the peak

Figure VII.5

Normalised internal friction scans for Fe-0.18 w/o Ti nitrided at various temperatures with constant nitrogen activity.

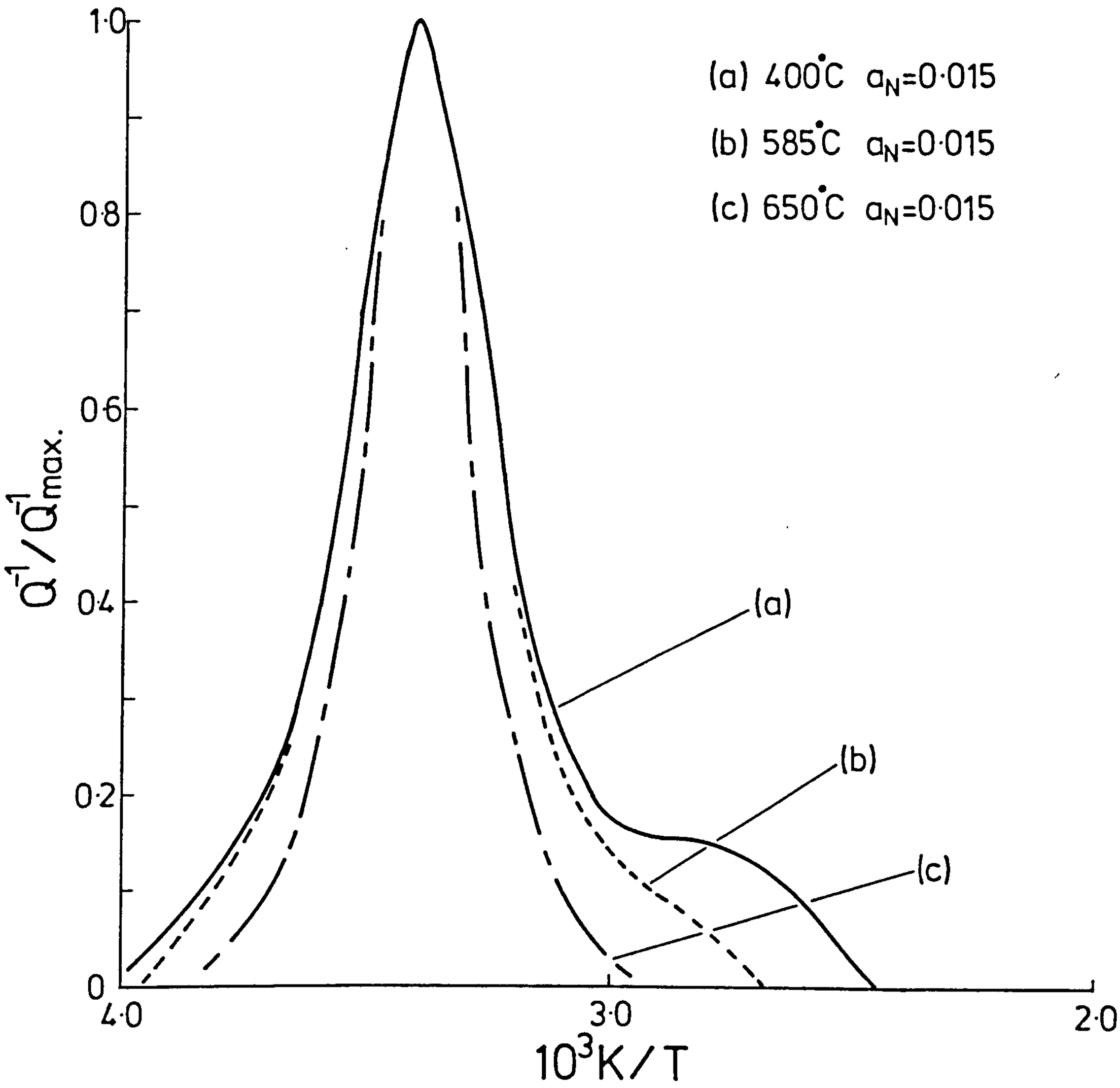
1·0
0·8
0·6
0·4
0·2
0
Q^{-1}/Q^{-1}_{max}
(a) 400°C a_N=0·015
(b) 585°C a_N=0·015
(c) 650°C a_N=0·015
(a)
(b)
(c)
4·0
3·0
2·0
$10^3 K/T$

positions and ΔH_1, ΔH_2 their respective activation energies. Table VII.1 indicates that the jump-processes which give rise to the high-temperature peak in nitrided Fe-Ti alloys have activation energies which lie in the range 80-120 kJ/mole which are not much greater than that for nitrogen in random solid solution in iron, that is 75 kJ/mole. For this reason it is proposed that these high-temperature spectra must be due to jumps by isolated nitrogen atoms between iron-atom octahedra modified slightly by the proximity of Ti atoms at varying next-nearest neighbour distances from the jump. This view is supported by internal friction experiments on pure iron which shows no relaxation peaks when the nitrogen atoms are in non-random solid solution, that is, present as nitrogen-clusters.

Variations in the composition and structure of nitrided alloys can also be brought about by aging at high temperatures. Several wires of an Fe-0.18 w/o Ti alloy were nitrided in a $8NH_3:92H_2$ gas mixture at 585°C and hydrogen reduced at nitriding temperature. Individual nitrided wires were then aged at 800°C in argon filled silica capsules before all the wires were re-nitrided using the initial nitriding conditions. The changes in Snoek and high-temperature peaks as a result of aging are illustrated in Figure VII.6(a). The Snoek peak height increases with aging time up to 100 h and thereafter remains approximately constant as the Ti-N clusters gradually transform to the equilibrium precipitate. This

Figure VII.6

Internal friction spectra of Fe-0.18 w/o Ti initially nitrided in $8NH_3:92H_2$ at 585°C for 18 h and hydrogen reduced at 585°C for 18 h; aged at 800°C, then re-nitrided in $8NH_3:92H_2$ at 585°C for 3 h and brine quenched. Variation with aging time at 800°C of (a) peak damping, and (b) high-temperature damping.

(a)

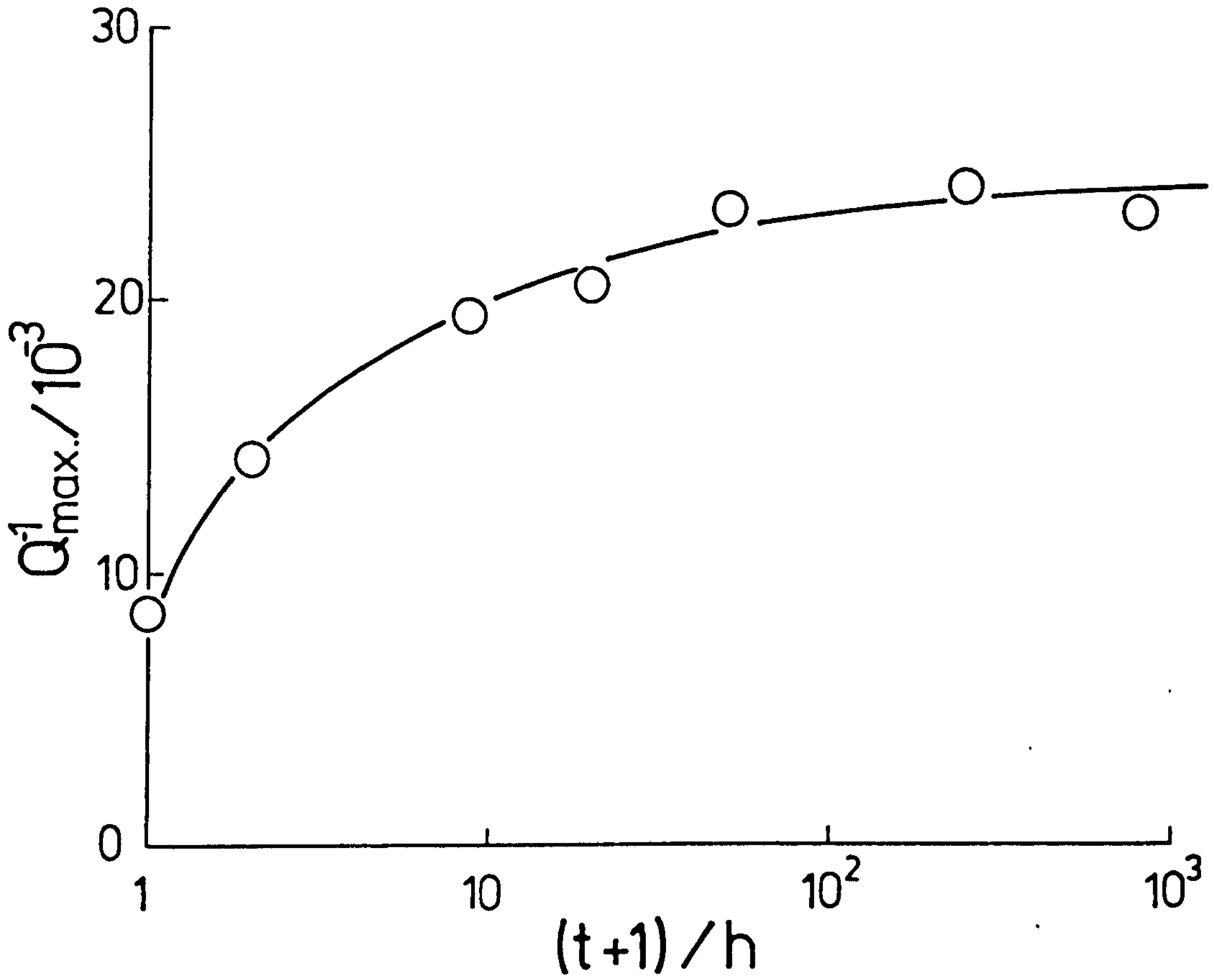
30
20
10
0
$Q^{-1}_{max.} / 10^{-3}$
1
10
10^2
10^3
(t+1) / h

(b)

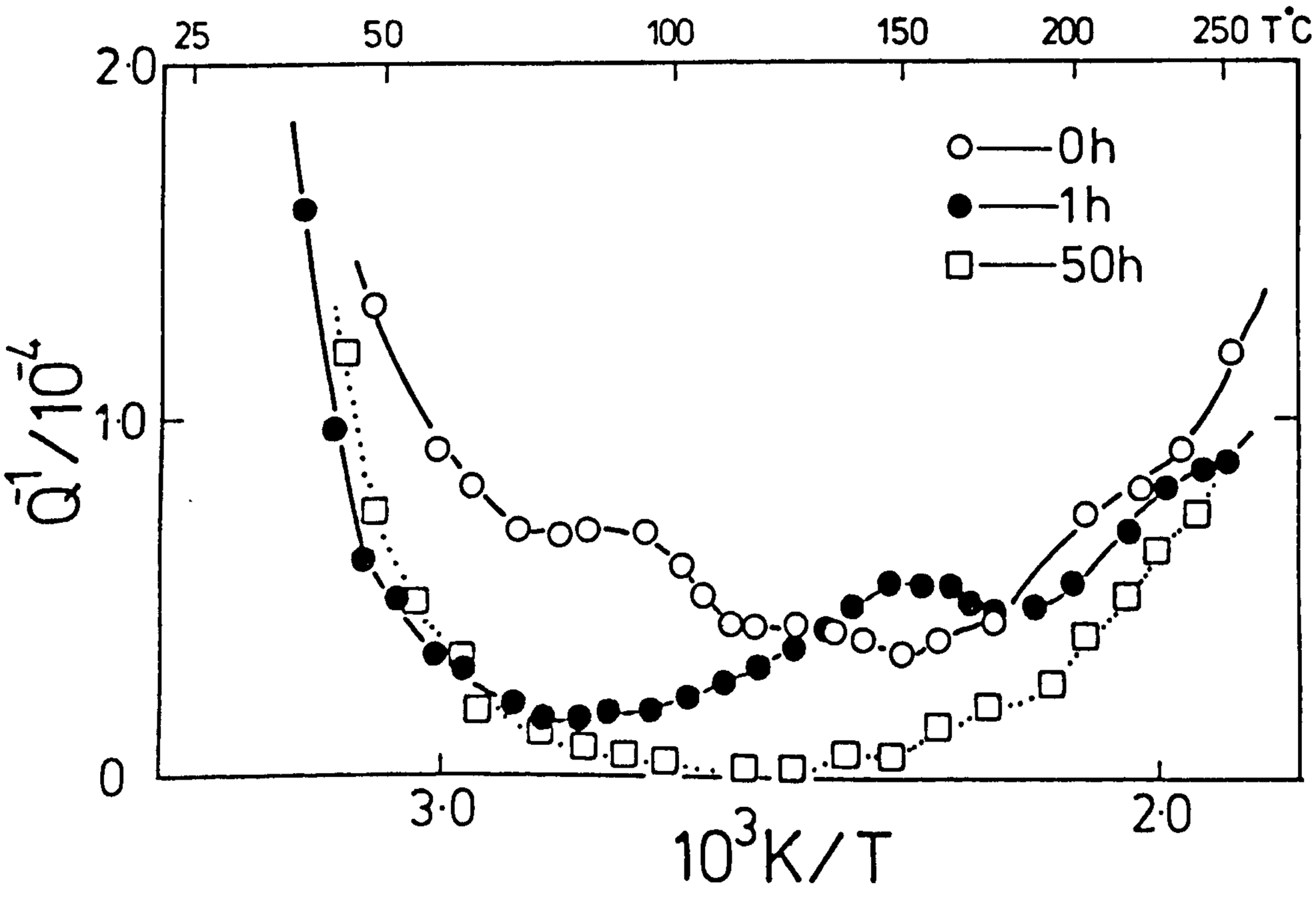
25
50
100
150
200
250 T°C
2·0
1·0
0
$\bar{Q}^1 / 10^{-4}$
3·0
2·0
$10^3 K / T$
0—0h
●—1h
□—50h

Table VII.1

Possible activation energies for the substitutional-interstitial peaks observed in nitrided Fe-Ti alloys

T, °K	T, °C	ΔH_2*, kJ/mole	10^3 K/T
323	50	83 ± 5	3.096
353	80	90 ± 5	2.833
373	100	95 ± 5	2.681
393	120	101 ± 5	2.545
413	140	106 ± 5	2.421
453	180	116 ± 5	2.208
473	200	121 ± 5	2.114

*Obtained from equation VII.1 with H_1 = 75 kJ/mole and T_1 = 293K.

variation in Snoek peak height indicates the segregation of nitrogen atoms onto existing particles during the quench from re-nitriding temperature is reduced as the particles coarsen. However the behaviour of the high-temperature peak is quite different, see Figure VII.6(b), the position

of maximum damping moving from about 86°C to 150°C on aging for 1 h at 800°C. This shift corresponds to a change of about 15 kJ/mole in the average activation energy for the range of relaxation processes giving rise to the high-temperature peak. In such a short time large scale movement of Ti atoms is not possible and these changes result from the localised rearrangement of Ti atoms so as to form "ideal" monolayers thereby modifying the energy of the iron-atom octahedral sites surrounding them. As the aging time increases the activation energies of these "modified" nitrogen-atom jumps is further increased until after 50 h they have energies similar to or greater than those which characterise the cold-work peak (Fast, 1976). The clustering together of titanium atoms therefore leads to higher Snoek peaks and smaller high-temperature peaks as the particles coarsen to give incoherent TiN, this gradual coarsening process is shown in Figure VII.7. The matrix unit-cell dimensions of material aged as in Figure VII.6 are constant for times up to 11.5 h, which indicates the Ti-N clusters formed on nitriding are quite stable. However, the lattice parameter after aging at 800°C for times greater than 100 h falls to a value consistent with the ferrite matrix containing the equilibrium amount of nitrogen for the nitriding conditions used, that is, 0.050 w/o N by X-rays compared with 0.055 w/o N expected for nitriding at 585°C in a $8NH_3:92H_2$ gas mixture (see Figure IV.2).

Figure VII.7

Transmission electron micrographs of Fe-0.18 w/o Ti nitrided in $8NH_3:92H_2$ at 585°C for 18 h, hydrogen reduced at 585°C for 18 h then aged at 800°C for the times indicated.

(a),0h.

(b),11·5h.

(001)

2000Å

(c),50h.

(d),112h.

VII.3 Resolution of Internal Friction Damping Spectra

The internal friction spectra of nitrided Fe-Ti alloys consists of a Snoek peak at about 20°C, a high-temperature peak whose position varies with titanium content, and a cold-work peak at approximately 200°C in agreement with the work of Szabo-Miszenti (1970) who also considered the high-temperature peak to be a substitutional-interstitial interaction peak.

Most investigators (Dijkstra & Sladek, 1953; Ritchie & Rawlings, 1967; Nacken & Kuhlmann, 1966) in the study of iron ternary alloys use the summation of several single-relaxation time peaks of the Debye type to synthesise the experimental internal friction spectra. The peak contributions are defined by the Debye equation as follows:

$$Q_i^{-1} = \sum_i Q_{i,max}^{-1} \Big/ \cosh\left[\frac{\Delta H_i}{R}\left(\frac{1}{T} - \frac{1}{T_i}\right)\right] \qquad \ldots \text{ VII.3}$$

where Q_i^{-1} = Snoek damping of the ith peak

$Q_{i,max}^{-1}$ = maximum Snoek damping of the ith peak which occurs at $\omega\tau = 1$, where ω is the angular frequency of vibration and τ the relaxation time.

T = absolute temperature

T_i = absolute temperature at the peak

ΔH_i = activation energy of the ith relaxation

R = gas constant.

Such an analysis will not be attempted for the present work since there are many problems associated with this approach, especially if internal friction data are collected at constant frequency and varying temperature. Difficulties result since:

(a) The relaxation strengths and relaxation times may depend on temperature, so that the Debye peaks are not symmetrical about their centres in the internal friction against 1/T plot.

(b) Not all the interstitials in the various types of site need give rise to unique observable relaxation processes.

(c) With increasing interstitial content it is possible for sites which are nearer to Ti atoms to become blocked from jumping and the given relaxation can pass through a damping maximum.

With such uncertainties, and the need to estimate the values of activation energy to be used in equation VII.3, any analysis would be open to alternative interpretation. However the half-peak breadth of the high-temperature relaxation peaks are greater than those calculated from equation VII.3 showing them to be composed of a number of Debye peaks whose maxima occur when $\omega\tau = 1$ with a relaxation time given by:

$$\tau = \tau_o \exp (\Delta H/RT) \qquad \ldots \text{ VII.4}$$

Clearly the variations in relaxation times can result from variations in activation energy ΔH or in τ_o or possibly both. To separate the high-temperature peak from the Snoek peak the following approach has been used. From equation VII.3

$$\frac{\Delta H_i}{R}\left(\frac{1}{T} - \frac{1}{T_i}\right) = \cosh^{-1}\left(\frac{Q_{i,max}^{-1}}{Q_i^{-1}}\right) \qquad \ldots \text{ VII.5}$$

with $\cosh^{-1} x = \text{In}\left[x + \sqrt{(x^2 - 1)}\right]$ for $x \geq 1$.

By plotting the R.H.S. of equation VII.5 against 1/T an estimate of ΔH for the Snoek peak can be obtained. With this value of activation energy a calculated Snoek peak can be subtracted from the experimental results which have previously been corrected for background damping, thereby giving the high-temperature peak profile. Figure VII.8 shows examples of high-temperature peak profiles obtained in this way, in both cases a single Debye relaxation peak at peak damping is shown which has been calculated using equation VII.3 with an approximate activation energy for the relaxation peak obtained from equation VII.2. It is evident that this single Debye peak does not adequately define the observed profile and that the high-temperature peaks are due to a number of relaxation processes. In addition, Figure VII.8 shows that there is a change in the relative proportions of high-energy relaxation processes

Figure VII.8

High-temperature peak profiles for Fe-Ti alloys nitrided in 29 NH_3:71H_2 at 400°C for 280 h.

(a) Fe-0·07w%Ti nitrided 400°C a_N=0·015

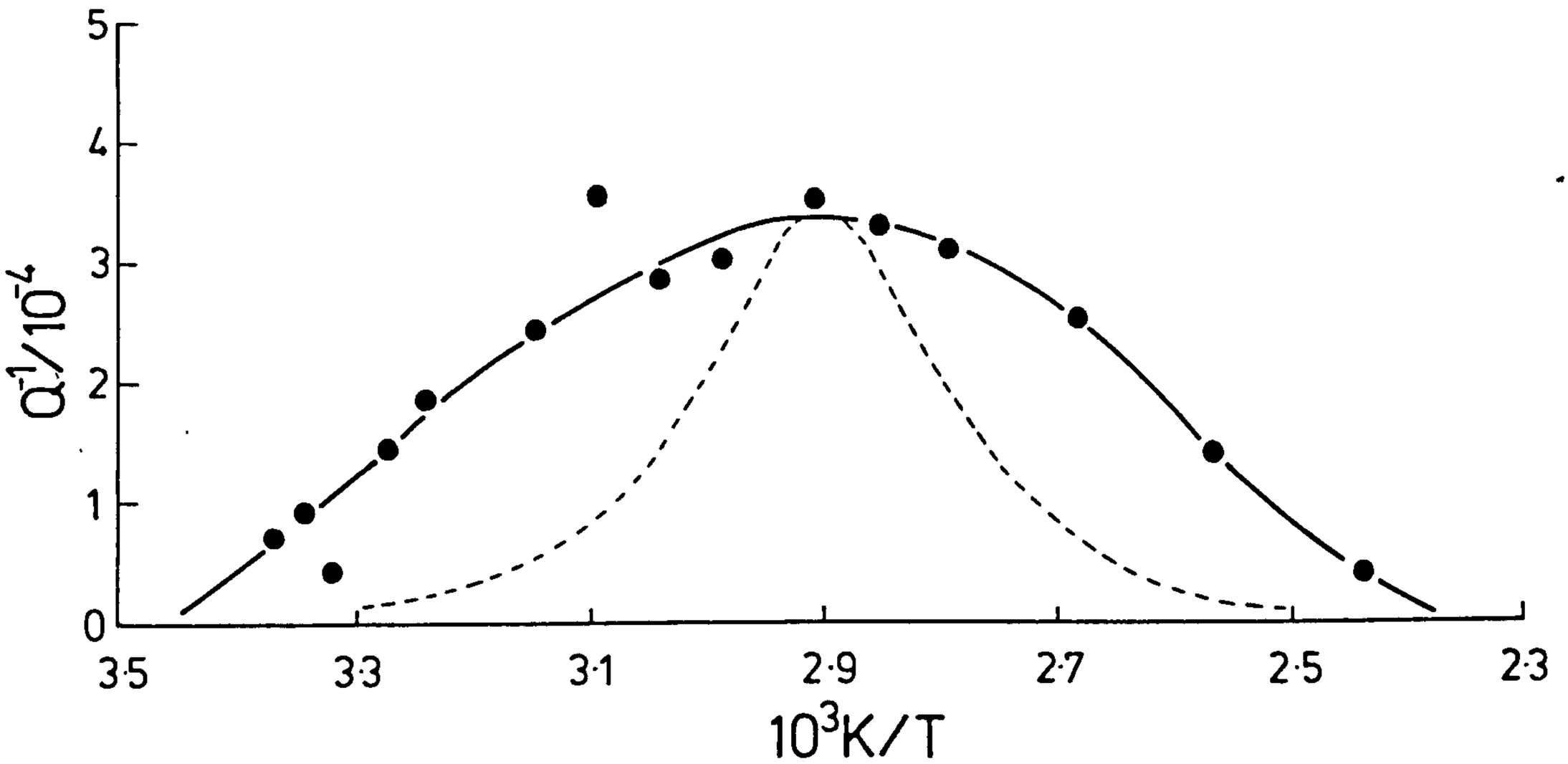

(b) Fe-0·32w%Ti nitrided 400°C a_N=0·015

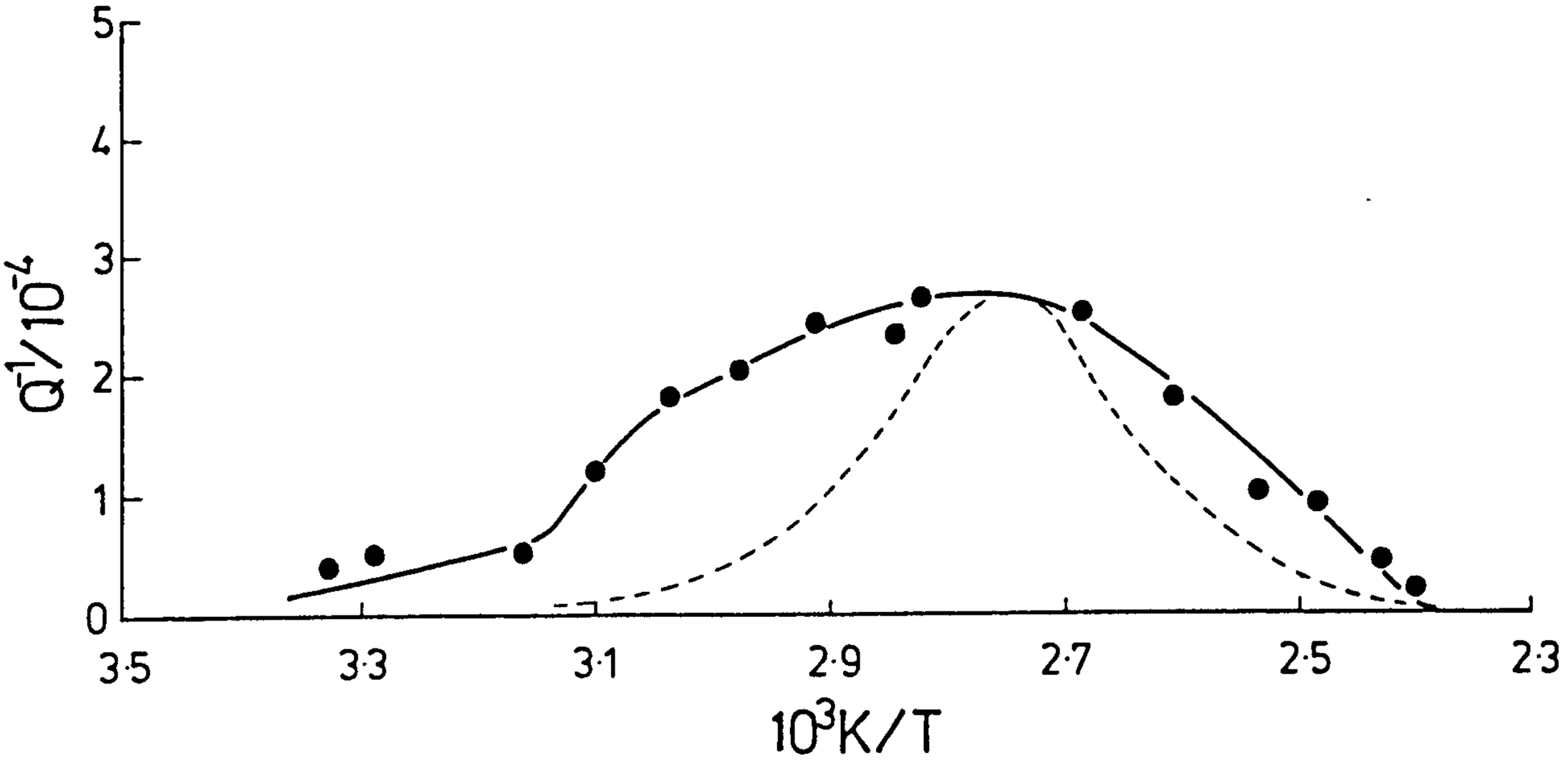

with titanium concentration which causes the substitutional-interstitial interaction peak to move to a slightly higher temperature with increasing titanium content in the alloy.

The nitrogen atom environments present in nitrided Fe-Ti alloys may therefore be defined as:

(a) a smaller amount of nitrogen than in pure iron in random solid solution and occupying normal iron-atom octahedra-Snoek sites;

(b) nitrogen occupying a range of iron-atom octahedral sites modified by the proximity and distribution of titanium atoms in adjacent sites;

(c) clustered nitrogen occupying octahedra containing one or more titanium atoms.

It is important to note that the total interstitial contents of nitrided alloys is very high which means the number of nitrogen atoms which contribute to internal friction must be relatively small to account for the magnitude of the damping peaks. Thus a large proportion of the interstitial atoms cannot move either because they have prohibitively high activation energies, or else they are blocked from doing so by the interstitial atoms surrounding them.

Previous work on the internal friction of iron alloys containing V, Cr, Mo and Ti indicated the presence of substitutional-interstitial interaction peaks after nitriding (Pope et al., 1975). It seems likely that the model proposed for the structure of dilute nitrided Fe-Ti alloys will be applicable to these systems but the actual position, that is activation energies, and magnitude of the peaks will depend upon the strength of interaction between the alloying element and nitrogen. A detailed analysis of these systems would prove useful in confirming the ideas outlined in this section and will extend further the present understanding of the interaction between nitrogen and nitride forming elements.

VII.4 Nitrogen Absorption Isotherms for Nitrided Fe-Ti Alloys

Specimens of Fe-Ti alloys were nitrided at various temperatures in gas mixtures whose ammonia content was below that required to form iron-nitrides. In low ammonia mixtures at 400°C the nitriding rate is very slow and values of nitrogen uptake were obtained by first nitriding in $30NH_3:70H_2$ and re-equilibrating at the required ammonia potential. In all cases nitriding was long enough to achieve constant weight.

Figure VII.9 shows the variation of nitrogen uptake with nitriding potential, R, for Fe-Ti alloys nitrided at

Figure VII.9

Nitrogen absorption isotherms for Fe-Ti alloys nitrided at 585°C.

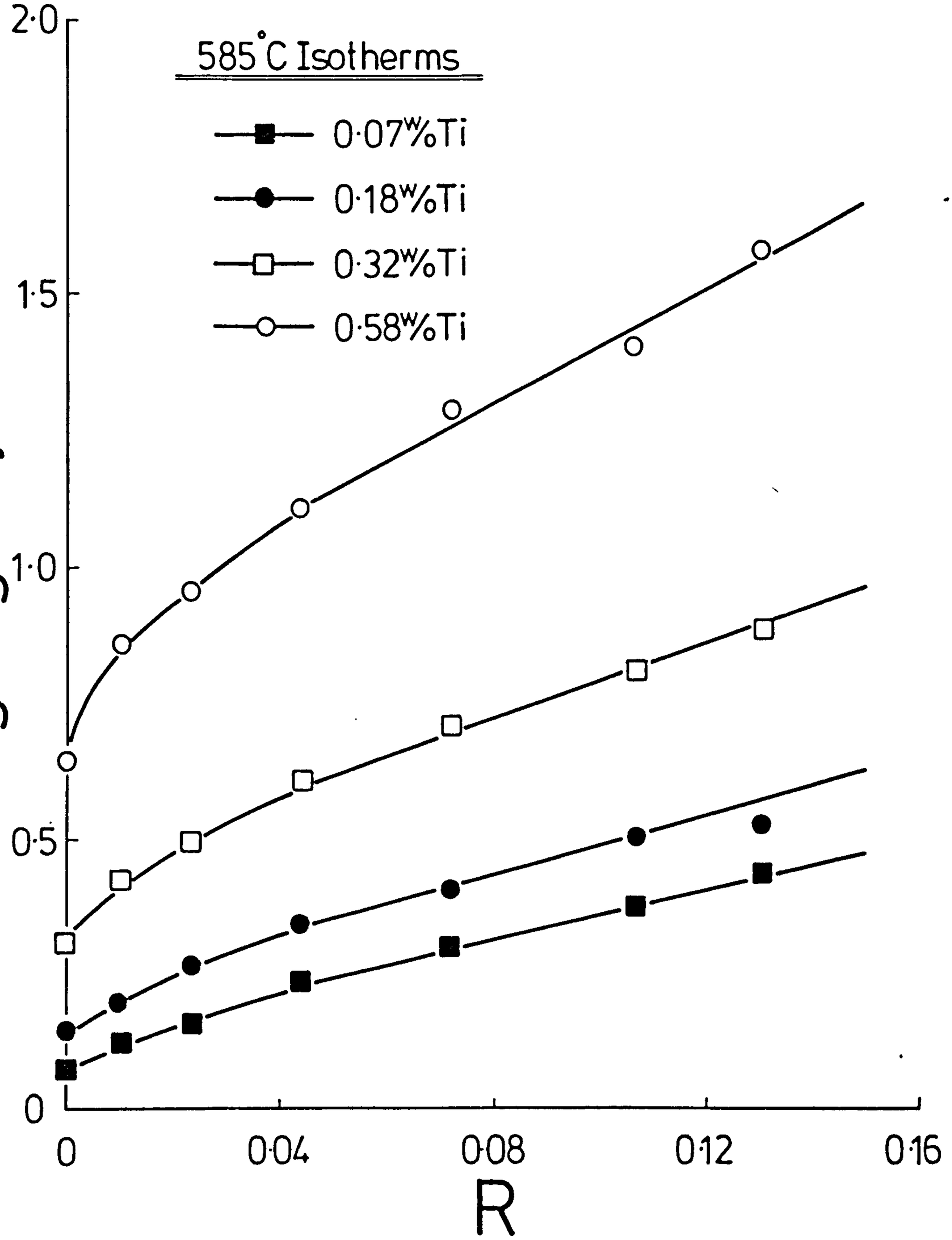
585°C Isotherms
0·07w%Ti
0·18w%Ti
0·32w%Ti
0·58w%Ti
weight gain, %N
2·0
1·5
1·0
0·5
0
0
0·04
0·08
0·12
0·16
R

585°C. Above a certain nitriding potential the isotherms vary linearly with R, the slope of the linear portions increasing with titanium content. By comparing isotherms obtained at different nitriding temperatures it was observed that the weight gain at constant nitrogen activity, and the slope of the linear portions of the weight gain versus R plot, both increase with decreasing temperature. On aging nitrided alloys in hydrogen the N:Ti atomic ratio of the alloys is reduced to about 1:1 irrespective of the original nitriding conditions, that is, the nitrogen content is always reduced to that which would be obtained by the formation of stoichiometric TiN. However, as shown in Section VII.2, lattice parameter measurements indicate that all of the nitrogen and titanium are still in solid solution, that is, present as Ti-N clusters. For short nitriding times at 585°C, and at lower nitriding temperatures, the nitrogen content of the alloy could be returned to its original value by re-nitriding. But prolonged nitriding at 585°C resulted in the nitrogen uptake being less than that observed on initial nitriding showing aging of the microstructure had taken place in these alloys. Equation VII.1 showed that the equilibrium constant, K_p', relevant to the nitriding of Fe-Ti alloys is given by:

$$K_p' = w/o\ N\ (1/R)$$

The linear portions of the absorption isotherms

therefore represent values of the equilibrium constant, K_p', from which a value of the enthalpy of reaction (ΔH_1) can be obtained by using the Clapeyron equation:

$$\frac{d(\ln K'_p)}{d(1/T)} = -\frac{\Delta H_1}{R} \qquad \ldots \text{VII.6}$$

where R is the gas constant. For each titanium content investigated the enthalpy of reaction is constant over the range of nitrogen activity studied as shown in Figure VII.10, in agreement with the work of Podgurski & Davis (1981).

The increased solubility of nitrogen in nitrided Fe-Ti alloys is due to the lowering of the activity coefficient (f_N) of nitrogen in iron by titanium in solid solution, the activity coefficient for the Fe-Ti-N system being given by:

$$\log f_N = e_N^N \{N\} + e_N^{Ti} \{Ti\} \qquad \ldots \text{VII.7}$$

where concentrations are in weight percents and e_N^N and e_N^{Ti} are interaction coefficients. It is usually assumed that e_N^N is small or zero and since the value of e_N^{Ti} is negative the activity coefficient is decreased by the addition of titanium in solid solution, that is, the solubility of nitrogen is increased. The activity coefficient can be further defined as:

Figure VII.10

Equilibrium constants for the nitriding reaction against reciprocal temperature for a series of Fe-Ti alloys.

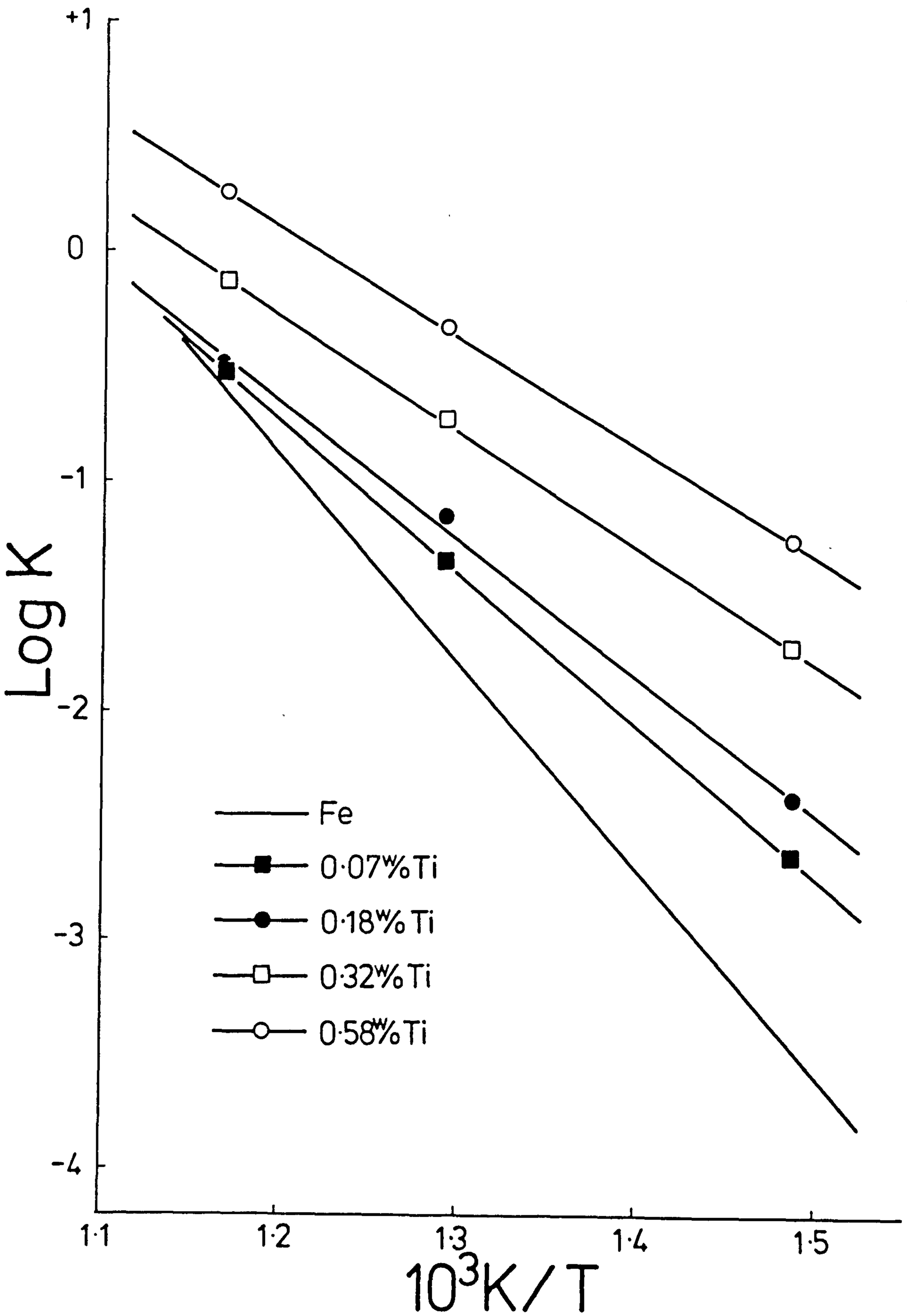
+1
0
-1
-2
-3
-4
Log K
Fe
0·07w% Ti
0·18w% Ti
0·32w% Ti
0·58w% Ti
1·1
1·2
1·3
1·4
1·5
10³K/T

$$\log f_N = \log \frac{\{N\}_{Fe}}{\{N\}_A} \qquad \ldots \text{ VII.8}$$

where $\{N\}_{Fe}$ and $\{N\}_A$ are the concentrations of nitrogen in pure iron and a nitrided Fe-Ti alloy respectively expressed as weight percentages. Combining equations VII.7 and VII.8 gives:

$$\log \{N\}_A = \log \{N\}_{Fe} - e_N^{Ti} \{Ti\} - e_N^N \{N\}_A \qquad \ldots \text{ VII.9}$$

From equation VII.9 it is seen that the general trends observed in Figure VII.9, for the linear portions of the isotherms, are in broad agreement with this thermodynamic argument. The nitrogen solubility increases with the total titanium content in the alloy and the increased nitrogen solubility with decreasing temperature arises from either the influence of temperature on the interaction coefficient e_N^{Ti} or an increase in the amount of titanium which is affecting the solid solution thermodynamics. Uncertainties regarding the actual amount of titanium at any nitriding temperature which is influencing the solid solution thermodynamics and the values of e_N^{Ti} and e_N^N prevent any detailed theoretical treatment of this problem. However, equation VII.9 cannot account for the rapid increase in nitrogen solubility at low nitriding potentials where there is insufficient nitrogen to saturate all the possible sites present in nitrided Fe-Ti alloys although the sites are in equilibrium with one another. This equilibrium may be

expressed as (see Section VII.3):

(a) ⟷ (b) ⟷ (c)

N (α-Fe sites) N ("modified" sites) N (cluster sites)

the stability of the sites increasing from left to right. The probability of filling any site will be related to its energy; since the cluster sites have the lowest energy occupation of such sites is certain. If at low R values the lower energy sites are filled in preference to those of higher energy, that is sites (b) in the previous section are deficient in nitrogen, then the observed isotherms are explained. With increasing R, the higher energy sites are also occupied and this progressive filling of all possible sites explains the shape of the absorption isotherms. By nitriding at lower temperatures the amount of iron contained in the Ti-N zones increases and the spectrum of potential energies shown by the metal-atom environments is broader and more uniform. Thus, the initial increase in nitrogen solubility is less marked as shown by Figure VII.11.

As shown previously, for a given titanium concentration the enthalpy change associated with the nitriding reaction is constant along the linear portions of the absorption isotherms and less than the values for absorption of nitrogen in pure iron. The difference in enthalpy between absorption of nitrogen in pure-iron and an Fe-Ti

Figure VII.11

Nitrogen absorption isotherms for Fe-Ti alloys nitrided at 400°C.

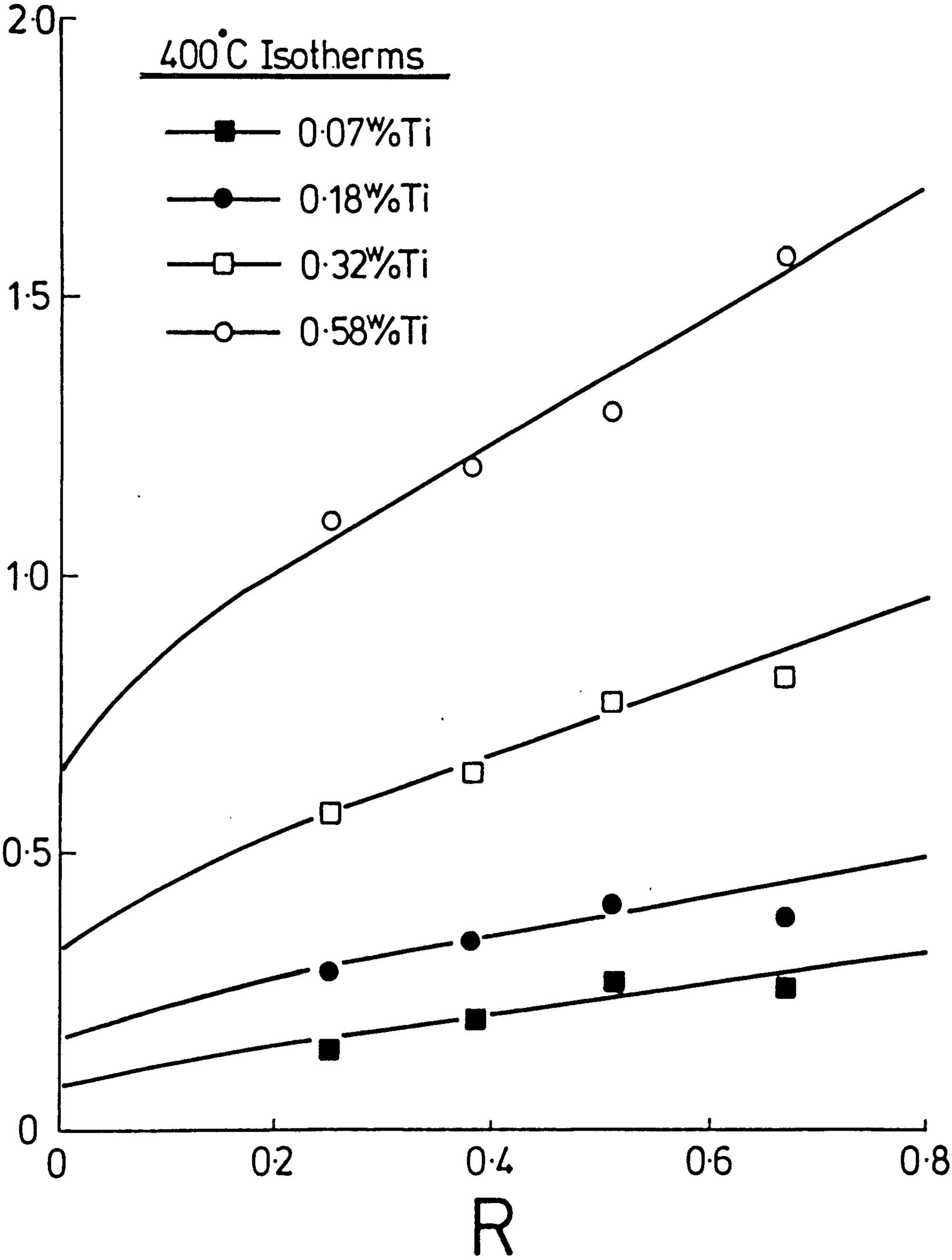
400°C Isotherms
0·07w%Ti
0·18w%Ti
0·32w%Ti
0·58w%Ti
weight gain, %N
2·0
1·5
1·0
0·5
0
0
0·2
0·4
0·6
0·8
R

alloy is given by ΔH_2, see Table VII.2. These enthalpy changes are negative and increase with titanium concentration. In addition ΔH_2 may be regarded as an indication of the average energy of the metal-atom sites which are being occupied along the linear portions of the absorption isotherms. It does not indicate that these sites have the same energy, contrary to the views of Podgurski & Davis (1981). It is the occupation of these Snoek and modified energy sites (sites (a) and (b), Section VII.3) which give rise to the peaks observed in internal friction experiments.

Table VII.2

Enthalpy changes ΔH_1 and ΔH_2 for nitrided Fe-Ti alloys

w/o Ti	ΔH_1, kJ/mole	ΔH_2*, kJ/mole
0	74	0
0.07	55	-19
0.18	50	-24
0.32	42	-32
0.58	39	-35

*$\Delta H_2 = \Delta H_1^{Fe-Ti-N} - \Delta H_1^{Fe-N}$

In Figure VII.5 it was shown that nitriding at different temperatures in the same activity of nitrogen resulted in large differences in the high-temperature internal friction peak profile. This behaviour reflects not only the effect of nitriding temperature but also the potential at which nitriding was carried out. For a constant nitrogen activity of 0.015, at 400°C nitriding is carried out on the linear portion of the isotherm resulting in occupation of a large proportion of all three kinds of metal-atom octahedra. However at 585°C, nitridng is on the curved part of the isotherm and therefore although a large proportion of low energy sites are filled only a small porportion of relatively higher energy sites are being occupied by nitrogen atoms (sites (a) and (b), Section VII.3). So at 585°C a low concentration of nitrogen atoms exist in sites which have energies characteristic of high-temperature damping, that is, $\geq$ 120 kJ/mole. By nitriding at a potential within the linear portion of Figure VII.9 all three types of site are filled and both the Snoek and high-temperature peaks increase as shown in Figure VII.12.

VII.5 Discussion

The experimental observations of Podgurski & Davis (1981) are very similar to those of the present investigation, but the interpretations of the enhanced nitrogen solubility in nitrided Fe-Ti proposed by the respective workers at Pittsburgh and Newcastle are widely different

Figure VII.12

Internal friction scans of Fe-0.18 w/o Ti alloys nitrided at 585°C.

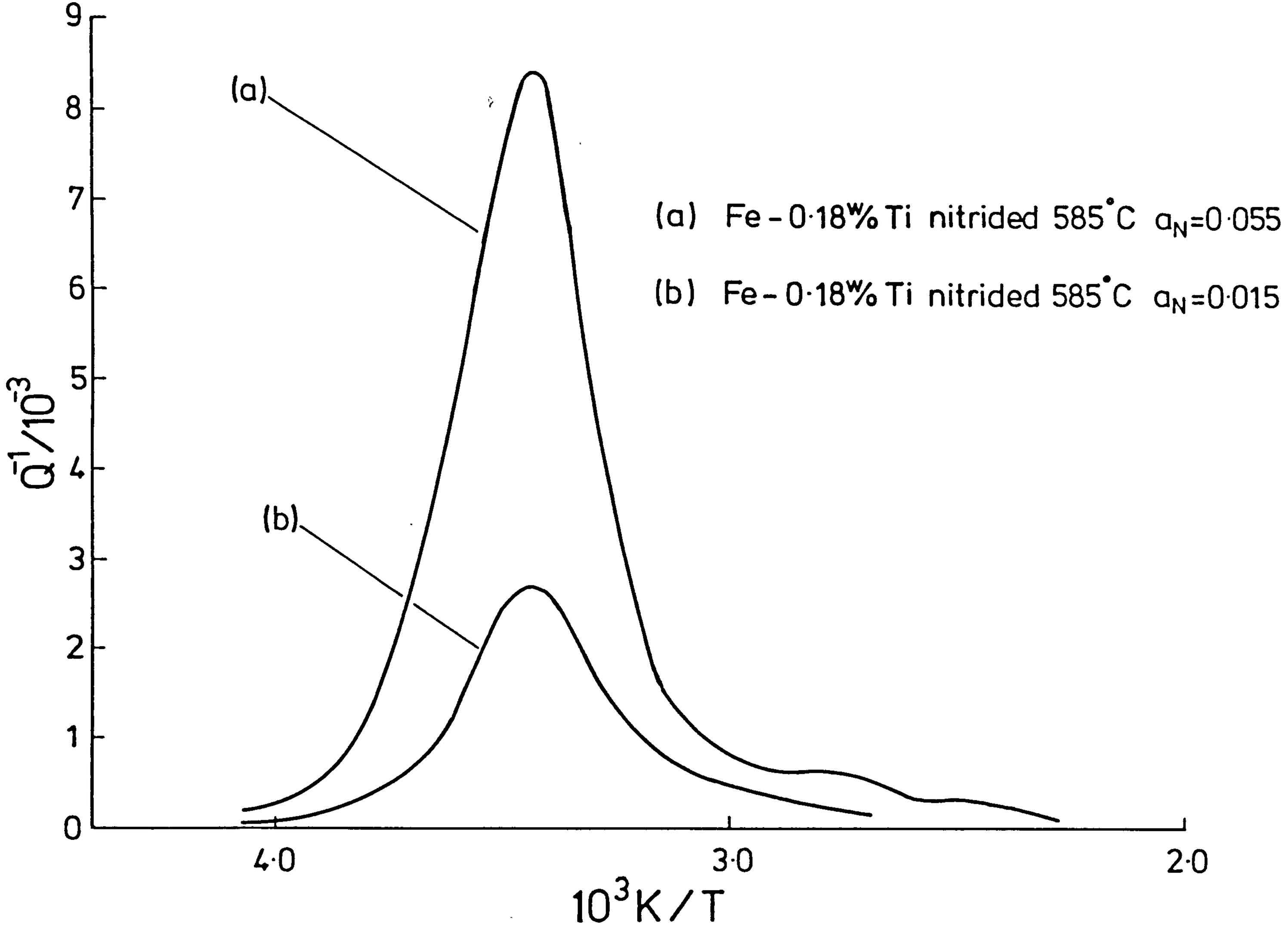

(a) Fe - 0·18% Ti nitrided 585°C a_N=0·055

(b) Fe - 0·18% Ti nitrided 585°C a_N=0·015

from one another. Podgurski & Davis consider the increase in nitrogen solubility along the linear portions of the absorption isotherms to be a consequence of the uniform increase in lattice strain which results when TiN_2 is dispersed on a molecular basis. This strain is said to increase with volume fraction of TiN_2 in order to explain the increase in nitrogen solubility with titanium concentration. However, electron microscopy (Jack 1976; Henderson, 1976) shows that in nitrided Fe-Ti alloys containing > 0.5 w/o Ti the titanium and nitrogen atoms are clustered on the $\{100\}_\alpha$ matrix planes as thin discs and not on a molecular basis. In addition, the model used by Podgurski & Davis (1981) to predict the enhanced nitrogen solubility is based on particles which have a small misfit with the ferrite matrix, which is invalid for nitrided Fe-Ti alloys due to the large expansion which occurs when nitrogen occupies an octahedral interstice in body-centred cubic iron. Also, lattice parameter measurements of nitrided and hydrogen reduced alloys show that all the strain is in the disc-shaped clusters and that the ferrite is unstrained, a fact confirmed by the internal friction measurements presented in this chapter. Perhaps the most convincing evidence that the iron matrix is unstrained comes from direct lattice imaging of the substitutional-interstitial clusters formed in Fe-5 w/o Mo, see Figure VII.13. The (002) fringe spacing is a maximum within the cluster, 1.65 Å, while in areas removed from the cluster it has a value of 1.43 Å; clearly the ferrite matrix is unstrained.

Figure VII.13

Fe-5 w/o Mo nitrided in $8NH_3:92H_2$ at 585°C, showing (002) lattice image of a Mo-N cluster.

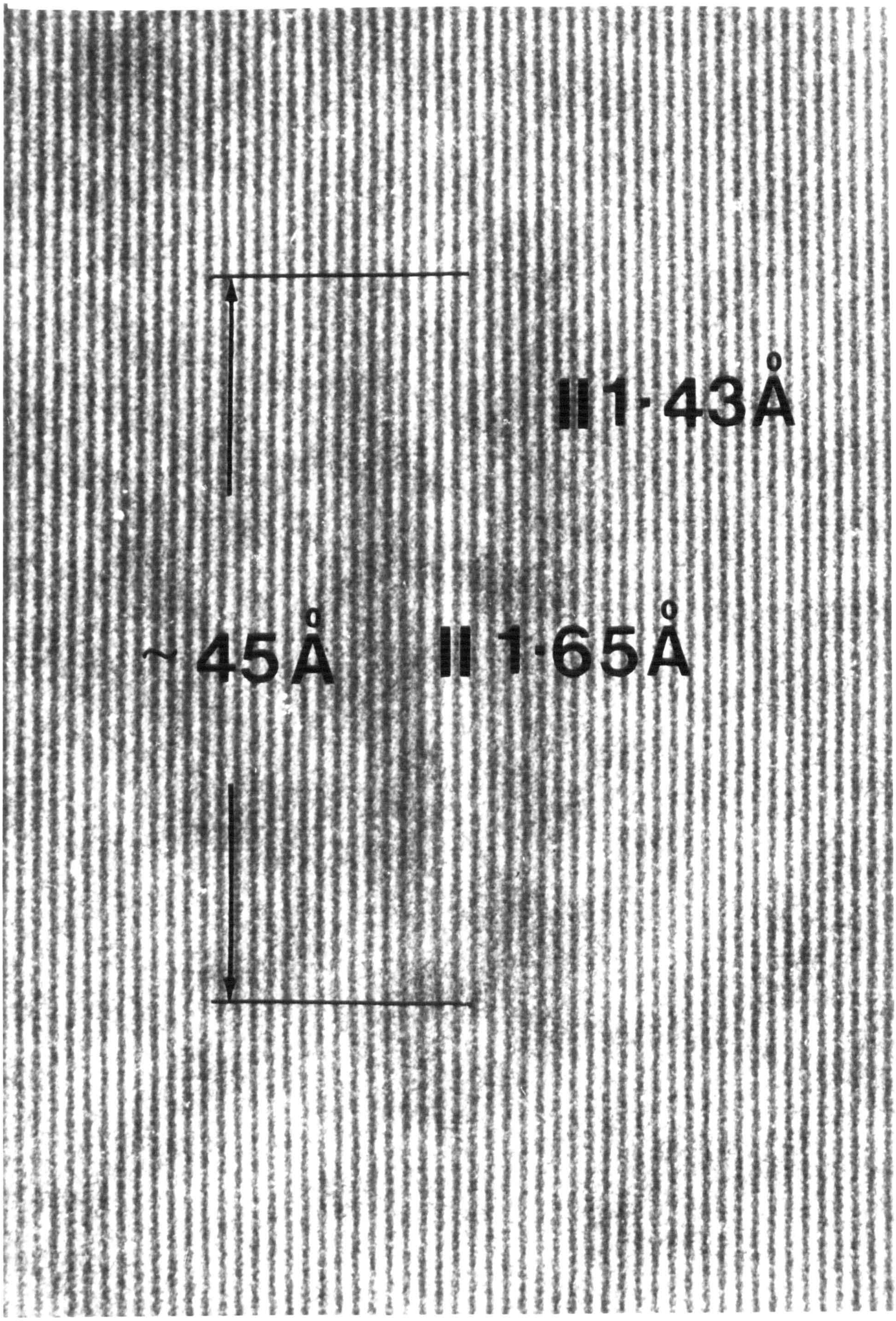
II 1·43Å
~45Å
II 1·65Å

The model proposed from the present work accounts for all the experimental observations and when Fe-Ti alloys containing greater than about 0.3 w/o Ti are nitrided the model presented in this work becomes equivalent to the "monolayer model" of Jack (1978) and therefore gives a complete explanation for the nitriding behaviour of iron-titanium alloys. However, Henderson (1976) showed in nitrided Fe-Ti alloys containing > 0.5 a/o Ti that hydrogen reduction removed two-thirds of the total clustered nitrogen leaving a N:Ti atomic ratio of 1:1, the remaining one-third being in a more stable chemical environment, that is, monolayer sites co-ordinated by 4Ti and 2Fe atoms (see Chapter II). The nitrogen atoms removed by hydrogen reduction were termed "excess" nitrogen and are co-ordinated by 5Fe and 1Ti atoms (Jack, 1978). Hydrogen reduction of nitrided Fe-Ti alloys containing <0.5 a/o Ti also results in a N:Ti atomic ratio of 1:1 and to be consistent with the model of high titanium alloys (Jack, 1978) it is proposed that the three sites suggested for nitrogen occupation in Section VII.3 be extended into four as follows:

(a) a smaller amount of nitrogen than in pure iron in random solid solution and occupying normal iron-atom octahedra - Snoek sites;

(b) nitrogen occupying a range of iron-atom octahedral sites modified by the proximity and

distribution of titanium atoms in adjacent sites;

(c) clustered nitrogen occupying octahedra containing one Ti atom;

(d) clustered nitrogen co-ordinated in octahedra by 2-4 Ti atoms.

Chapter VIII

QUENCH AGING OF NITRIDED Fe-Ti ALLOYS

VIII.1 Introduction

It was shown in Chapter VII that quenching dilute Fe-Ti alloys from nitriding temperature leaves a certain proportion of nitrogen atoms occupying normal Snoek sites and the concentration of nitrogen atoms in these sites is dependent on the titanium content. The low temperature transformations which occur during the quench-aging of nitrogen ferrite begin with the formation of solute-atom clusters, formed as thin platelets parallel to the three cube planes of the matrix and, by subsequent ordering of nitrogen atoms, continue with the formation of α''-$Fe_{16}N_2$. It was therefore interesting to investigate a nitrided and quenched Fe-Ti alloy to see if a similar transformation sequence occurred on aging at low temperatures.

Using a combination of electron microscopy, electron and X-ray diffraction, internal friction and hardness measurements the structures of Fe-0.18 w/o Ti quenched and then aged at room temperature and 100°C are compared with those of α-iron supersaturated with nitrogen and similarly treated.

VIII.2 Results and Discussion

Specimens of Fe-0.18 w/o Ti were nitrided at 585°C in an 11 NH_3:89H_2 gas mixture, quenched into iced brine and stored at -30°C before aging at 23° and 100°C.

It was shown in Chapter VII that there exist a range of nitrogen atom environments in nitrided Fe-Ti alloys, one of which consists of nitrogen atoms in octhedral interstices co-ordinated by six iron atoms; that is, nitrogen in random solid solution. In addition it was suggested that the high diffusivity of nitrogen resulted in condensation of nitrogen atoms onto existing Ti-N clusters during quenching from nitriding temperature. Figure VIII.1 shows that aging at room temperature removes further nitrogen from random solid solution and compares the behaviour of nitrided Fe-0.18 w/o Ti with that of pure nitrogen ferrite. The results are expressed as a percentage of nitrogen remaining in random solid solution based on the initial Snoek peak height obtained after quenching. After aging at room temperature for 10 h only 25 percent of the nitrogen remains in random solid solution for the Fe-Ti alloy compared with about 65 percent for pure nitrogen-ferrite. Over longer time periods the rate of nitrogen removal in the Fe-Ti alloy slows considerably, a small amount of nitrogen remaining in random solid solution even after 1000 h. This rapid removal of nitrogen at short aging times in the Fe-Ti alloy is due to

Figure VIII.1

Variation of nitrogen in random solid solution with aging time at 23° and 100°C for Fe-0.07 w/o N and Fe-0.18 w/o Ti-0.13 w/o N.

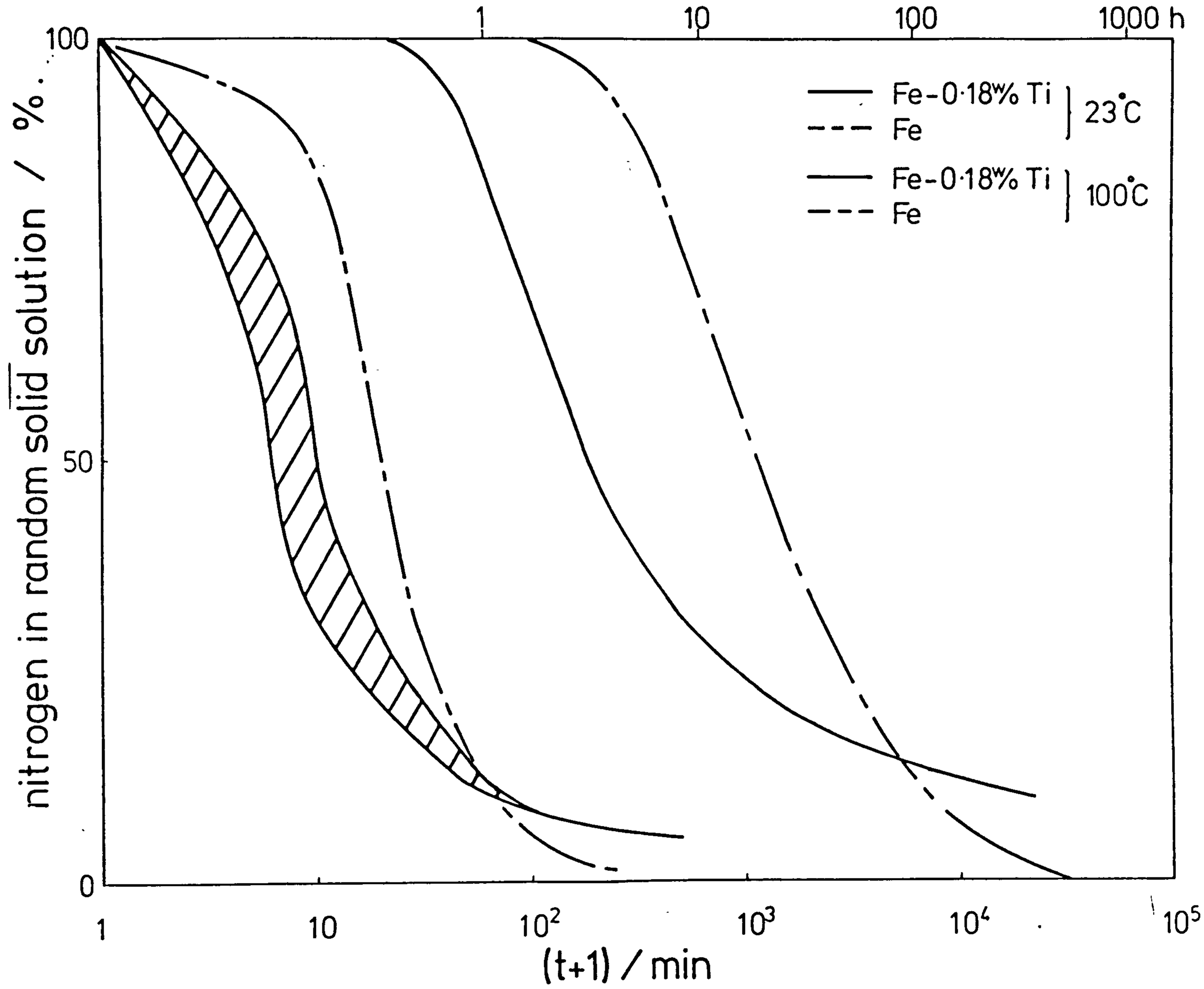
100
50
0
1
10
100
1000 h
Fe-0·18w% Ti
Fe
23°C
Fe-0·18w% Ti
Fe
100°C
nitrogen in random solid solution / %
1
10
10²
10³
10⁴
10⁵
(t+1) / min

the availability of a large number of heterogeneous sites, the Ti-N clusters, onto which nitrogen can cluster. While in pure nitrogen-ferrite sufficient time must elapse before a nucleus of stable size can be formed which can then grow. At short aging times the matrix unit-cell dimensions for both alloys are constant and much higher than that of ferrite (2.8664 Å) indicating that the nitrogen atoms are in non-random solid solution and not precipitated as a titanium or iron nitride; see Figure VIII.2. Transmission electron microscopy of nitrided Fe-Ti aged for 10 h at 23°C shows a bimodal distribution of particle size (see Figure VIII.3 series (a)), the larger particles are due to the nitrogen in excess of a N:Ti atomic-ratio of 1:1 condensing onto existing substitutional-interstitial Ti-N zones present in the material and formed at nitriding temperature. These "Fe-N" clusters therefore form on the cube planes of ferrite. In comparison aging of the iron-nitrogen alloy, Figure VIII.3 series (b), results in the clustering of nitrogen atoms to form pure Fe-N clusters. Continued aging causes both types of iron-nitrogen cluster to grow until after 50 h the "Fe-N" clusters in the nitrided iron-titanium have a diameter of about 120 Å compared with 400 Å for nitrogen clusters in pure iron, see Figure VIII.3. Eventually, the nitrogen clusters in both alloys transform to coherent α"-$Fe_{16}N_2$, as identified by electron diffraction, with an accompanying decrease in matrix unit-cell dimensions as shown by Figure VIII.2.

Figure VIII.2

Variation of the lattice parameter of Fe-0.07 w/o N and Fe-0.18 w/o Ti-0.13 w/o N with aging at 23° and 100°C.

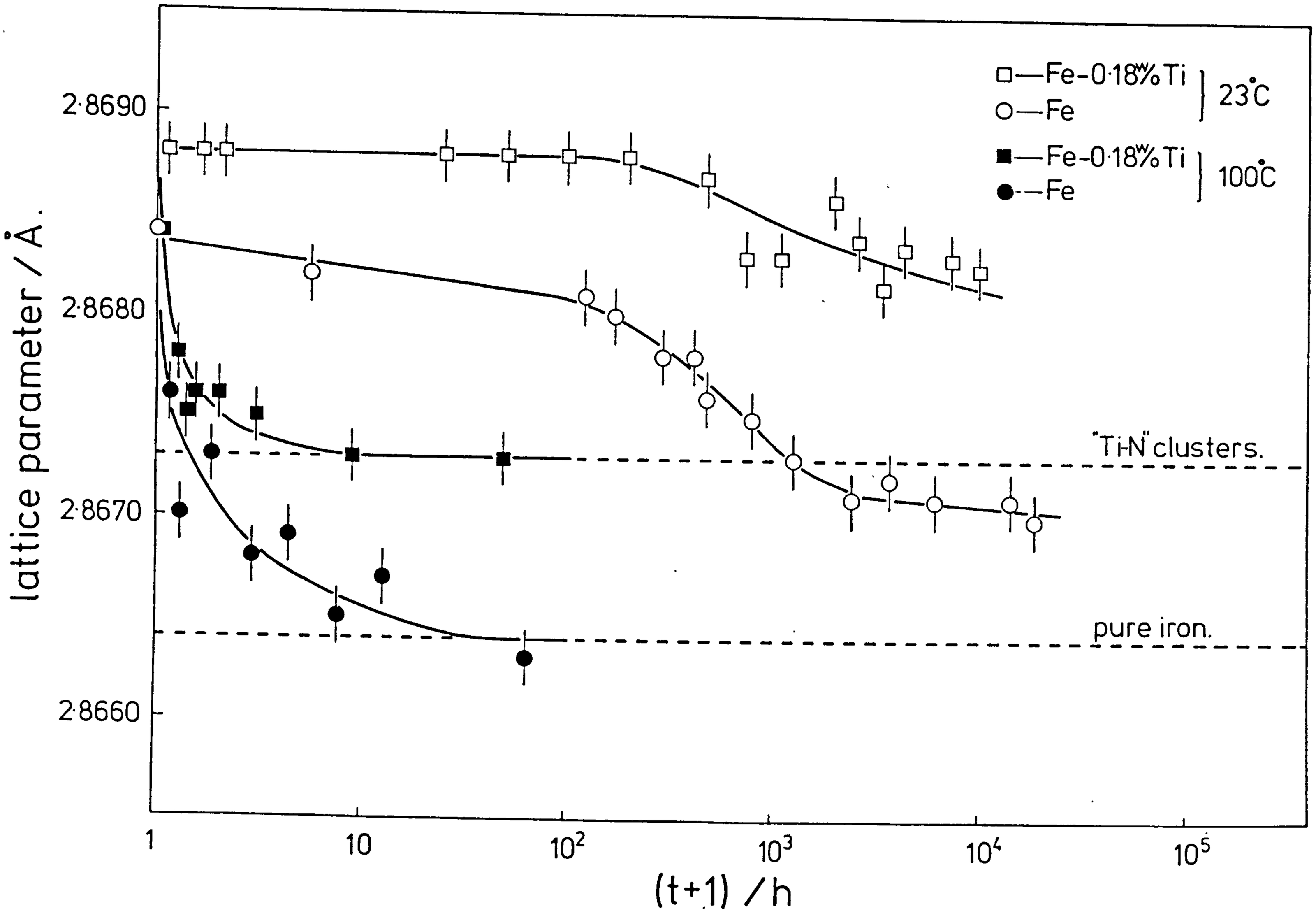
□—Fe-0·18ʷ% Ti
○—Fe
23°C
■—Fe-0·18ʷ% Ti
●—Fe
100°C
"Ti-N" clusters.
pure iron.
lattice parameter / Å.
2·8690
2·8680
2·8670
2·8660
1
10
10²
10³
10⁴
10⁵
(t+1) / h

Figure VIII.3

Bright field electron micrographs of Fe and Fe-0.18 w/o Ti nitrided at 585°C and aged at room temperature.

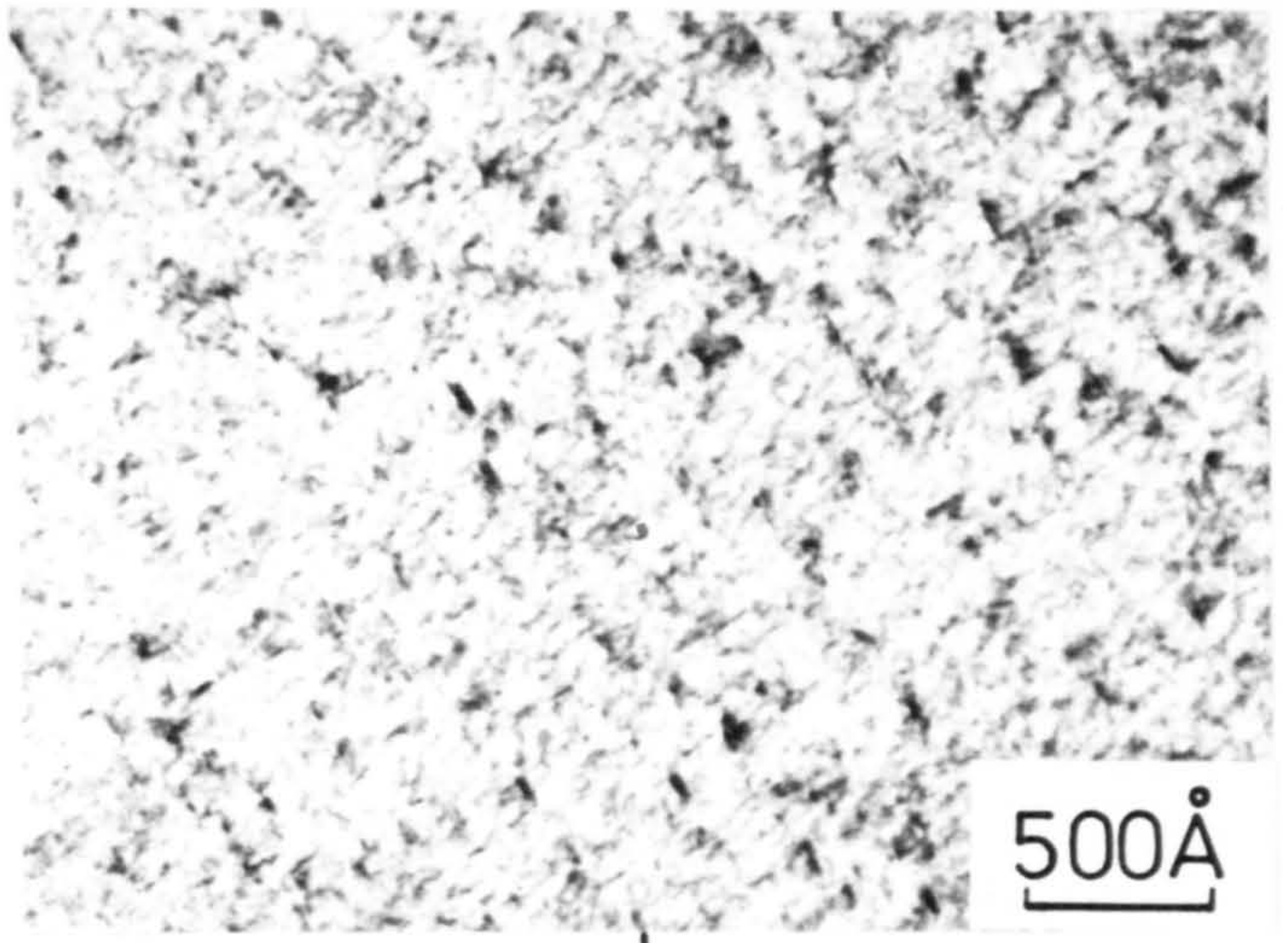

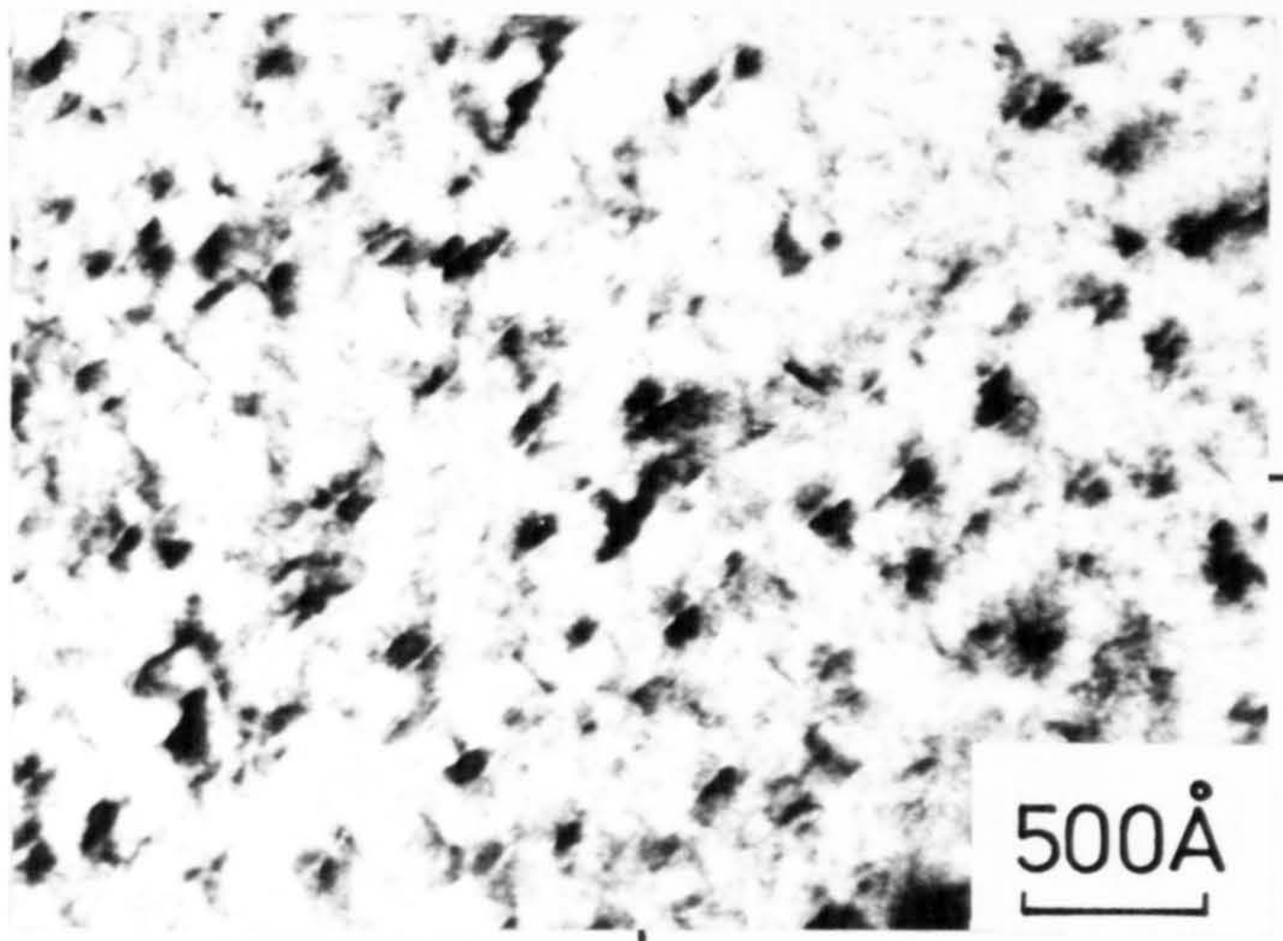

(a)

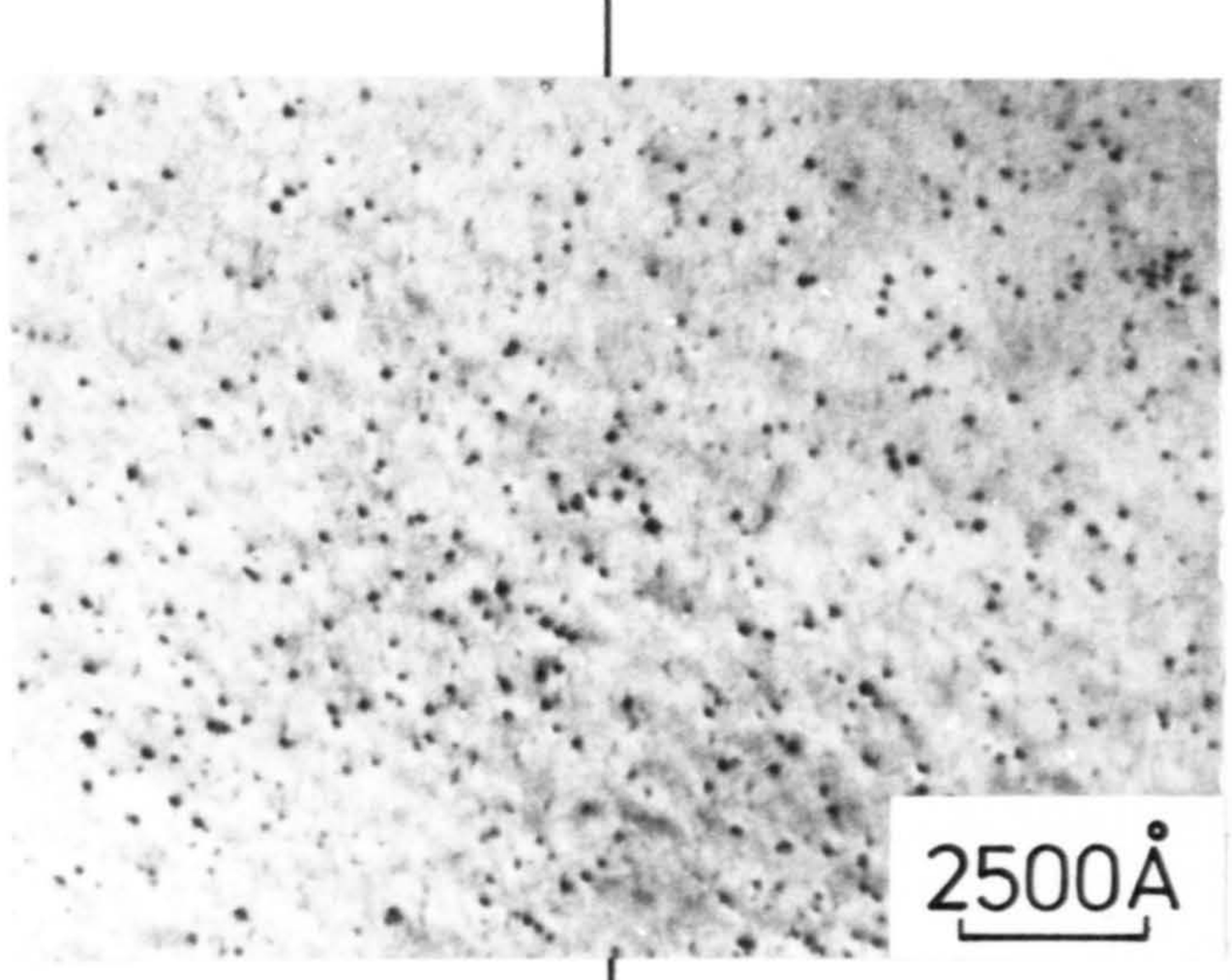

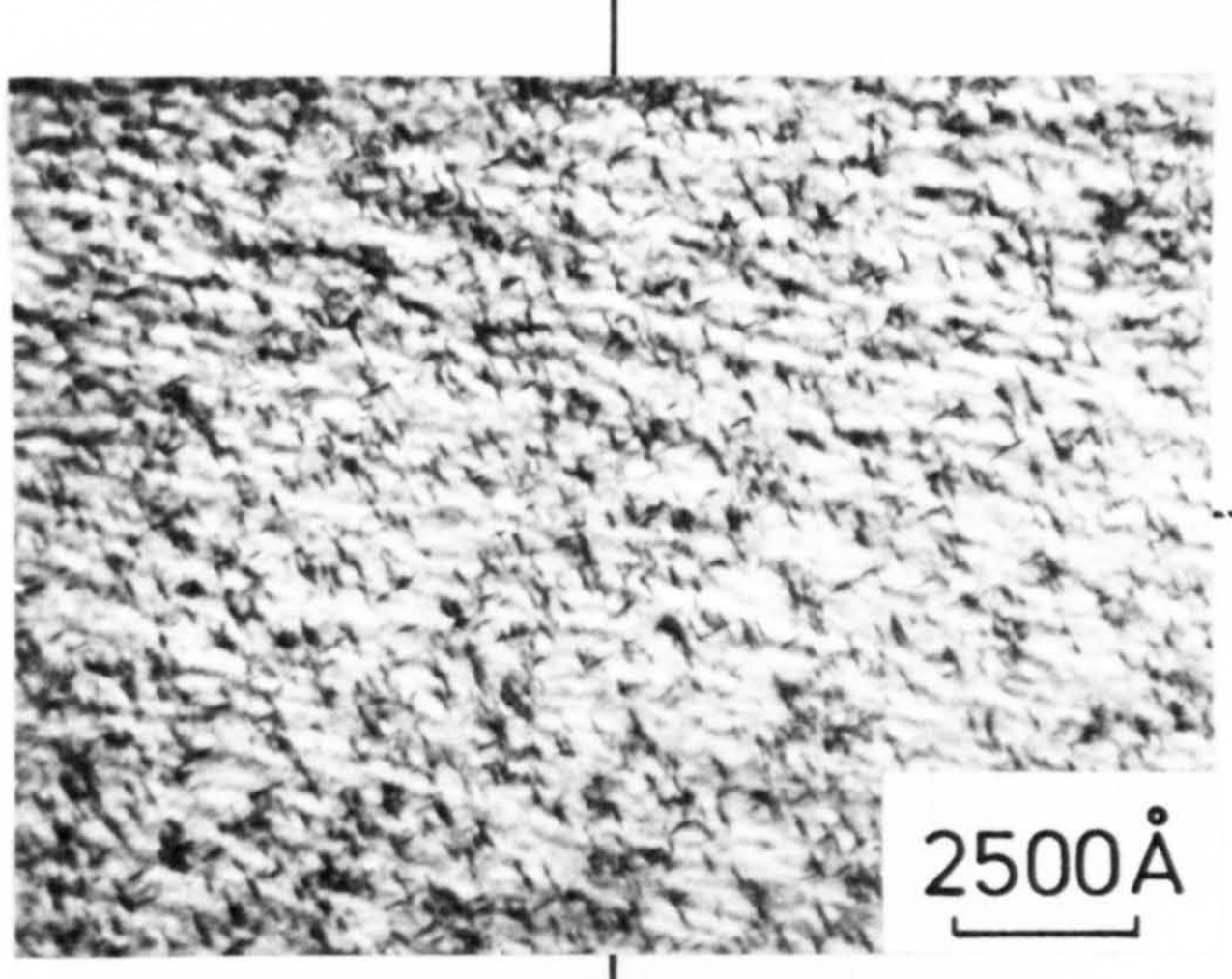

(b)

10hrs.

(001)

50hrs.

An alternative explanation of the above observations is that Fe-N clusters form separately from, and are not dependent on, the existing Ti-N clusters. However, Figure VIII.4 shows that the "Fe-N" clusters formed in Fe-0.18 w/o Ti at room temperature are more stable than clusters in pure nitrogen-ferrite. This suggests the co-ordination of some nitrogen atoms by Fe_5Ti metal-atom octahedra and also by metal-atom octahedra which are influenced by titanium atoms in close proximity and so confirms the first suggestion. It will be shown later that condensation of nitrogen atoms onto existing Ti-N clusters does in fact occur, this transfer of nitrogen from Snoek to higher energy sites in the lattice causing important changes in the internal friction spectra of samples aged both at 23° and 100°C.

Aging at 100°C leads to a rapid decrease in the amount of nitrogen in random solid solution as "Fe-N" clusters form in Fe-0.18 w/o Ti, Figure VIII.1. The rate of nitrogen removal from random solid solution being much faster than in nitrogen-ferrite aged at the same temperature. The spread in the results for the Fe-Ti alloy, the cross-hatched area of Figure VIII.1, reflects the complex nature of the transformation of "Fe-N" clusters to α''-$Fe_{16}N_2$. This transformation is very rapid and is accompanied by a decrease in matrix unit-cell dimensions, see Figure VIII.2, but the minimum value observed is not that of pure iron (2.8664 Å) but corresponds to a N:Ti

Figure VIII.4

Variation of nitrogen in solid solution for Fe-0.07 w/o N and Fe-0.18 w/o Ti-0.13 w/o N with aging at 23° and 100°C.

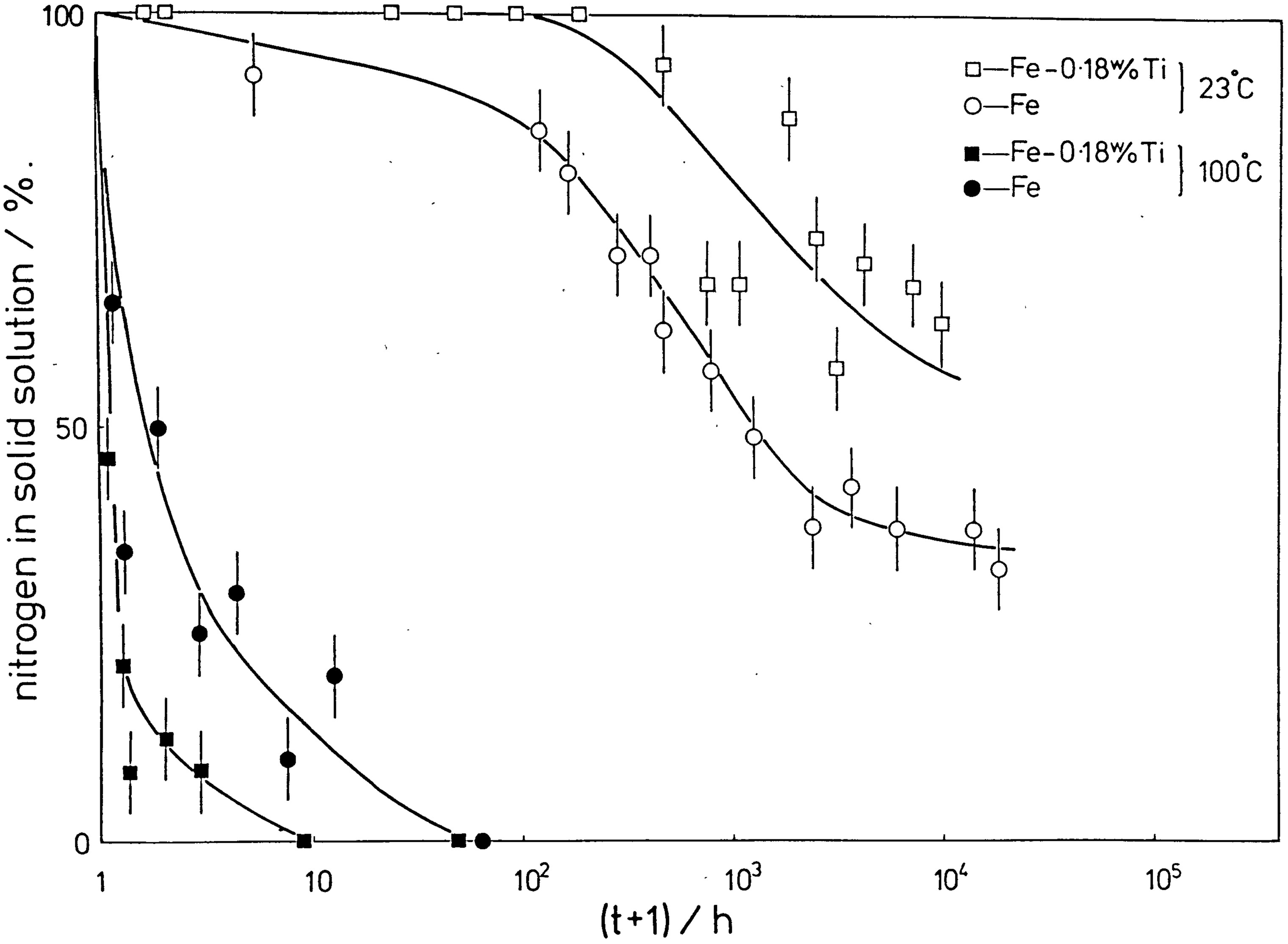
100
50
0
nitrogen in solid solution / %.
1
10
10^2
10^3
10^4
10^5
(t+1) / h
□—Fe-0·18w% Ti
○—Fe
23°C
■—Fe-0·18w% Ti
●—Fe
100°C

atomic ratio of 1:1 (2.8673 Å) which can be interpreted as being the lattice parameter of a ferrite matrix containing a mixture of α''-$Fe_{16}N_2$ precipitates and Ti-N clusters. The lattice parameter of nitrogen-ferrite aged at 100°C does fall to the value of pure iron as the nitrogen-clusters overage to the equilibrium precipitate α''-$Fe_{16}N_2$. It is interesting to note that the lattice parameters of both alloys aged for 10,000 h at 23°C are still significantly higher than their respective base values (dotted lines in Figure VIII.2) although they would be expected to approach these values eventually. A possible explanation of this behaviour is that the precipitates form a stable array which once produced is very resistant to further coarsening. The two necessary conditions for array formation are (Perovic et al., 1979):

(i) that the precipitates must be present in sufficient quantity that the interparticle spacing is comparable with the precipitate dimensions,

(ii) that the precipitates individually give rise to tetragonal distortions within the parent phase.

These conditions are satisfied for both alloys and so it seems that the high lattice parameters could be explained by a stabilization of the particle distribution at long aging times.

After aging the Fe-Ti alloy at 100°C for 20 min transmission electron microscopy shows a heterogeneous clustering of nitrogen onto the existing homogeneous dispersion of Ti-N clusters, Figure VIII.5(a). Comparing Figure VIII.5(a) and 5(b) shows that the largest precipitates in Fe-0.18 w/o Ti are smaller than the α''-$Fe_{16}N_2$ precipitates in pure nitrogen-ferrite aged under identical conditions. From the lattice parameter measurements given in Figure VIII.4, aging for this time at 100°C results in the nitrided Fe-Ti alloy apparently having around 20 percent of the nitrogen atoms in non-random solid solution. However, the smaller particles of α''-$Fe_{16}N_2$ shown in Figure VIII.5(a) are coherent with the parent phase and will therefore diffract X-rays as if they were merely strained regions of the matrix resulting in an apparent nitrogen concentration in non-random solid solution. The presence of these small particles of α''-$Fe_{16}N_2$ also causes broadening of the matrix X-ray reflections, a point discussed later in the chapter. Continued aging of Fe-0.18 w/o Ti at 100°C results in a microstructure similar to that of pure nitrogen-ferrite with the unit-cell dimensions falling to a value corresponding to that of a matrix containing dispersed Ti-N zones only, see Figure VIII.2.

Comparing the internal friction spectra of nitrided Fe-Ti alloys aged at 23° and 100°C shows that although the behaviour of the Snoek peak is similar, at 23°C not all

Figure VIII.5

Bright field electron micrographs of (a) Fe-0.18 w/o Ti-0.13 w/o N and(b) Fe-0.07 w/o N aged 100°C for 20 min.

(a)

2000Å

(001)

(b)

of the nitrogen available is participating in the transformation sequence since the high-temperature peak initially does not fall on aging, see Figure VIII.6. It has been suggested in Chapter VII that the high-temperature peak results from nitrogen atom jumps between metal-atom octahedra which are affected by the proximity and distribution of Ti-atom next-nearest neighbours and that these nitrogens are relatively more stable than nitrogen in Snoek sites. By aging at room temperature the nitrogen atoms in normal Snoek sites will diffuse toward existing Ti-N zones forming "Fe-N" clusters which also incorporate the nitrogen atoms which contribute to the high-temperature peak. A proportion of these nitrogens will still occupy modified iron-atom octahedra which accounts for the high-temperature peak damping observed in Figure VIII.6(a). With increased aging time these "Fe-N" clusters transform to α"-$Fe_{16}N_2$ by ordering of nitrogen atoms causing them to become too strongly bound to be moved by the applied torsional stress. This decline in the high-temperature peak at long aging times at 23°C correlates fairly well with the fall in lattice parameter, (see Figure VIII.2) which reflects the transformation of "Fe-N" clusters to α"-$Fe_{16}N_2$ precipitates. At 100°C clustering of nitrogen and transformation to α"-$Fe_{16}N_2$ is rapid which accounts for the simultaneous decrease in Snoek and high-temperature peaks. Only a small Snoek peak and no high-temperature peak remains after aging for 4 h as shown in Figure VIII.6(b).

Figure VIII.6

Variation of internal friction spectra for Fe-0.18 w/o Ti nitrided in $11NH_3:89H_2$ at 585°C for 18 h and brine quenched; aged at (a) room temperature, and (b) 100°C, for the times indicated.

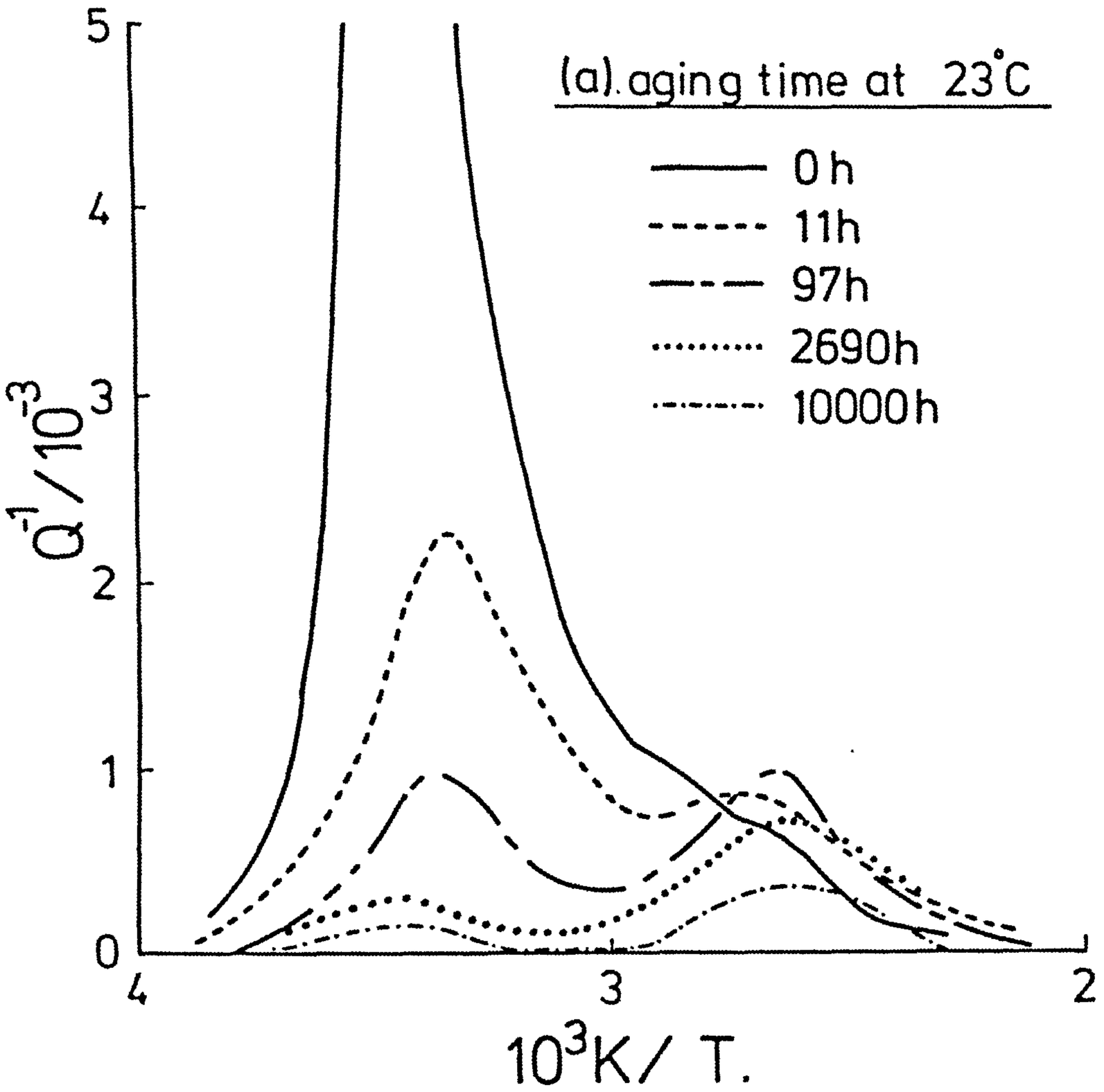
(a). aging time at 23°C
0 h
11h
97h
2690h
10000h
$Q^{-1}/10^{-3}$
10^3K/ T.

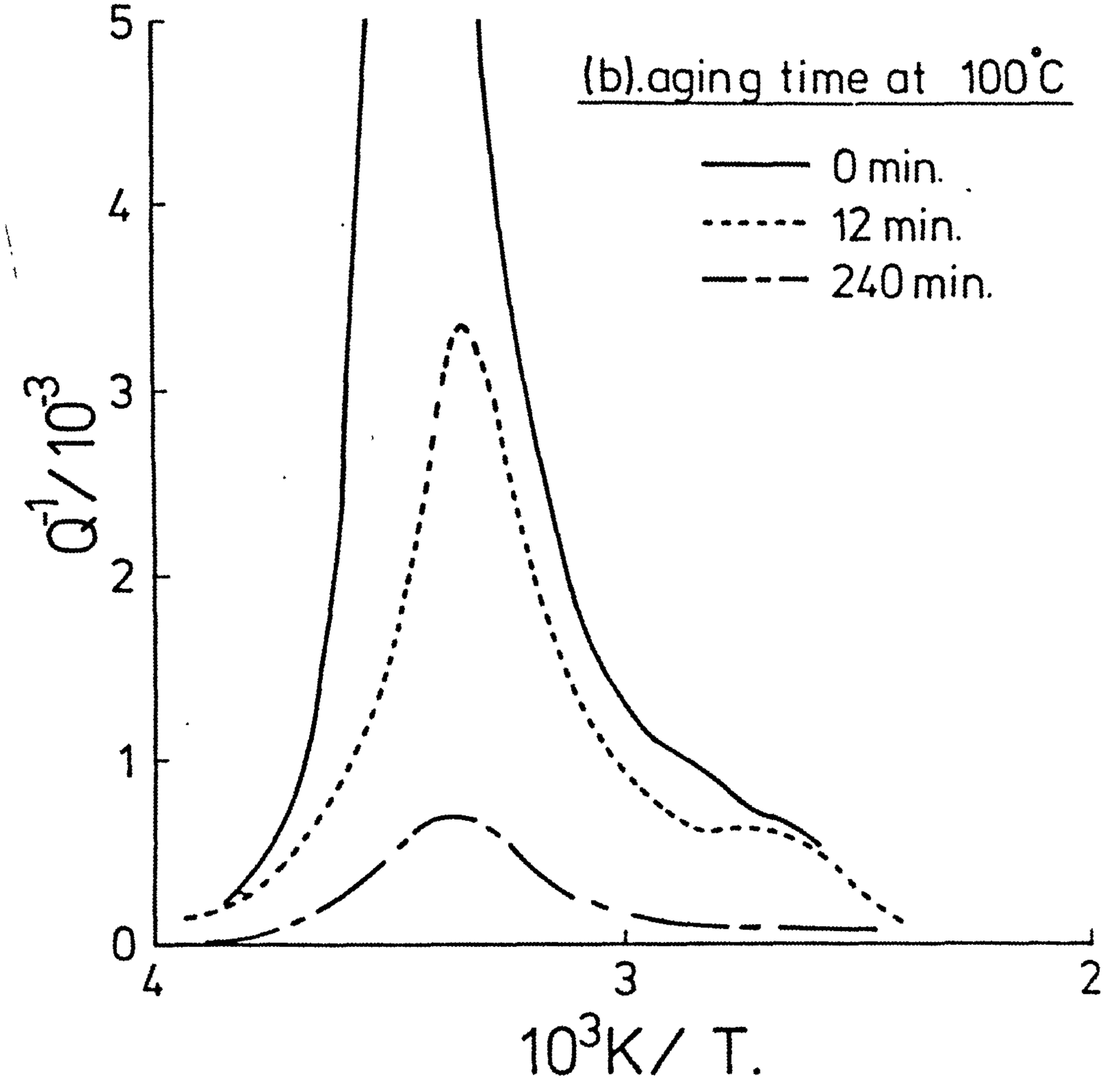
(b). aging time at 100°C
0 min.
12 min.
240 min.
$Q^{-1}/10^{-3}$
10^3K/ T.

At both aging temperatures the transformation of "Fe-N" clusters to α"-$Fe_{16}N_2$ precipitates in nitrided Fe-0.18 w/o Ti is accompanied by broadening of the matrix X-ray powder diffraction lines and changes in microhardness. Figure VIII.7(a) shows that the room temperature microhardness increases slowly with aging time, in addition to the high strengthening already produced by formation of Ti-N zones at nitriding temperature. In contrast, aging at 100°C leads to maximum hardness after about 1 h which subsequently decreases as α"-$Fe_{16}N_2$ coarsens. These changes in microhardness are obviously related to the presence of "excess" nitrogen in nitrided Fe-0.18 w/o Ti and the strengthening seems to be additive to that already produced by the Ti-N zones; the strength increments which result on aging will therefore depend not only on the precipitate size and distribution but also on the coherency strains set up during transformation, the relative importance of each changing during the aging process. Similar observations in Fe-N alloys have been made by Ferguson (1981) aging at 23°C and 100°C and by Krzyminski (1969) aging in the range 20° to 300°C.

Figure VIII.7(b) shows that these changes in microhardness are accompanied by changes in the breadth of X-ray matrix reflections. The integral breadth was calculated from microdensitometer traces obtained from the {220} reflection, the α_1 and α_2 components being resolved

Figure VIII.7

Variation in (a) hardness and (b) integral breadth for Fe-0.18 w/o Ti nitrided in $11NH_3:89H_2$ at 585°C for 18 h and aged at 23° and 100°C.

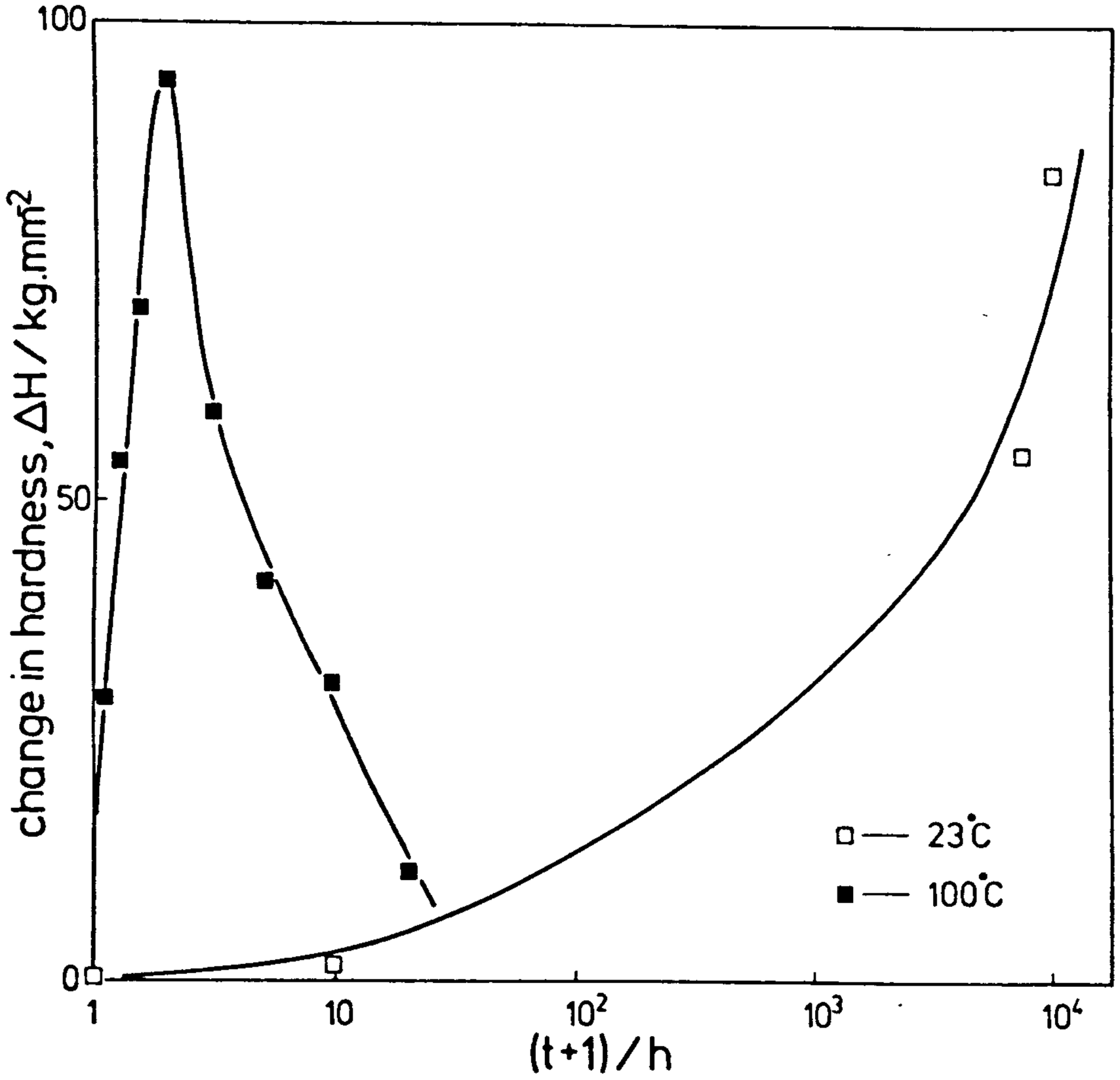
100
50
0
change in hardness, ΔH / kg.mm²
1
10
10²
10³
10⁴
(t+1) / h
23°C
100°C

(a)

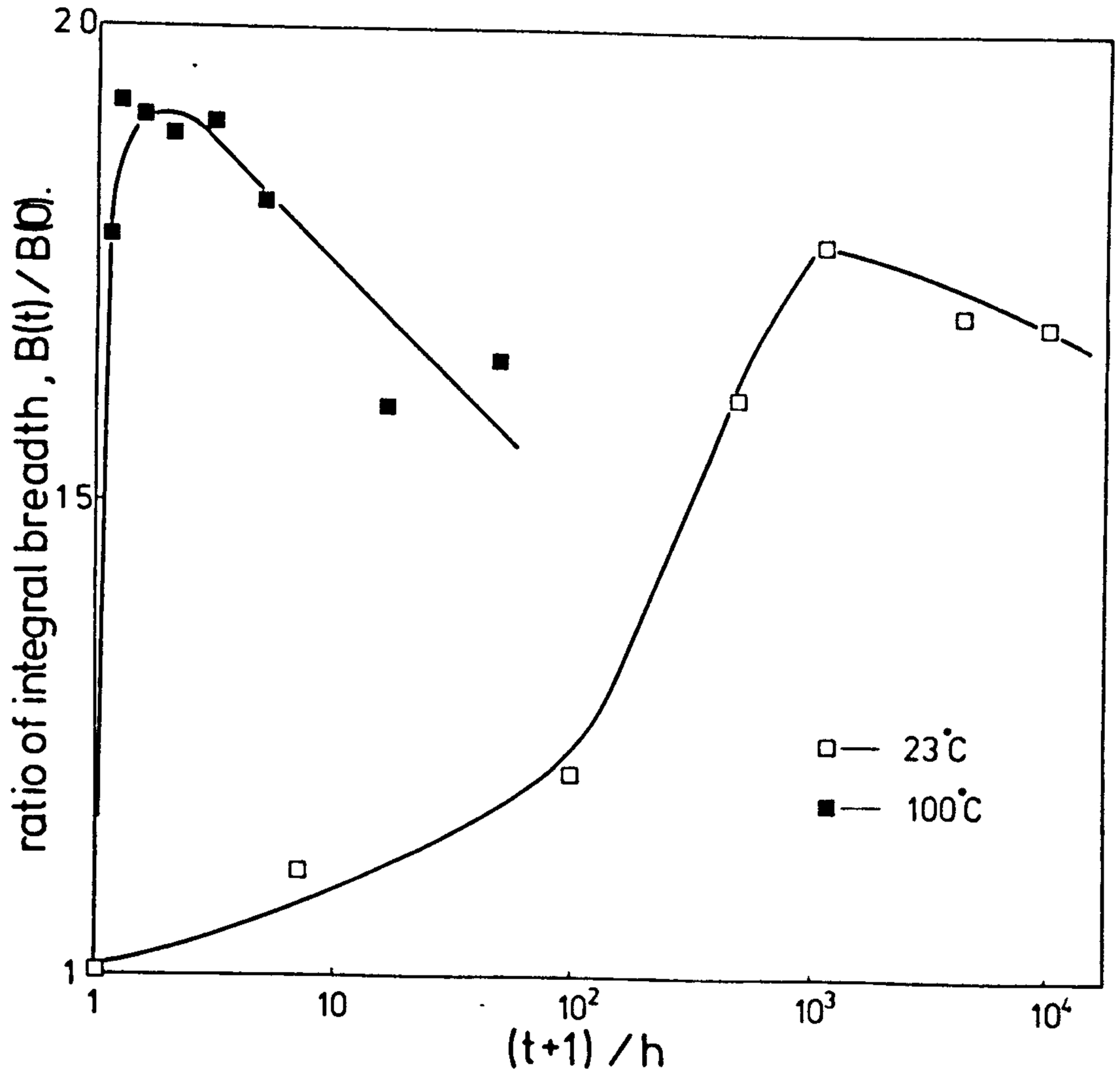
20
15
1
ratio of integral breadth, B(t) / B(0).
1
10
10²
10³
10⁴
(t+1) / h
23°C
100°C

(b)

by the graphical method of Rachinger (1948). The area under the α_1 component when divided by the peak height yields a value for integral breadth, and for ease of comparison the results are presented as the ratio of integral breadth at time, t, to that at time zero. Initially the diffraction lines of the matrix are sharp which is characteristic of a material containing GP zones which are coherent with the matrix. The lattice parameter indicates that all solutes are effectively in solid solution; that is, the matrix contains "Fe-N" and Ti-N clusters. After aging at room temperature for 100 h the integral breadth increases as the transformation "Fe-N" clusters to α''-$Fe_{16}N_2$ precipitates begins, which also results in a corresponding decrease in matrix-unit cell dimensions, see Figure VIII.2. Following Warren (1958), the broadening of peak profiles is due to either a reduction in the size of coherently diffracting domains (crystallite-size broadening), faulting on certain (hkl) planes, or by distortions within the crystallites (strain-broadening). In the present work it seems that the strains produced in the matrix due to ordering of nitrogen atoms to form coherent α''-$Fe_{16}N_2$ accounts for the broadening of the peak profiles. As the precipitates become incoherent, the driving force being a reduction in the total strain energy of the system, this strain will be relieved and the integral breadth decreases, as observed in Fiugre VIII.7(b) for specimens aged at 100°C. Associated with this peak broadening are shifts in the peak positions of the matrix X-ray reflections.

The unit-cell dimensions of the ferrite matrix can be determined for each X-ray reflection, and when these are plotted against the Nelson-Riley function the plots shown in Figure VIII.8(a) are obtained. For as-nitrided material and alloys aged at 100°C for long times such plots are linear, while aging at 100°C for short times results in non-linear Nelson-Riley plots. Similar anomalous Nelson-Riley plots have been observed during the aging of pure iron-nitrogen alloys at 18°C and 250°C (Jack & Maxwell, 1952b). In Figure VIII.8(b) the deviations from a linear Nelson-Riley plot for particular X-ray reflections are plotted, these deviations being measured from a line whose slope is identical to that of the as-nitrided material. The intercept of this line, a_o, is estimated from internal friction experiments and at longer times (> 20 min) the a_o value is constant at 2.8673 Å the unit-cell dimension corresponding to a N:Ti atomic ratio of 1:1. The deviations shown in Figure VIII.8(b) are not meant to represent the actual peak shifts which may occur during aging but represent trends in the behaviour of particular X-ray reflections. From Figure VIII.8(b) the maximum peak shifts occur after aging at 100°C for about 1 h and, like the line broadening, seem to be associated with the transformation "Fe-N" clusters to coherent α"-$Fe_{16}N_2$. This suggestion is supported by the results obtained from aging at 23°C where no peak shifts occur during the formation of "Fe-N" clusters, it is only when the nitrogen atoms subsequently order to form coherent α"-$Fe_{16}N_2$ that

Figure VIII.8

(a) Nelson-Riley plots of Fe-0.18 w/o Ti nitrided in $11NH_3 89H_2$ at 585°C for 18 h and aged at 100°C.

(b) Deviations from a linear Nelson-Riley plot with aging time at 100°C for particular {hkl} X-ray reflections.

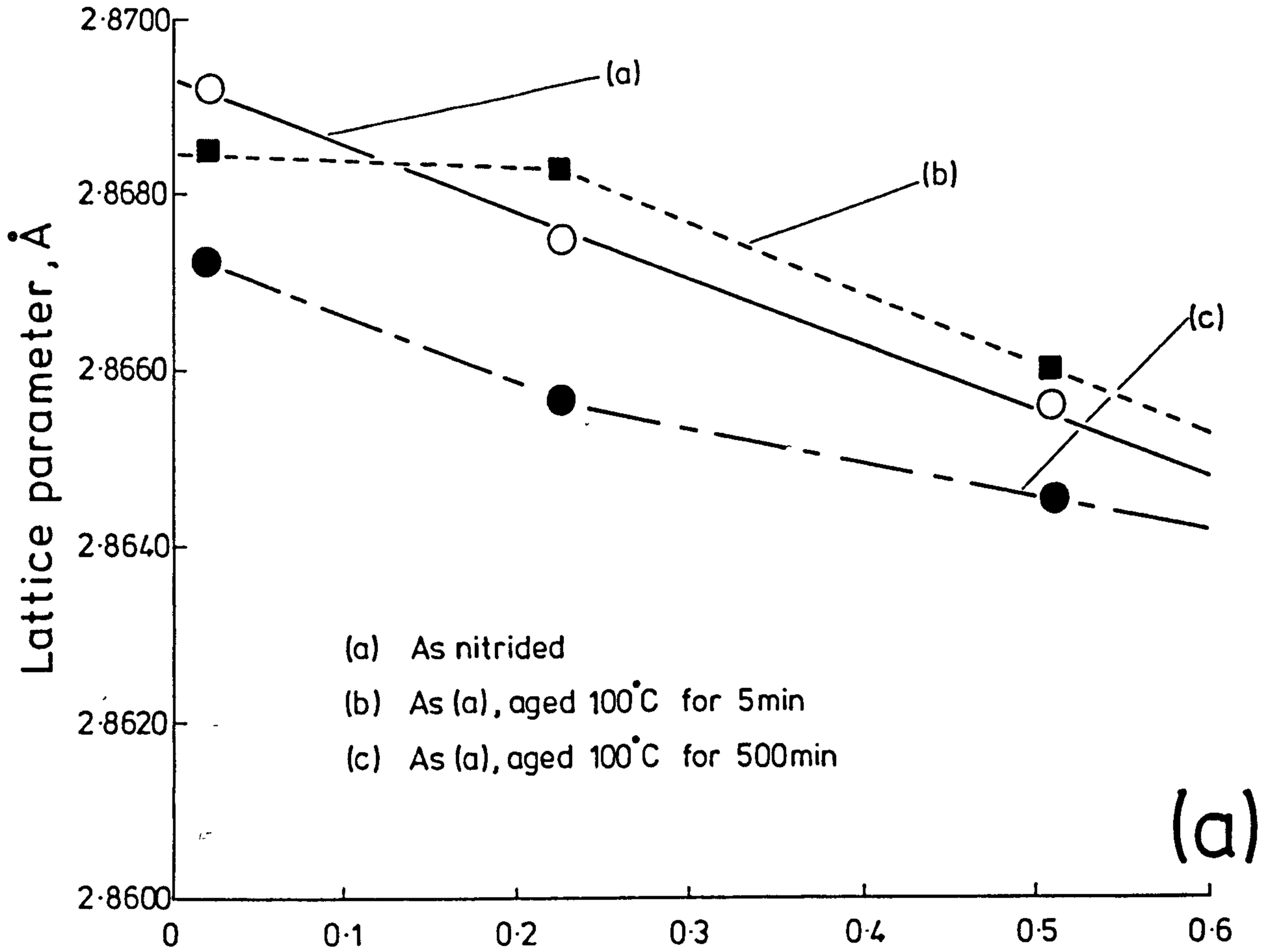
2·8700
2·8680
2·8660
2·8640
2·8620
2·8600
Lattice parameter, Å
(a)
(b)
(c)
(a) As nitrided
(b) As (a), aged 100°C for 5min
(c) As (a), aged 100°C for 500min
0
0·1
0·2
0·3
0·4
0·5
0·6
Nelson–Riley function
(a)

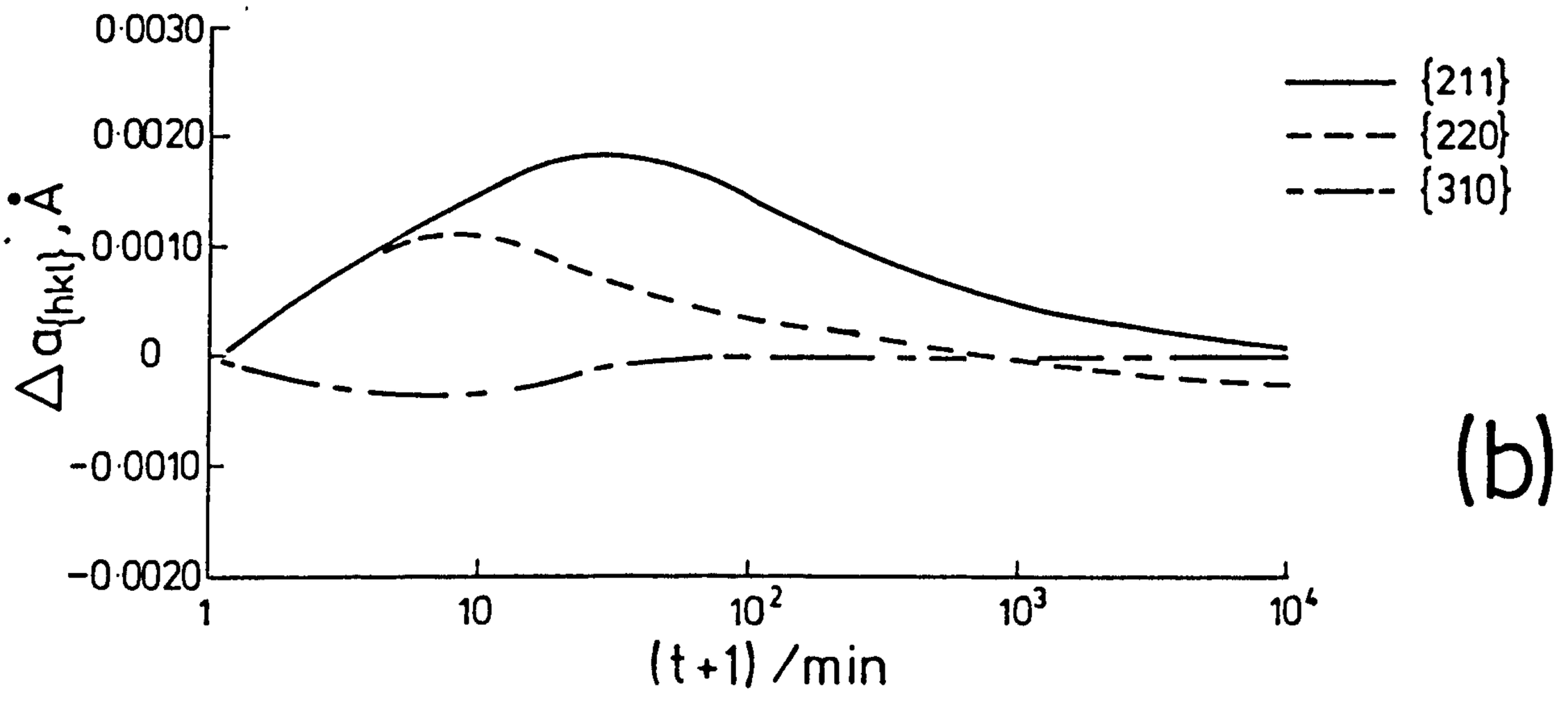
0·0030
0·0020
0·0010
0
-0·0010
-0·0020
Δa{hkl}, Å
1
10
10²
10³
10⁴
(t+1)/min
{211}
{220}
{310}
(b)

peak shifts and line broadening are observed.

A series of Fe-Ti alloys were nitrided at 500°C in a 16 NH_3:84H_2 gas mixture and quenched. Lattice parameter measurements confirmed all the solutes to be in solid solution indicating the presence of Ti-N clusters in the ferrite matrix. The alloys were then aged at 200°C for 100 h and lattice parameter measurements, see Table VIII.1, showed that all nitrogen in excess of the 1:1 composition for Ti-N clusters had precipitated as α"-$Fe_{16}N_2$ during aging. Optical microscopy of the aged alloys, Figure VIII.9, shows no evidence of precipitation in the higher titanium alloys, micrographs (d) and (e) of Figure VIII.9, although they contain large amounts of excess nitrogen as shown in Table VIII.1. As observed at lower aging temperatures, the excess nitrogen condenses onto the Ti-N clusters formed at nitriding temperature. However, with increasing titanium concentration in the initial alloy there will be a greater proportion of lower energy metal-atom octahedral sites available for occupation by nitrogen atoms around a Ti-N cluster, hence the nitrogens which condense onto the Ti-N zones to form "Fe-N" clusters will increase in stability with increasing titanium concentration. It is the higher volume fraction of Ti-N zones formed with increasing titanium concentration, and the greater stability of nitrogen which subsequently condenses onto these zones, which explains the optical micrographs

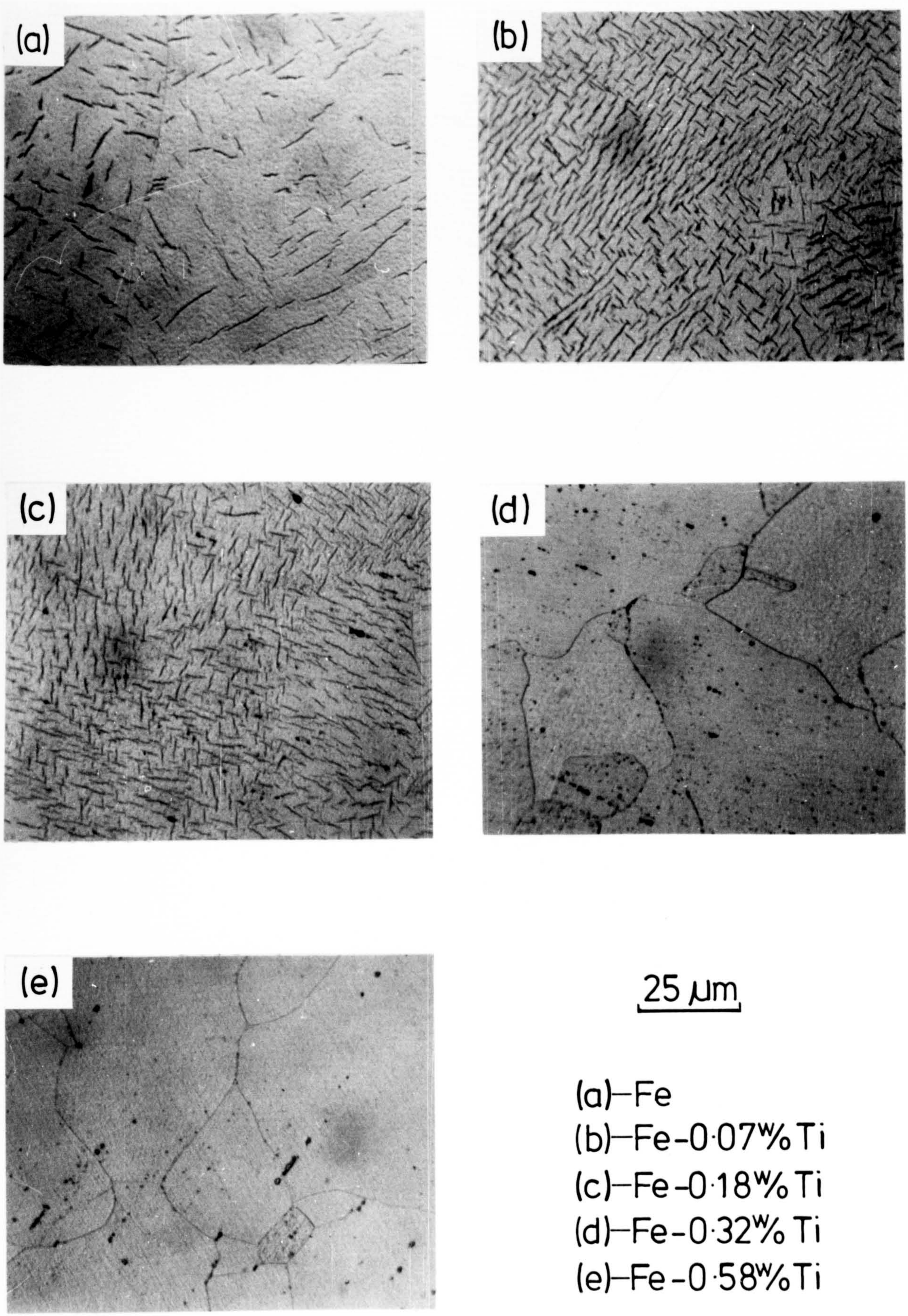

(a)—Fe
(b)—Fe-0·07w% Ti
(c)—Fe-0·18w% Ti
(d)—Fe-0·32w% Ti
(e)—Fe-0·58w% Ti

Table VIII.1

Lattice parameters and weight percentage nitrogen precipitated for nitrided iron and iron-titanium alloys after aging at 200°C for 100 h.

w/o Ti	a (calculated) Å*	a (observed) Å	w/o N ppt **
0	2.8664	2.8664	0.035
0.07	2.8670	2.8672	0.060
0.18	2.8674	2.8675	0.085
0.32	2.8693	2.8693	0.135
0.58	2.8712	2.8704	0.230

*Calculated lattice parameter for a N:Ti atomic ratio of 1:1.

**This nitrogen concentration is calculated from the total weight gain minus the amount of nitrogen combined as TiN.

---

shown in Figure VIII.9. The "Fe-N" clusters eventually transforming to α''-$Fe_{16}N_2$ precipitates, the rate of transformation decreasing with increasing titanium concentration in the starting alloy.

VIII.3 Conclusion

The experimental observations for nitrided and quenched Fe-Ti alloys are explained if the nitrogen retained in random solid solution ages by heterogeneous clustering and subsequent precipitation on existing Ti-N zones already present and formed at nitriding temperature. These zones retain a 1Ti:1N atom-ratio throughout the transformation sequence:

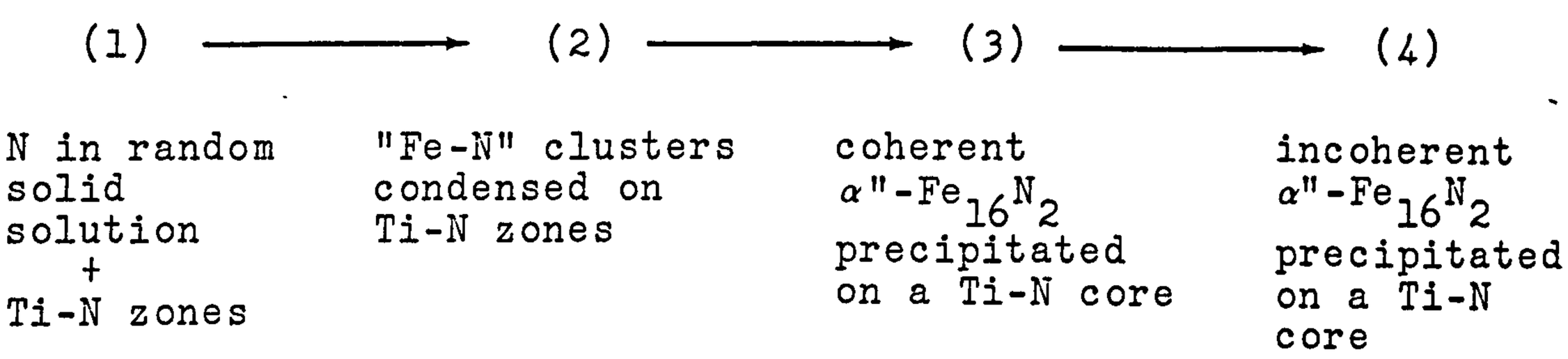

The transformations are analogous to those of quench-aged nitrogen-ferrite except that the stabilities of both the "Fe-N" clusters and the α"-$Fe_{16}N_2$ are enhanced by the Ti-N clusters on which they form.

Chapter IX

STRENGTHENING MECHANISMS IN Fe-Ti-N ALLOYS

IX.1 Introduction

A dispersion of second-phase particles is used extensively to produce strong steels, and these second-phase particles can behave in one of two different ways when the alloy yields. If the particles also yield, they are described as "deformable" and if they do not, they are "non-deformable". In either case the theoretical treatments of second-phase particle strengthening are based on a model in which the glide dislocation bows out between the particles as shown in Figure IX.1 and, when the included angle φ between the two arms of the dislocation reaches a critical value, φ_c, the dislocation breaks away from the obstacle. At this critical point the obstacle strength, F, is related to the dislocation line tension, E, by the equation:

$$F = 2E \cos (\varphi/2) \qquad \ldots \text{IX.1}$$

When the breaking angle $\varphi = 0$, the particle behaves as an impenetrable obstacle (Orowan hardening), while for values of $\varphi > 0$, the particle can be sheared by the glide dislocation with the required shearing force, F. The shear stress τ_c needed to cause the dislocation to break away from the

Figure IX.1

Basic model used in the theoretical treatments of second-phase particle strengthening.

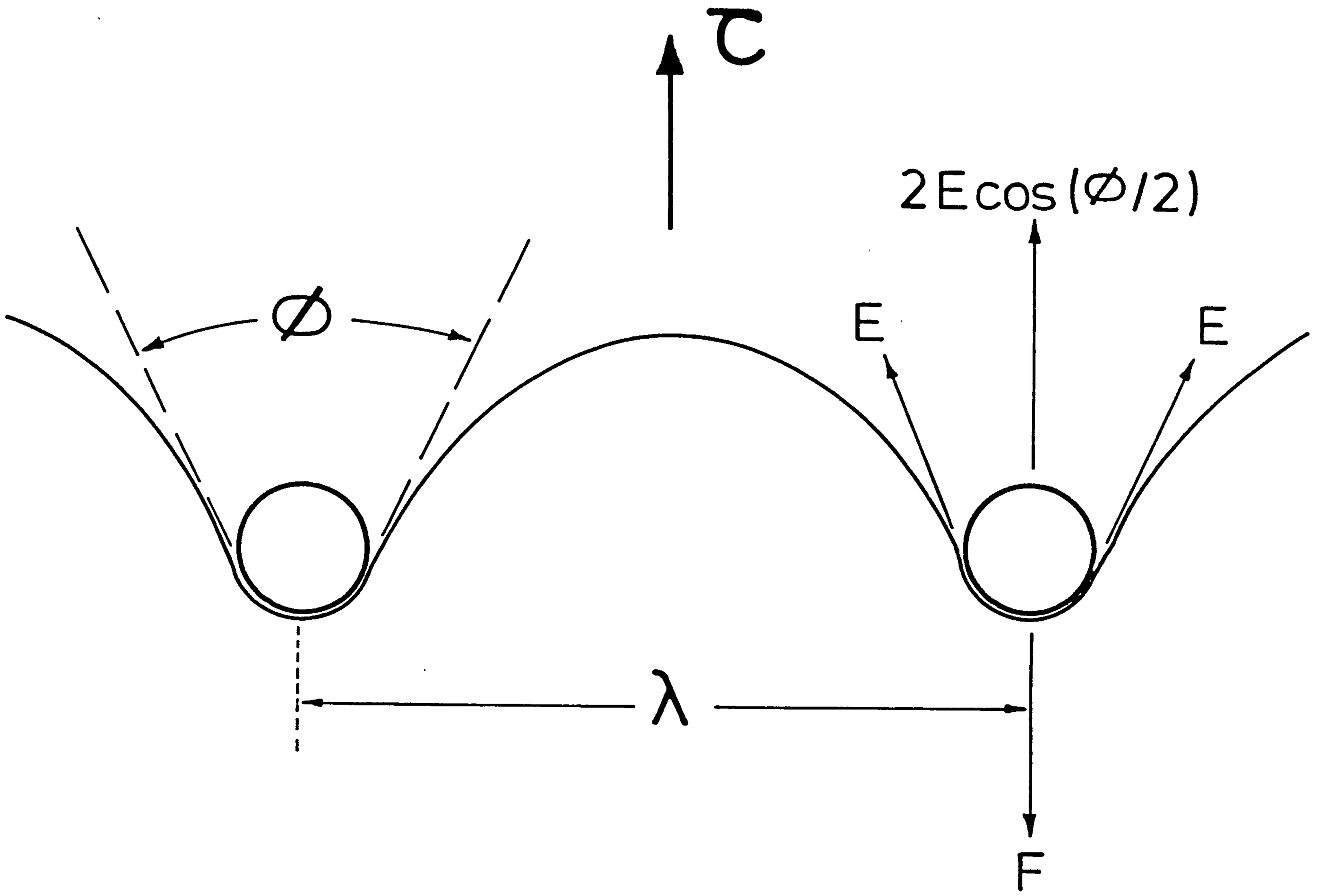
τ
2E cos (∅/2)
∅
E
E
λ
F

particle is given by:

$$\tau_c \; b \, \lambda = \; F$$

or $$\tau_c = \frac{F}{b\lambda} = \frac{2E \cos (\varphi_{c/2})}{b\lambda} \qquad \ldots \text{ IX.2}$$

where λ is the effective spacing between the particles and b is the Burgers vector. An appropriate definition of λ is the planar spacing (that is the average distance moved between particles in the slip plane) which is related to N_A, the number of particles intersecting the slip plane, by the equation:

$$\lambda = B/N_A^{\frac{1}{2}} = BL \qquad \ldots \text{ IX.3}$$

where B is a constant of the order of unity and L equals $(N_A)^{-\frac{1}{2}}$. From the computer experiments of Forman & Makin (1966) and Kocks (1966) the appropriate value of B, for the case of a random array of impenetrable particles, is about 1.2.

In the case of particles that can be sheared by glide dislocations the effective spacing is increased because the dislocation does not bow so much as it breaks away from the particle. For these weak particles the value of λ is given approximately by the Friedel relationship:

$$\lambda = \left\{\frac{2E}{\tau_c \; b \; N_A}\right\}^{1/3} = \left\{\frac{2EL^2}{\tau_c \, b}\right\}^{1/3} \qquad \ldots \text{ XI.4}$$

Substituting this value of λ into equation IX.2 gives:

$$\tau_c = \frac{2E}{bL} \left[\cos\ (\varphi_c/2)\right]^{3/2} \qquad \ldots \text{ IX.5}$$

In order to distinguish clearly between the Friedel and Orowan limits Brown & Ham (1971) suggest the use of two equations:

Orowan:- $$\tau_c = \frac{0.8\ Gb}{L} \cos\ (\varphi_c/2) \qquad \ldots \text{ IX.6}$$

for $0 \leqslant \varphi_c \leqslant 100^\circ$

Friedel:- $$\tau_c = \frac{Gb}{L} \left[\cos\ (\varphi_c/2)\right]^{3/2} \qquad \ldots \text{ IX.7}$$

for $100^\circ \leqslant \varphi_c \leqslant 180^\circ$

where G is the shear modulus of the matrix.

Both equations IX.6 and IX.7 are based upon the simplest line tension approximation in which $E = \frac{1}{2}Gb^2$ and where L is the mean planar spacing.

(a) Particles which act as impenetrable barriers; Orowan hardening

The maximum strengthening effect of second-phase particles occurs when they act as impenetrable obstacles and force the dislocation to bow out and by-pass the particles. The initial relationship predicting the yield stress was proposed by Orowan (1948):

$$\tau = \frac{2E}{bL} \qquad \ldots \text{ IX.8}$$

The many modifications that have been made to this basic equation include : (i) the introduction of the Kocks/Forman and Makin statistical factors (discussed above) to convert L to the effective interparticle spacing; (ii) the use of more refined estimates of dislocation line tension E; and (iii) allowance for the mutual interaction of the bowed-out arms of the dislocation on either side of the particle. The currently accepted version of the Orowan equation for a set of spherical particles of radius R is (Kelly, 1973):

$$\tau = \frac{0.83\ Gb}{2\pi\,(1-\upsilon)^{\frac{1}{2}}} \frac{\ell n\ (2R/r_o)}{(L-2R)} \qquad \ldots \text{ IX.9}$$

where υ is Poisson's ratio and r_o is the dislocation core radius. There is evidence (Kelly, 1972) to suggest that disc-shaped particles are more effective strengtheners than spherical particles and in order to apply the Orowan hardening mechanism to discs equation IX.9 must be modified. These modifications will be presented in Section IX.4 of the present chapter where the strengthening of ferrite by disc-shaped particles of titanium nitride is discussed.

(b) Particles which are deformed.

In the case of particles that are cut by glide

dislocations ($\varphi > 0$) the value of F that is required to cut the particles, or alternatively the breaking angle φ, must be calculated and substituted into either equation IX.2 or equations IX.6 and 7. There are a number of possible sources of this additional shearing force F, most of which are discussed in review articles; see for example Kelly & Nicholson (1963), Brown & Ham (1971) and Martin (1980). These are:

(i) Elastic coherency strains surrounding a particle that does not fit the matrix exactly; coherency hardening.

(ii) The energy necessary to create the additional particle/matrix interface when the particle is sheared by the dislocation; surface hardening.

(iii) The additional work required to create an internal interface or antiphase boundary in the case of internally ordered particles; chemical or order hardening.

(iv) Differences between the stacking-fault energy of particle and matrix when these are either both face-centred cubic or both close-packed hexagonal structures; stacking-fault hardening.

(v) Differences between the elastic moduli of matrix and particle; modulus hardening.

The strengthening which may be expected from each source of hardening has been calculated by many workers and the results obtained are reviewed by Kelly (1973) and Martin (1980). In nitrided materials it is possible that a number of the above processes may operate, and the work now presented was carried out in order to identify these and their relative importance.

Before discussing the experimental results it is important briefly to consider the effect of temperature on the yield strength of an alloy containing a dispersion of second-phase particles. In general, the force due to localised obstacles on a dislocation varies with the area swept out as shown in Figure IX.2; Kocks et al. (1975). At absolute zero these barriers cannot be overcome unless σ exceeds the local glide resistance $\hat{\tau}$ but, at any temperature above absolute zero, thermal fluctuations redistribute energy and so a finite probability exists that the dislocation can penetrate the peaks in the τ/a curve. A dislocation travelling from left to right in Figure IX.2 is under a positive driving force $b(\sigma - \tau)$ in some regions and would move to position S and be stable. If thermal fluctuations transfer the dislocation from the stable to the unstable equilibrium position (U) the amount of energy which must be supplied is given by the shaded area and once at U the dislocation moves to the next stable position S'. This shaded area is known as the activation energy, ΔG, and is given by:

Figure IX.2

Force/area profile for short-range obstacles (after Kocks et al., 1975).

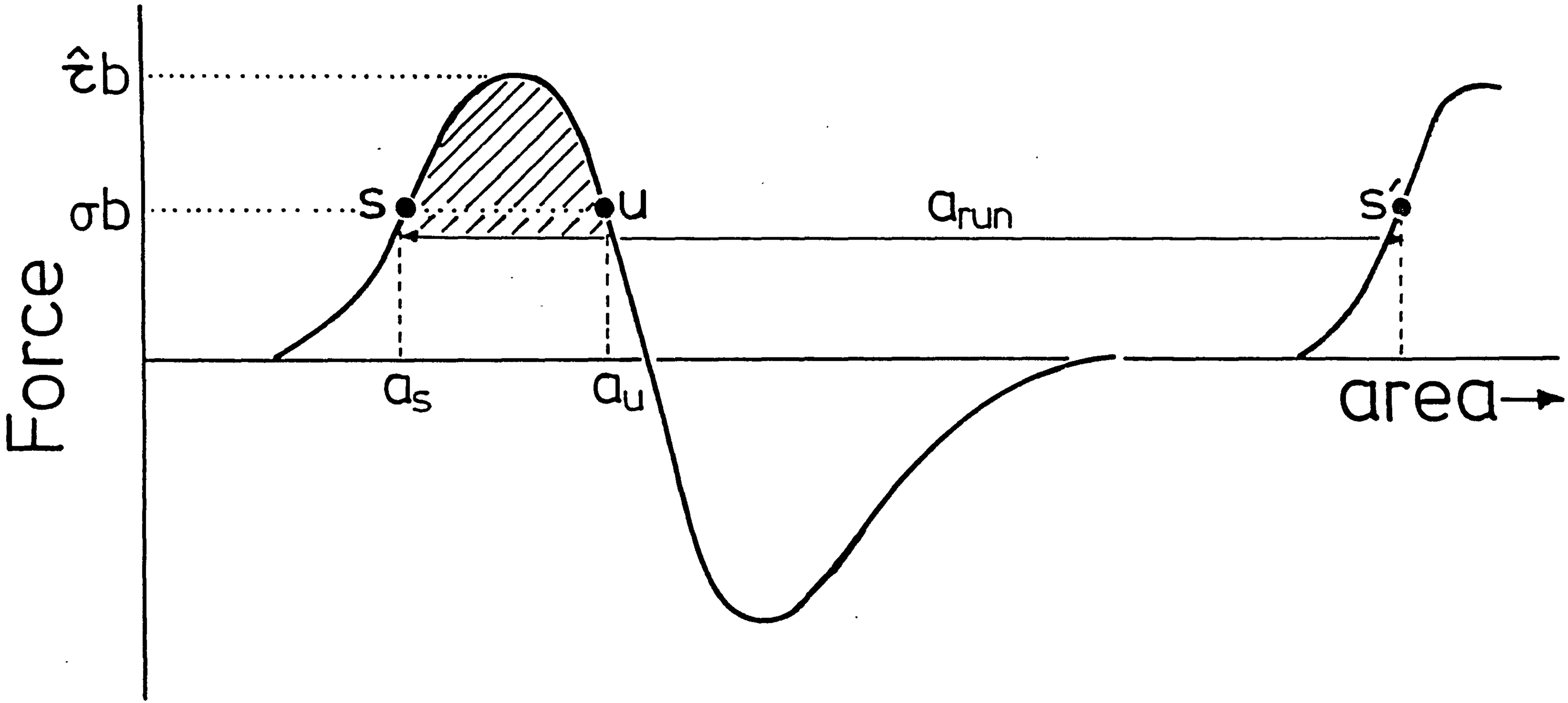
$\hat{\tau}_b$
σ_b
s
u
a_{run}
s'
Force
a_s
a_u
area→

$$\Delta G = \int_{a_S}^{a_U} (\tau_{line} - \sigma)\, b.da \qquad \ldots \text{IX.10}$$

The probability, p_B, of an equilibrium fluctuation in energy greater than a given value ΔG at a given temperature T is equal to a Boltzmann term involving this energy, that is:

$$p_B = \exp - \frac{\Delta G}{kT} \qquad \ldots \text{IX.11}$$

where k is Boltzmann's constant.

For short-range obstacles, which are especially sensitive to thermal activation, a useful generalization of equation IX.10 is:

$$\Delta G = F_o \left\{ 1 - \left(\frac{\sigma}{\hat{\tau}} \right)^p \right\}^q \qquad \ldots \text{IX.12}$$

where F_o is the total free energy necessary to overcome the obstacle without the aid of thermal fluctuations, and p and q are positive integers which describe the "tail" and "top" of the peak in the glide resistance diagram. It can be seen from equation IX.12 that the activation energy ΔG decreases from F_o to zero as σ is raised from zero to $\hat{\tau}$.

In order to consider the temperature or strain-rate dependence of the flow stress for any particular obstacle

profile, equation IX.12 is substituted into the strain-rate equation:

$$\dot{\epsilon} = \dot{\epsilon}_o \exp(-\Delta G/kT) \qquad \ldots \text{IX.13}$$

where $\dot{\epsilon}$ is the strain-rate and $\dot{\epsilon}_o$ is assumed to be a constant. Each obstacle profile will be defined by particular values of p and q which result in various stress/temperature relationships and thereby provide a means of deciding between particular interaction profiles for short-range obstacles. This approach will be used in Section IX.5 to gain information about the interaction profile which results when a dislocation encounters a substitutional-interstitial cluster formed by nitriding ferritic alloys.

IX.2 The Effect of Nitriding Potential and Time on Mechanical Properties

Nitriding Fe-Ti alloys in the temperature range 400-650°C leads to the formation of substitutional-interstitial GP zones (see Chapter VII) with resulting increases in strength. In Figure IX.3 the variation of yield strength as a function of nitriding potential (R) is shown for Fe-0.15 w/o Ti nitrided at 650°C; these are maximum values obtained on nitriding. After short nitriding times (5 h) in $1NH_3:99H_2$ the yield stress is about 700 MN/m^2 which increases after 18 h to about 900 MN/m^2 with a corresponding reduction in uniform elongation; see Figure IX.4(a).

Figure IX.3

Yield stress against nitriding potential (R) for Fe-0.15 w/o Ti nitrided at 650°C for 5 h; selected samples are then hydrogen reduced at 500°C for 18 h.

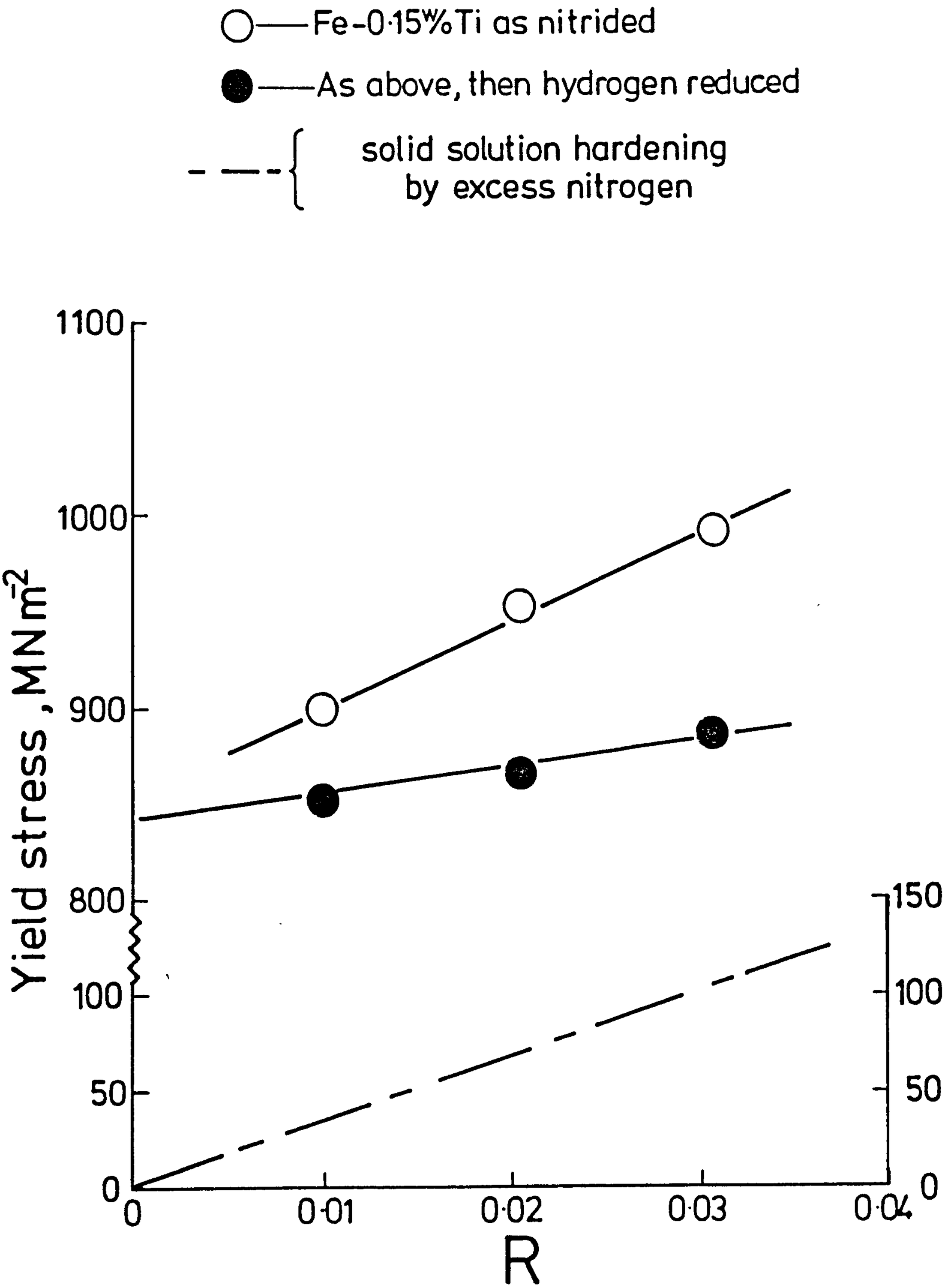
○—— Fe-0·15w% Ti as nitrided
●—— As above, then hydrogen reduced
- — - { solid solution hardening by excess nitrogen
Yield stress, MNm-2
1100
1000
900
800
100
50
0
150
100
50
0
0
0·01
0·02
0·03
0·04
R

Figure IX.4

Variation of (a) uniform elongation, and (b) weight gain for Fe-0.15 w/o Ti nitrided with increasing nitrogen potentials at 650°C for 5 h; selected samples are then hydrogen reduced at 500°C for 18 h.

(a)

○—Fe-0·15%Ti as nitrided, 5h

●—As above, then hydrogen reduced

◭—Fe-0·15% Ti as nitrided, 18h

– – – Nitrogen solubility in pure iron

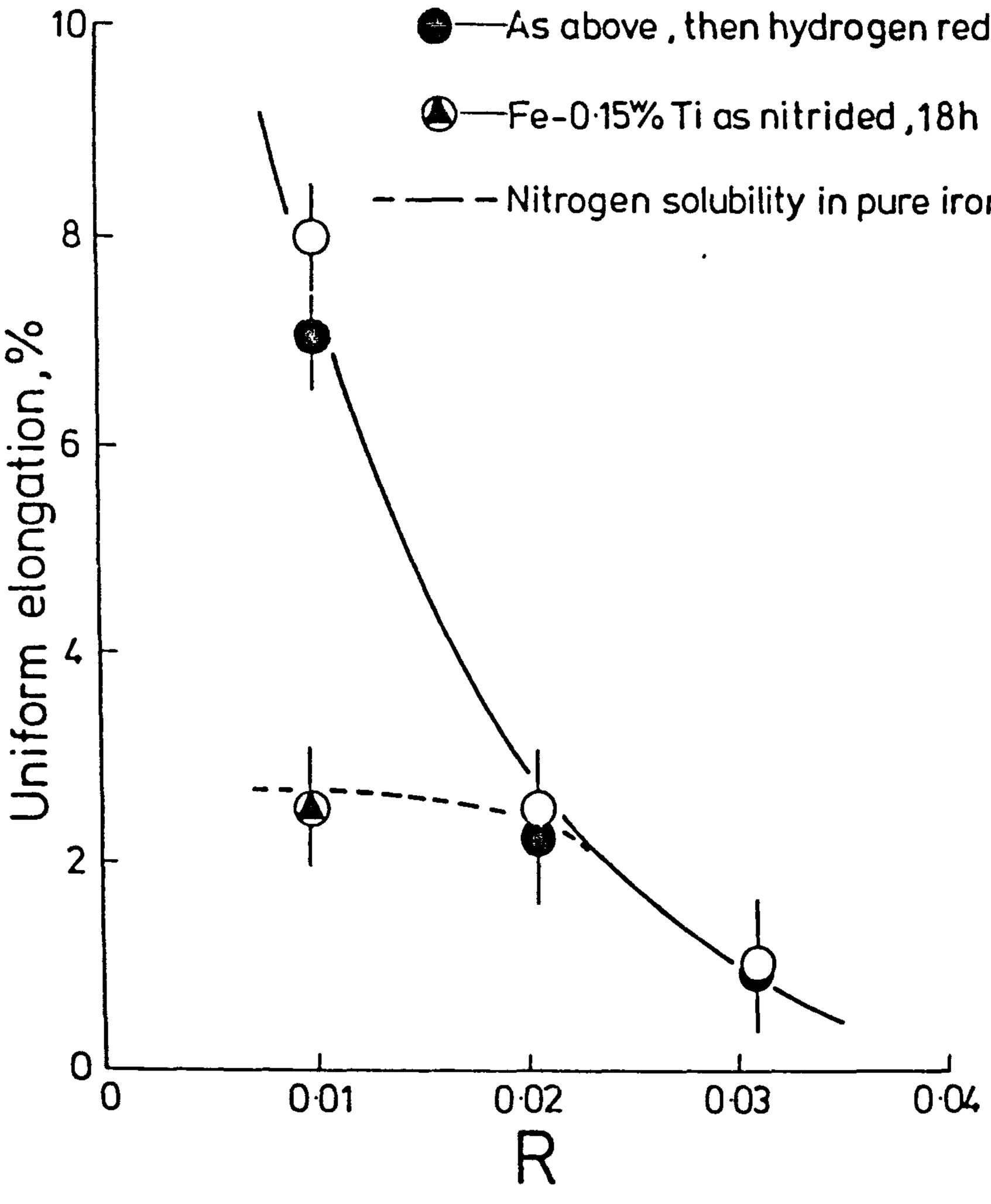

(b) Code, see (a)

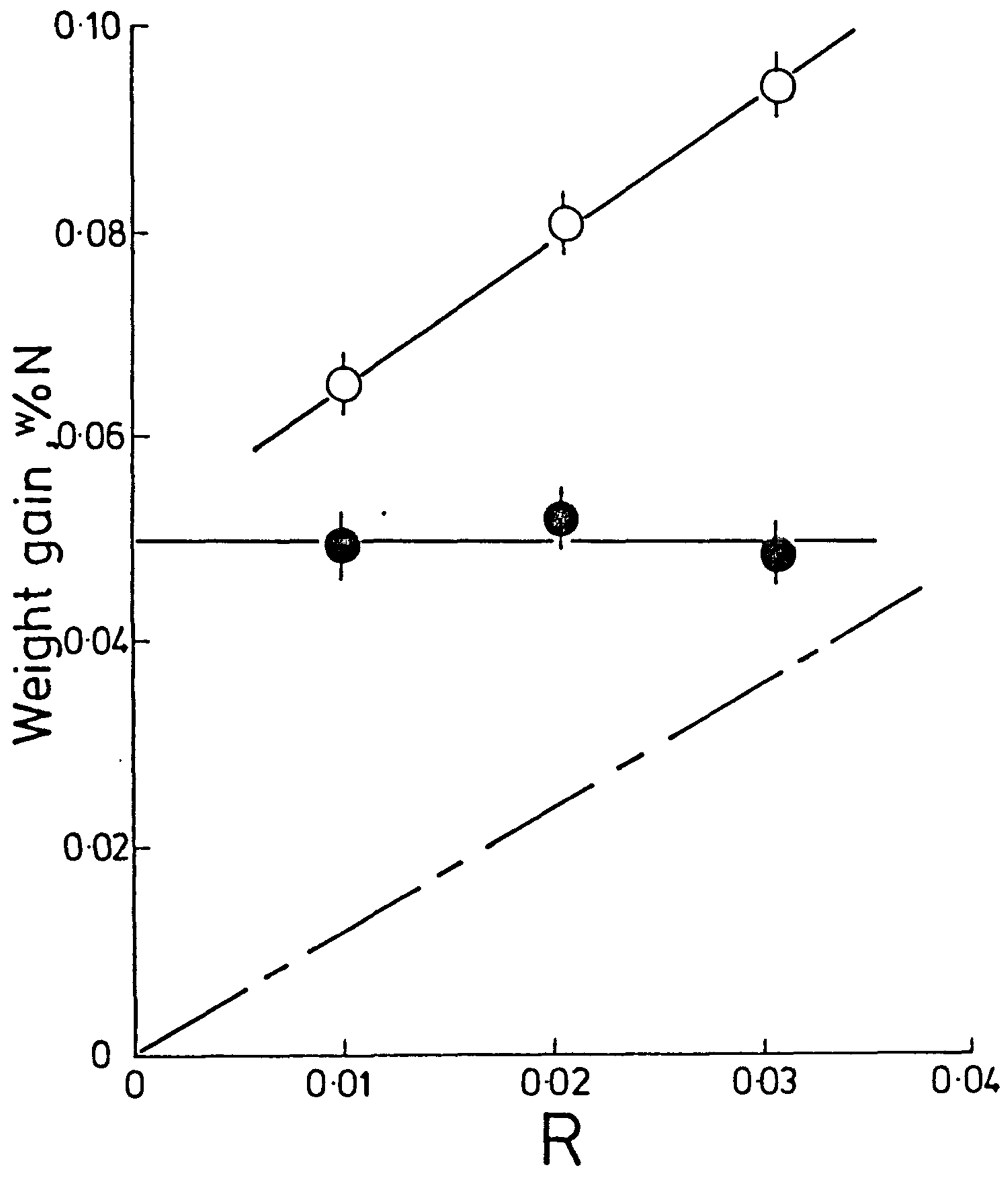

The observations cannot be explained by incomplete nitriding at short times since the amount of nitrogen taken up is approximately constant (0.065 w/o N) for all specimens nitrided in $1NH_3:99H_2$. It is therefore suggested that the increases in strength are due to refinements in the composition and/or distribution of the substitutional-interstitial clusters at nitriding temperature; this point will be considered in more detail later.

From Figure IX.3 the yield stress increases with R and Figure IX.4(a) shows that this is accompanied by a reduction in uniform elongation. The full curve represents the variation in elongation for a constant nitriding time of 5 h while the dashed curve shows the effect of prolonged (18 h) nitriding. It should be noted that at high R values, or prolonged nitriding at low R values, failure occurs before reaching the ultimate tensile stress. Weight gains presented in Figure IX.4(b) show that the amount of nitrogen taken up during nitriding increases with R and exceeds the sum required for the formation of stoichiometric TiN plus the equilibration of the ferrite matrix with nitrogen. At the same time, lattice parameter measurements indicate that both Ti and N solutes are effectively in solid solution and so, taken with transmission electron microscopy observations of disc-shaped particles of 110-130 Å diameter on the $\{100\}_\alpha$ planes, give unequivocal evidence of GP zones in the ferrite matrix. The nitrogen in excess of "TiN" is removed by

hydrogen reduction (see Figure IX.4(b)) to give a N:Ti atom ratio of about 1:1 but its removal does not lead to improved ductility (see Figure IX.4(a)) even though aging of the microstructure has taken place. This suggests that the poor ductility of nitrided Fe-Ti alloys results from the formation of a high volume fraction of coherent particles and not from the presence of excess nitrogen. The solid solution hardening effect of nitrogen in ferrite is extremely high, 575 MN/m^2 per a/o N (Baird & Jamieson, 1966; Bergstrom & Roberts, 1972), and the increases in strength with increasing R can be attributed to the excess nitrogen effectively being in solid solution. The dashed line in Figure IX.3 is the calculated contribution to strength of excess nitrogen if it is assumed to be in solid solution. In fact, there is evidence from internal friction experiments that nitrogen does remain in solution when Fe-Ti alloys are air-cooled from nitriding temperature and, as shown in Chapter VIII for nitrided and quenched Fe-0.18 w/o Ti, that this excess nitrogen can be aged at low temperatures to give further increases in strength above those obtained after nitriding.

It is believed that the poor ductility of nitrided material is also influenced by grain boundary precipitation of TiN since nitriding at 650°C gives precipitate-free grain boundary zones 950-1350 Å wide. Figure IX.5(a) shows a grain boundary with particles which disrupt the boundary fringe pattern, while in Figure IX.5(b) there is

Figure IX.5

Transmission electron micrographs of precipitation at grain boundaries.

(a) Fe-0.18 w/o Ti nitrided $7NH_3$:$93H_2$ at 585°C for 3 h.

(b) Fe-0.15 w/o Ti nitrided $7NH_3$:$93H_2$ at 585°C for 3 h, then hydrogen reduced at 585°C for 3 h and aged at 800°C for 112 h.

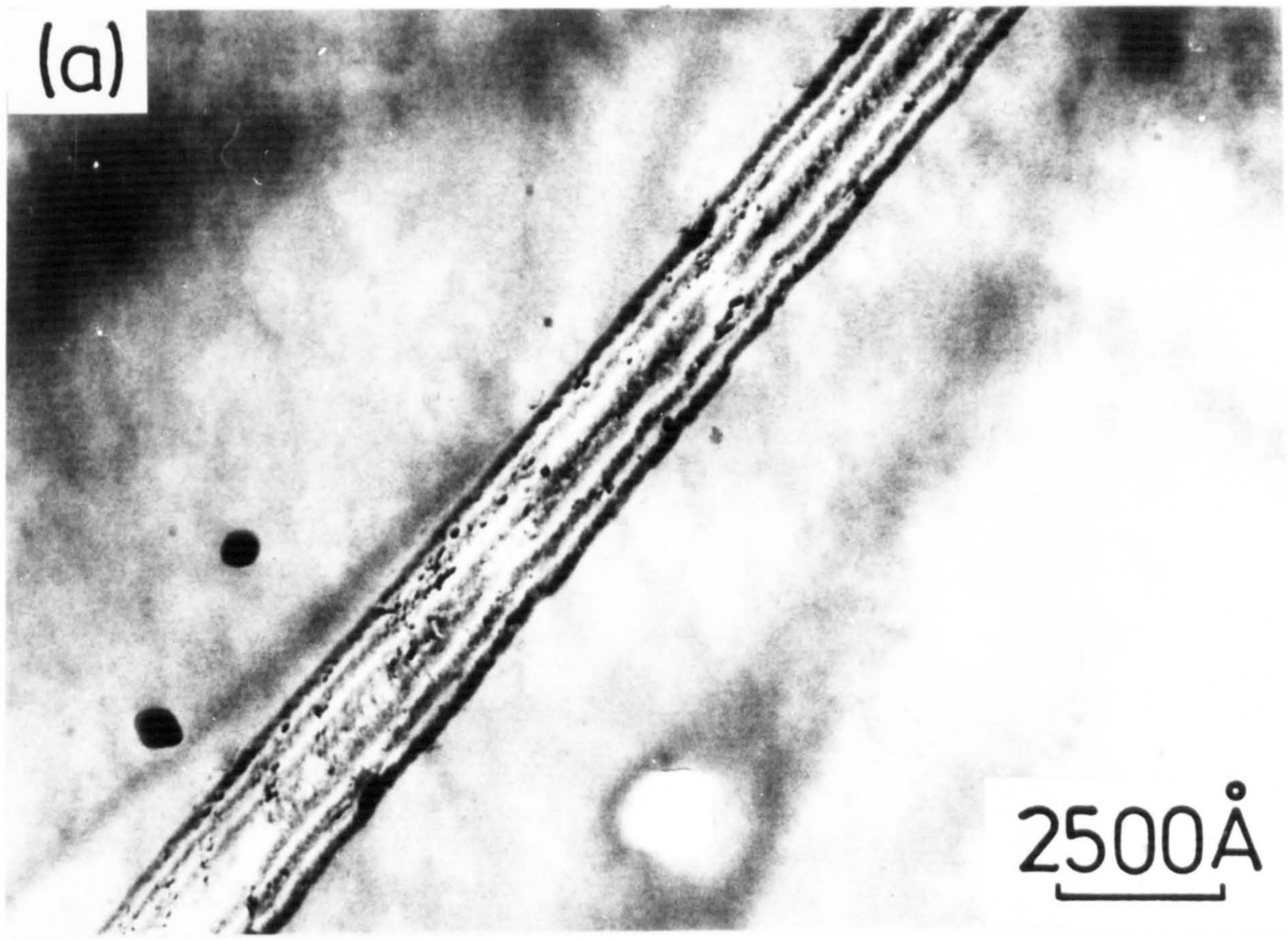
(a)
2500Å

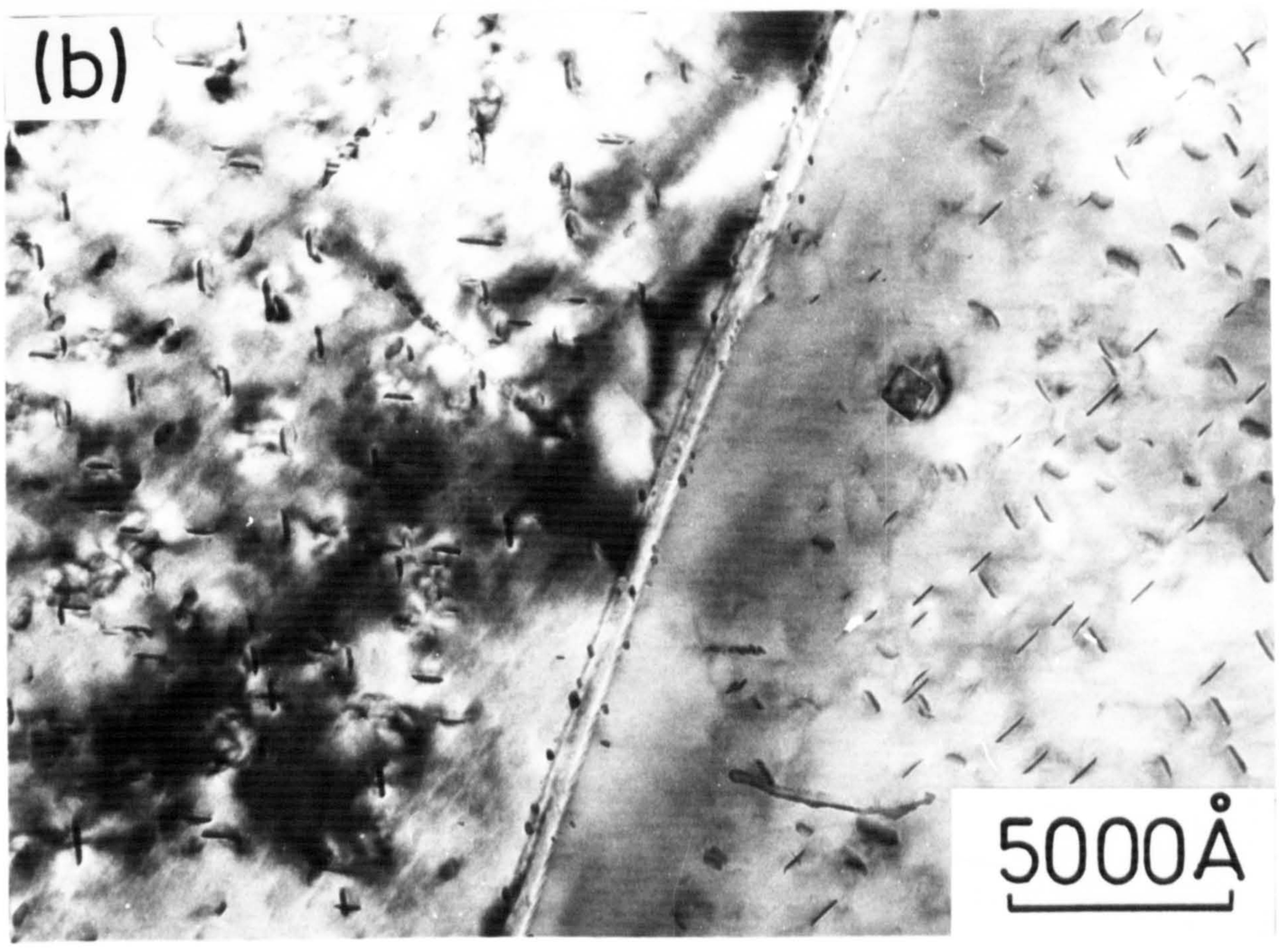
(b)
5000Å

a precipitate-free zone in Fe-0.15 w/o Ti nitrided and then aged at 800°C with clearly observed particles in the boundary. Scanning electron microscopy shows that failure of Fe-0.15 w/o Ti nitrided at 650°C occurs via a number of fracture mechanisms which depend on R and nitriding time. At low R and short nitriding times (5 h) a mixture of micro-void coalescence, intergranular and transgranular cleavage fracture modes are observed while at longer nitriding times or higher R values micro-void coalescence is not observed. Figure IX.6(a) shows that the annealed alloy fails by micro-void coalescence while material nitrided in $2NH_3$:$98H_2$, Figure IX.6(b), shows a mixture of intergranular and cleavage failure, as does the same alloy which has been hydrogen reduced prior to mechanical testing; see Figure IX.6(c). On the grain boundary facets of samples which fractured intergranularly, there are "dimples" which are assumed to be titanium nitride and related to the grain boundary precipitate-free zones observed by transmission electron microscopy.

IX.3 Grain Size Dependence of Mechanical Properties for Fe-0.18 w/o Ti

Figure IX.7 shows that the yield stress (σ_y) of Fe-0.18 w/o Ti nitrided at 650°C varies with grain size (d) according to the relationship first proposed by Hall (1951) and Petch (1953):

Figure IX.6

Scanning electron fractographs of Fe-0.15 w/o Ti

(a) un-nitrided

(b) nitrided in $2NH_3$:$98H_2$ at 650°C for 5 h

(c) nitrided as in (b), then hydrogen reduced at 500°C for 18 h.

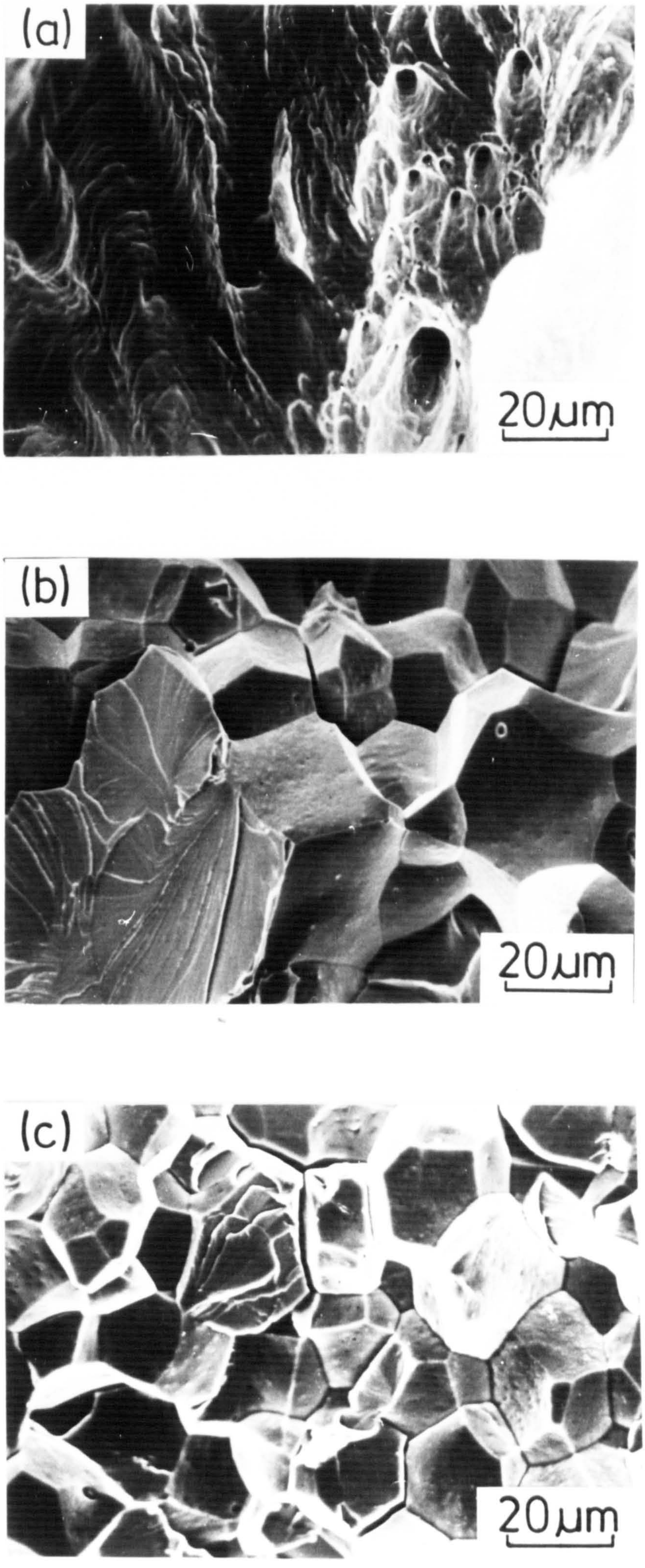
(a)
20 μm
(b)
20 μm
(c)
20 μm

Figure IX.7

Effect of grain size on the mechanical properties of Fe-0.18 w/o Ti nitrided in NH_3:H_2 at 650°C for 5 h; selected specimens are hydrogen reduced at 500°C for 18 h.

(a) Nitrided then hydrogen reduced – yield stress

(b) Nitrided in a $1NH_3:99H_2$ gas mixture

(c) Nitrided in a $3NH_3:97H_2$ gas mixture

(d) As (a) – microhardness

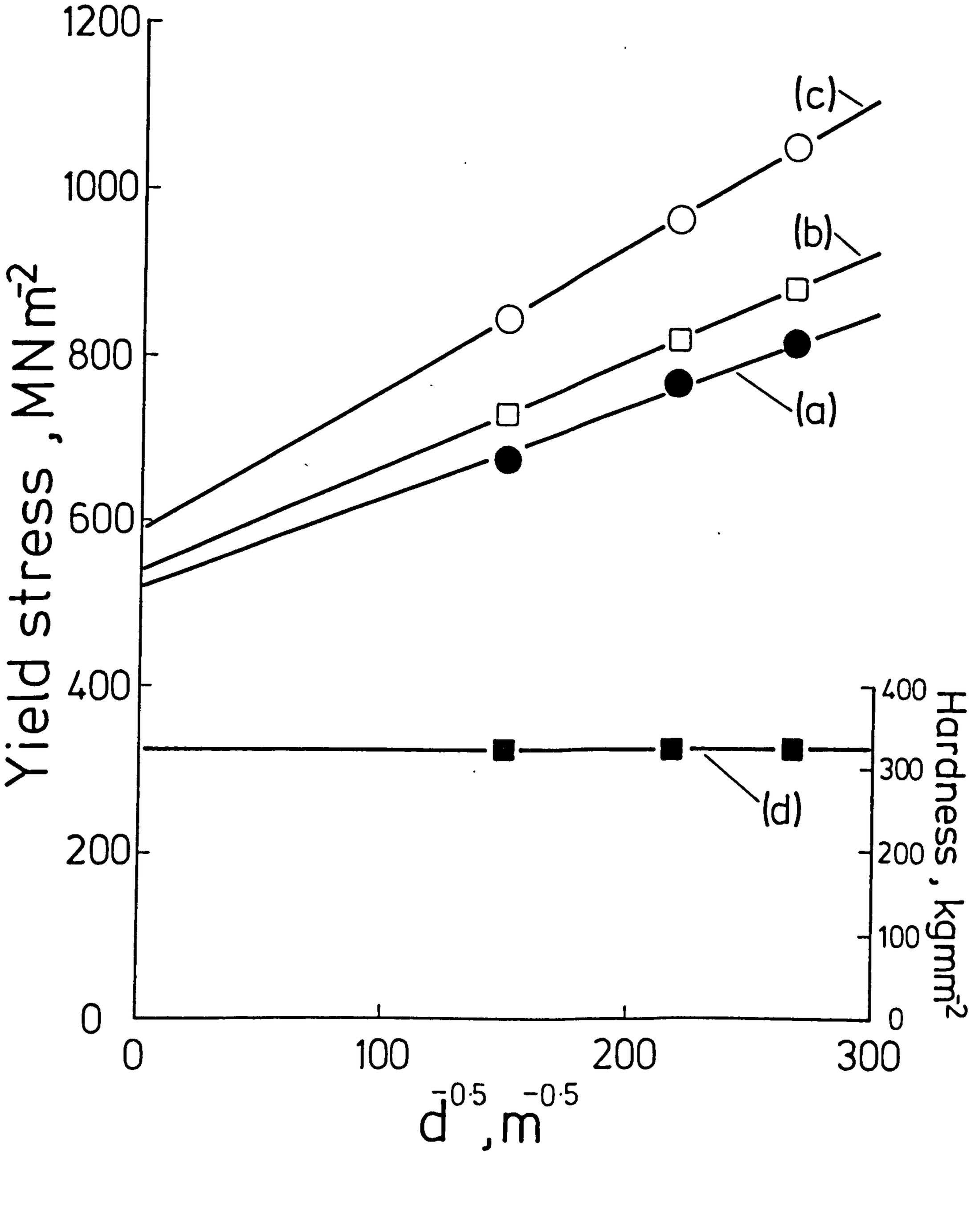

$$\sigma_y = \sigma_o + k_y \, d^{-\frac{1}{2}} \qquad \ldots \text{ IX.14}$$

where σ_o is termed the friction stress and represents the force restricting the motion of free dislocations on the slip plane, and k_y is a measure of the resistance to propagation of yield from grain to grain.

The variation in microhardness obtained from impressions made within the interior of grains (see Figure IX.7(d)) is constant with grain size indicating that the initial intragranular resistance to plastic deformation is the same in the three grain sizes studied. Consequently the grain size dependence of k_y is not complicated by any grain size dependence of the friction stress. The values of k_y and σ_o obtained as a result of nitriding Fe-0.18 w/o Ti at 650°C are dependent on the amount of excess nitrogen present in the lattice as shown by Figure IX.7, their values being given in Table IX.1 along with values from other systems for comparison. It is evident from Table IX.1 that locking of dislocations in nitrided and hydrogen-reduced material, i.e. due only to substitutional-interstitial clusters, is remarkably high and 1.4 times the maximum value obtained in iron-nitrogen alloys (see for example Cottrell & Fisher, 1963; Dingley & McLean, 1967).

The elastic interaction energy (ΔE_e) of a strain centre with the stress field (σij) of a dislocation can be expressed in the form (Cochardt et al., 1955):

$$\Delta E_e = - \sigma_{ij} \, e_{ij} \, v \qquad \ldots \text{ IX.15}$$

where e_{ij} is the strain produced by the strain centre over a volume v. Using this approach, Douthwaite & Evans (1973)

Table IX.1

Values of friction stress (σ_o) and Hall-Petch slope (k_y) for several body-centred cubic alloys

Material	σ_o, MN/m^2	k_y, $MN/m^{3/2}$	Reference
Fe-0.18 w/o Ti nitrided and hydrogen reduced	520	1.11	present investigation
Fe-0.18 w/o Ti nitrided in $1NH_3:99H_2$	540	1.29	
Fe-0.18 w/o Ti nitrided in $3NH_3:97H_2$	595	1.70	
Fe containing nitrogen	48	0.78	Cracknell & Petch (1955)
Fe containing boron	40	1.08	Codd & Petch (1960)
Fe-Co ordered	60	0.31	Marcinkowski & Fisher (1965)
Fe-Co disordered	320	0.14	

calculated that the maximum interaction energy between a tetragonal distortion and a ⟨111⟩ screw dislocation in ferrite is given by:

$$\Delta E_{e,max} = \frac{\sqrt{2}}{3} G e_T v \qquad \ldots \text{IX.16}$$

where G is the shear modulus and $e_T = e_c - e_a$, the principal strains along [001] and [100] directions respectively. From equation IX.16 the value of ΔE_e, and thus k_y, is determined by the tetragonal expansion of the ferrite lattice caused by an interstitial atom. In the case of boron the value of k_y is higher than that of nitrogen since its resultant tetragonal strain is greater, see Table IX.1. For Ti-N clusters the increase in k_y cannot be explained in a similar manner since the expansion of the lattice is determined principally by nitrogen and as a result should give a value of about 0.8 $MN/m^{3/2}$. The increased interaction energy may be due to differences in atomic bonding around a Ti-N cluster i.e. the result of a chemical term (E_c) in addition to the elastic interaction (E_e). The idea of a chemical interaction was proposed by Codd & Petch (1960) to explain the difference in locking strengths between carbon and nitrogen, where the amount of "residual chemical bonding" at a dislocation to which the impurity atom becomes attached is greater in the case of nitrogen.

The Hall-Petch equation, for a pile-up model, may be expressed as:

$$\tau = \tau_o + \left[\frac{m_1 \; G \; \tau_c b}{\pi (1-\nu)}\right]^{\frac{1}{2}} d^{-\frac{1}{2}} \qquad \ldots \text{ IX.17}$$

where b is the Burgers vector of the dislocations, ν is Poisson's ratio, τ_c the stress necessary to generate dislocations from a source, and m_1 the Taylor orientation factor which takes into account the local stress increment necessary to activate dislocations on unfavourably orientated planes. To obtain the applied tensile stress required to propagate slip across grain boundaries, τ in equation IX.17 must be multiplied by m_2 the overall Taylor orientation factor which relates shear stresses to tensile stresses. Hence

$$\sigma_y = m_2 \; \tau_o + m_2 \left[\frac{m_1 \; G \; \tau_c \; b}{\pi (1-\nu)}\right]^{\frac{1}{2}} d^{-\frac{1}{2}} \qquad \ldots \text{ IX.18}$$

In Fe-Co alloys ordering leads to an increase in k_y, see Table IX.1, which is attributed to the restriction of cross-slip at grain boundaries making propagation of slip across the boundaries more difficult (Armstrong et al., 1962), that is, ordering affects m_2 and perhaps τ_c in equation IX.18. The slip distribution in nitrided materials is markedly inhomogeneous (Jones, 1976), and restriction in the number of planes along which dislocations can move may explain the high observed value of k_y since the orientation factor m_2 will be increased. A similar argument might explain the increase in k_y with increasing amounts of excess nitrogen (see Figure IX.7 and Table IX.1) if

this nitrogen influences the slip characteristics of the material and hence any stress concentration effects. It is also possible that the Ti-N clusters and excess nitrogen influence the value of τ_c making it more difficult to create a dislocation source. If a grain boundary source model is used instead of a pile-up model, a Hall-Petch relation is again valid (Li & Chou, 1970):

$$\sigma = \sigma_o + \alpha G b \sqrt{3m}\, d^{-\frac{1}{2}} \qquad \ldots \text{IX.19}$$

where α is a constant and m the total length of dislocations emitted per unit area of grain boundary at the time of yielding. The dislocation sources are grain boundary ledges, and the segregation of the excess nitrogen onto grain boundaries may stabilise the ledge structure, thereby increasing the ledge density and hence the value of k_y.

In the Hall-Petch equation the friction stress consists of a temperature independent (σ_o^+) and temperature dependent (σ_o^*) component (Heslop & Petch, 1956). Nitriding greatly increases σ_o (see Table IX.1) through the formation of substitutional-interstitial clusters; the excess nitrogen also affects σ_o but to a lesser extent. However, it is not immediately clear whether Ti-N clusters affect the temperature independent component, σ_o^+, in the same way as Heslop & Petch (1956) observed with interstitial carbon and nitrogen. It has already been shown in Section IX.2 that excess nitrogen increases σ_o

by solid solution hardening, but to avoid complications caused by dynamic strain-aging this nitrogen was removed before investigating the temperature dependence of σ_o and k_y. Figure IX.8 shows the results from such an analysis and clearly both σ_o and k_y are temperature dependent, indicating that the Ti-N clusters add to the temperature dependent component, σ_o^*, of friction stress. Over the range -196° to 25°C the temperature dependence of σ_o observed by Heslop & Petch (1956) corresponded to the variation of the Peierls-Nabarro force for α-iron which becomes very small at 25°C. As a result, σ_o for pure iron is approximately constant above room temperature and decreases by only 14 MN/m^2 at 600°C (Baird & Jamieson, 1966). The temperature dependence of friction stress for nitrided and hydrogen reduced Fe-0.18 w/o Ti (Figure IX.8(a)) must therefore result from the thermally activated movement of glide dislocations as they encounter Ti-N clusters in the iron matrix, and any mechanism which is proposed for the strengthening of Ti-N alloys by nitriding must account for this temperature dependence of yield strength.

Figure IX.8(b) shows the temperature dependence of k_y to be very marked and similar to that observed by Dingley & McLean (1967) for iron containing interstitial nitrogen and carbon. In the pile-up models proposed by Hall (1951) and Petch (1953) the critical process for yield in materials having strongly pinned grown-in

Figure IX.8

Temperature dependence of the constants in the Hall-Petch equation, (a) friction stress and (b) Hall-Petch slope, for Fe-0.18 w/o Ti nitrided in $3NH_3$:$97H_2$ at 650°C for 5 h and then hydrogen reduced at 500°C for 18 h.

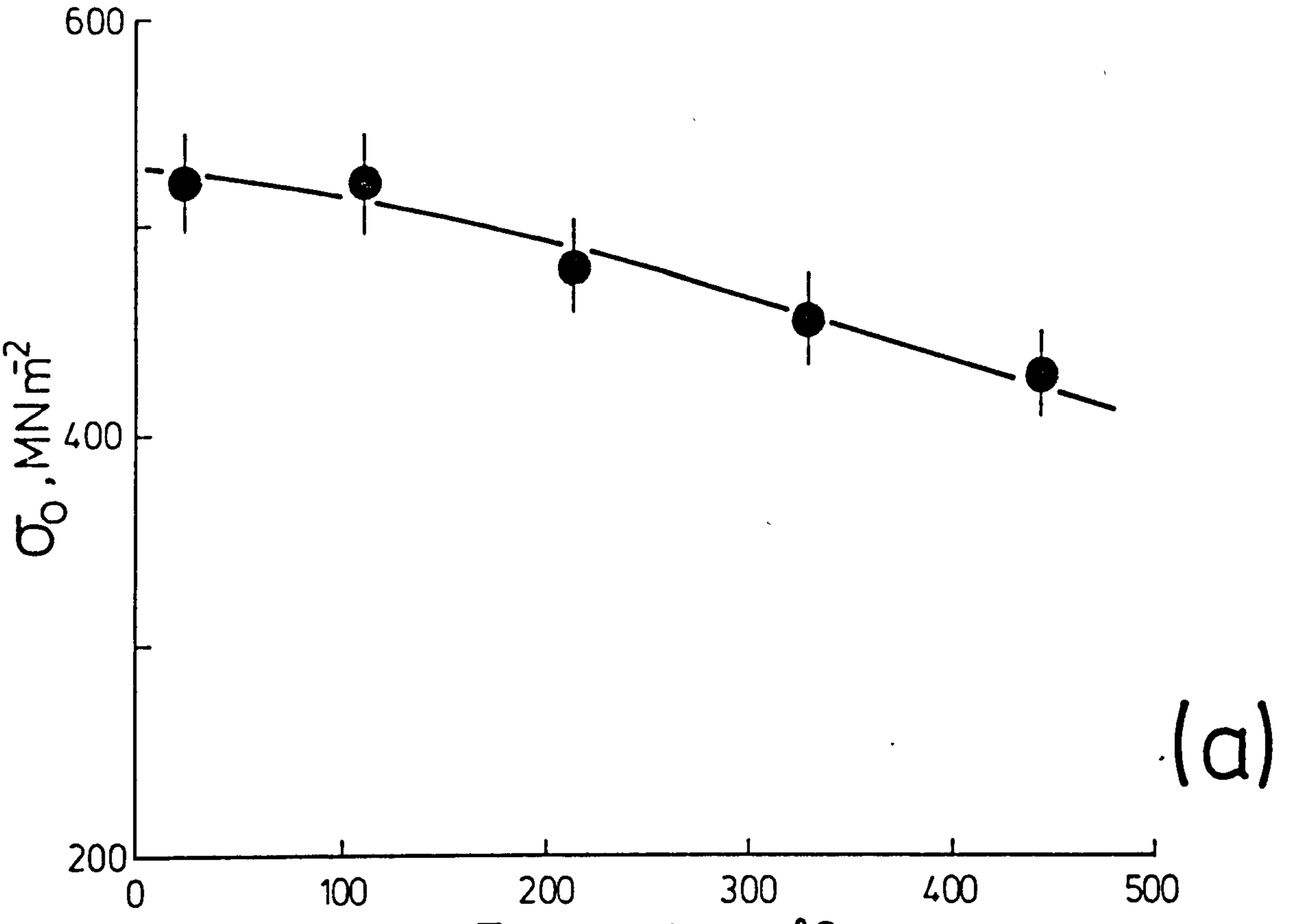
600
400
200
σ_0, MNm^{-2}
0
100
200
300
400
500
Temperature, °C
(a)

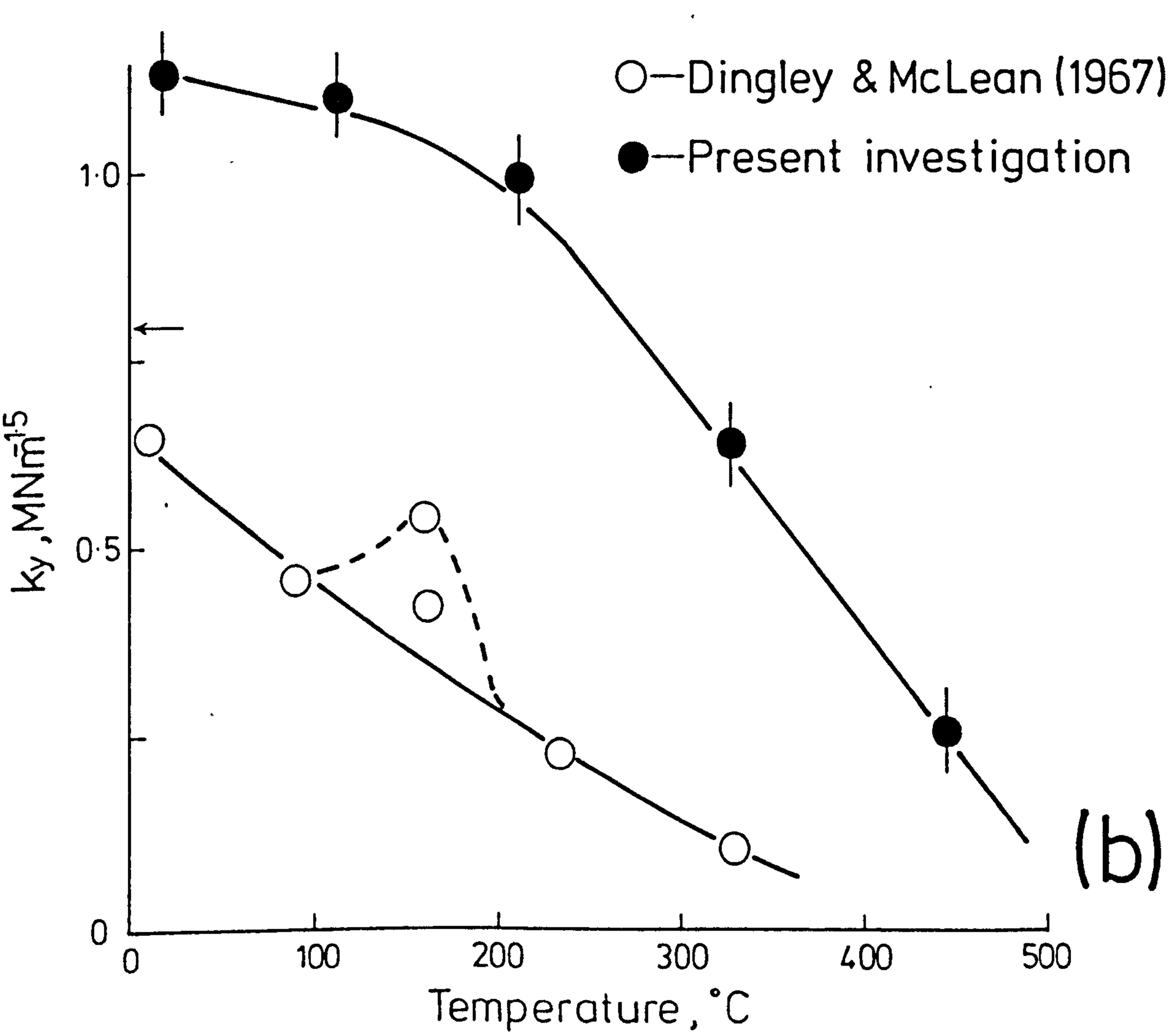
1·0
0·5
0
k_y, MNm$^{-1.5}$
O—Dingley & McLean (1967)
●—Present investigation
0
100
200
300
400
500
Temperature, °C
(b)

dislocations is the unpinning or generation of sufficient dislocation sources to produce macroscopic deformation. The creation of a dislocation loop should be insensitive to thermal activation whereas unpinning of a locked dislocation should be strongly temperature dependent (Cottrell, 1963). The results obtained show that in nitrided and hydrogen reduced Fe-0.18 w/o Ti the critical process for yield must be the unpinning of strongly locked dislocations.

If the dispersion of substitutional-interstitial clusters is aged to give disc-shaped particles of incoherent titanium nitride, the resultant values of k_y and σ_o are shown in Figure IX.9. For the discussion in Section IX.4 it was necessary to calibrate the microhardnesses obtained for aged materials with intergranular friction (σ_o). Following Tabor (1951), hardness impressions are proportional to flow stress (σ_f) at some representative strain taken in the present work to be 6%. The flow stress at a given plastic strain (ϵ) shows a dependence on grain size (d) similar to that of yield stress (Armstrong et al., 1962):

$$\sigma_f = \sigma_o(\epsilon) + k_\epsilon \, d^{-\frac{1}{2}} \qquad \ldots \text{ IX.20}$$

From Figure IX.9 the value of k_y (0.27 $MN/m^{3/2}$) is obviously greater than k_ϵ, comparing the gradients of (b) and (d) respectively, in agreement with the results

Figure IX.9

Effect of grain size on the mechanical properties of Fe-0.18 w/o Ti nitrided in $3NH_3:97H_2$ at 650°C for 5 h, then hydrogen reduced at 500°C for 18 h and aged at 800°C for 112 h.

(a) Nitrided then hydrogen reduced

(b) As(a), aged 800°C for 100h – yield stress

(c) As (b) – microhardness

(d) As (b) – flow stress at $\epsilon = 0{\cdot}06$

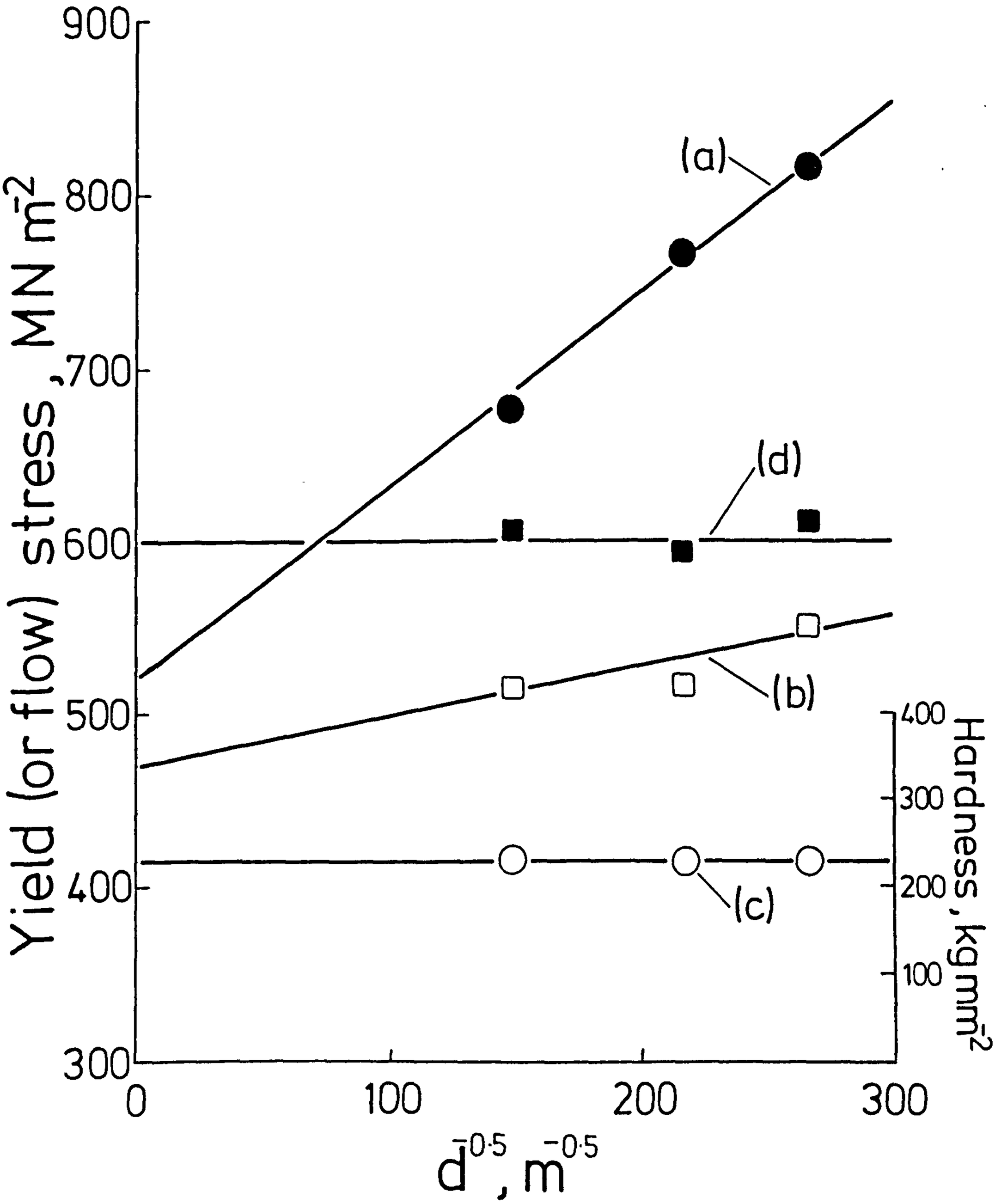

obtained from mild steel by Armstrong et al., (1962). The proportionality factor between microhardness and intergranular friction was obtained by comparing the microhardness value to the flow stress at 6% strain, and was found to be 3.9 for the Reichert microhardness tester used.

IX.4 The Mechanical Properties of Aged Fe-Ti-N Alloys

It was shown in Section IX.2 that time at nitriding temperature can influence the resulting mechanical properties of nitrided Fe-Ti alloys. Nitriding temperature was also found to be important, for example an alloy nitrided and hydrogen reduced at 585°C has a yield strength of about 600 MN/m^2, while nitriding at the same nitrogen activity and 650°C followed by hydrogen reduction gives 880 MN/m^2. Strength differences brought about by a change in nitriding temperature have also been observed by Henderson (1976) and Cuddy & Podgurski (1977). In order to investigate this effect, and also the influence of aging upon the dispersion of Ti-N clusters, alloys were nitrided, hydrogen reduced and aged as shown in Figure IX.10. Clearly the aging response of nitrided and hydrogen reduced material depends on the initial nitriding conditions and subsequent aging temperature. Aging Fe-Ti alloys at 650°C after nitriding and hydrogen reduction at 400°C always leads to hardness increases, whereas only Fe-0.18 w/o Ti shows an increase when

Figure IX.10

Variation in microhardness with aging time and temperature for nitrided Fe-Ti alloys

(a) nitrided in $7NH_3$:$93H_2$ at 585°C for 18 h; hydrogen reduced at 585°C for 18 h; aged at 800°C.

(b) nitrided in $29NH_3$:$71H_2$ at 400°C for 285 h; hydrogen reduced at 400°C for 90 h; aged at 650°C.

(a)

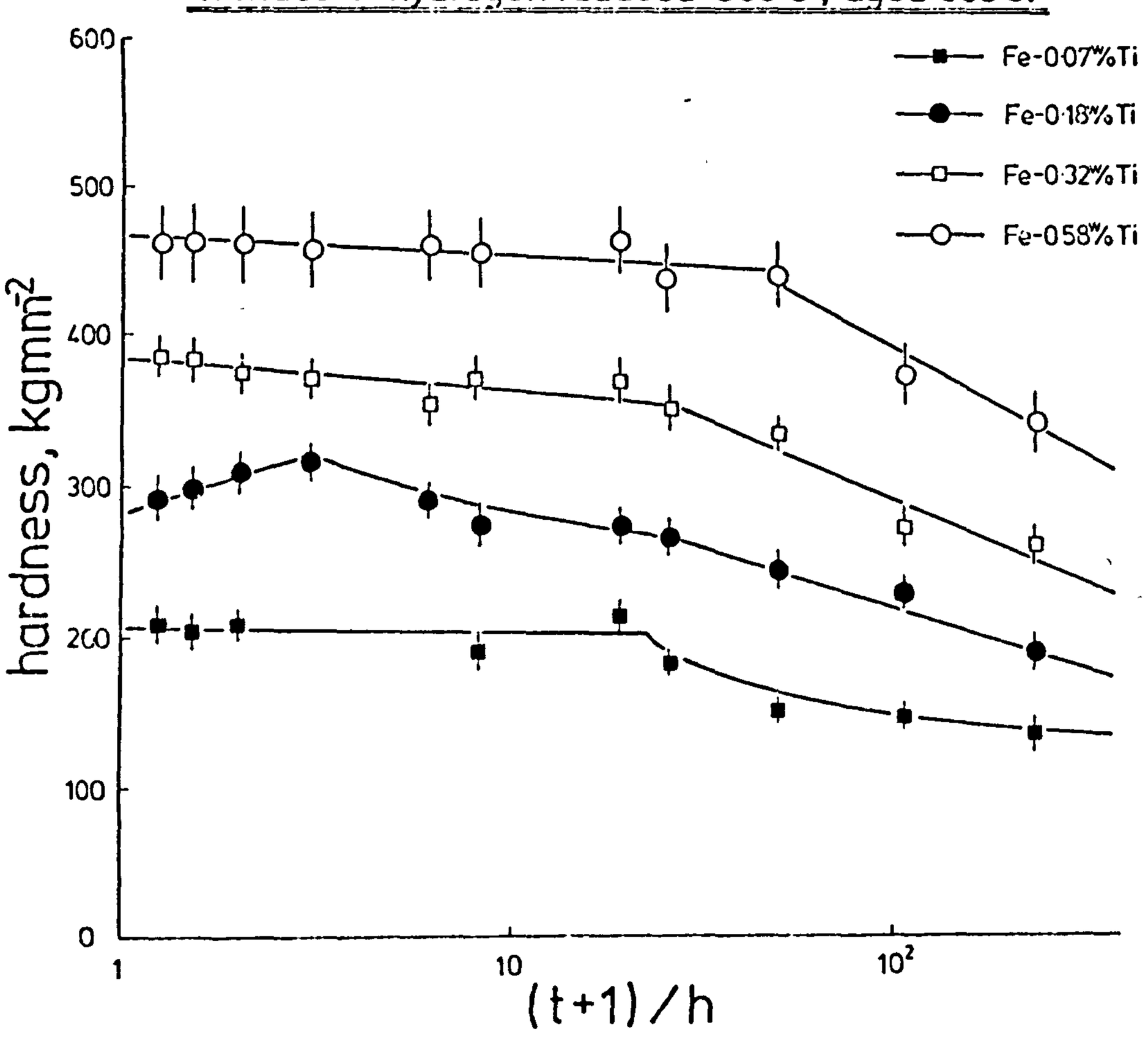
nitrided & hydrogen reduced 585°C , aged 800°C.
Fe-0·07%Ti
Fe-0·18%Ti
Fe-0·32%Ti
Fe-0·58%Ti
hardness, kgmm⁻²
600
500
400
300
200
100
0
1
10
10²
(t+1)/h

(b)

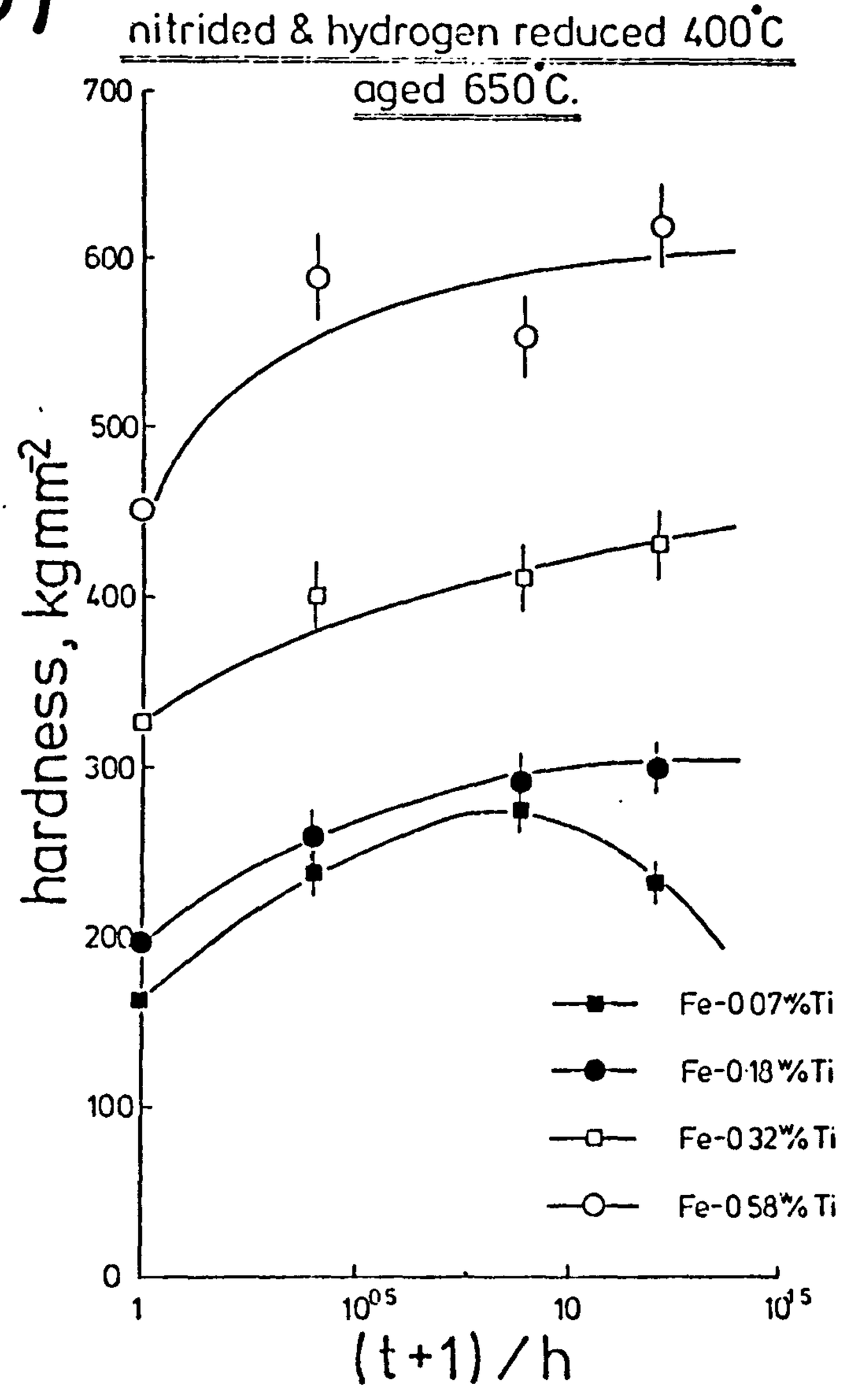
nitrided & hydrogen reduced 400°C
aged 650°C.
Fe-0·07%Ti
Fe-0·18%Ti
Fe-0·32%Ti
Fe-0·58%Ti
hardness, kgmm⁻²
700
600
500
400
300
200
100
0
1
10^0·5
10
10^1·5
(t+1)/h

nitriding and hydrogen reduction is performed at 585°C followed by aging at 800°C. The zone structure on nitriding at 400°C is therefore quite different from that at 585°C. If iron atoms are incorporated into the zone structure at low nitriding temperatures, its subsequent rejection on aging will cause a change in the obstacle strength and hence increase the resistance to cutting by glide dislocations. In addition, the dispersion of GP zones may change even though the chemical composition remains constant, again altering the force required to move a dislocation through the Ti-N clusters. For alloys containing >0.18 w/o Ti, the GP zones formed by nitriding and hydrogen reduction at 585°C are quite stable, the changes in zone composition and/or dispersion which occur at the commencement of aging at 800°C are small and no strength increases are observed. For alloys nitrided and hydrogen reduced at 400°C and aged at 650°C these changes are directly observed as strength increases.

Aging for longer times at 800°C (see Figure IX.10(a)) results in a change of slope in the hardness/time curves which suggests a change in hardening mechanism, i.e. a change from cutting to looping of obstacles by glide dislocations. The hardness values presented in Figure IX.10(a) were taken within a grain and reflect both the flow stress and work-hardening behaviour of the material and are related to the intergranular friction (σ_o).

Changes in the initial work-hardening rate (WHR) allow distinction to be made between the cutting of obstacles by glide dislocations, characterised by a low WHR, and Orowan looping which causes an increase in WHR. Figure IX.11 shows the changes in WHR which occur when Fe-0.18 w/o Ti, nitrided and hydrogen reduced at 585°C, is aged at 800°C. As in Figure IX.10, an initial increase in yield strength at short aging times is accompanied by a low WHR. As aging continues the yield strength falls continuously as the particles coarsen with a corresponding increase in WHR. These results indicate a gradual transition from a regime in which particles are cut by glide dislocations to an Orowan process where the particles become undeformable. The Orowan loops formed around the particles accumulate as strain proceeds, and eventually give rise to a high work-hardening rate. The change in slope indicated in Figure IX.10(a) therefore represents a change from a cutting to a looping type deformation of obstacles by glide dislocations.

As nitrided and hydrogen reduced Fe-0.18 w/o Ti is overaged important changes in the fracture behaviour result; see Figure IX.12. The material before aging (Figure IX.12(a)) fails by a mixture of transgranular cleavage and a small amount of micro-void coalescence. Aging for 1 h at 800°C results in larger proportions of micro-void coalescence (Figure IX.12(b)) which increases further until after 11.5 h only micro-void coalescence is

Figure IX.11

Variation in yield stress and work-hardening rate for Fe-0.18 w/o Ti nitrided in $7NH_3:93H_2$ at 585°C for 2.5 h, then hydrogen reduced at 585°C for 3 h and aged at 800°C.

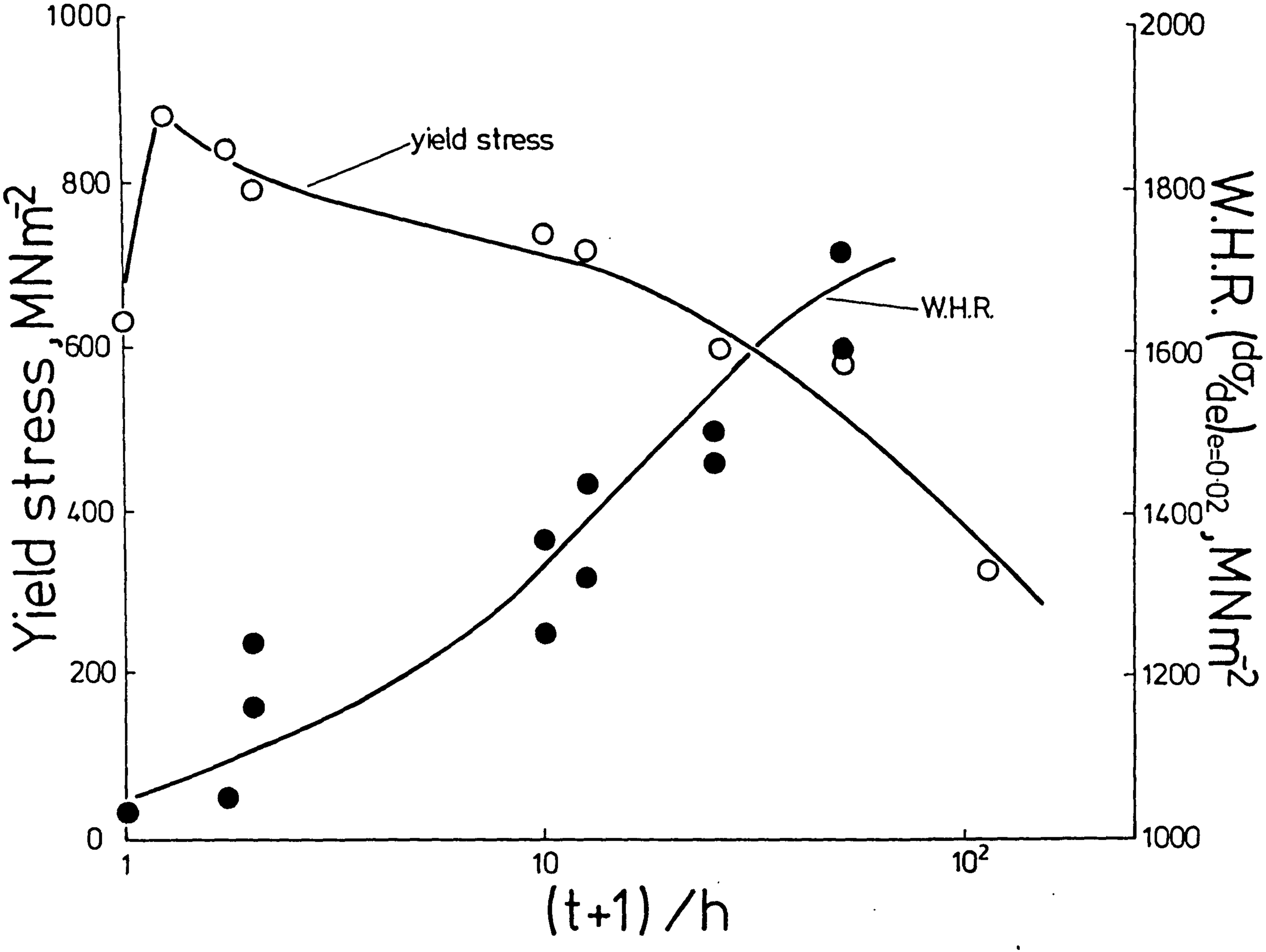
1000
800
600
400
200
0
Yield stress, MNm⁻²
yield stress
W.H.R.
2000
1800
1600
1400
1200
1000
W.H.R. (dσ/de)e=0·02, MNm⁻²
1
10
10²
(t+1)/h

Figure IX.12

Scanning electron micrographs of Fe-0.18 w/o Ti nitrided in $7NH_3:93H_2$ at 585°C for 2.5 h, then hydrogen reduced at 585°C for 3 h and aged at 800°C.

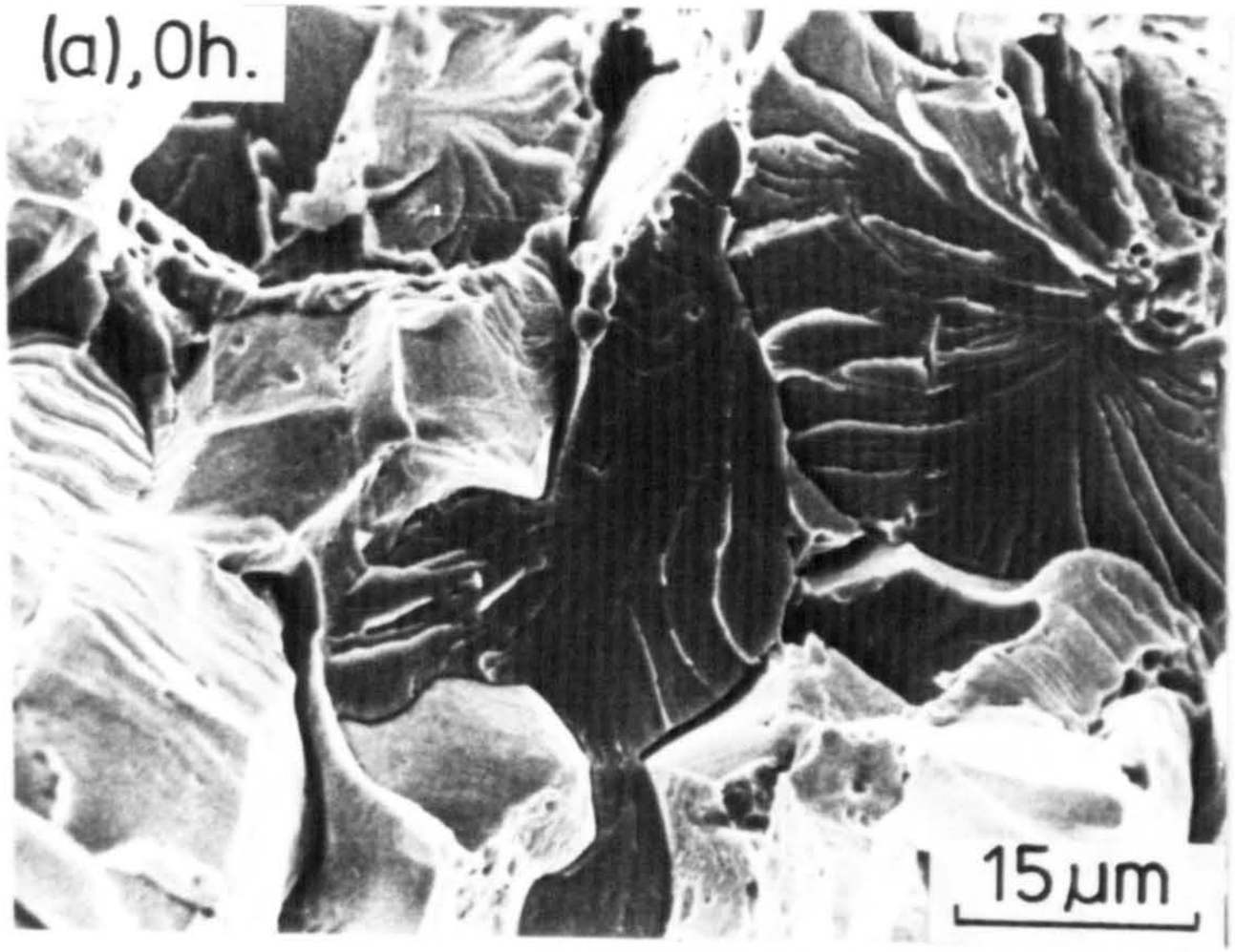
(a), 0h.
15 µm

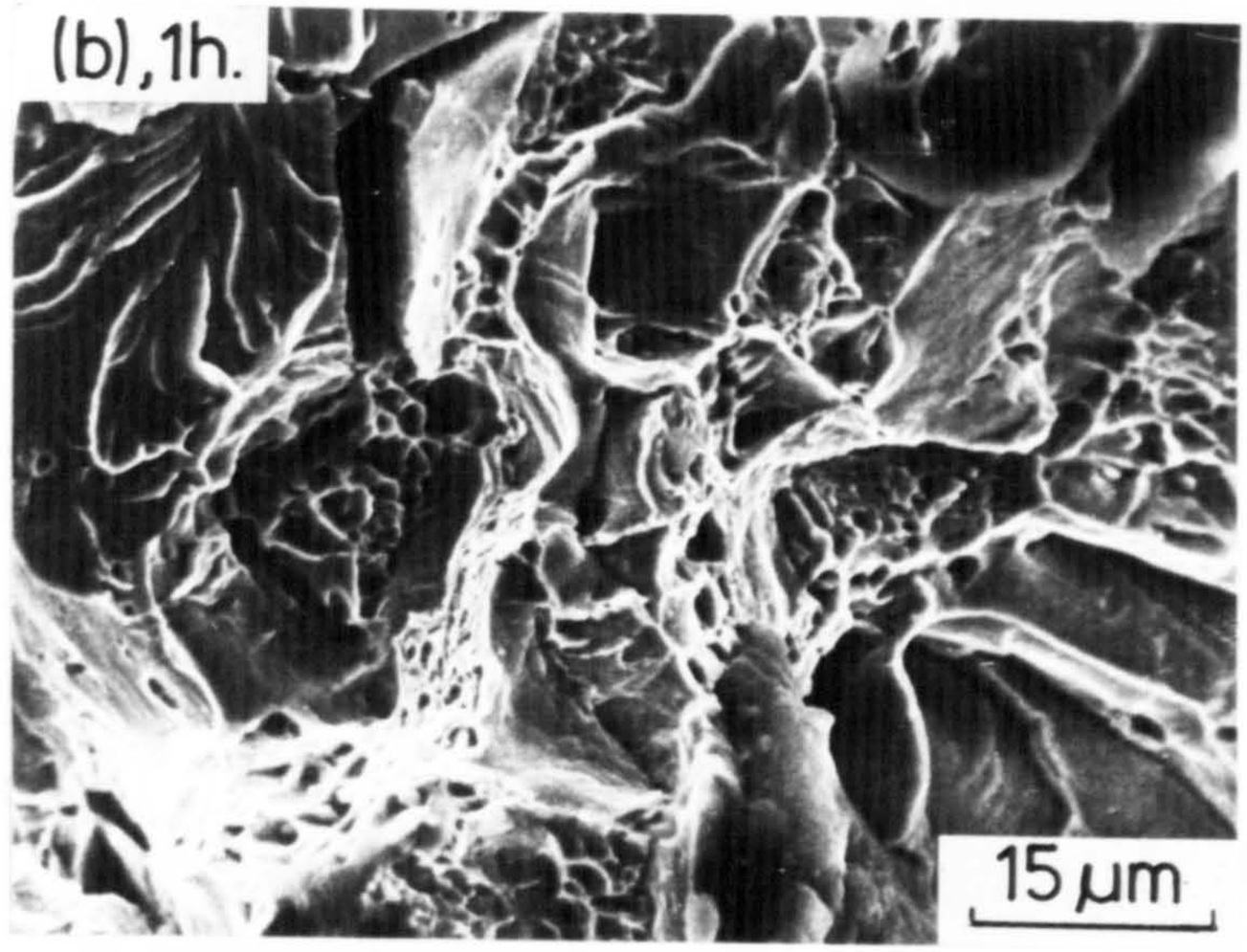
(b), 1h.
15 µm

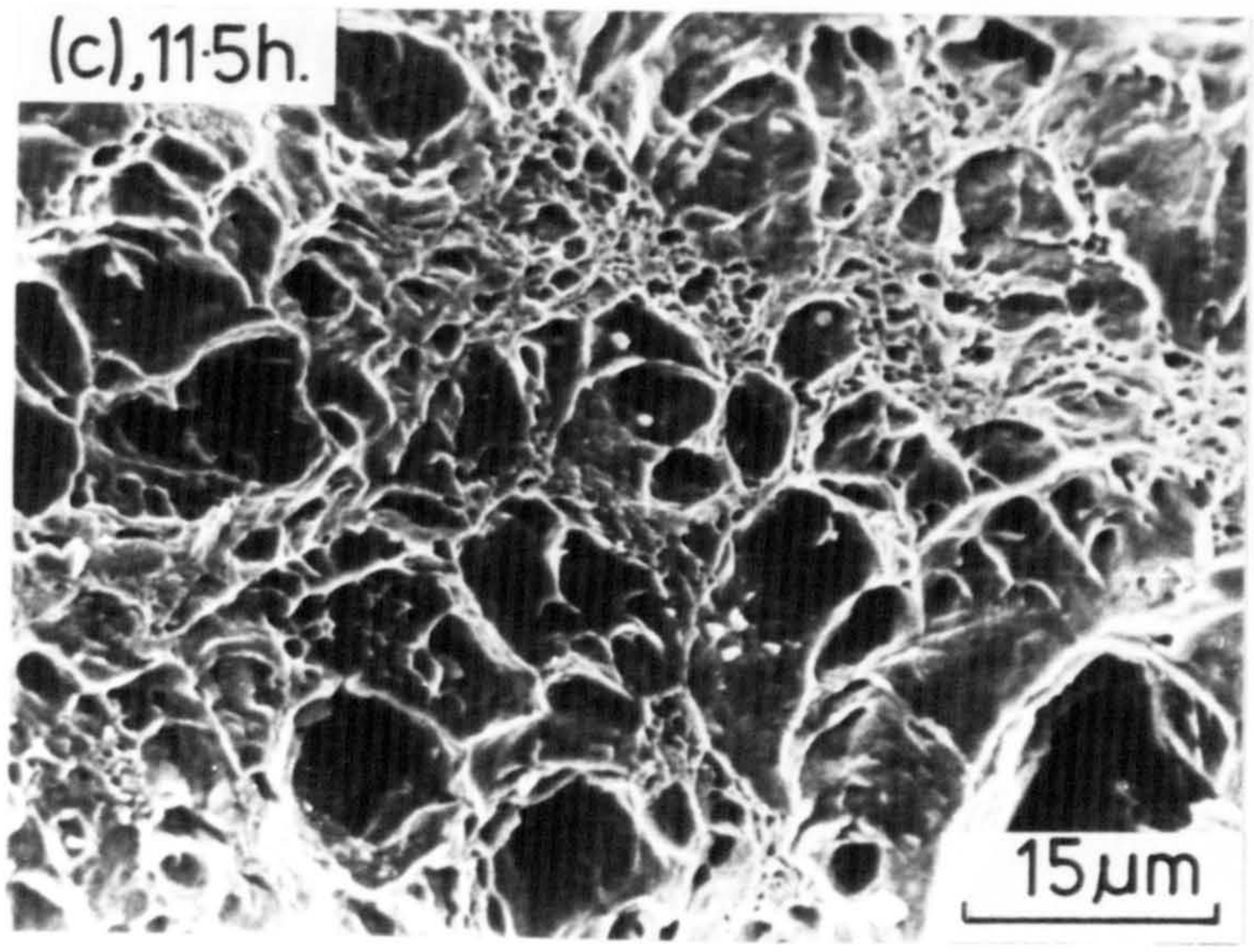
(c), 11·5h.
15 µm

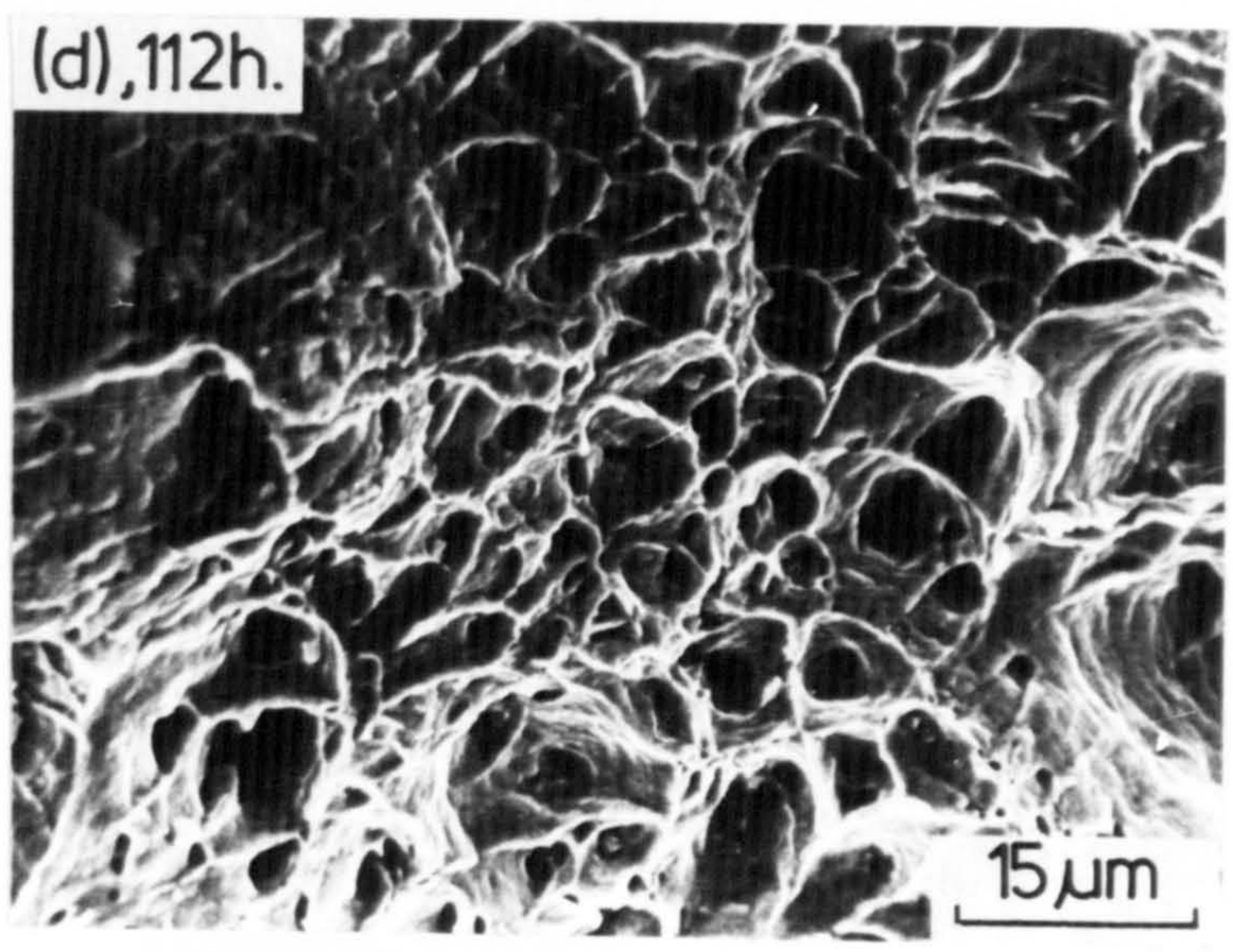
(d), 112h.
15 µm

observed; see Figure IX.12(c). However, the yield strength prior to aging and after aging for 11.5 h is approximately the same (see Figure IX.11) yet the fracture behaviours of the alloys are quite different. For as-nitrided materials or alloys aged for short times, glide dislocations cut the particles causing a reduction in particle resistance along the glide plane and, by making it easier for slip to continue on this plane, give a coarse slip distribution (Hornbogen & Zum Gahr, 1975). When combined with the high stresses necessary for plastic flow, this type of slip distribution causes a reduction in specimen ductility as measured by elongation in a tensile test; see Figures IX.12(a) and (b). Overaging causes glide dislocations to loop the particles and the Orowan loops harden the slip plane which causes the slip distribution to become finer with resulting increases in ductility; see Figure IX.12(c) and (d). The poor ductility which accompanies particle shear has also been observed by other investigators. For example, Jones (1976) in nitrided Fe-V alloys and Watson & Brown (1974) in age-hardened Fe-Si-Ti report reduced ductility when glide dislocations cut second-phase particles. In such systems crack nucleation occurs where slip bands intersect with one another and with grain boundaries. Similar effects have been observed in age-hardened Ti-Mo alloys by Gysler et al. (1974).

In the later stages of aging nitrided Fe-Ti alloys,

as mentioned above, the particles act as impenetrable barriers and force the dislocation to bow out and by-pass the obstacles. At this point it is possible to identify, by transmission electron microscopy, disc-shaped particles of titanium nitride. Figures IX.13(a) and (b) show bright and dark field images obtained by aging nitrided and hydrogen reduced Fe-0.32 w/o Ti for 50 h at 800°C. The $(200)_{TiN}$ reflection (streaked along <100> due to the thinness of the plates) was used to form the dark field image and the plate diameter is about 340 Å. If an Orowan relationship applies according to equation IX.6, the increase in yield stress compared with the annealed alloy should give a linear plot with the inverse of the planar spacing (L). As shown in Figure IX.14(a), where the mean free path Λ has been substituted for L, this is observed. The gradient (y) of the straight line is given by:

$$y = 0.8\ m_2\ Gb \cos(\varphi_c/2) \qquad \ldots\ IX.21$$

where $\varphi_c = 0$ for Orowan hardening and m_2 is the Schmid or Taylor factor which relates a tensile stress (σ) to a shear stress (τ); this factor lies between 2.2 and 3.1 (Kocks, 1970; Embury, 1971). Rewriting equation IX.21 with $\varphi_c = 0$ gives:

$$y = 0.8\ m_2\ Gb \qquad \ldots\ IX.22$$

The calculated gradient is in the range $3.8\text{-}5.4 \times 10^{-5}$ MN/m, the chief uncertainty being in the Taylor factor.

Figure IX.13

Transmission electron micrographs of Fe-0.32 w/o Ti nitrided in $7NH_3:93H_2$ at 585°C for 3 h, then hydrogen reduced at 585°C for 2.5 h and aged at 800°C for 50 h

(a) bright field, $\bar{g}$ = 200

(b) dark field of (a) using TiN reflection.

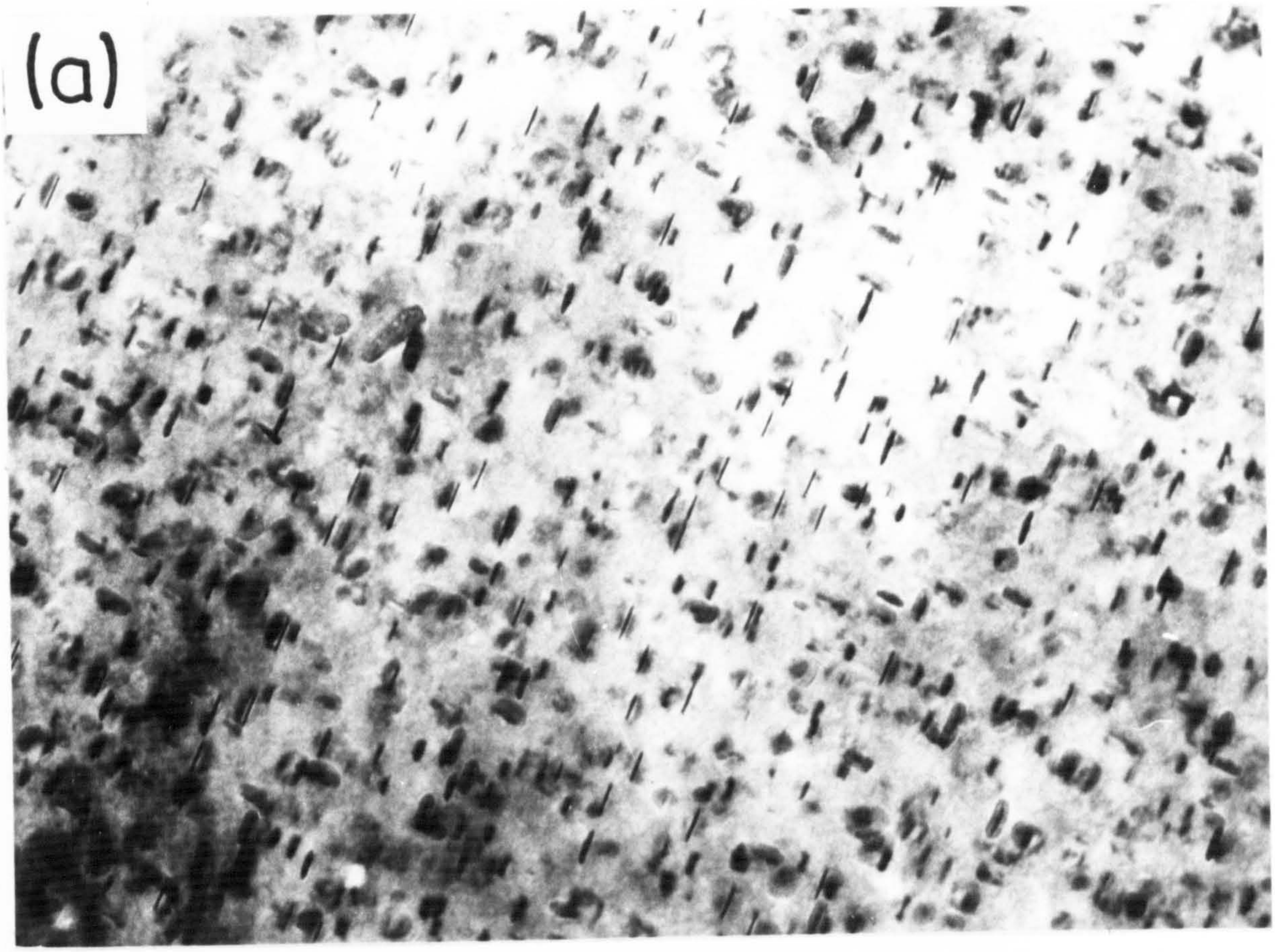

(001)

2000 A

Figure IX.14

Variation of (a) yield stress and (b) estimated friction stress with reciprocal mean free path (Λ), for Fe-Ti alloys nitrided and aged at high temperatures.

■——Chen (1965)
○——Hamano & Tsuya (1979)
●——Present investigation

(a)

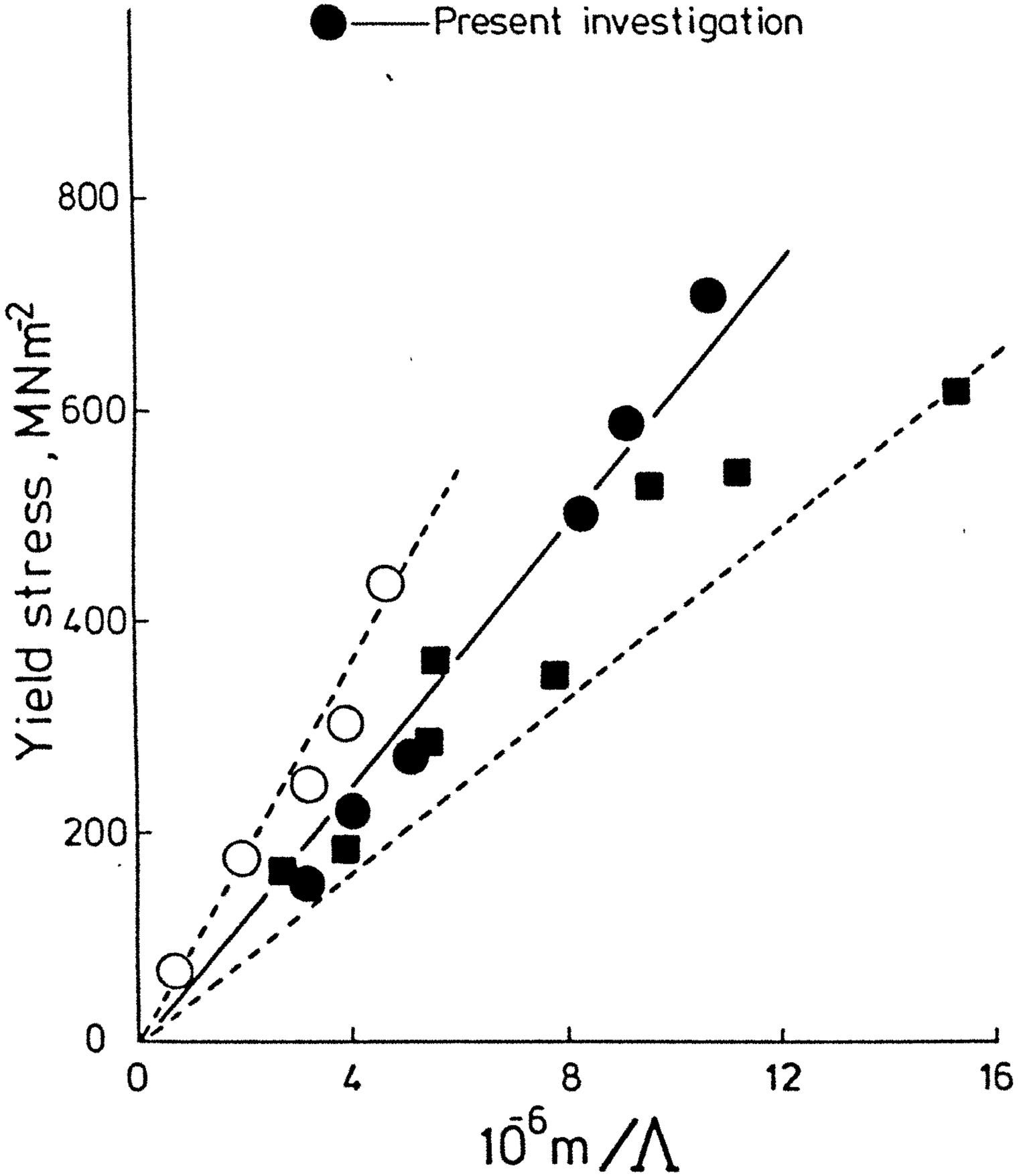

(b)

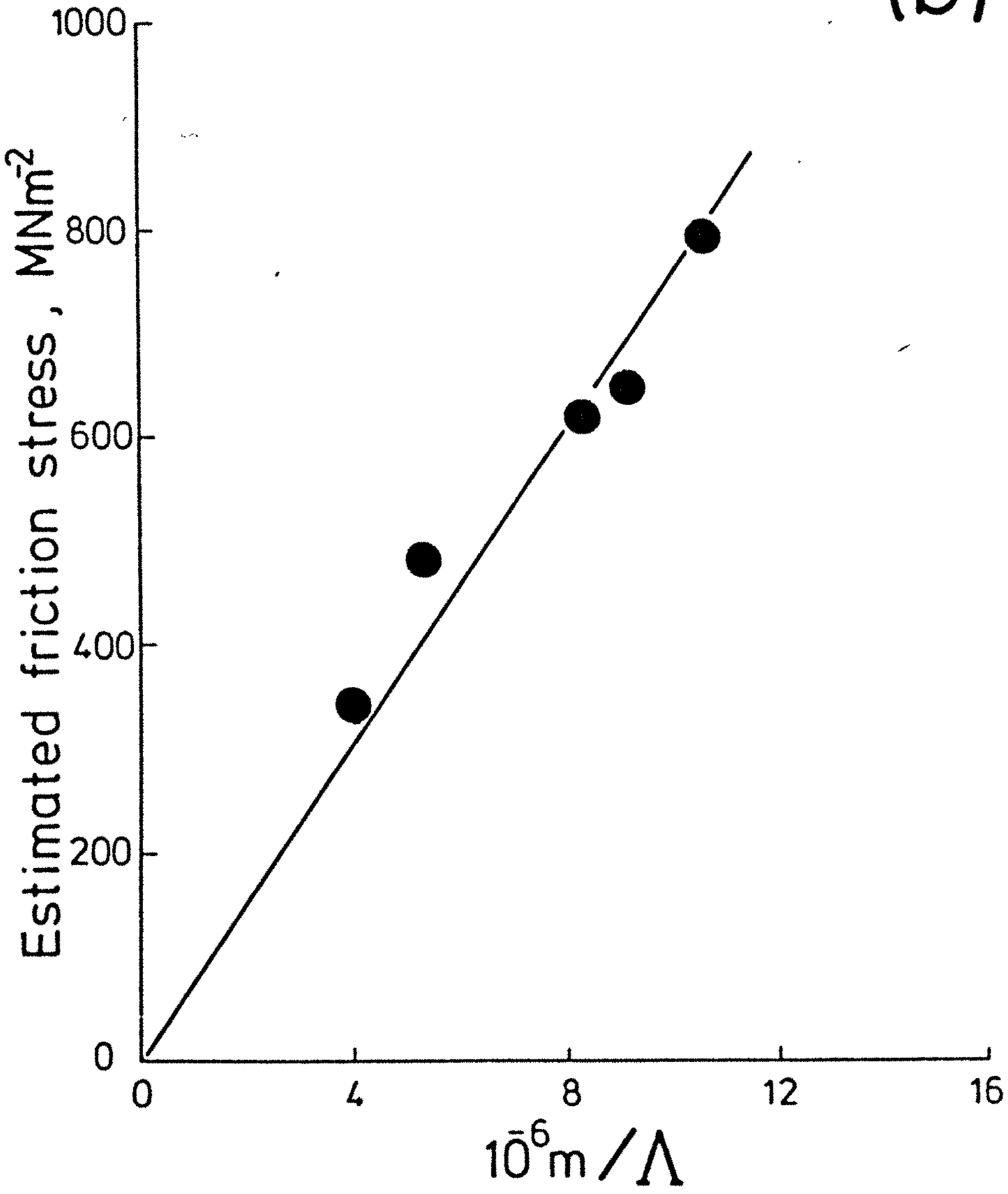

It is in reasonable agreement with the results of Chen (4.9×10^{-5} MN/m; 1965) and those of the present investigation (6.2×10^{-5} MN/m) but in poorer agreement with Hamano & Tsuya (8.4×10^{-5} MN/m; 1979). The increases in yield strength in the Orowan region can be calculated from an expression for disc-shaped particles equivalent to equation IX.9 developed by Hirsch & Humphreys (1969):

$$\Delta\tau = \frac{0.4}{\pi} \frac{Gb}{L(1-\upsilon)^{\frac{1}{2}}} \ln\left(\frac{X}{b}\right) \qquad \ldots \text{IX.23}$$

where X is a measure of the particle diameter intersecting the slip plane which, for aligned discs (Kelly, 1972), is:

$$X = 2D/\pi \qquad \ldots \text{IX.24}$$

Using a Taylor factor of 3.1 equation IX.23 combined with equation IX.24 gives the values of yield stress in Table IX.2 where the agreement between theory and experiment becomes progressively worse as the yield strength increases. Since the tests were carried out on polycrystalline specimens, a Hall-Petch equation is expected to apply and so variations in both σ_o and k_y will affect the yield stress. Although the effect of aging on k_y is usually neglected it might account for the differences between theory and experiment at high values of yield stress. Another factor may be the use of mean free path instead of interparticle spacing. Figure IX.14(b) attempts to

Table IX.2

Comparison between theory and experiment for nitrided iron-titanium alloys aged to give an Orowan hardening mechanism

$\Delta\tau$, MN/m^2, Theory	$\Delta\sigma$, MN/m^2, Theory	$\Delta\sigma$, MN/m^2, Experiment
143	445	710
126	390	585
84	260	500
88	273	270
69	214	220
55	170	150

overcome the problem of k_y variation by using microhardness measurements within single grains to estimate the variation in σ_o; the latter is related to hardness by the factor 3.9; see Section IX.3. As shown in Figure IX.14(b), a straight line is obtained when estimated friction stress is plotted against reciprocal mean free path (Λ) and its slope, 7.6×10^{-5} MN/m, is only slightly greater than that predicted by theory. The difference is expected because the estimated friction stress corresponds to some finite value of strain and hence is influenced by the different work-hardening rates characterized by particular particle dispersions. It seems therefore, that the only totally

satisfactory way of testing whether a particular strengthening mechanism agrees with experimental observations is to use single crystals.

IX.5 Temperature Dependence of Yield Strength in Fe-Ti-N Alloys

The increases in microhardness on nitriding and hydrogen reduction of iron-titanium alloys when plotted against the square root of atomic percentage titanium gives a straight line; see Figure IX.15 which includes previous Newcastle results (Henderson, 1976). Similar behaviour is reported by Kirkwood et al. (1974). This dependence of strength on volume fraction may occur for several of the possible sources of hardening by deformable particles given at the beginning of the present chapter, e.g. coherency, modulus, and chemical hardening. Thus, in order to differentiate between these three alternatives it is necessary to consider the temperature dependence of yield strength.

Figure IX.16 shows the variation of yield strength with temperature for polycrystalline Fe-Ti alloys nitrided and hydrogen reduced at 585°C to give Ti-N clusters. The plot can be divided into three distinct regions labelled (a), (b) and (c). In region (a) there is a strong dependence of yield stress on temperature identical to that observed when testing pure iron (Christian, 1970) or

Figure IX.15

Increase in microhardness against square root of atomic percentage titanium for alloys nitrided in $7NH_3:93H_2$ at 585°C and hydrogen reduced at 585°C.

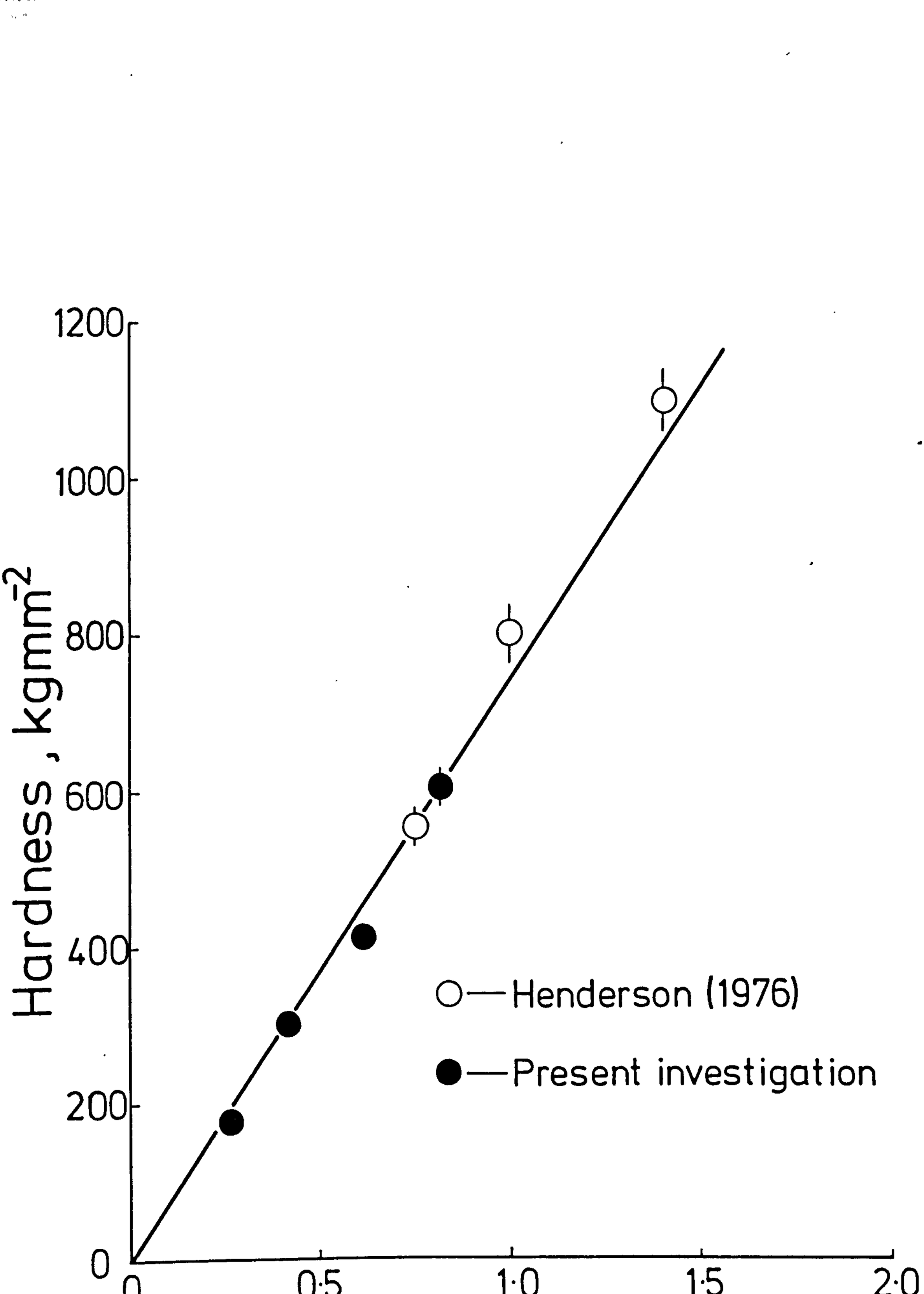
Hardness, kgmm-2
1200
1000
800
600
400
200
0
0
0·5
1·0
1·5
2·0
(Ti, a%)1/2
○—Henderson (1976)
●—Present investigation

Figure IX.16

Temperature dependence of yield stress for polycrystalline Fe-Ti alloys.

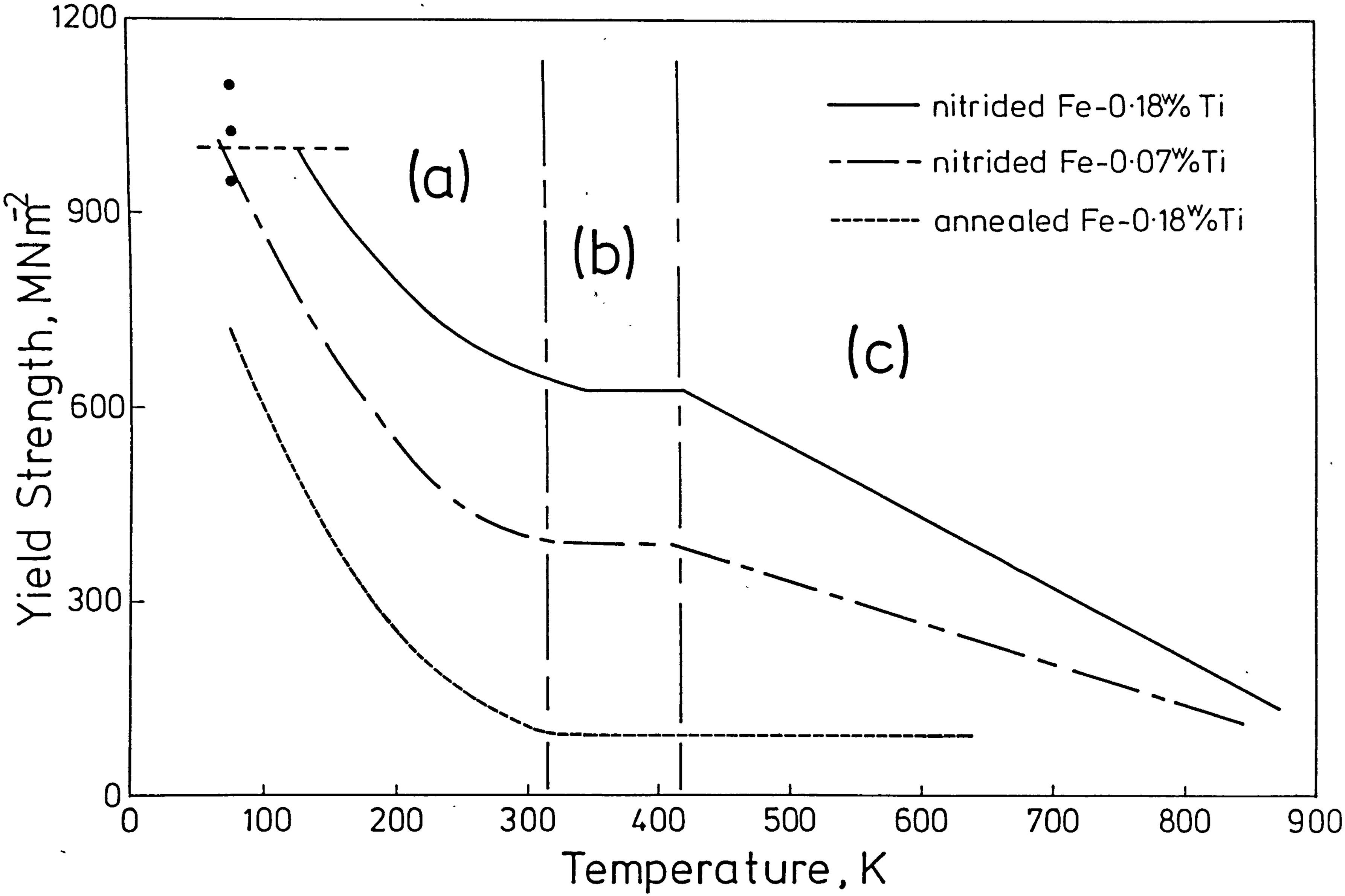
1200
900
600
300
0
Yield Strength, MNm⁻²
(a)
(b)
(c)
nitrided Fe-0·18% Ti
nitrided Fe-0·07%Ti
annealed Fe-0·18%Ti
0
100
200
300
400
500
600
700
800
900
Temperature, K

annealed Fe-0.18 w/o Ti, and is due to the Peierls-Nabarro force for body-centred cubic iron. Note that at 77°K no yield was observed for Fe-0.18 w/o Ti due to brittle grain boundary failure. The present results and those of Spitzig (1981) show that the hardening which results from nitriding Fe-Ti alloys is linearly additive to the lattice friction stress, in agreement with the views of Orowan (1954). In region (b) the yield stress is independent of temperature, but as the temperature is increased a third region (c) is observed where the yield strength again varies with temperature. This latter region is similar to that observed by Jones et al. (1979) for nitrided Fe-0.15 w/o V and attributed by these authors to the thermal activation of chemical-bond rupture in the substitutional-interstitial mixed clusters formed by nitriding. However, the (c) regions of the curves shown in Figure IX.16 suggest thermal activation of an unlocking process (the k_y effect; see Section IX.3) in addition to the temperature dependence resulting from dislocation glide over localised obstacles and it is impossible to separate these two thermally activated processes. Therefore, without resorting to single crystals, information relating to the temperature dependence of yield strength for a matrix containing a particular distribution of particles can be obtained only from the effect of temperature on the friction stress, obtained from a grain size analysis, or by using microhardness measurements within single grains of a polycrystal.

For a range of Fe-Ti alloys nitrided and hydrogen reduced at 585°C the change in microhardness with temperature is shown in Figure IX.17. Clearly, there is a very marked temperature dependence of flow stress. Of the mechanisms listed in Section IX.1(b), only chemical strengthening should be accompanied by a strong temperature dependence. The results of Figure IX.17 therefore confirm the suggestions made by Kirkwood et al. (1974) and Henderson (1976), and the experimental work of Jones et al. (1979), that a chemical strengthening mechanism accounts for the high strengths of nitrided materials. The modulus model proposed by Spitzig (1981) does not account for the observed temperature dependence of yield strength. Since this dependence changes with the distribution of Ti-N zones in the material, an increased titanium concentration at a constant nitriding temperature gives a finer distribution of zones and hence an increased temperature dependence; this is also observed in Figure IX.17.

Further evidence that the obstacles formed on nitriding Fe-Ti alloys are short-range (chemical hardening) and not long-range (modulus and coherency hardening), is obtained from the analysis in terms of thermal activation theory of the data given in Figure IX.17. The shape of the obstacle profile is determined by the quantities p and q in equation IX.12:

Figure IX.17

Change in microhardness with temperature for Fe-Ti alloys nitrided in $7NH_3:93H_2$ at 585°C for 18 h, then hydrogen reduced 585°C for 18 h.

nitrided & hydrogen reduced

—■— Fe-0·07^{w}%Ti

—●— Fe-0·18^{w}%Ti

—□— Fe-0·32^{w}%Ti

—○— Fe-0·58^{w}%Ti

change in hardness, kgmm^{-2}

700
600
500
400
300
200
100
0

300
500
700
900

Temperature, K

$$\Delta G = F_o \left\{ 1 - \left(\frac{\sigma}{\hat{\tau}} \right)^p \right\}^q \qquad \ldots \text{ IX.12}$$

and of the interaction profiles available in the literature (Ono, 1968), two appear to approximate to the force/area profile experienced by a dislocation as it approaches a Ti-N cluster. The first is the Fleischer potential, Figure IX.18(a), which may be expressed as:

$$\Delta G = F_o \left\{ 1 - \left(\frac{\sigma}{\hat{\tau}} \right)^{\frac{1}{2}} \right\}^2 \qquad \ldots \text{ IX.25}$$

and which gives a linear $\sigma^{\frac{1}{2}}/T^{\frac{1}{2}}$ plot, neglecting the variation in obstacle spacing with applied stress. The second is the Mott-Nabarro potential, Figure IX.18(b), expressed as:

$$\Delta G = F_o \left\{ 1 - \left(\frac{\sigma}{\hat{\tau}} \right) \right\}^{3/2} \qquad \ldots \text{ IX.26}$$

giving a linear $\sigma^{2/3}/T^{2/3}$ plot if the variation in obstacle spacing with applied stress is taken into account. Both potential expressions give straight lines in their respective experimental σ/T plots, showing that the interactions which occur in as-nitrided material are short-range and confirming that chemical hardening makes a major contribution to the strength of nitrided Fe-Ti alloys. As shown previously in the present chapter, aging the as-nitrided structure at high temperature leads to a change from cutting to a by-passing mechanism, and Figure IX.19 shows that this change is accompanied by a gradual loss in

Figure IX.18

Stress/temperature relationships for the experimental results of Figure IX.17.

(a) Fleischer potential

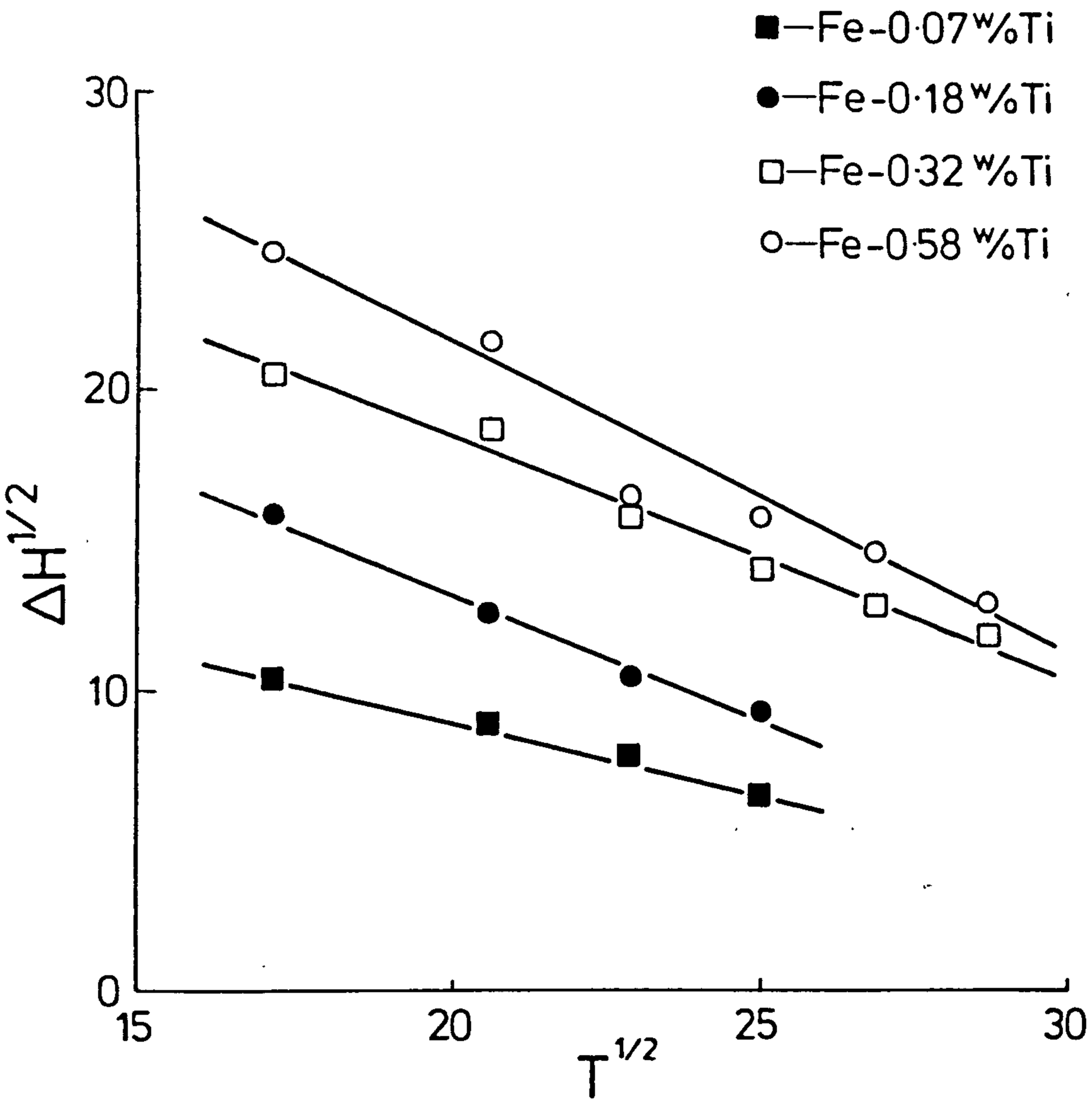

(b) Mott - Nabarro potential

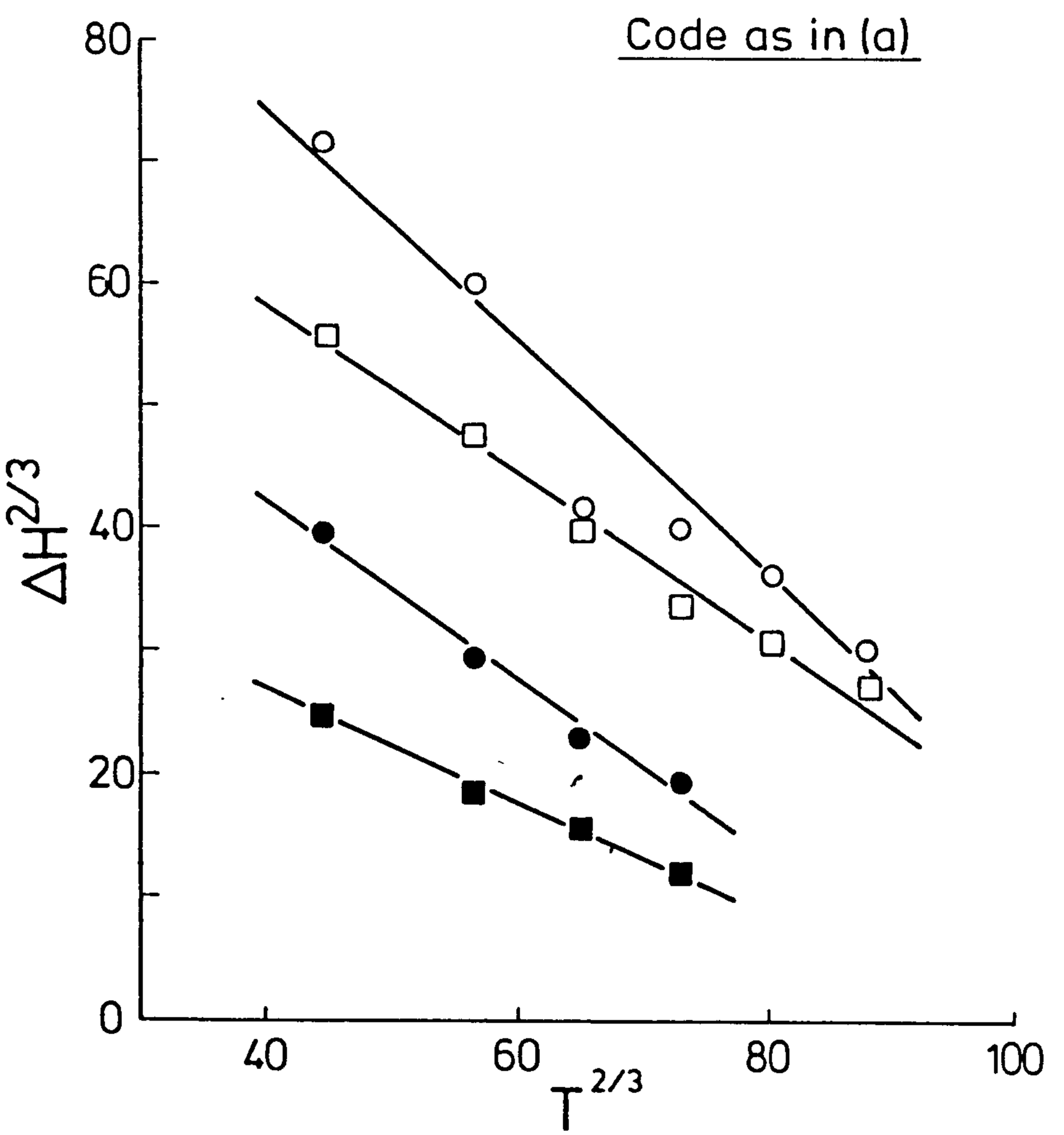

Figure IX.19

Change in hardness against temperature for Fe-0.18 w/o Ti nitrided in $7NH_3:93H_2$ at 585°C for 2.5 h, then hydrogen reduced 585°C for 3 h and aged at 800°C for the times indicated.

nitrided & hydrogen reduced
Fe-0·18^{w}% Ti aged 800°C.

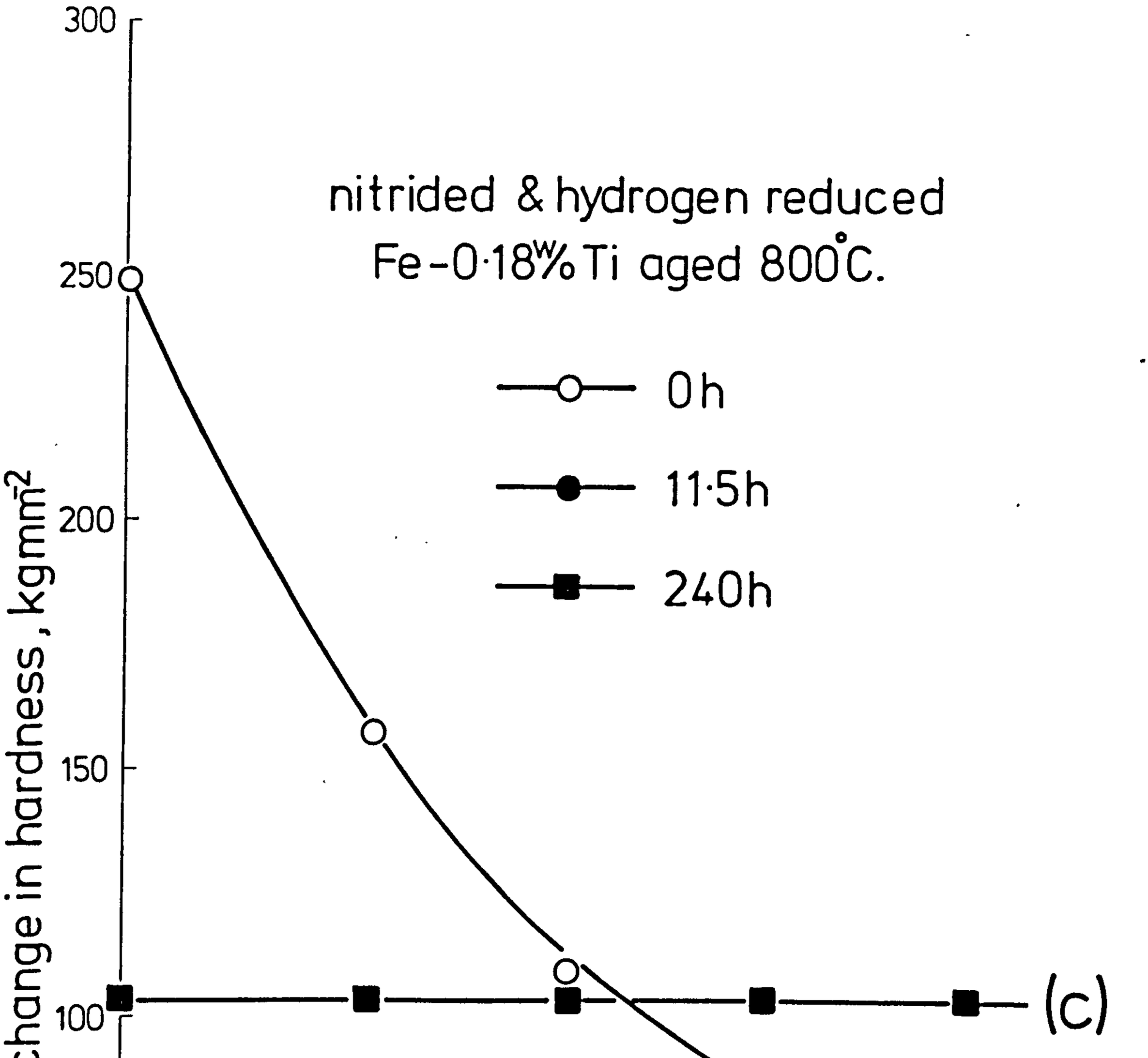

temperature dependence of yield stress. Any temperature dependence of yield strength for the Orowan process, Figure IX.19(c), arises from variations of elastic moduli with temperature and is therefore slight.

IX.6 Strengthening Mechanisms - General Discussion

The initial strengths of nitrided iron-titanium alloys are remarkably high for such small volume fractions and correspond to 4500 MN/m^2 per a/o Ti. This is much higher than solid-solution strengthening due to interstitial nitrogen in body-centred cubic iron, i.e. 575 MN/m^2 per a/o N (Baird & Jamieson, 1966; Bergstrom & Roberts, 1972). Due to the complex nature of the structure it seems that more than one mechanism is likely to control the flow stress. Of the cutting processes, coherency strengthening, modulus strengthening and chemical strengthening have all been proposed as major contributors and it is therefore relevant to calculate the relative contributions of these mechanisms to the total yield strength of the material. In these calculations a Taylor factor of 3.1 is used, giving maximum values to the strength increments which may result for any particular mechanism.

(a) Coherency hardening.

An estimate of coherency hardening can be made by regarding the stress field around the particle as being

equivalent to a loop of edge dislocation. According to Saada (1960), the force required to move a dislocation through the particle is then equivalent to that required to move it through a forest of dislocations intersecting the slip plane. The applied stress is given by:

$$\Delta\tau = \frac{Gb_p}{5\ell} \qquad \ldots \text{ IX.27}$$

where ℓ is the average separation of fixed dislocations threading the glide plane, b_p is their Burgers vector (taken to be the discontinuity in elastic displacement obtained when a Burgers circuit is made through the particle and matrix) and G is the shear modulus.

An estimate of b_p can be obtained by imaging the Ti-N clusters in a {100} matrix zone with $\bar{g}$ = 200 to give Ashby-Brown strain contrast (Ashby & Brown, 1963a,b) with a line of no contrast perpendicular to $\bar{g}$. In Table IX.3 the strengthening due to coherency hardening for two values of plate thickness (t) are given. Although the results are dependent on the value of t, they indicate coherency hardening has its greatest influence at small particle sizes. When the particles coarsen the contribution from coherency hardening falls quickly and accounts for about 15-30% of the total strength increment observed in Fe-0.18 w/o Ti nitrided at 650°C.

(b) Modulus hardening.

It is suggested by Spitzig (1981) that modulus

Table IX.3

Estimates of the hardening to be expected from a coherency model in nitrided Fe-Ti alloys

Zone Parameters	$\Delta\tau$, MN/m^2 Theory	$\Delta\sigma$, MN/m^2 Theory	$\Delta\sigma_o$, MN/m^2 Expt.	$\frac{\Delta\sigma_o(\text{Theory})}{\Delta\sigma_o(\text{Expt.})}$;%
D = 120 Å, t = b, b_p = 0.5 Å	38	120	420*	29
D = 120 Å, t = 10 Å, b_p = 0.5 Å	24	73	420*	17
D = 40 Å, t = b, b_p = 1 Å	166	515	430**	100
D = 40 Å, t = 10 Å, b_p = 1 Å	82	245	430**	57

*Value of friction stress estimated from grain size analysis.

**Value of friction stress estimated from yield stress with k_y = 1 $MN/m^{3/2}$.

hardening when combined with coherency hardening accounts for the total strengthening in nitrided Fe-Ti alloys. Although modulus hardening has been used to explain the strengthening in several systems e.g. Fe-Cu (Russell & Brown, 1972; Kelly, 1973) and Al-Zn-Mg (Melander & Persson, 1978), its temperature dependence results from the variation of the elastic moduli of matrix and precipitate with temperature, this variation being small. It seems improbable that such a mechanism could account for the strong temperature dependence of yield strength observed in the present work. However, it is interesting to calculate the strengthening which could be expected from modulus hardening. Due to the lack of a rigorous analysis for disc-shaped particles, the equation due to Kelly (1973) for spheres of radius (r) will be used and should be valid for small zones (Melander & Persson, 1978):

$$\Delta\tau = \frac{\Delta G}{4\pi^2}\left(\frac{3\Delta G}{Gb}\right)^{\frac{1}{2}}\left[0.8 - 0.143\ \mathrm{In}\ \left(\frac{r}{b}\right)\right]^{3/2} r^{\frac{1}{2}} f^{\frac{1}{2}} \quad \ldots \text{ IX.28}$$

where ΔG is the difference in shear modulus between matrix and precipitate and G is the matrix shear modulus.

Using accepted values of the shear moduli, for 40 Å particles the strength increment due to a modulus effect is about $\Delta\tau \approx 35\ MN/m^2$ corresponding to a tensile stress of 110 MN/m^2. An additional estimate can be made using an equation derived by Melander & Persson (1978), which

gives an increment in yield stress of 150 MN/m^2. Thus, modulus hardening could account for about 30% of the observed strength increases in nitrided Fe-0.18 w/o Ti.

(c) Chemical hardening.

The stress required to force dislocations through deformable spherical particles at room temperature (Kelly & Nicholson, 1963) has been modified by Stephenson (1973b) for disc-shaped particles to give:

$$\Delta\tau = \frac{2\gamma_p}{b}\left(\frac{ft}{D}\right)^{\frac{1}{2}} + \left(\frac{f}{Dt}\right)^{\frac{1}{2}}\left\{\frac{(b.n)\gamma_s}{b} + \frac{G\ b\ \cos^2\alpha}{2}\right\} \quad \ldots \text{IX.29}$$

where γ_p is the internal interface energy, γ_s the surface energy, n the unit vector of the matrix lattice and α the angle between the dislocation line and its Burgers vector.

The first term in equation IX.29 is due to disordering and is known as chemical or order hardening. The remaining terms are due to (i) the creation of a new surface interface, that is, surface hardening, and (ii) the energy required to increase the length of the dipole of edge dislocation arising from production of jogs when the dislocation enters the particle. In a chemical strengthening model all energy terms are small relative to γ_p, the energy required to shear bonds within the particle.

In order to obtain an estimate for the increase in

yield strength due to chemical hardening a value of γ_p can be obtained from the data given in Figure IX.17. Considering the Fleischer potential which may be expressed as:

$$\left(\frac{\sigma}{\hat{\tau}}\right)^{\frac{1}{2}} = 1 - \left(\frac{T}{T_o}\right)^{\frac{1}{2}} \qquad \ldots \text{IX.30}$$

where σ is the yield strength at temperature T, $\hat{\tau}$ is the yield stress at 0^oK, and T_o is the temperature at which the obstacle can be overcome by thermal fluctuations alone. At 0^oK the following equation applies:

$$v.\hat{\tau} = F_o = \gamma_p \, \delta A \qquad \ldots \text{IX.31}$$

where F_o is related to the work expended during yielding in the creation of new surface area (δA), and v is the activation volume. The average area intersected by a random cross-section through a matrix containing a dispersion of disc-shaped particles of diameter (D) and thickness (t) is Dt (Fullman, 1953) and by putting $v = \ell b^2$, where ℓ is the separation of particles on the slip plane, equation IX.31 may be written as:

$$\gamma_p = \frac{\hat{\tau} \ell b^2}{Dt} \qquad \ldots \text{IX.32}$$

By converting the hardness values in Figure IX.17 to friction stresses as before, the value of γ_p calculated from equation IX.32 lies in the range 0.62-1.10 J/m^2. To check these values an additional estimate of γ_p was

obtained from the temperature dependence of yield stress from Figure IX.16, neglecting thermal activation of k_y, and gave γ_p = 0.94 J/m^2. If the temperature dependence of k_y is taken into account the value of γ_p is 0.75 J/m^2. These are maximum values of γ_p since they are based on the assumption that chemical strengthening is the only mechanism operating. If a value of γ_p equal to 1 J/m^2 is assumed, substituting the data from Table IX.3 into equation IX.29 results in calculated strength increments which can account for at least 50% of those observed, see Table IX.4. The experimental results of Spitzig (1981) can also be interpreted using a chemical model.

Table IX.4

Estimates of the hardening to be expected from a chemical model in nitrided Fe-Ti alloys

Zone Parameters	$\Delta\tau$, MN/m^2 Theory	$\Delta\sigma$, MN/m^2 Theory	$\Delta\sigma_o$, MN/m^2 Expt.	$\frac{\Delta\sigma_o \text{ (Theory)}}{\Delta\sigma_o \text{ (Expt.)}}$; %
D = 120 Å t = b	57	180	420	43
D = 120 Å t = 10 Å	115	360	420	86
D = 40 Å t = b	98	305	430	71
D = 40 Å t = 10 Å	200	620	430	100

Again, taking a value of γ_p = 1 J/m^2 and the zone parameters given by Spitzig (1981) the calculated increase in the shear stress is 16.5 MN/m^2 or 66% of the observed strength increment. The values of γ_p calculated for nitrided Fe-Ti alloys are similar to those found in other precipitation hardening systems: 0.53-1.53 J/m^2 in Al-Cu (Boyd & Nicholson, 1971); 0.50-1.28 J/m^2 in Fe-Si-Ti (Schwartz & Ralph, 1969; Brown & Whiteman, 1969); 1.30-1.70 J/m^2 in nitrided Fe-V (Jones et al., 1979).

The strengthening of Fe-Ti alloys can therefore be accounted for predominately by chemical hardening, which explains the marked temperature dependence of yield strength, together with a possible contribution from coherency hardening at small particle sizes.

IX.7 Electron Metallography of Deformed Alloys

The dislocation structures observed in alloys strengthened by second-phase particles are a consequence of the dislocation-particle interactions which take place during deformation. By transmission electron microscopy the interaction, distribution and character of dislocations can be observed directly and related to the mechanical properties of the material.

In Figure IX.20 the deformation structure in annealed Fe-0.18 w/o Ti, strained one percent at liquid nitrogen temperature, is compared with the structures of the same

Figure IX.20

Transmission electron micrographs of Fe-0.18 w/o Ti

(a) annealed; deformed 1% at -196°C; $\bar{g}$ = 110

(b) nitrided in $7NH_3$:$93H_2$ at 585°C; hydrogen reduced at 585°C; deformed 1% at -96°C; $\bar{g}$ = 110

(c) as in (b) but deformed 1% at 23°C; $\bar{g}$ = 110

(d) as in (b) but deformed 1% at 300°C; $\bar{g}$ = 110.

(a)

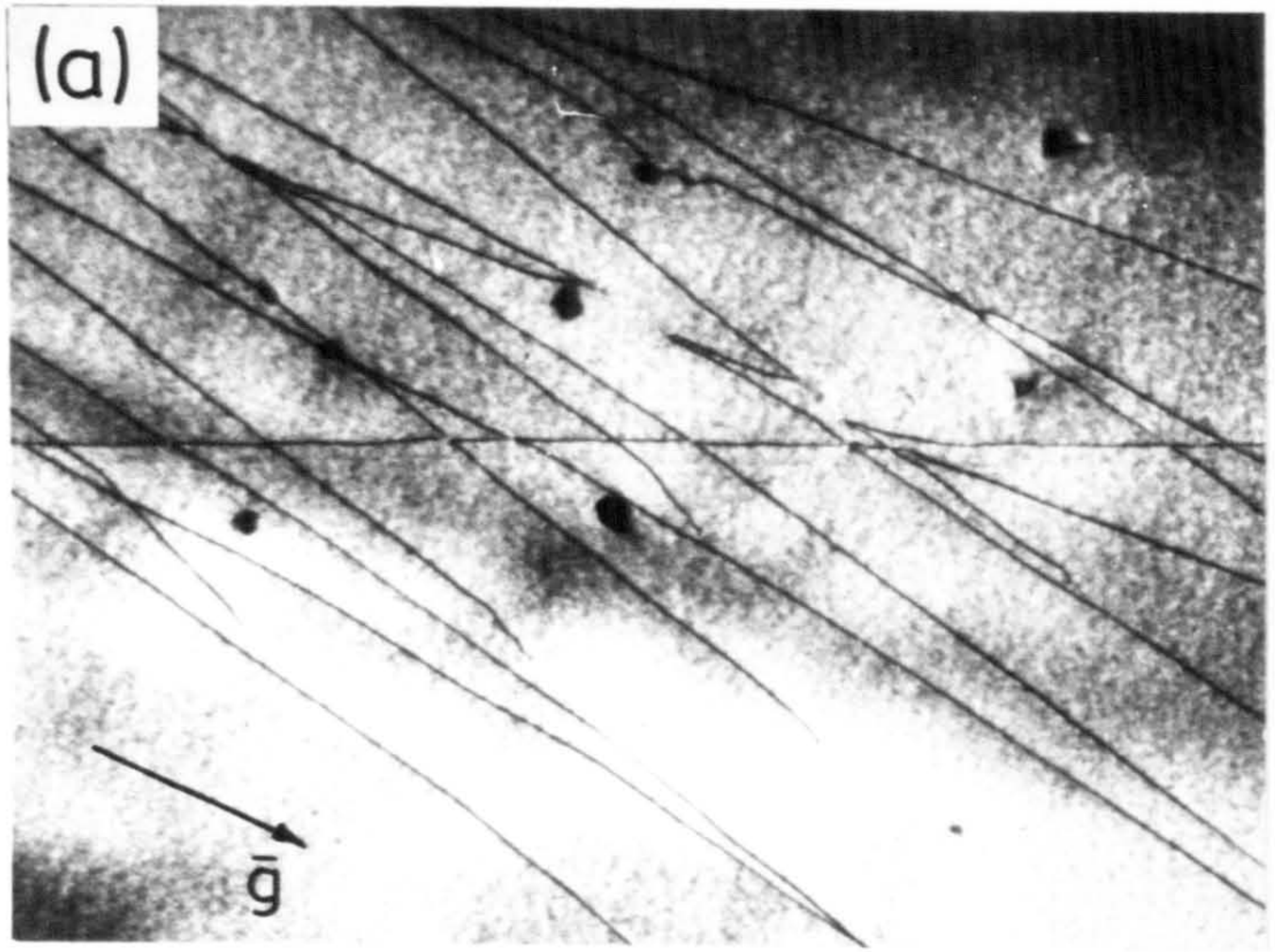

(b)

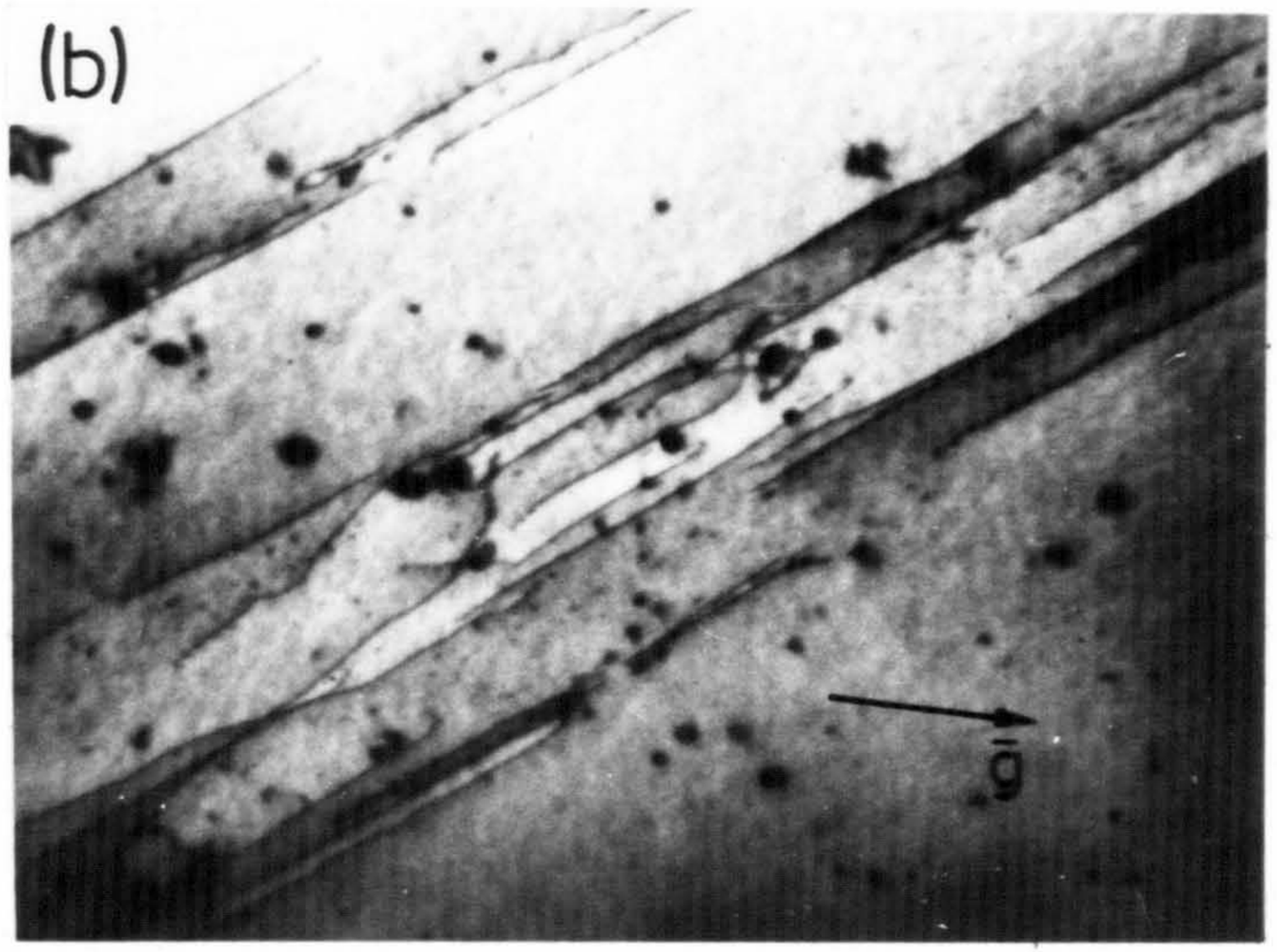

(111)

5000 Å

(c)

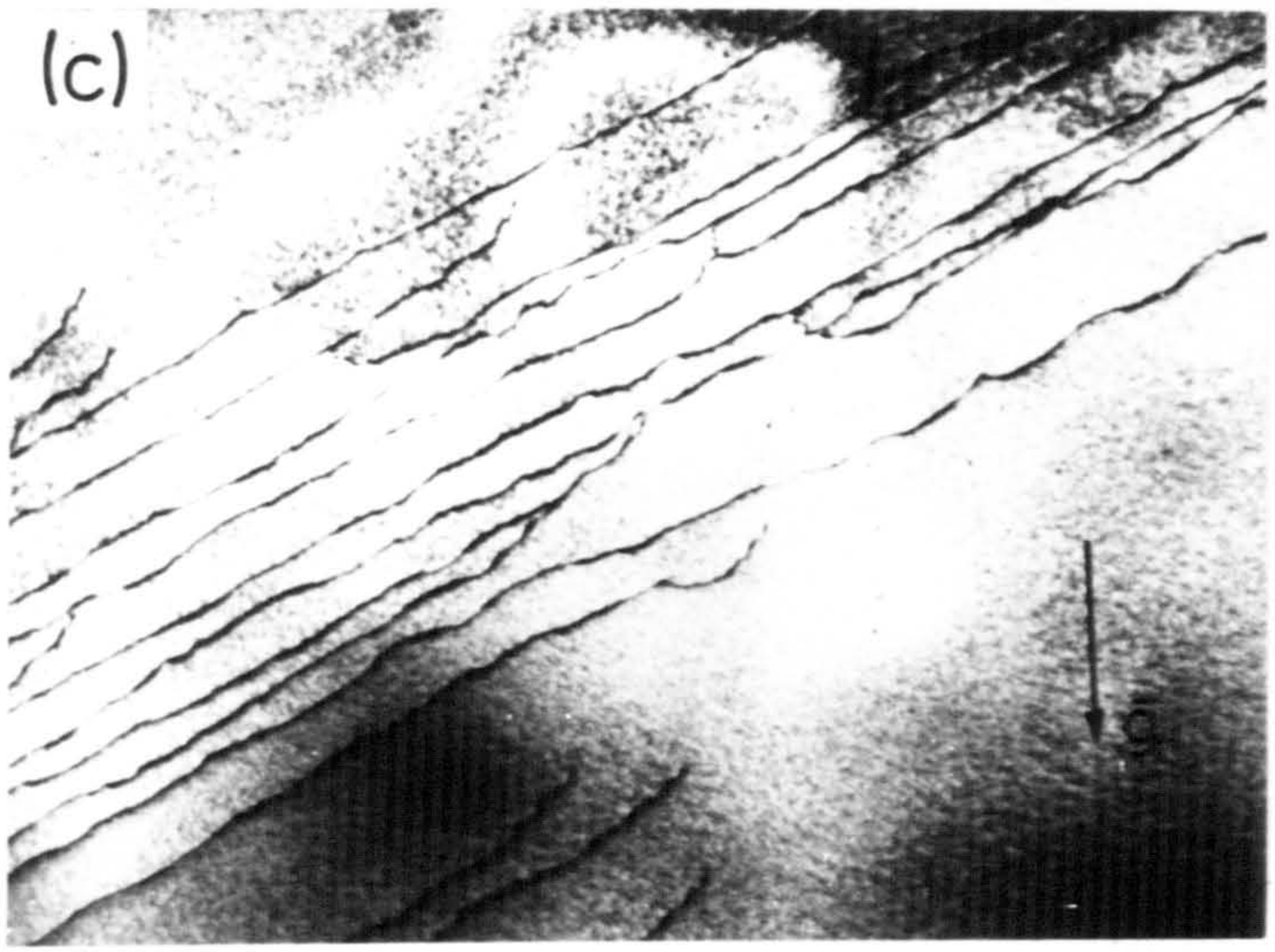

(d)

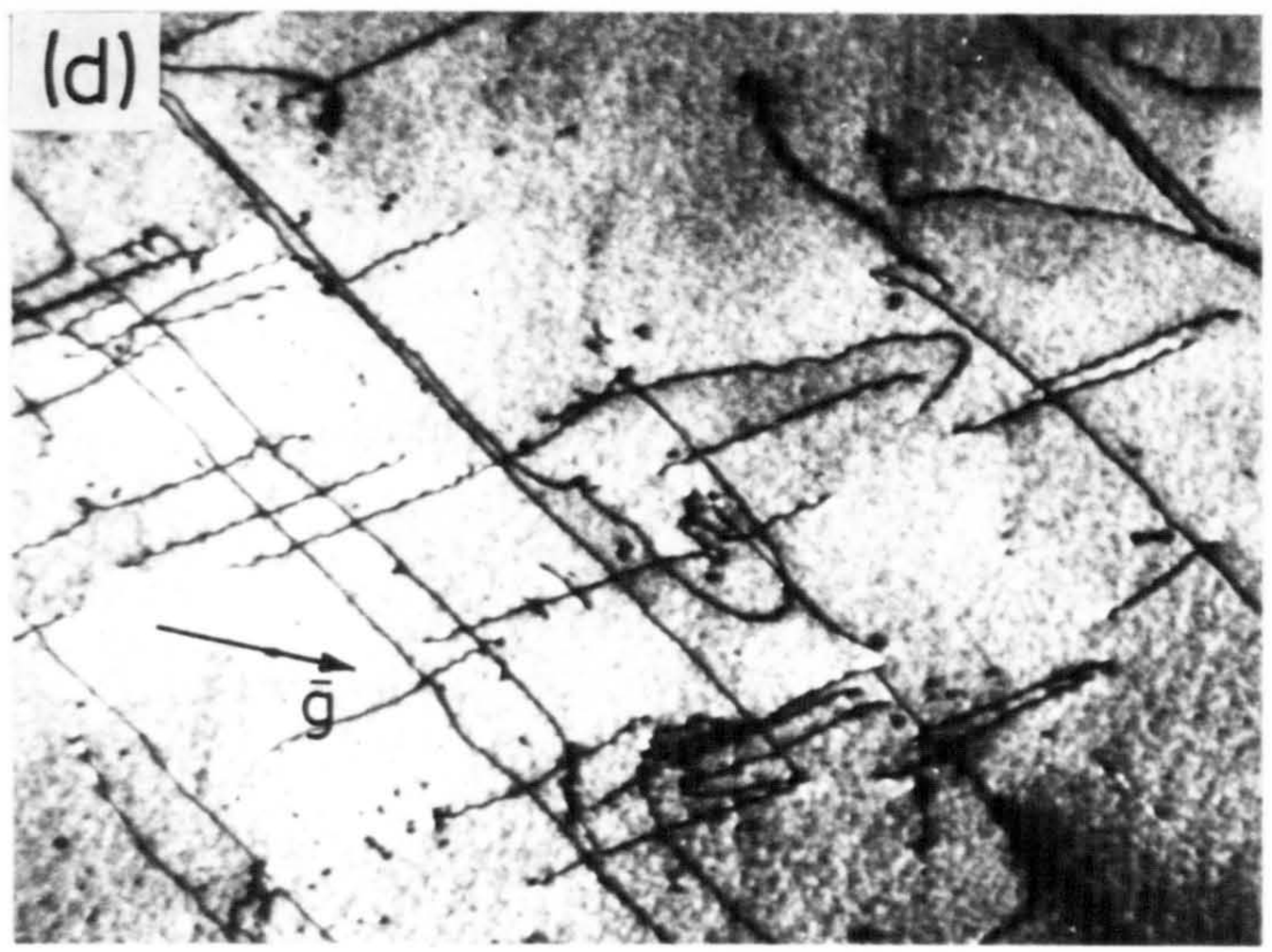

alloy nitrided and hydrogen reduced at 585°C to give a fine dispersion of substitutional-interstitial clusters but strained one percent at progressively higher temperatures. The dislocation structures in the annealed alloy, Figure IX.20(a), and nitrided and hydrogen reduced material deformed at -96°C and 23°C, Figure IX.20(b) and (c) respectively, are very similar and consist of long straight screw dislocations of Burgers vector $^{a}/2\langle 111\rangle$ (determined by standard $\bar{g}.b$ analysis). In the nitrided material the dislocations occur in bands which are separated by regions of low dislocation density; see Figure IX.20(b). All the dislocations in a given band have the same Burgers vector, except for changes in sign, since no contrast occurs from dislocations in a given band under imaging conditions such that $\bar{g}.b = 0$. These structures are very similar to those reported by Low & Turkalo (1962) in Fe-Si alloys and by Foxall & Statham (1970) in Nb-Mo alloys. It has been suggested by Christian (1970) that the dislocation structures can be correlated with the level of frictional stress (σ_o) operating in the material irrespective of whether this is produced by low temperatures, high strain rates, or in the present case by constant activity nitriding. In all cases the observation of pure screw dislocations of Burgers vector $^{a}/2\langle 111\rangle$ is a consequence of the reduced mobility of screw dislocations compared with edge dislocations. The reduced mobility may be related to the drag force caused by jog formation along the length of the screw dislocation (these jogs can be clearly seen

in Figure IX.20(c) and (d)) or because the low-energy configuration of a screw dislocation in body-centred cubic iron is sessile and for its movement must be changed into a high-energy glissile configuration (Duesbery & Hirsch, 1967).

Deformation at higher temperatures, Figure IX.20(d), shows that the screw dislocations no longer lie in such well defined bands since dislocation movements become easier due to cross-slip, and loop debris caused by the pinching-off of extended jogs can be seen in some regions. Although the exact dislocation-particle interaction cannot be identified, the general character of the dislocations and the type of slip observed are consistent with the particles having been sheared during deformation.

Figure IX.21 shows examples of the dislocation structures in nitrided material aged at high temperatures. In Figure IX.21(a) the dislocations are tangled around the precipitates and some dislocations actually interconnect the particles, demonstrating the ease of dislocation movement in overaged alloys and the ability of the structure to work-harden. Figure IX.21(b) shows that the Ti-N clusters formed on nitriding have transformed in situ to TiN, and gives evidence for their initial formation on the three cube planes of the ferrite. Two orientations are visible edge-on with the third, revealed by dislocation contract, lying in the plane of the foil. Some of the

Figure IX.21

Transmission electron micrographs of Fe-0.18 w/o Ti nitrided in $3NH_3$:$97H_2$ at 650°C for 5 h, then hydrogen reduced at 650°C for 5 h and aged into the Orowan region.

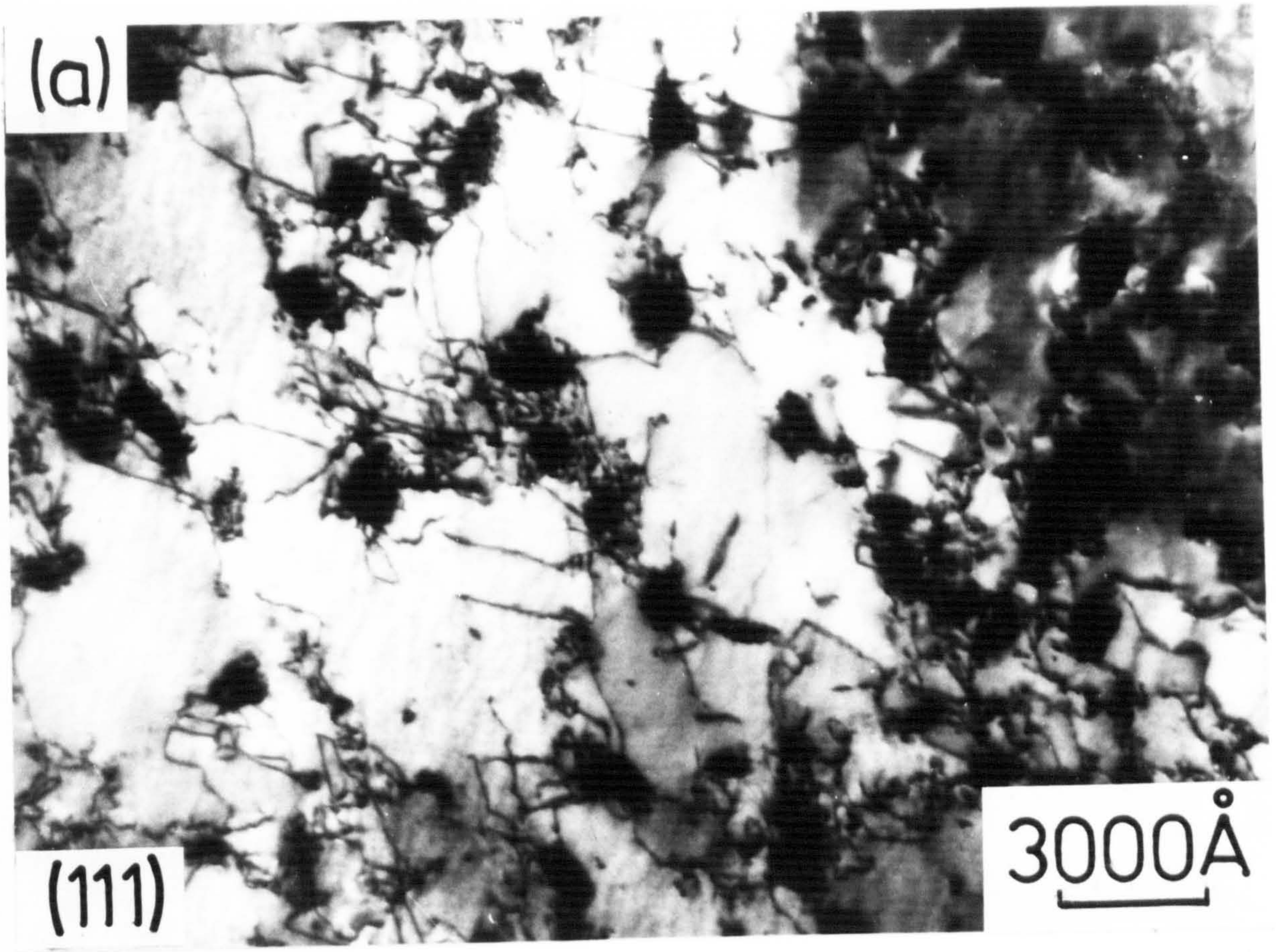
(a)
3000Å
(111)

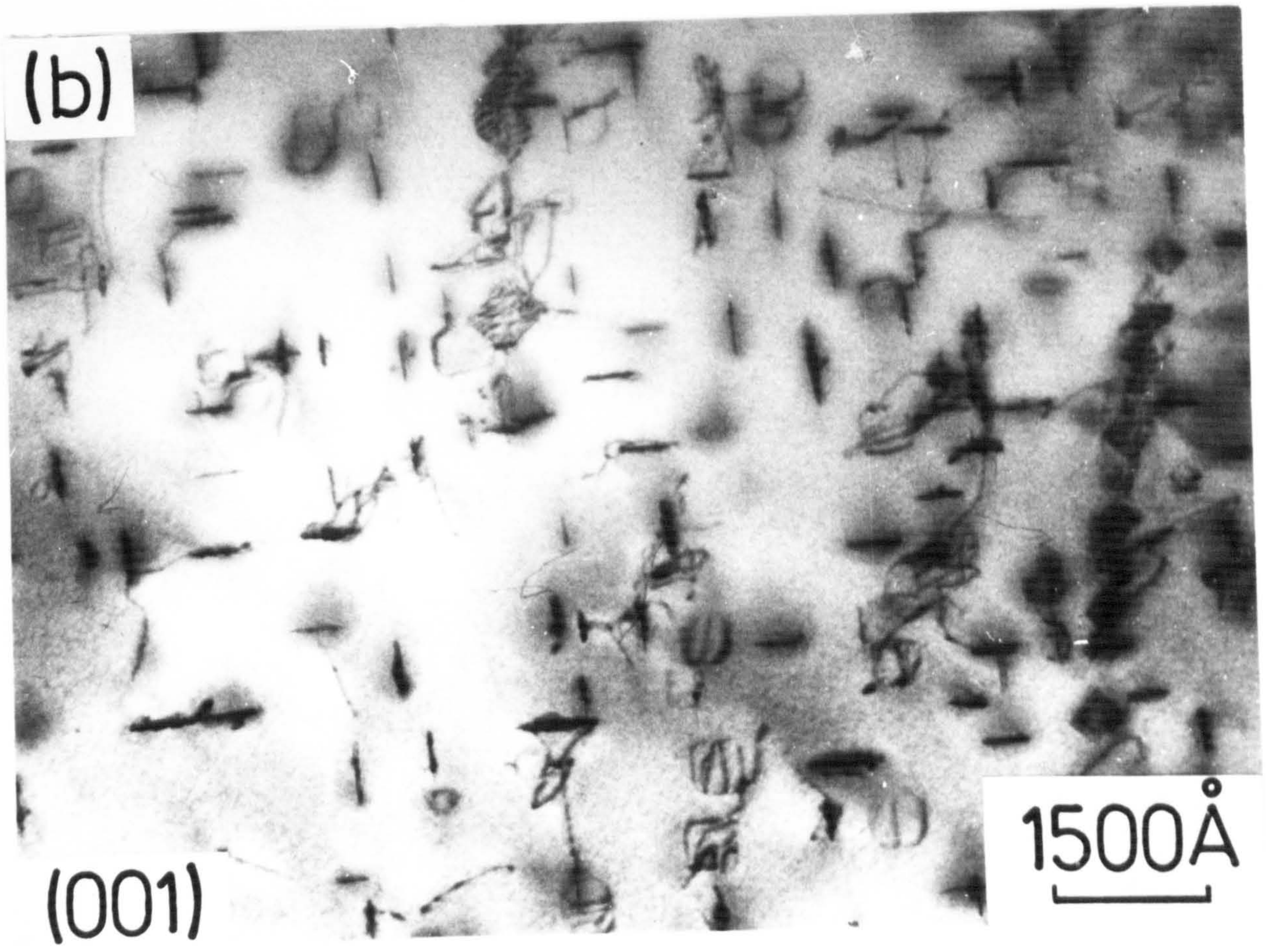
(b)
1500Å
(001)

dislocations in overaged alloys will originate at the particle-matrix interface due to the need to maintain continuity as the matrix deforms around the undeformed particles. Although no dislocation loops are visible, it is evident that the particles have been by-passed.

IX.8 Conclusions

(1) In nitrided Fe-Ti alloys the zones formed on nitriding are initially cut by long straight screw dislocations of Burgers vector $^{a}/2\langle 111\rangle$ and the yield strength is highly temperature dependent. These observations suggest chemical strengthening as the dominant strengthening mechanism and the proposal is supported by detailed friction stress calculations. On over-aging the zones to give equilibrium TiN precipitates, dislocation looping occurs by an Orowan-type mechanism.

(2) Iron is rejected from the initially formed Ti-N clusters when the nitrided alloys are aged at the nitriding or higher temperatures. These changes in zone composition and structure cause increases in yield strength that are related to the internal friction observations described in Chapter VII.

(3) Increases in the temperature-dependent component of the friction stress and of the Hall-Petch slope occur

as a result of nitriding. The changes in Hall-Petch slope are attributed to:

(a) the inhomogeneous slip distribution in nitrided alloys, which also accounts for the poor ductility of nitrided materials; and

(b) the segregation of excess nitrogen to grain boundaries, and its precipitation as titanium nitride.

The temperature dependence of the Hall-Petch slope shows that unpinning rather than creation of dislocations occurs at yield.

Chapter X

THE INFLUENCE OF COLD WORK ON THE MECHANICAL PROPERTIES OF Fe-Ti-N ALLOYS

X.1 Introduction

The strengthening produced by merely cold-working a material is well known and has many applications but even greater strengths result when deformation is combined with precipitation. Since the generation of dislocations is unavoidable in any fabrication operation it seemed desirable to investigate the possible benefits of nitriding an "as-fabricated component" without a recovery anneal.

X.2 The Effect of Nitriding Potential on Mechanical Properties

Figure X.1 compares the yield strengths of Fe-0.18 w/o Ti nitrided at 650°C for 5 h in various gas potentials. The alloys were either cold-worked (90% reduction) or annealed prior to nitriding. Clearly the yield strength of cold-worked and nitrided material is much higher than that of annealed and nitrided although, in both cases, it is a function of the nitriding potential (R). Hydrogen reduction causes a fall in the yield strength of cold-worked and nitrided material as loosely bound nitrogen is removed from the lattice leaving only nitrogen combined

Figure X.1

Yield stress against nitriding potential (R) for Fe-0.15 w/o Ti alloys; (a) cold-worked before nitriding at 650°C for 5 h; (b) annealed prior to nitriding at 650°C for 5 h; selected samples were hydrogen reduced at 500°C for 18 h.

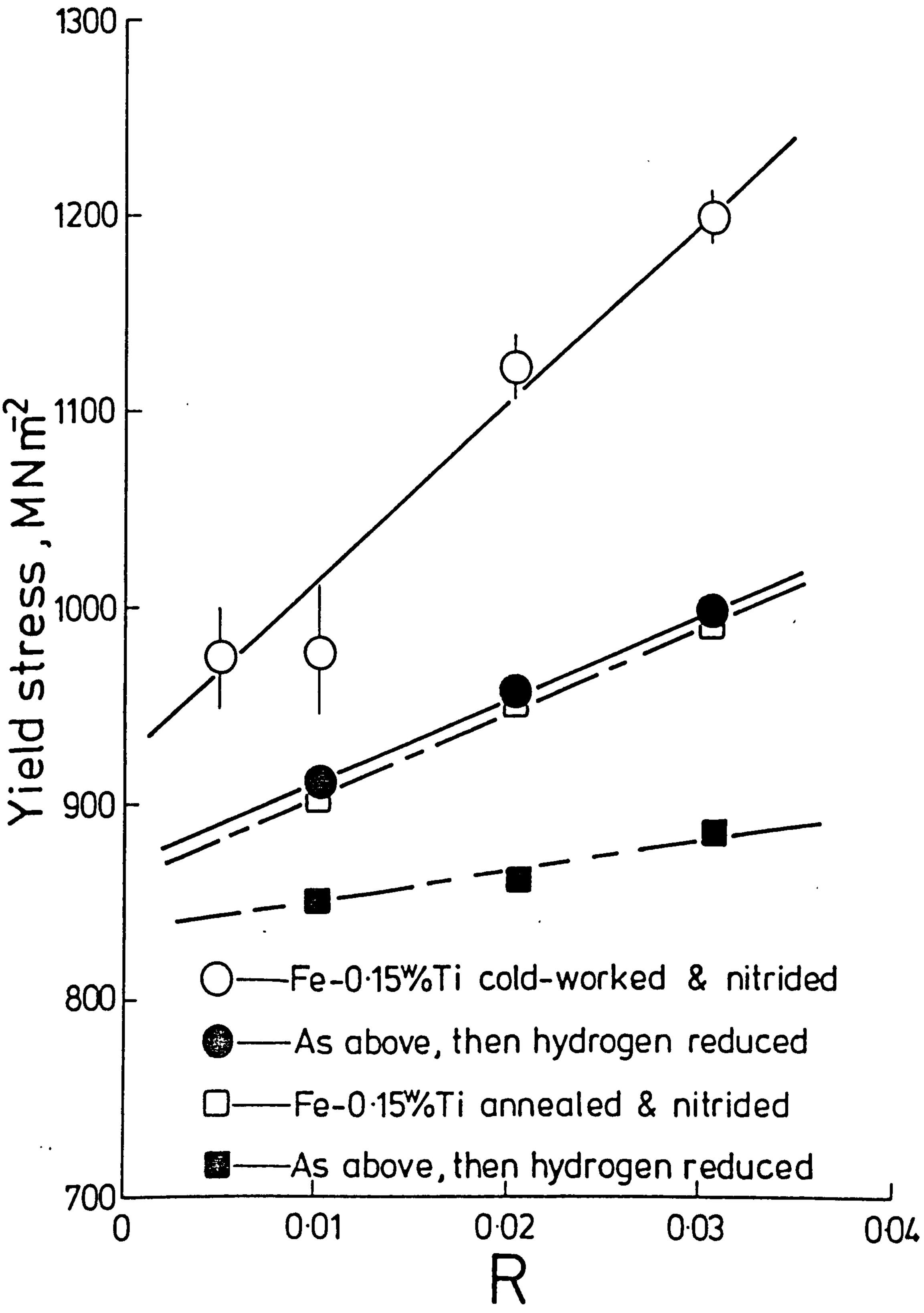
1300
1200
1100
1000
900
800
700
Yield stress, MN m⁻²
0
0·01
0·02
0·03
0·04
R
○——Fe-0·15w%Ti cold-worked & nitrided
●——As above, then hydrogen reduced
□——Fe-0·15w%Ti annealed & nitrided
■——As above, then hydrogen reduced

with titanium in the ratio 1N:1Ti; see Figure X.2(b). Due to the complex nature of the microstructure it is not possible to determine whether the titanium and nitrogen atoms are clustered to form a Ti-N zone, as in annealed and nitrided materials, or whether they are present as TiN precipitates. Figure X.2(a) shows that the ductility of cold-worked and nitrided material is greater than that of annealed and nitrided and independent of R and is not affected by the removal of the excess nitrogen after hydrogen reduction.

The optical micrograph in Figure X.3(a) is of a cold-worked sample through-nitrided in $3NH_3:97H_2$ at 650°C and clearly shows the change in structure between the case and core of the specimen. As nitriding proceeds from the surface, the cold-worked structure is pinned by heterogeneous precipitation of Ti-N clusters or precipitates onto dislocations, while recovery and recrystallisation takes place in the core before the nitriding front can penetrate more than a few hundred microns. A through-nitrided specimen therefore consists of a surface layer in which the cold-worked structure is retained, and a central region which is similar to a fine-grained annealed and nitrided structure. Scanning electron microscopy shows that the mode of failure depends on depth into the sample; a general view of a fracture face is shown in Figure X.3(b). At the outer regions the fractograph has a banded appearance with a few partially recrystallised

Figure X.2

Variation of (a) uniform elongation and (b) weight gain for Fe-0.15 w/o Ti alloys treated as in Figure X.1.

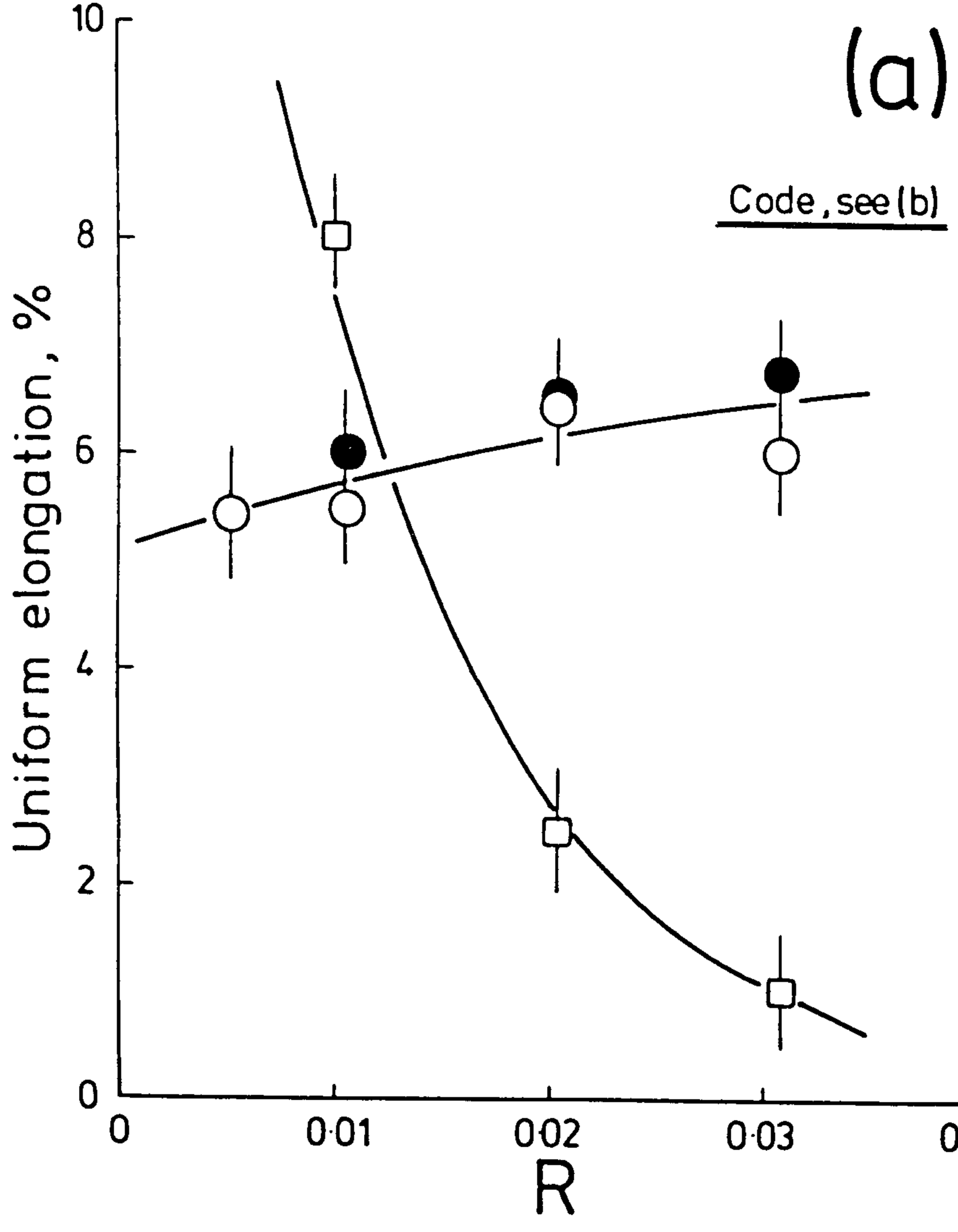
(a)
Code, see (b)
Uniform elongation, %
10
8
6
4
2
0
0
0·01
0·02
0·03
0·04
R

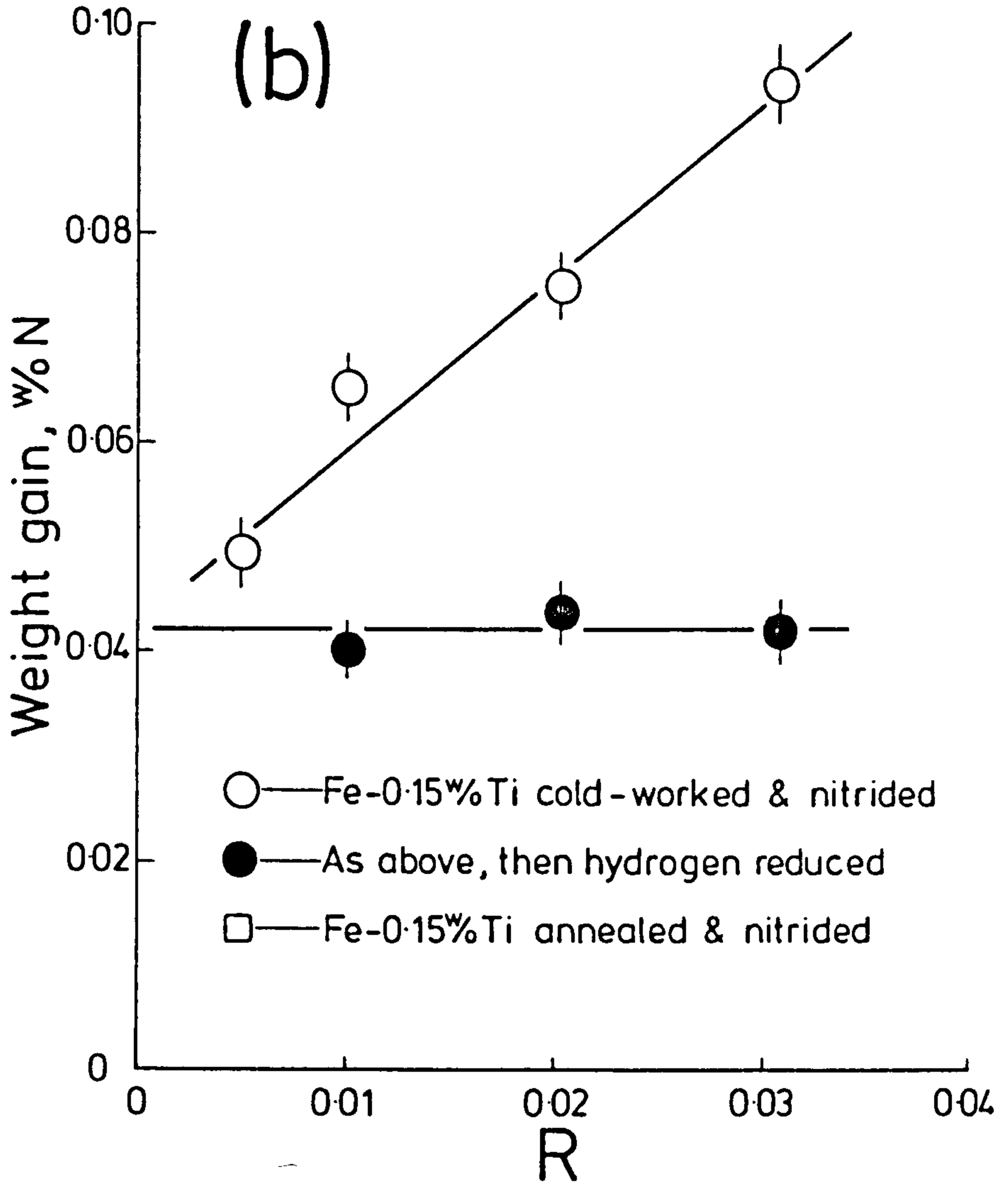
(b)
Weight gain, w% N
0·10
0·08
0·06
0·04
0·02
0
0
0·01
0·02
0·03
0·04
R
Fe-0·15w% Ti cold-worked & nitrided
As above, then hydrogen reduced
Fe-0·15w% Ti annealed & nitrided

Figure X.3

Micrographs of Fe-0.15 w/o Ti

(a) cold-worked 90%; nitrided in $3NH_3$:$97H_2$ at 650°C for 5 h; optical micrograph.

(b) as in (a); scanning electron fractograph.

(c) and (d) as (b); higher magnification fractographs of selected regions.

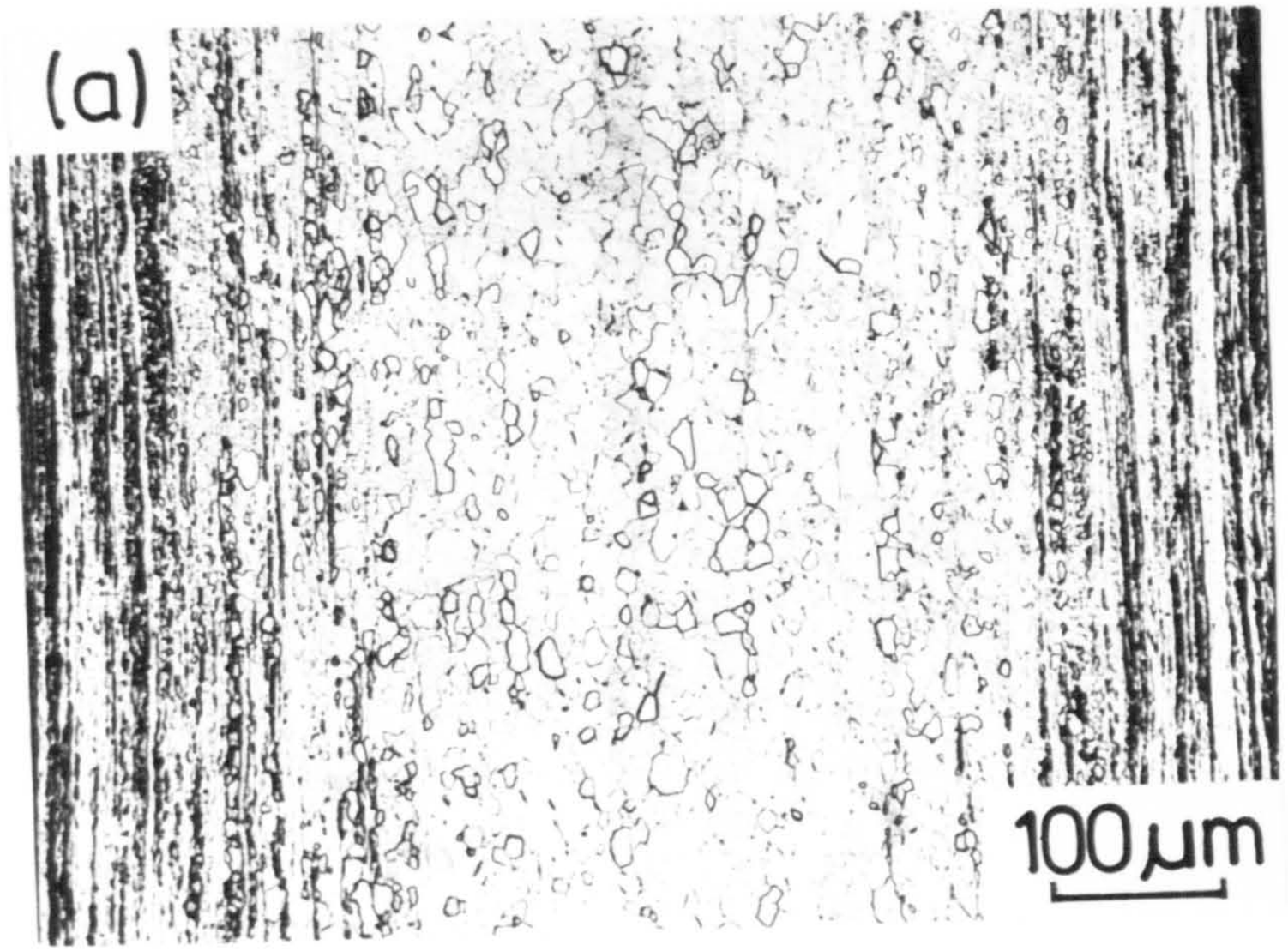
(a)
100 µm

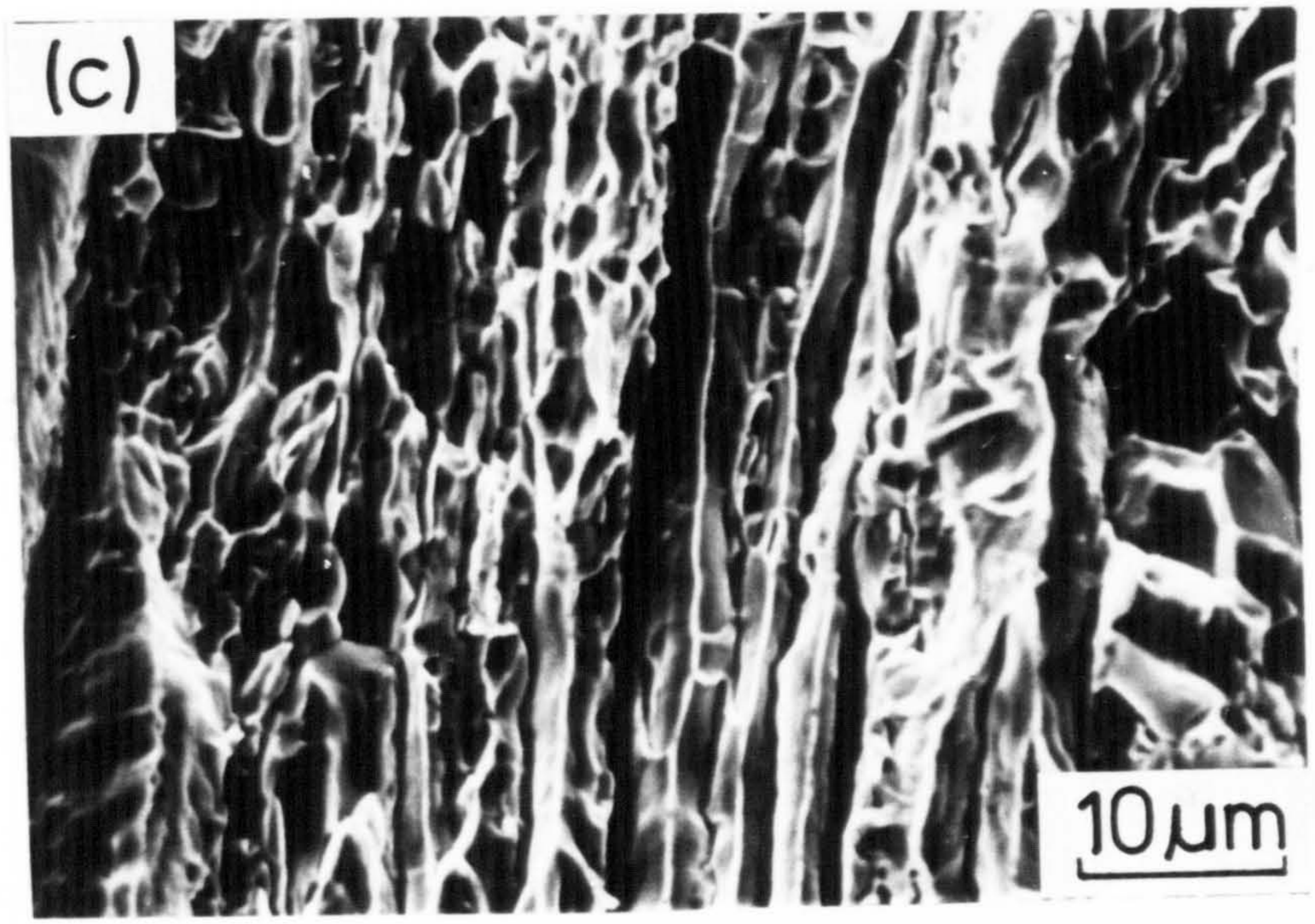
(c)
10 µm

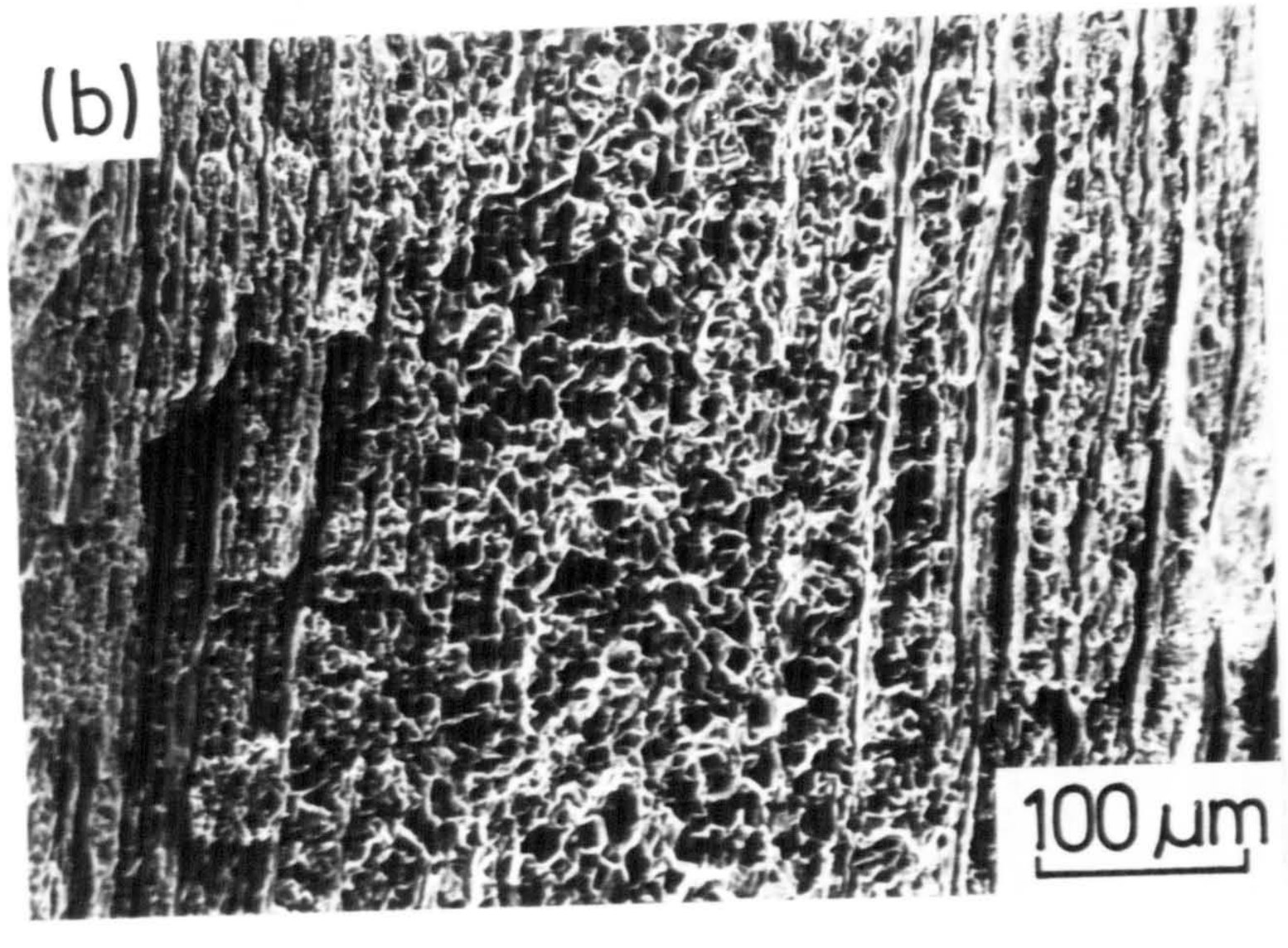
(b)
100 µm


(d)
10 µm

grains clearly visible in FigureX.3(c) while intergranular and cleavage failure has occurred in the core, Figure X.3(d), identical to the failures observed in annealed and nitrided materials; see Figure IX.6(b). This suggests that, in a cold-worked and nitrided material, although the core fails prematurely the tough case prevents the complete failure of the specimen. The increased ductility of cold-worked and nitrided material is due to the replacement of grain boundaries in the surface layers by a fine dislocation sub-cell structure.

The nitriding front advances at a rate dictated by internal nitriding kinetics (see Chapter II) with the subscale depth (X) given by:

$$X^2 = \frac{48}{7} \frac{\{N\}}{\{Ti\}} .D.t \qquad \ldots X.1$$

At high nitriding potentials (high [N]) the rate of nitriding is such that a large proportion of the cold-worked structure is pinned into the material. The converse is true at low nitriding potentials. The strength obtained is therefore a balance between a loss due to recovery and recrystallisation and a gain resulting from dislocation pinning and homogeneous clustering. Thus, by varying the nitriding potential the cold-work contribution to total strength will change and so accounts for the dependence of yield stress on R as shown in Figure X.1.

By varying the time of nitriding at 650^{o}C with a

constant nitriding potential ($3NH_3:97H_2$) the competitive nature of the nitriding process was investigated and Figure X.4 shows the results expressed as a percentage of the through-nitriding time (55 mins) as given by equation X.1. Both yield and ultimate tensile strength are approximately linear functions of nitriding time showing, in the initial stages of nitriding, that any loss in strength from recovery and recrystallisation is compensated by a gain from nitriding. With increasing time, the core recrystallises and the total gain in strength results from homogeneous clustering of titanium and nitrogen atoms to form Ti-N zones. The complex nature of the strengthening process, where the properties are continually changing with depth, makes impossible any quantitative calculations or predictions of strength e.g. by treating the material as a composite. Figure X.4 also shows that the uniform elongation initially increases due to recovery and recrystallisation of the core but decreases to the through-nitrided value as the nitriding front progresses into the specimen.

Figure X.5 illustrates the microstructures which develop at various stages. Figure X.5(a) is an optical micrograph of a specimen nitrided for 10 min which shows signs of recrystallisation in the core of the specimen with a banded structure at the outside. The extent of pinning at the edges of the specimen is seen more clearly in Figure X.5(b) where the same material of Figure X.5(a) has been annealed in hydrogen for 4 h at 650°C. This is

Figure X.4

Variation in mechanical properties with nitriding time for Fe-0.15 w/o Ti cold-worked 90% and nitrided in $3NH_3:97H_2$ at 650°C.

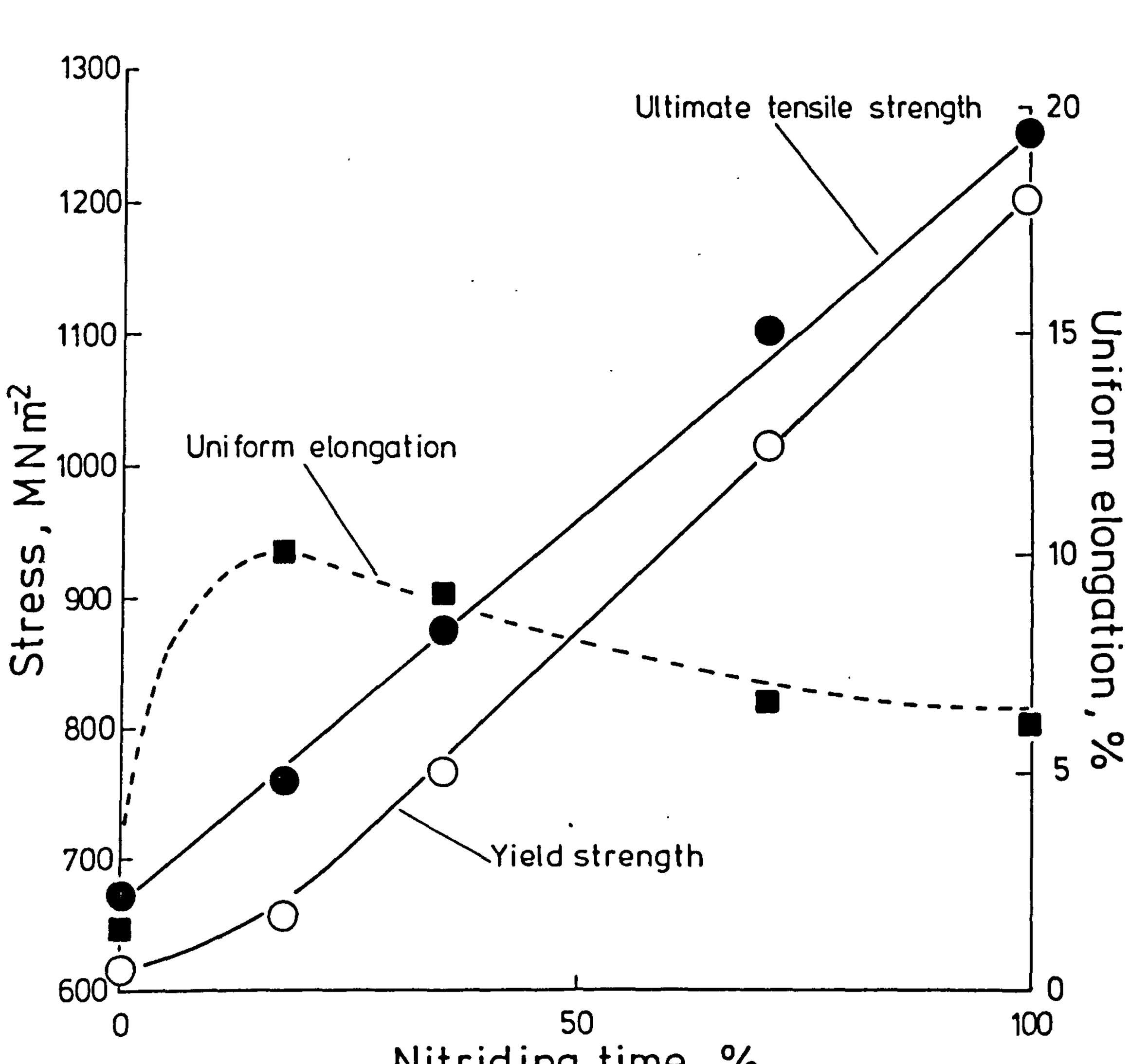
1300
1200
1100
1000
900
800
700
600
Stress, MN m⁻²
Ultimate tensile strength
Uniform elongation
Yield strength
20
15
10
5
0
Uniform elongation, %
0
50
100
Nitriding time, %

Figure X.5

Micrographs of cold-worked Fe-0.15 w/o Ti nitrided in $3NH_3:97H_2$ at 650°C

(a) optical micrograph of material nitrided for 10 min.

(b) as (a); annealed in hydrogen at 650°C for 4 h.

(c) optical micrograph of material nitrided for 40 min; annealed in hydrogen at 650°C for 4 h.

(d) scanning electron fractograph of surface region in (c).

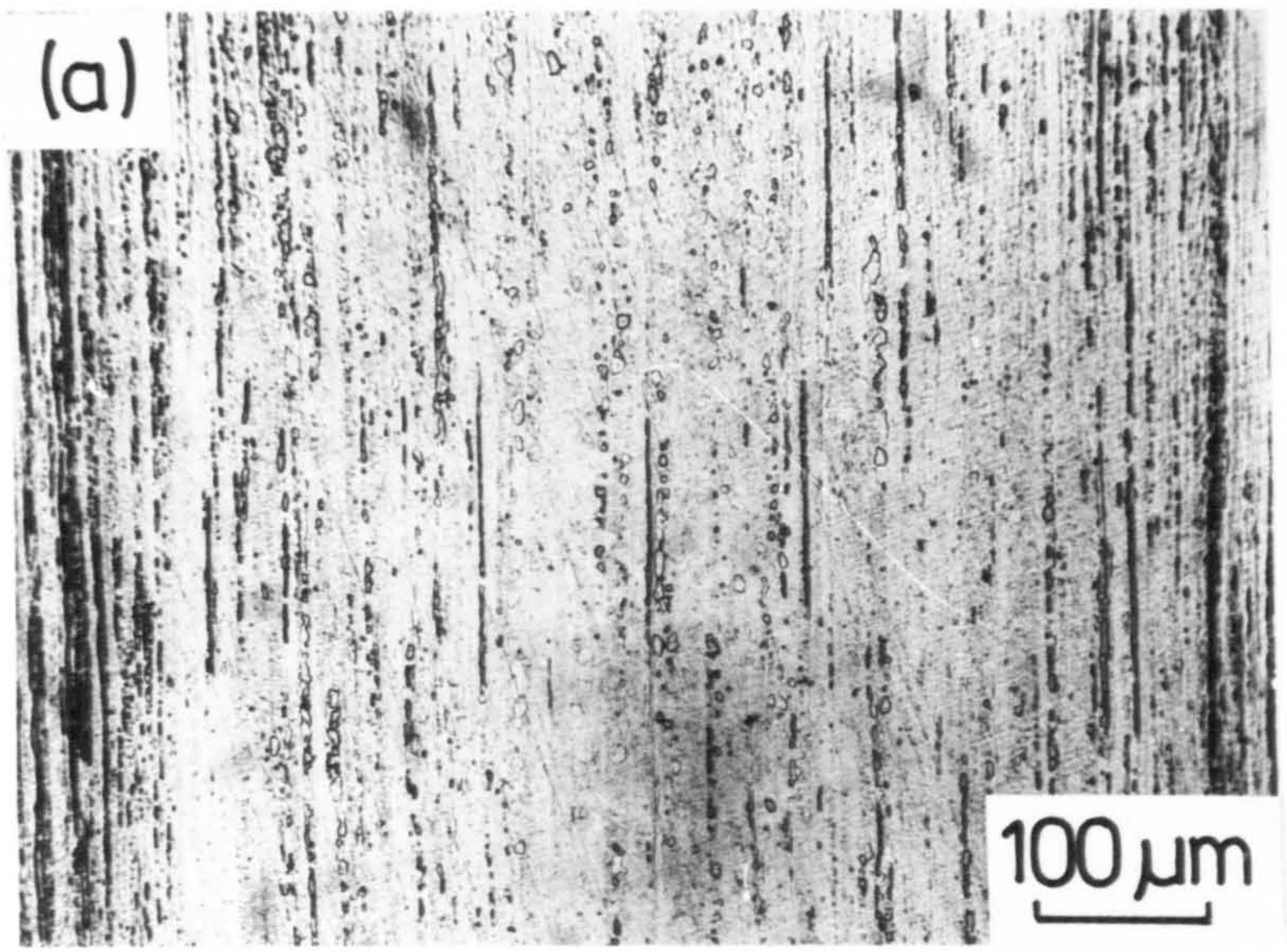
(a)
100 µm

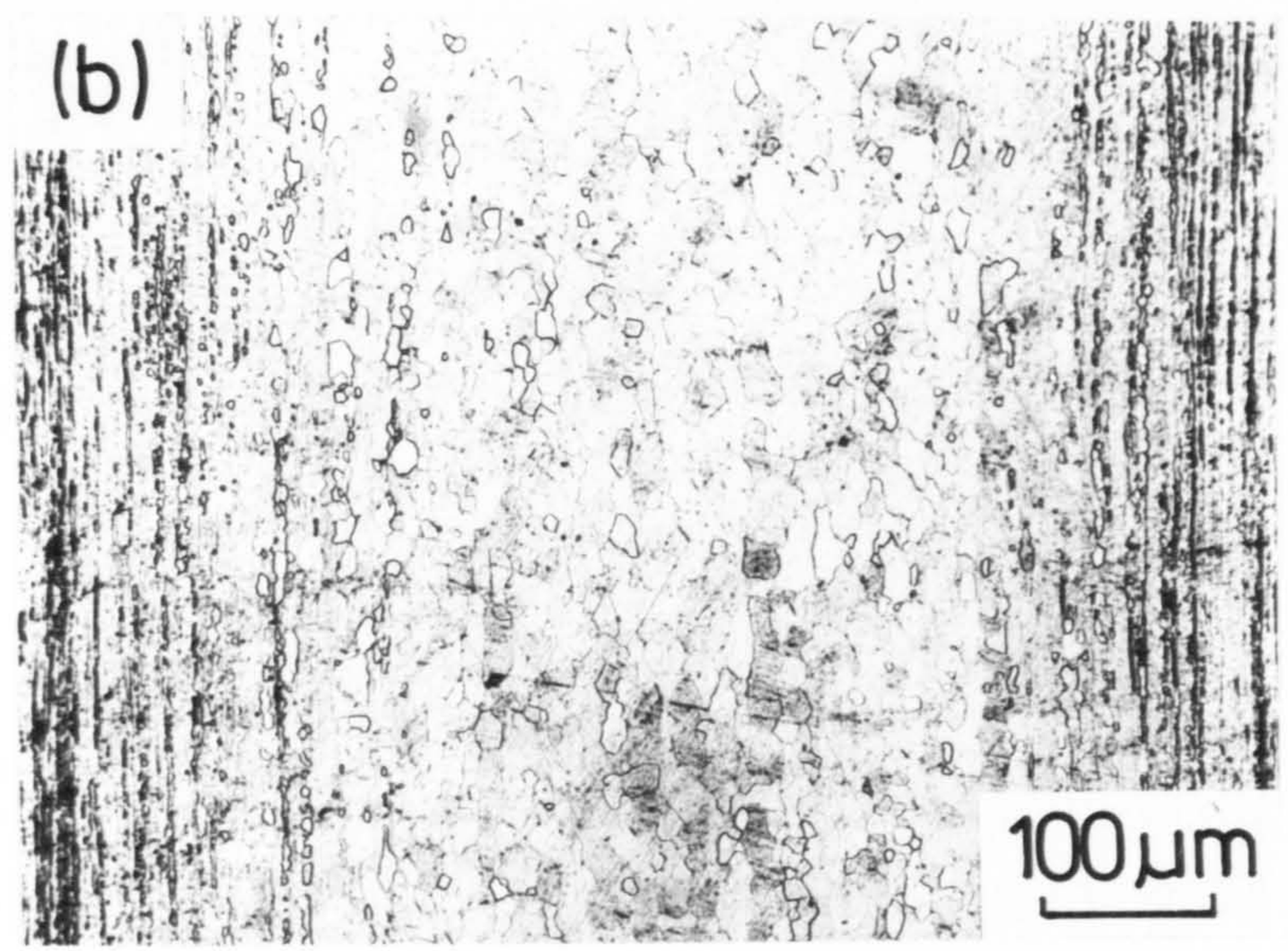
(b)
100 µm

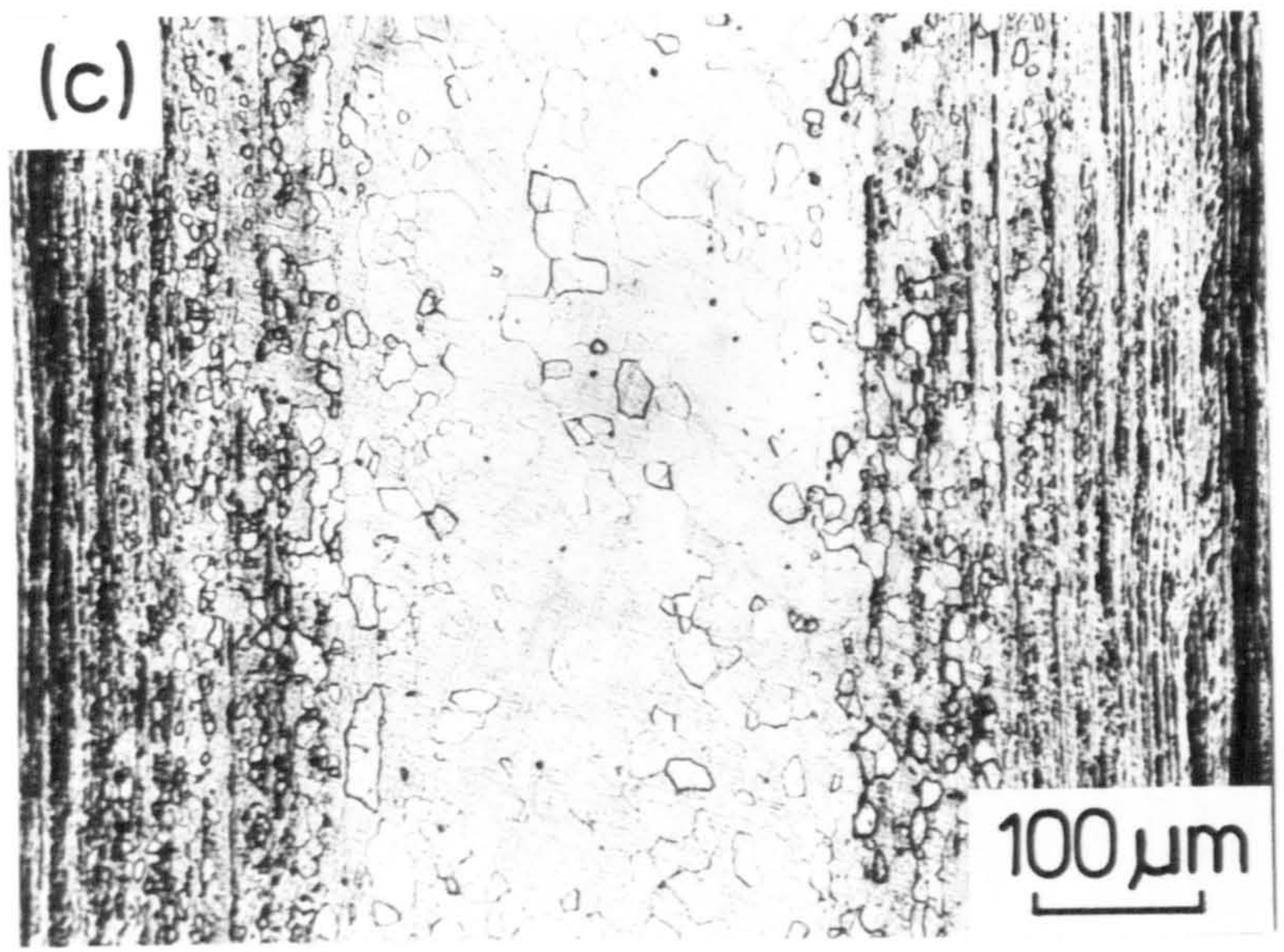
(c)
100 µm

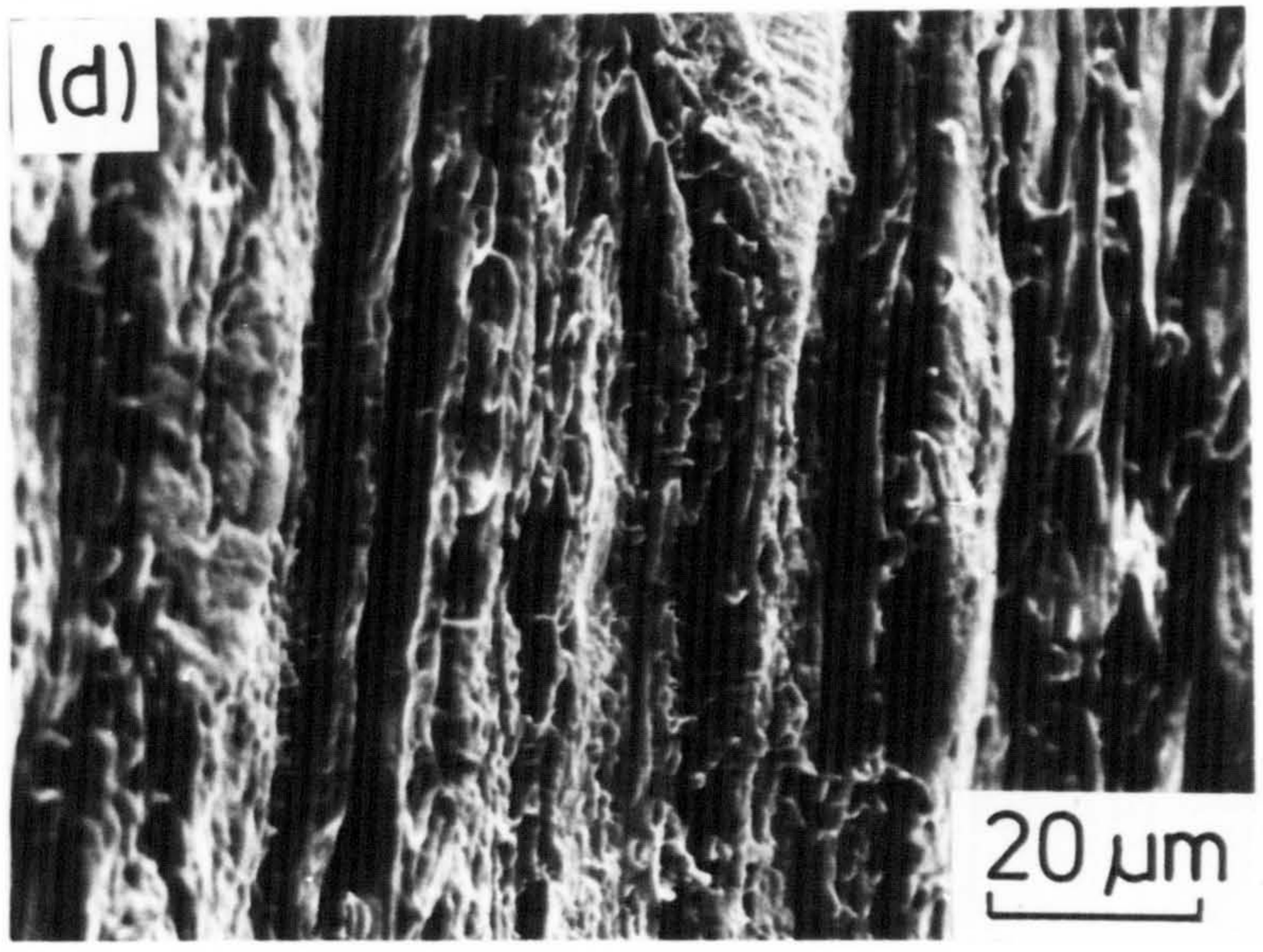
(d)
20 µm

compared with Figure X.5(c) in which a specimen nitrided for 40 min and again annealed in hydrogen clearly shows an increase in the amount of "locked in" structure at longer nitriding times. Scanning electron microscopy shows a clear demarkation between the un-nitrided core and the nitrided case, the core failing by micro-void coalescence typical of a ductile material, while the nitrided surface fails so as to give a banded structure; see Figure X.5(d). The origins of the banded structure will be discussed in Section X.4.

X.3 The Influence of Nitriding Temperature on the Properties of Cold-Worked Fe-Ti Alloys

In Section X.2 the temperature of nitriding was constant and nitrogen potential and time dictated the resulting microstructures and properties of the product. The nitriding temperature was then varied keeping a constant nitrogen activity at the specimen surface and using the same Fe-0.15 w/o Ti alloy as previously.

Figure X.6 shows the variation of yield stress with time for the un-nitrided cold-worked alloy at three different annealing temperatures. At 450°C there is an initial decrease in strength that reaches a constant value after about 1 h when a stable subgrain structure has been established. Similar observations have been reported during

Figure X.6

Variation in yield stress and microstructure of Fe-0.15 w/o Ti cold-worked 90% and annealed in hydrogen at 450°, 550° and 650°C for the times shown.

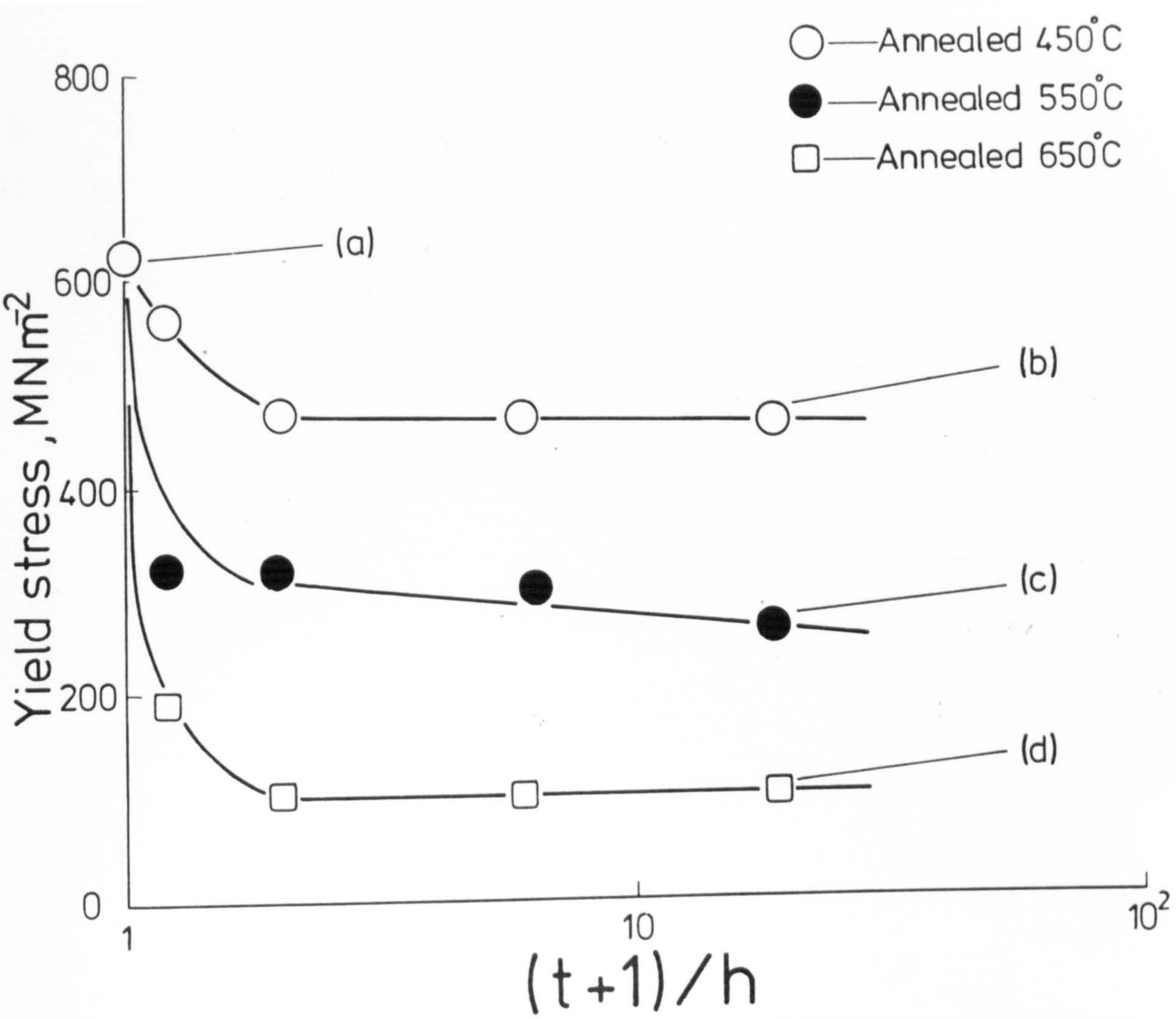
Annealed 450°C
Annealed 550°C
Annealed 650°C
800
600
400
200
0
Yield stress, MNm⁻²
(a)
(b)
(c)
(d)
1
10
10²
(t+1)/h

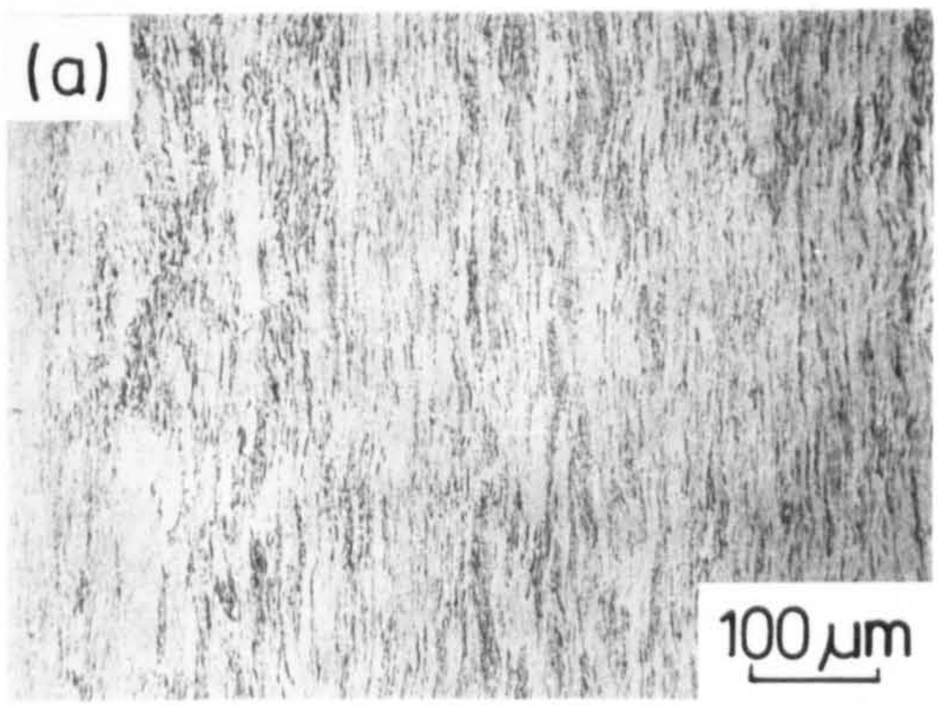
(a)
100 μm

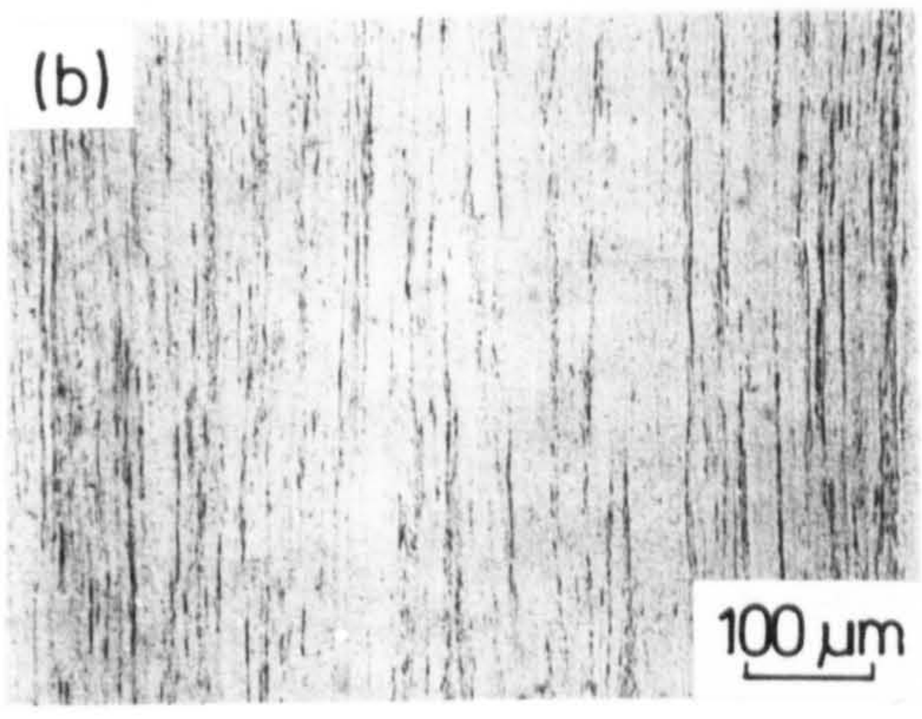
(b)
100 μm

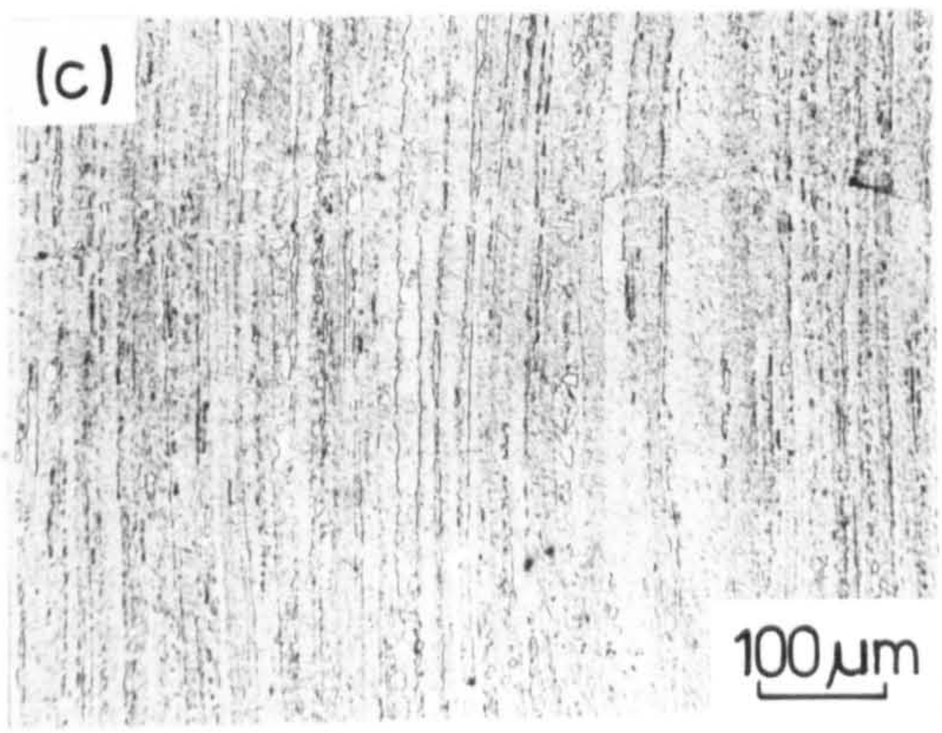
(c)
100 μm

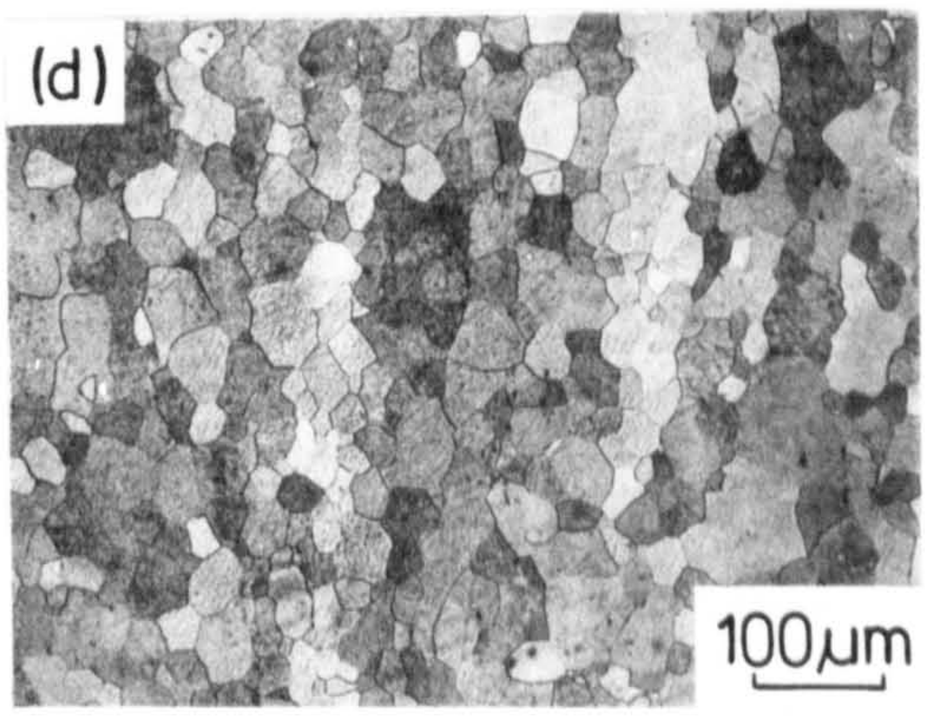
(d)
100 μm

the annealing of pure iron (Keh, 1962). After 18 h at 450°C the optical microstructure, Figure X.6(b), seems very similar to that of the alloy in its cold-worked condition, Figure X.6(a). When the alloy is annealed at 550°C, again there is an initial rapid decrease in yield stress due to recovery, falling less rapidly with increasing time as new grains begin to grow. Grain growth is clearly visible after 18 h, Figure X.6(c). At 650°C, the nitriding temperature used for the work described in Section X.2, the yield strength decreases very rapidly as recovery and recrystallisation takes place, and in the plateau region marked grain growth has clearly occurred; see Figure X.6(d).

In Table X.1 the yield strengths of specimens through-nitrided at different temperatures but at the same nitrogen activity are listed. Perhaps surprisingly, the strengths do not differ greatly even though the specimens have widely differing microstructures and the weight gains, also given in Table X.1, reflect the complex nature of the nitriding process. At 450°C the alloy might be expected to take up more nitrogen than at 550°C (see Chapter VII) but this is not observed because nitriding at 450°C leads only to recovery without a marked reduction in dislocation density and it is the variation in dislocation density that explains the weight gain data. If a precipitate or cluster produced heterogeneously on a dislocation has a smaller amount of excess nitrogen associated with it than

Table X.1

Yield strength and weight gain results for Fe-0.15 w/o Ti cold-worked 90% prior to nitriding at 450, 550 and 650°C with a nitrogen activity of about 0.030.

Nitriding conditions	Weight gain, w/o N	Yield stress, MN/m^2
450°C, a_N = 0.028	0.086	960
as above, hydrogen reduced at 500°C	0.056	910
550°C, a_N = 0.030	0.098	1150
as above, hydrogen reduced at 550°C	0.054	940
650°C, a_N = 0.026	0.076	1150
as above, hydrogen reduced at 650°C	0.044	960

one that is homogeneously formed within the ferrite lattice, then the variation in the relative proportions of heterogeneous and homogeneous sites will determine the total nitrogen pick-up for any product and the weight gain data are explained.

Figure X.7 contrasts the structure of material nitrided at 450°C with the same material nitrided at 650°C. At low nitriding temperatures the structure is basically that of a cold-worked sample which has recovered, Figure X.7(a), while at 650°C recrystallisation takes place in the centre of the sample, as shown in Figure X.7(b), the observations being in agreement with the microstructures of Figure X.6. The fracture behaviours of the samples are very different from one another. Figure X.7(c), a fractograph of material nitrided at 450°C, shows a banded structure with regions of micro-void coalescence at the top of each band and the fracture face shows a number of cracks running parallel to the tensile axis and along the direction of rolling. At 650°C, Figure X.7(d), banding is observed only at the edges of the specimen, although on a much finer scale than that at 450°C, and intergranular and cleavage failure occurs in the recrystallised core. The true stress/true strain curves for these samples are shown in Figure X.8. For material nitrided at 650°C a Luder's region is observed followed by a small amount of work-hardening up to the ultimate tensile strength. The Luder's strain in specimens nitrided at 650°C increases with nitriding potential

Figure X.7

Micrographs of cold-worked and nitrided Fe-0.15 w/o Ti (a) and (c) optical micrograph and scanning electron fractograph of material nitrided in $24NH_3:76H_2$ at 450°C for 24.5 h.

(b) and (d) optical micrograph and scanning electron fractograph of material nitrided in $2NH_3:98H_2$ at 650°C for 2 h.

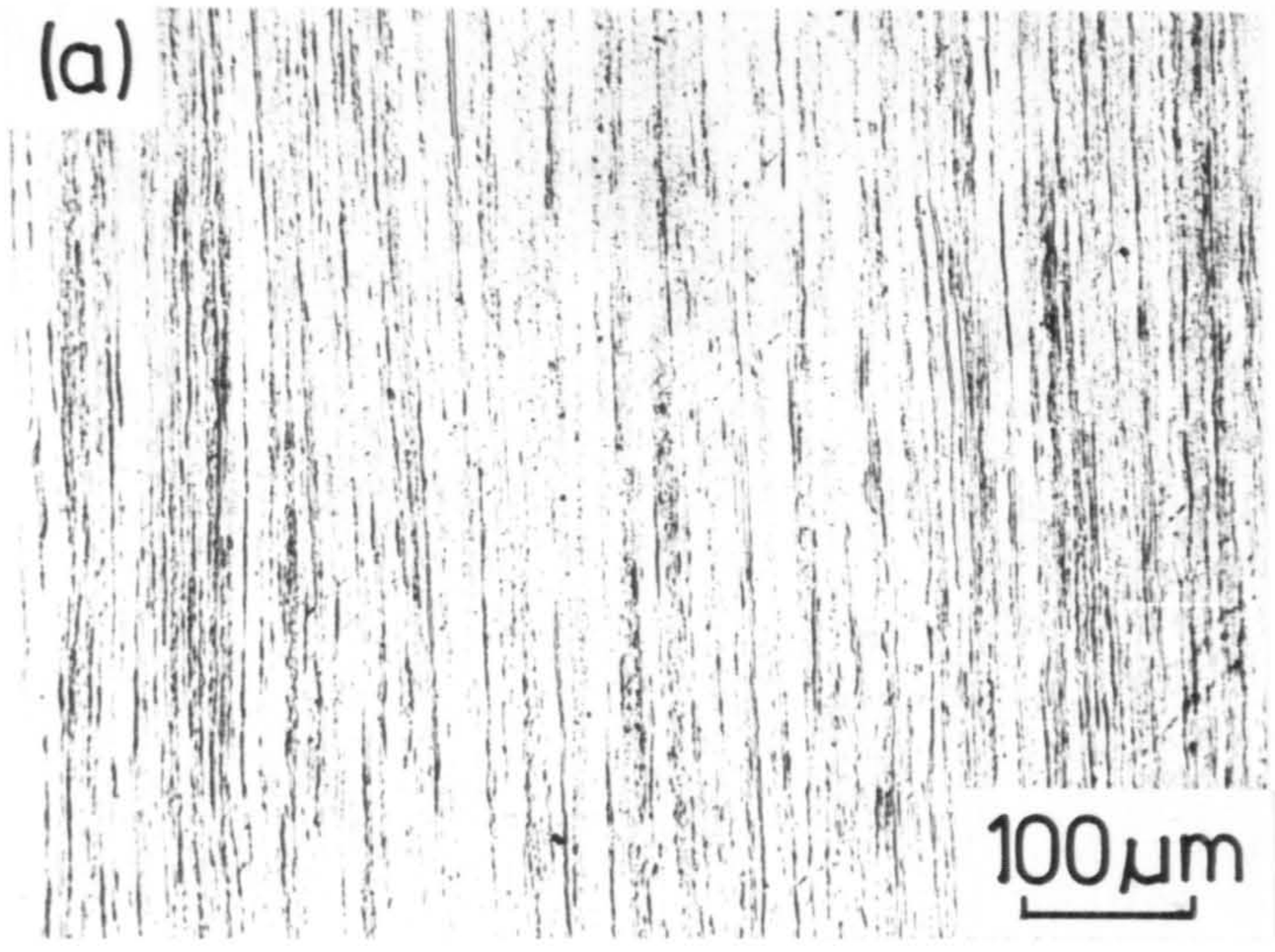
(a)
100 µm

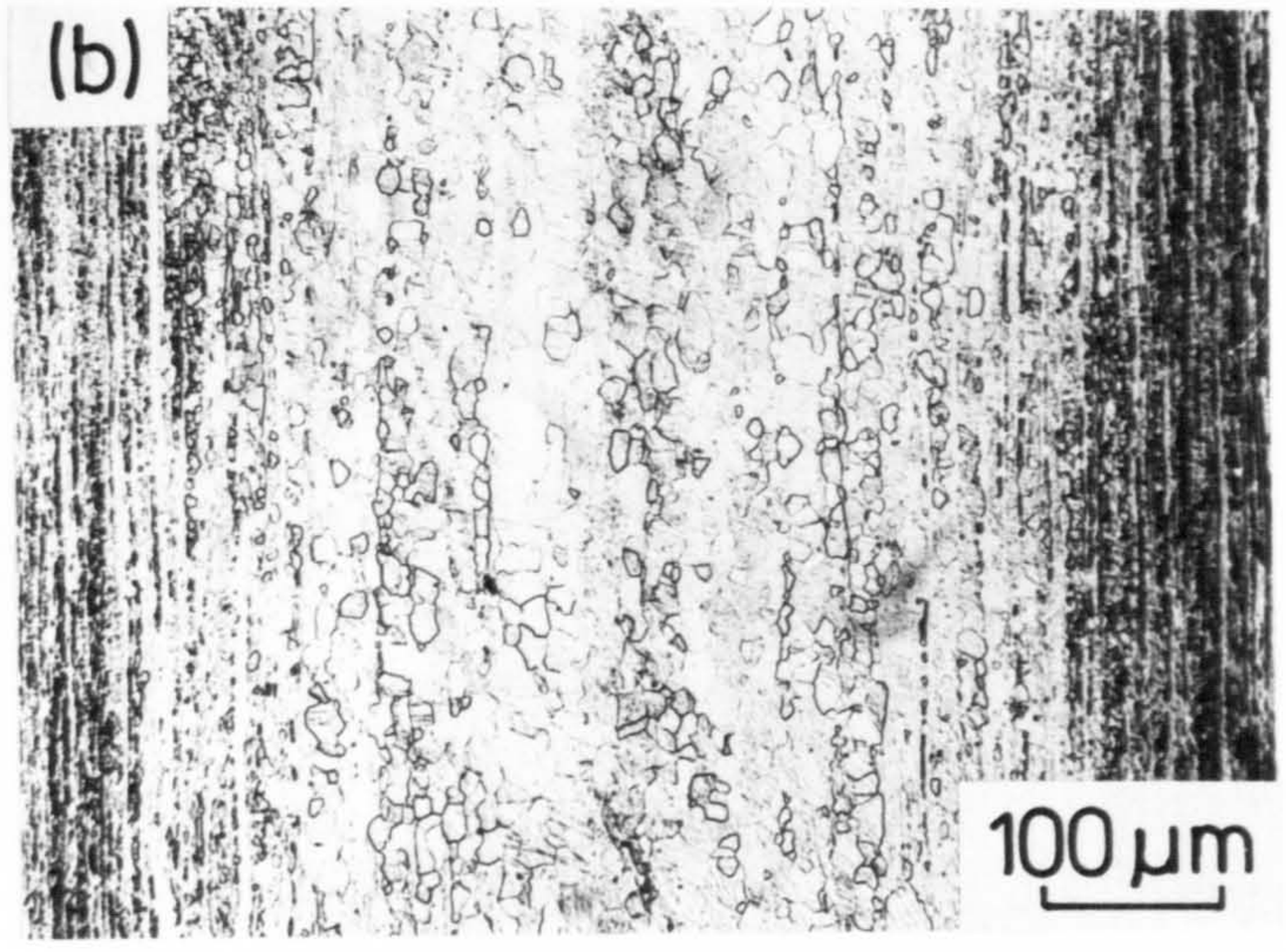
(b)
100 µm

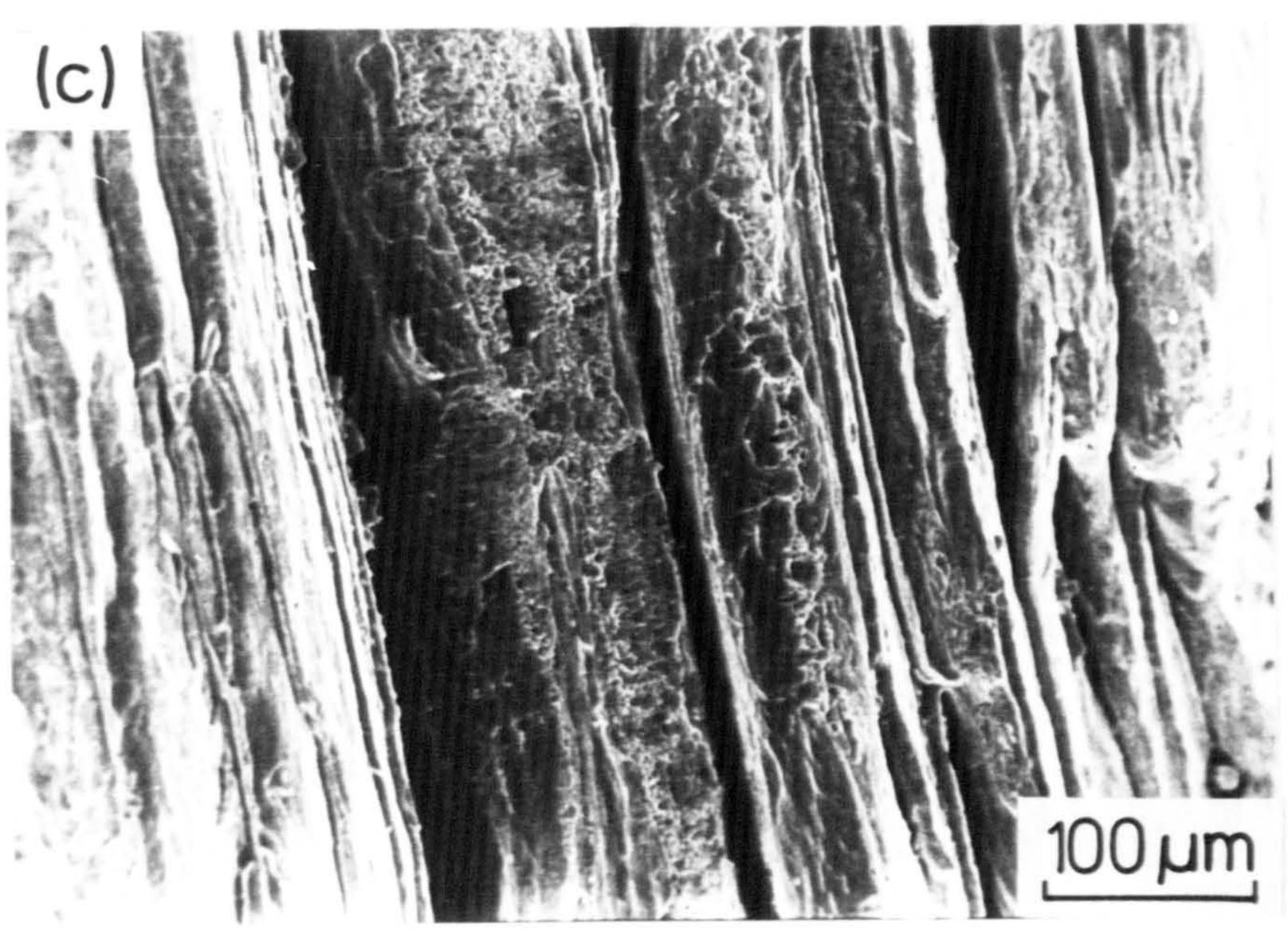
(c)
100 µm

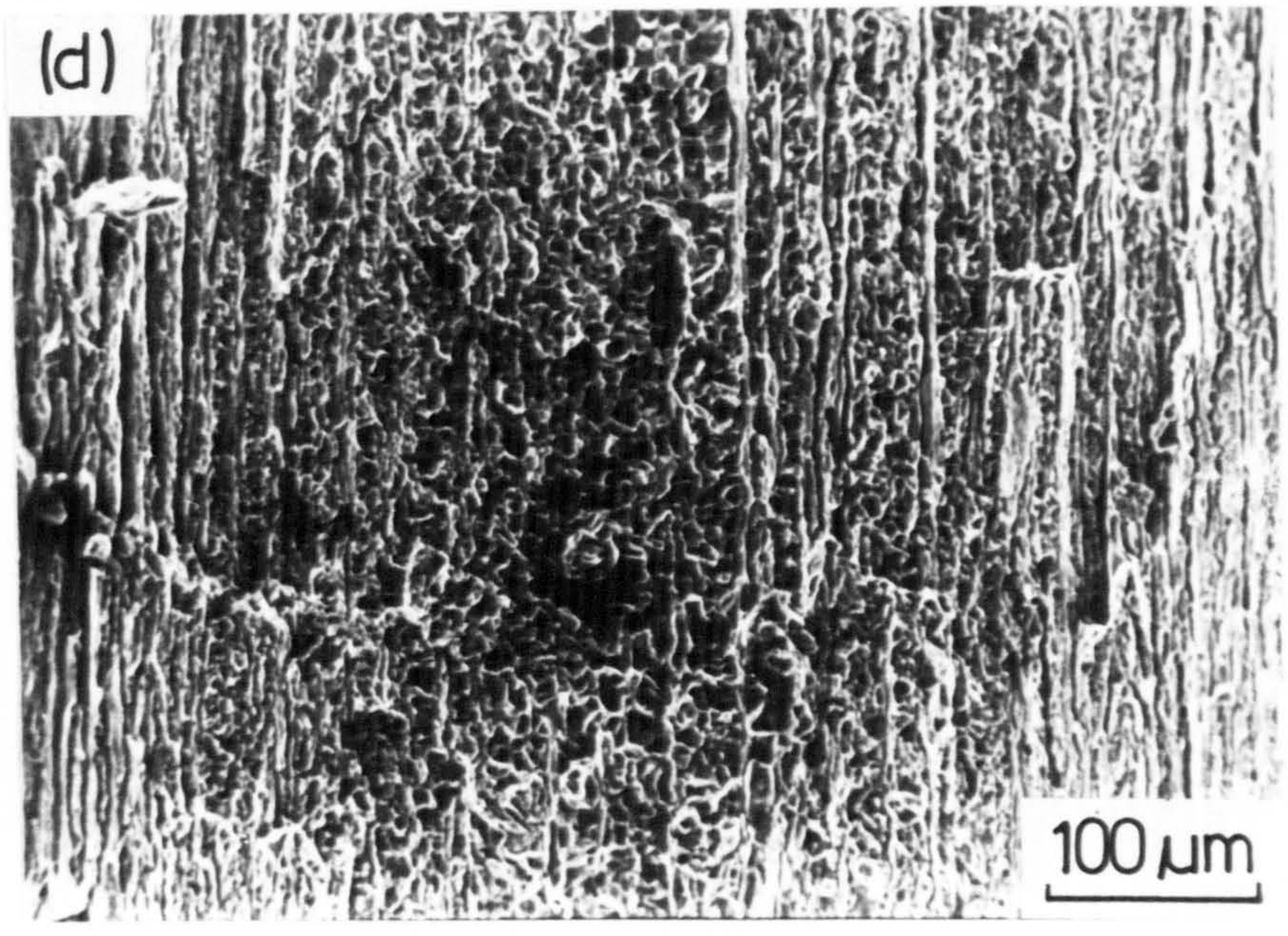
(d)
100 µm

Figure X.8

True stress-true strain curves of cold-worked Fe-0.15 w/o Ti after various nitriding treatments.

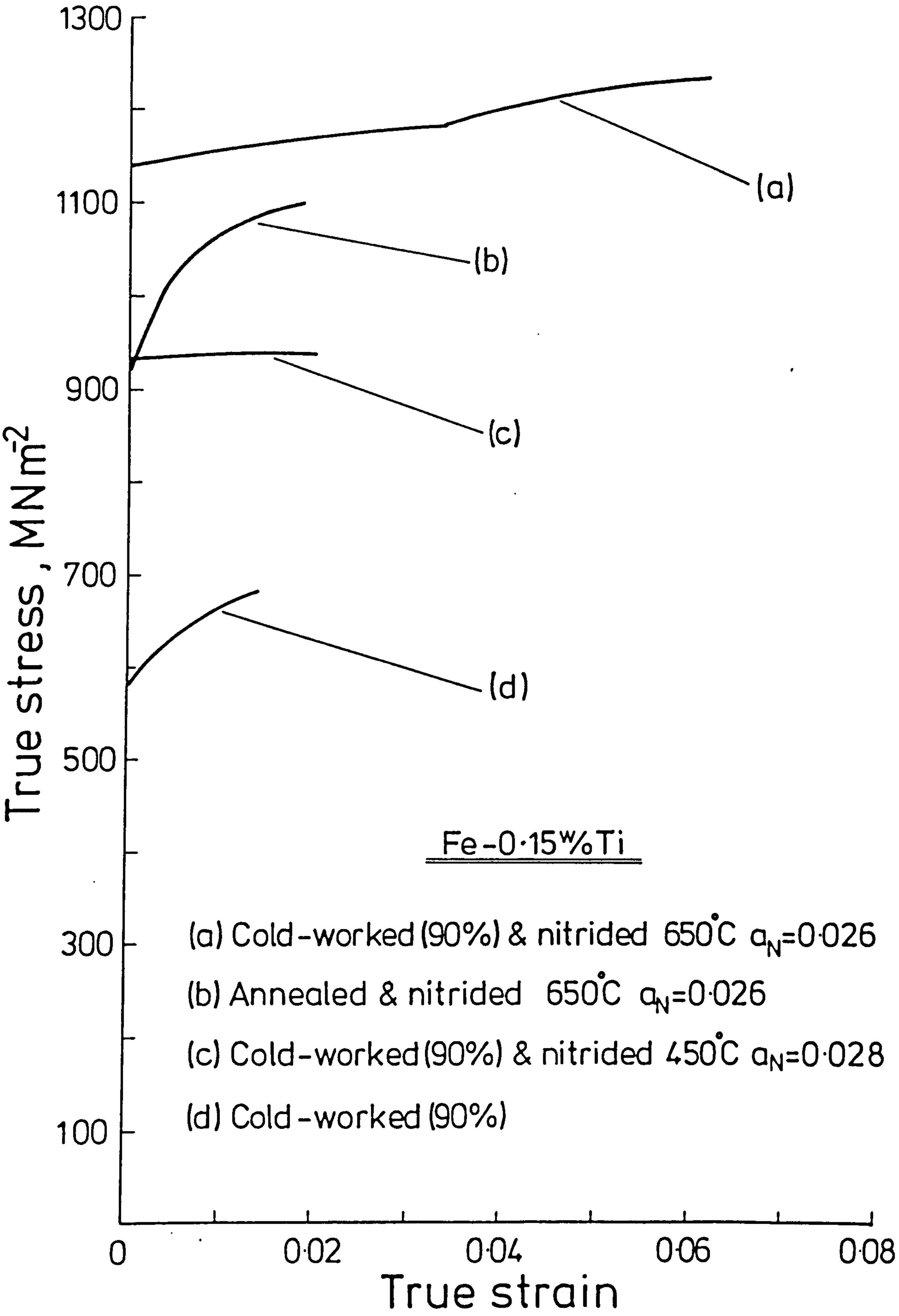
1300
1100
900
700
500
300
100
True stress, MNm-2
(a)
(b)
(c)
(d)
Fe-0·15w%Ti
(a) Cold-worked (90%) & nitrided 650°C a_N=0·026
(b) Annealed & nitrided 650°C a_N=0·026
(c) Cold-worked (90%) & nitrided 450°C a_N=0·028
(d) Cold-worked (90%)
0
0·02
0·04
0·06
0·08
True strain

and can be correlated with the proportion of cold-worked structure retained after nitriding. As the amount of cold-worked structure increases, the propagation of yield through the structure becomes more difficult and the Luder's strain increases. For a specimen nitrided at 450°C, Figure X.8(c), failure occurs as the Luder's band is propagating through the structure, and by comparison with Figure X.8(d) the total elongation is similar to that of the cold-worked specimen. Materials annealed (b) and cold-worked (a) prior to nitriding are also compared in Figure X.8 and the increased ductility of cold-worked and nitrided material is immediately apparent. If the area under the true stress/true strain curve is regarded as a measure of toughness, the true stress (σ) and true strain (ϵ) after yield are related by:

$$\sigma = K \epsilon^{n} \qquad \ldots \text{ X.2}$$

where n is the work-hardening index and K the strength at unit strain. It follows that the energy per unit volume (E) is given by:

$$E = K \int_{\epsilon_y}^{\epsilon_{max}} \epsilon^{n} d\epsilon + \tfrac{1}{2} \sigma_y \epsilon_y$$

$$\therefore \quad E \simeq \frac{K}{n+1} \cdot \epsilon_{max}^{n+1} \qquad \ldots \text{ X.3}$$

For the cold-worked and nitrided alloy shown in Figure X.8(a) E is about 85 MJ while for annealed and nitrided E equals 32 MJ. On this simple basis, the cold-worked alloy is therefore approximately 2.5 times tougher.

X.4 The Variation of Mechanical Properties of Nitrided Fe-Ti Alloys with Percentage Cold-Work

Fe-0.18 w/o Ti alloys with reductions of 47, 70 and 90 percent were nitrided at 585°C over a range of nitrogen activities (a_N) and the results are given in Table X.2. For each of the reductions there is no dependence of yield stress on nitrogen activity, although there is a tendency towards higher yield strengths with increasing reduction. Immediately after yield in a tensile test, for specimens cold-worked 90 and 70 percent prior to nitriding, there is a drop in the stress and the material behaves in a plastically unstable manner. No work-hardening takes place and the stress continues to fall until fracture; see Figure X.9(a). For material cold-worked to 47 percent reduction prior to nitriding, a small load drop occurs after yield, but the material recovers and work-hardens up to the ultimate tensile strength where necking occurs and leads to failure as shown in Figure X.9(b). This behaviour on nitriding at 585°C is in contrast with that observed in cold-worked alloys nitrided at 650°C at the same nitrogen activity. Here, as shown by Figure X.9(c), the elongation is much greater. It therefore seems desirable

Figure X.9

Nominal stress-strain curves for Fe-Ti alloys cold-worked by different amounts prior to nitriding.

(a) Fe-0·18^{w}% Ti cold-worked (90%) & nitrided 585°C a_N=0·045

(b) As above but 47% reduction

(c) Fe-0·15^{w}% Ti cold-worked (90%) & nitrided 650°C a_N=0·040

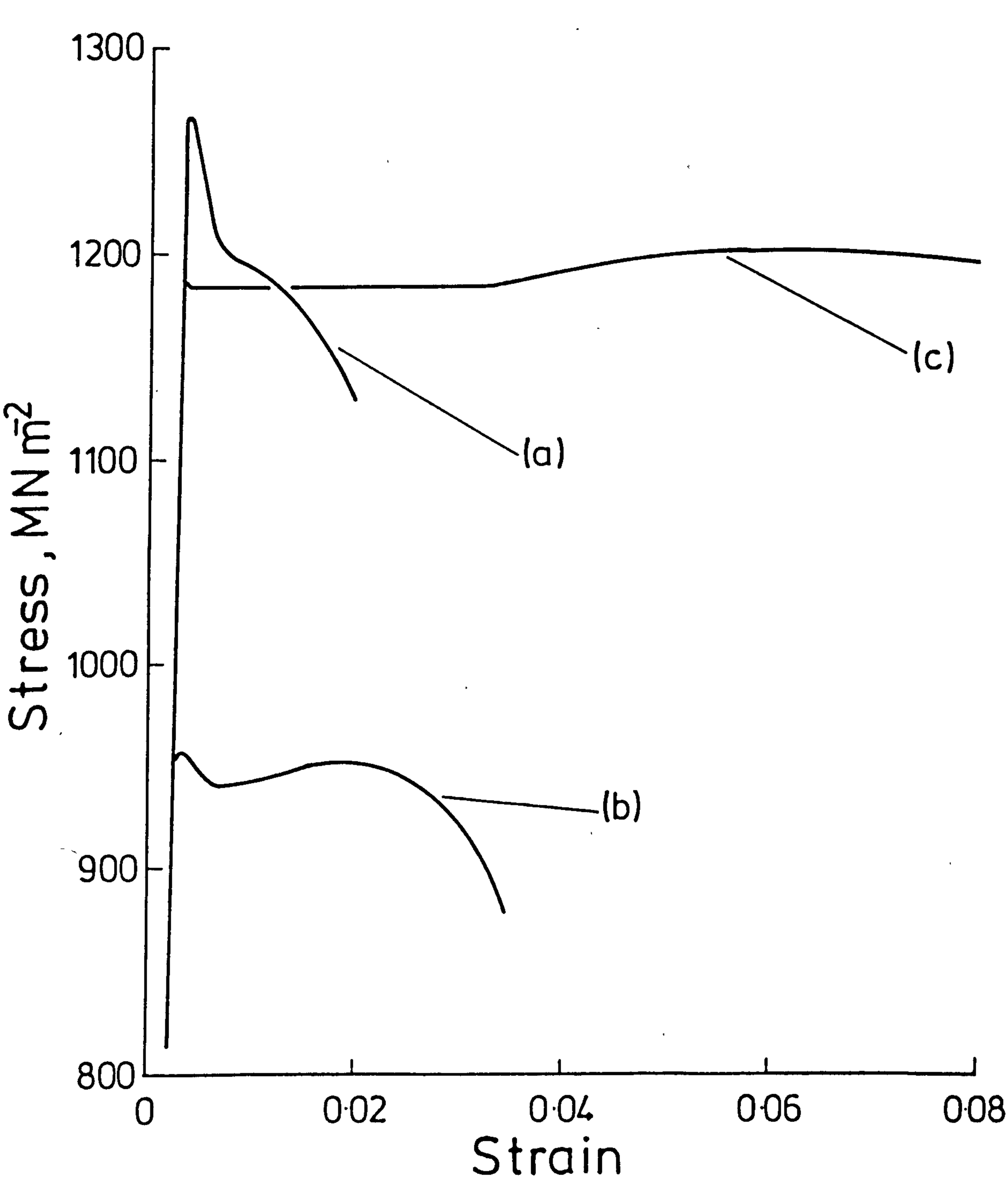

to allow the material to recrystallise to some extent in order to achieve reasonable elongations in cold-worked and nitrided alloys, a point discussed later in this Section.

Table X.2

Variation in yield stress for Fe-Ti alloys cold-worked prior to nitriding at 585°C

a_N in pure iron	% Reduction		
	47	70	90
0.018	1085*	1090	1220
0.045	960	1130	1270
0.079	1040	1185	1230
0.100	1040	1120	1250

*All stresses MN/m^2

Figure X.10(a) is an optical micrograph taken perpendicular to the tensile axis of an alloy cold-worked 90% and nitrided at 585°C with a nitrogen activity of about 0.1 and tested to failure. Extensive cracking has taken place and these cracks can be seen clearly in the corresponding scanning electron fractograph, Figure X.10(b), and seem to be associated with the banding produced by the cold deformation. In a cold-worked alloy a high proportion of boundaries run parallel to the rolling direction and if precipitation occurs during nitriding on these boundaries, they will be a source of weakness in a subsequent tensile test. Figure X.11(a) represents an idealised model of the specimen after nitriding. As the material is strained and in order to sustain continuity with surrounding regions, grains will rotate and if they contain what are effectively regions of a brittle phase, i.e. the shaded areas in Figure X.11(a), then delamination occurs and results in very high local stresses in regions labelled A in Figure X.11(b). Each small strip will fail in the same way as a tensile specimen shears off. This behaviour is actually observed in Figure X.10(a). Failure of the small strips is totally ductile and shows extensive micro-void coalescence; see Figure X.10(c). In Figure X.10(d), that of an alloy nitrided under the same conditions but cold-worked only 47% prior to nitriding, the strips are less numerous and joined together by small filaments. The ductility of this material is greater (see Figure X.9(b)) because the lower percentage of cold-work prior to nitriding

Figure X.10

Micrographs of cold-worked Fe-0.18 w/o Ti

(a) optical micrograph of material cold-worked 90% prior to nitriding in $12NH_3{:}88H_2$ at 585°C for 2.5 h.

(b) as in (a); scanning electron fractograph.

(c) as in (b); higher magnification of a selected area.

(d) scanning electron fractograph of material cold-worked 47% prior to nitriding in $12NH_3{:}88H_2$ at 585°C for 2.5 h.

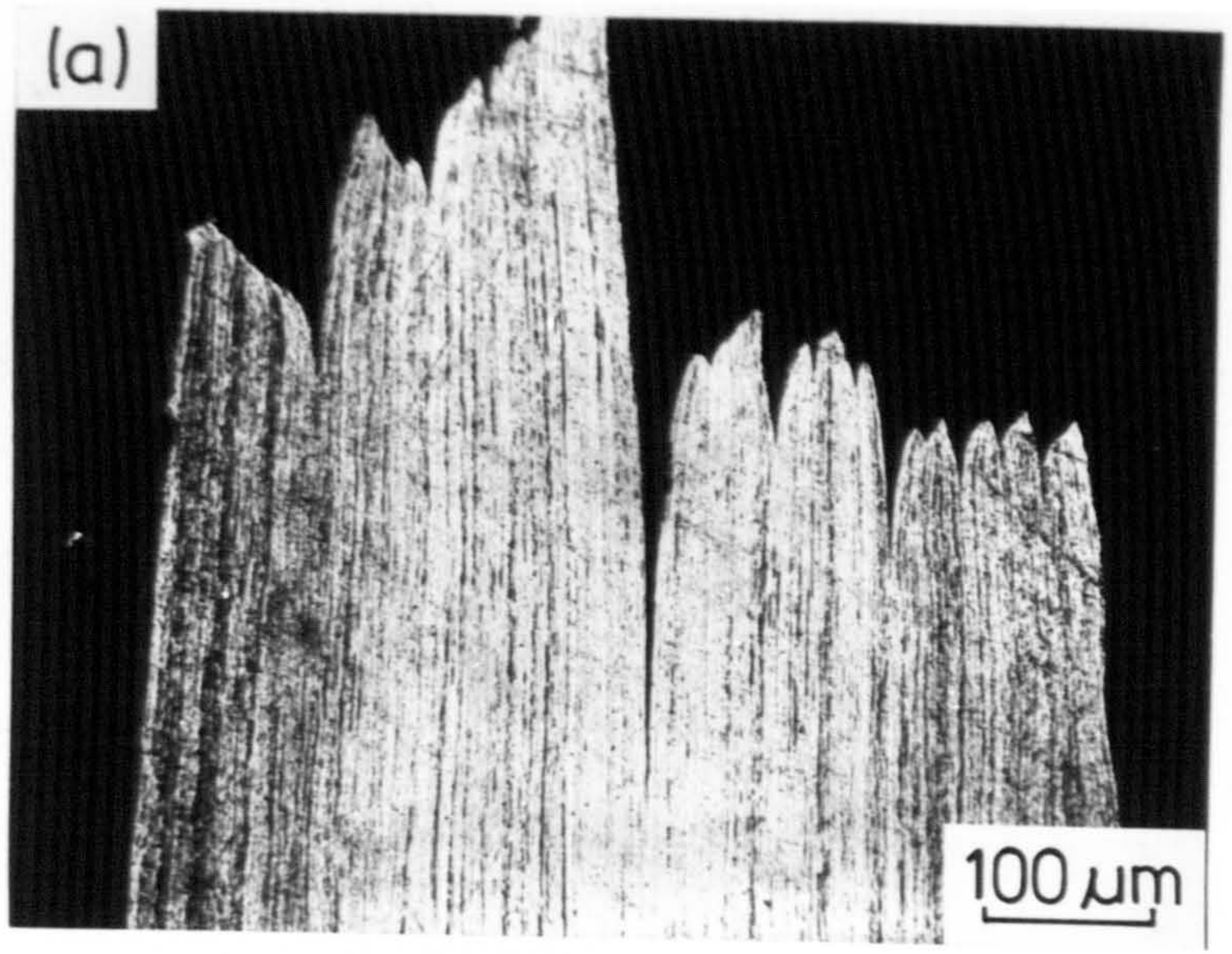
(a)
100 µm

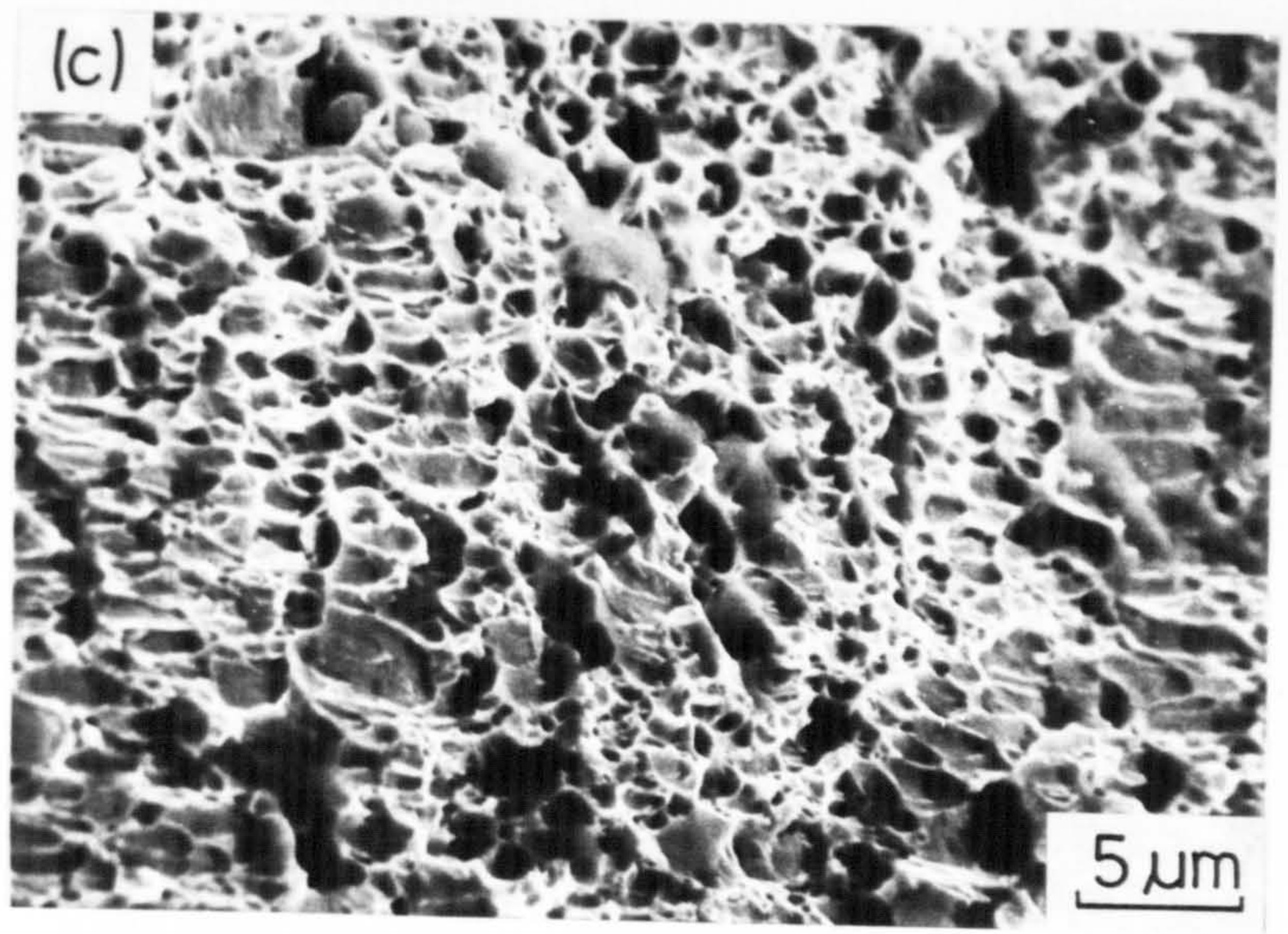
(c)
5 µm

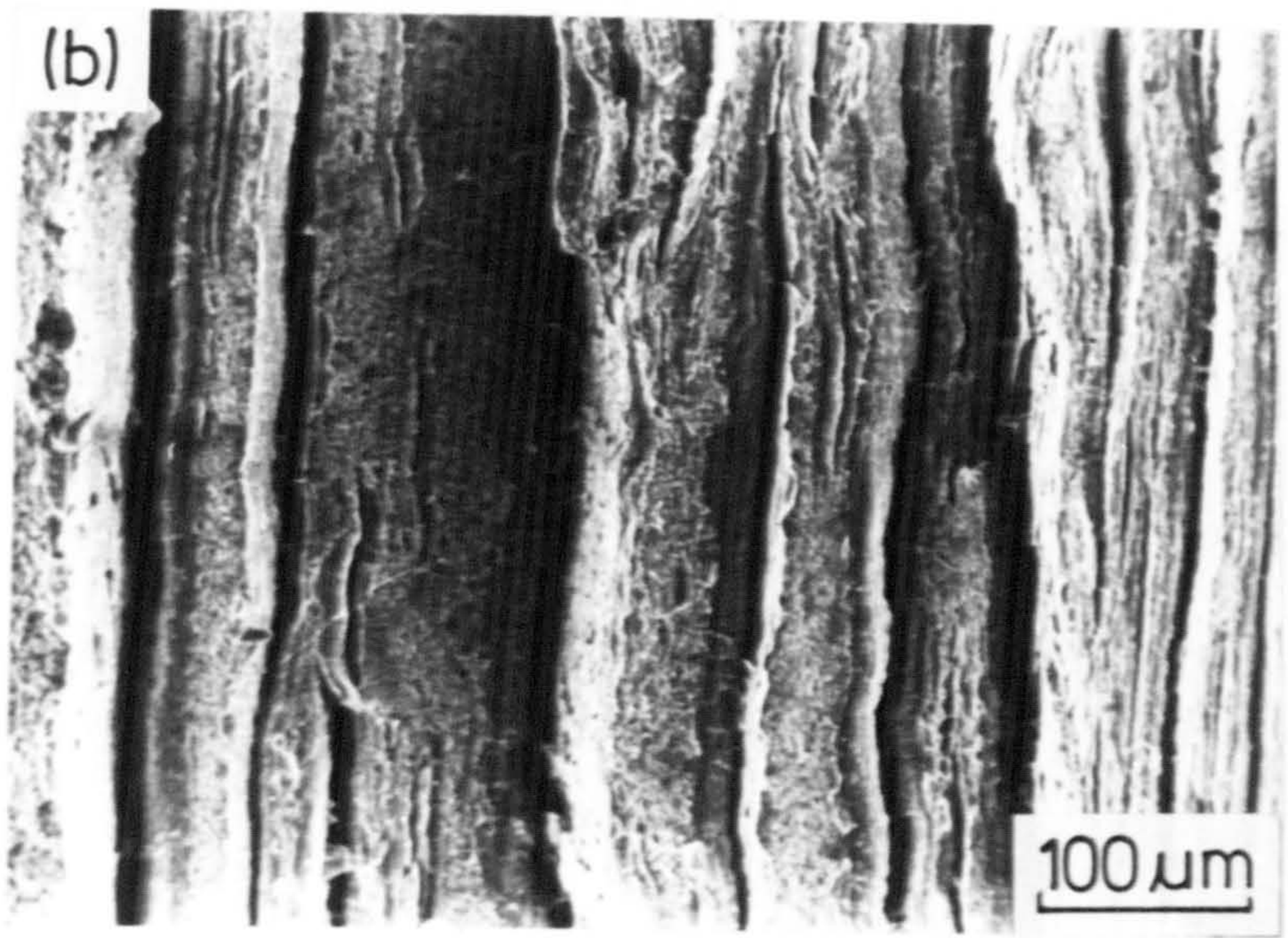
(b)
100 µm

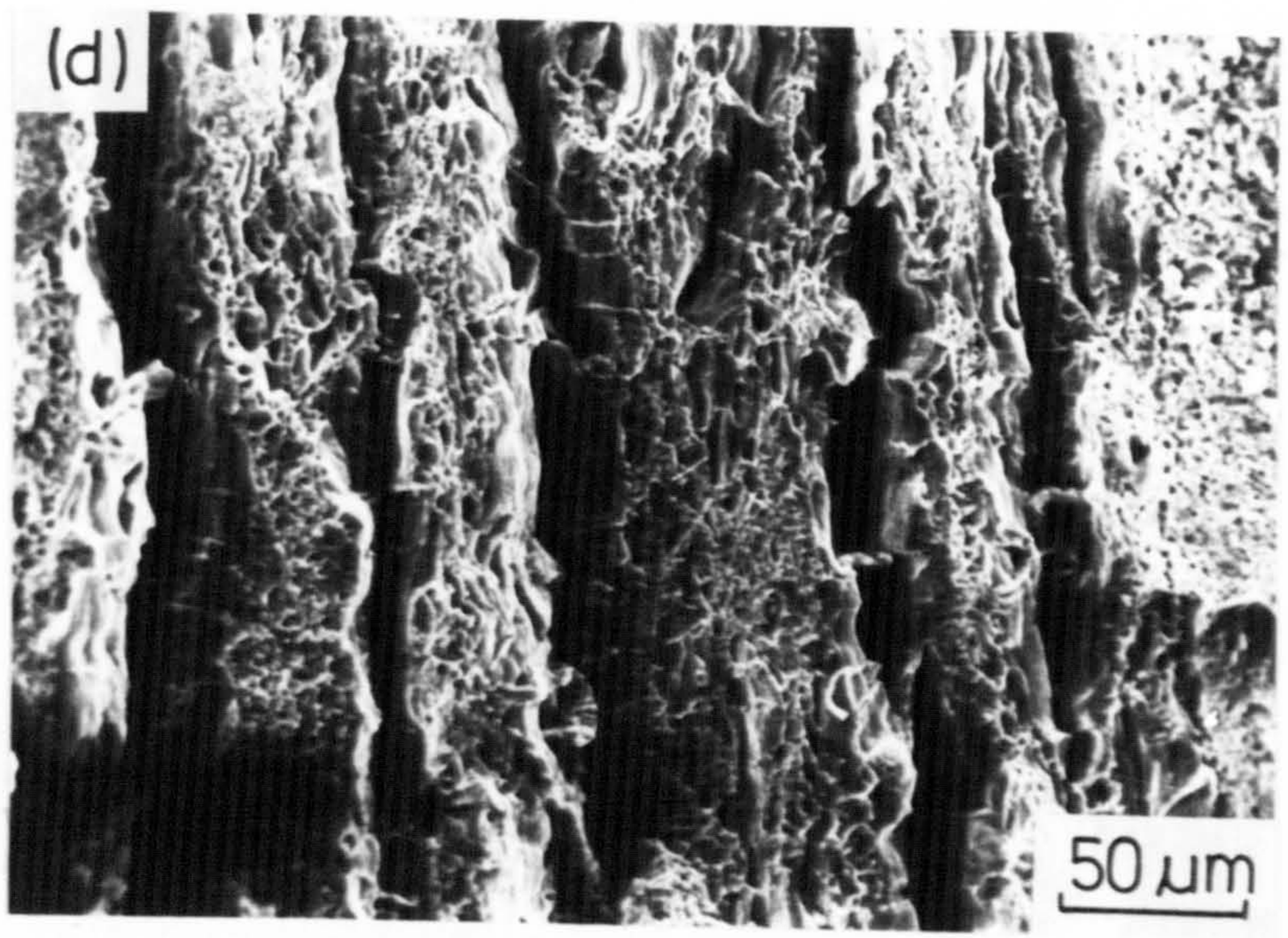
(d)
50 µm

Figure X.11

Schematic fracture behaviour of cold-worked and nitrided material.

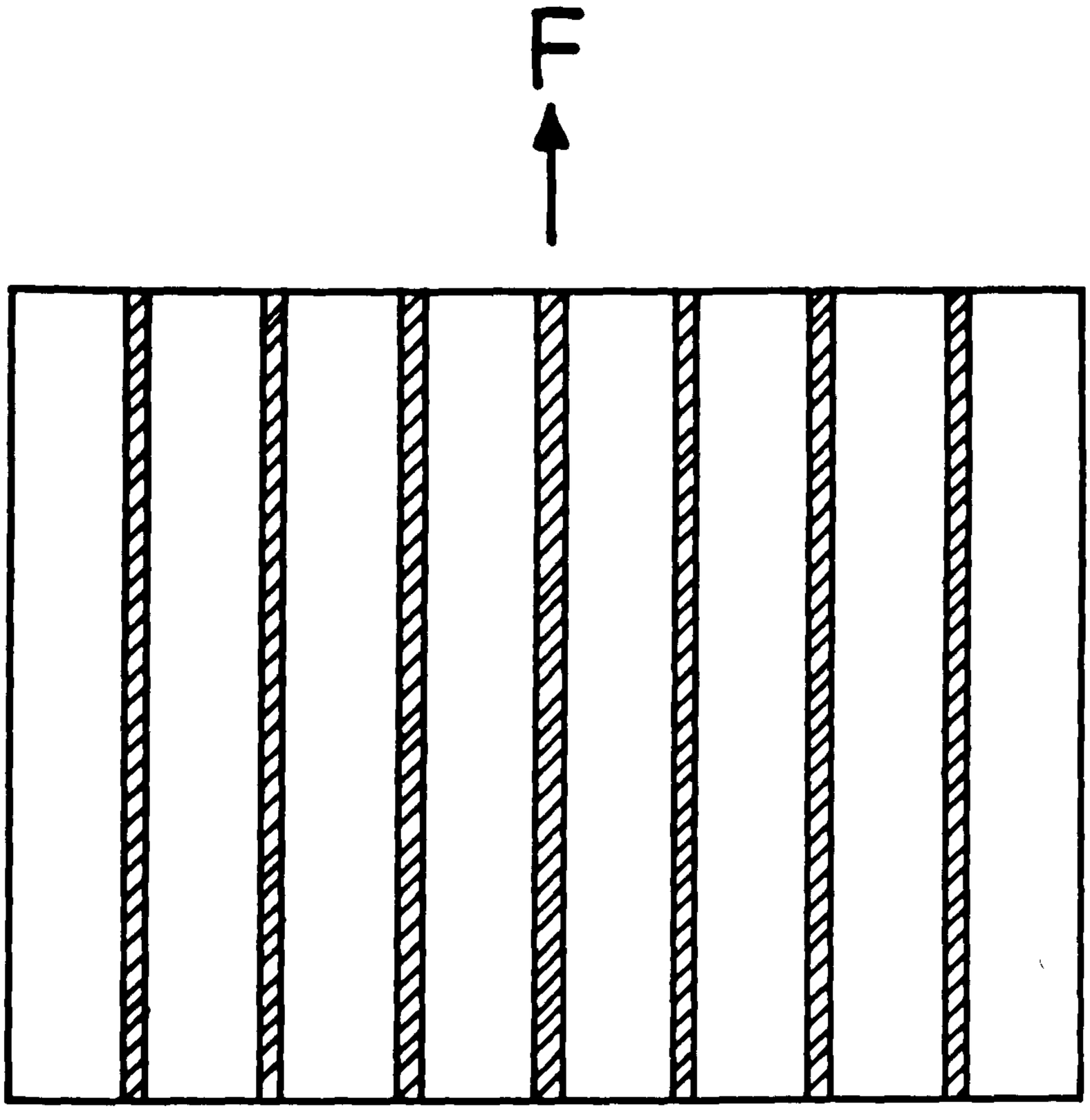

(a)

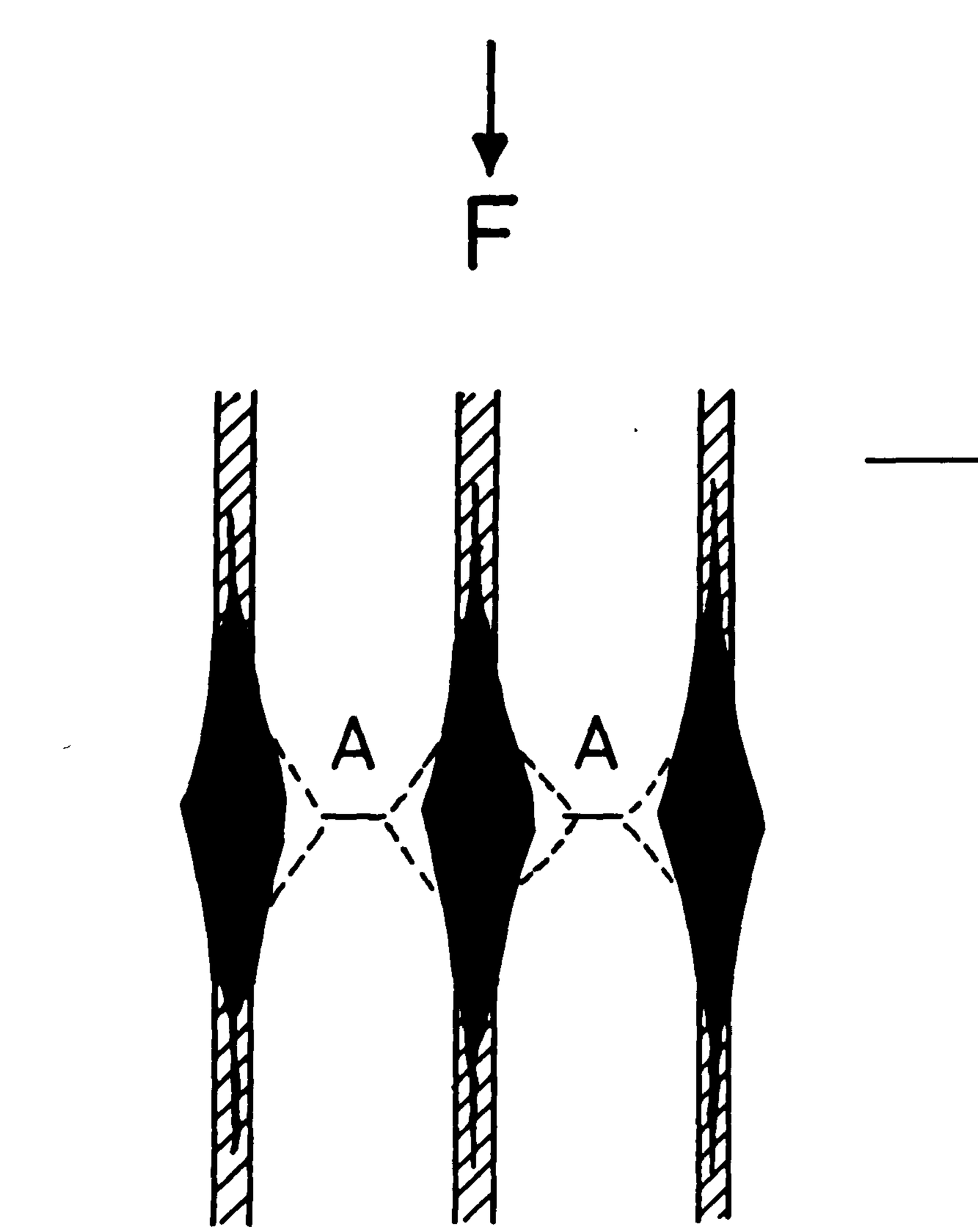

(b)

gives a less banded microstructure.

It seems that if cold-working prior to nitriding is used to improve the mechanical properties of ferritic alloys, the reductions must be small. Alternatively, a higher nitriding temperature can be used which allows limited recrystallisation to break up the banded structure produced by the cold work. When recrystallisation does not take place in alloys that have undergone large reductions prior to nitriding, the nitrided product is brittle on a macroscopic scale due to precipitation on subgrain boundaries that are preferentially aligned parallel to the rolling direction.

X.5 High-Temperature Aging of Cold-Worked and Nitrided Fe-Ti Alloys

The optical and scanning electron micrographs shown previously demonstrate the retardation of recrystallisation that results when precipitation of titanium nitride or Ti-N clusters occurs within the deformation cell structure. Figure X.12(a) shows that a dispersion of particles affects the recrystallisation when aging is carried out at high temperatures, i.e. Fe-0.15 w/o Ti cold-worked 90% prior to nitriding at 650°C in $3NH_3$:$97H_2$ and then aged at 800°C for 240 h. The optical micrograph shows some banding at the edges of the specimen with recrystallised grains in

Figure X.12

Micrographs of Fe-0.15 w/o Ti, cold-worked (90%) then nitrided in $3NH_3$:$97H_2$ at 650°C for 5 h, then hydrogen reduced at 650°C for 5 h and aged at 800°C for 240 h. (a) and (b) optical micrographs.

(c) and (d) electron micrographs of surface region in (a).

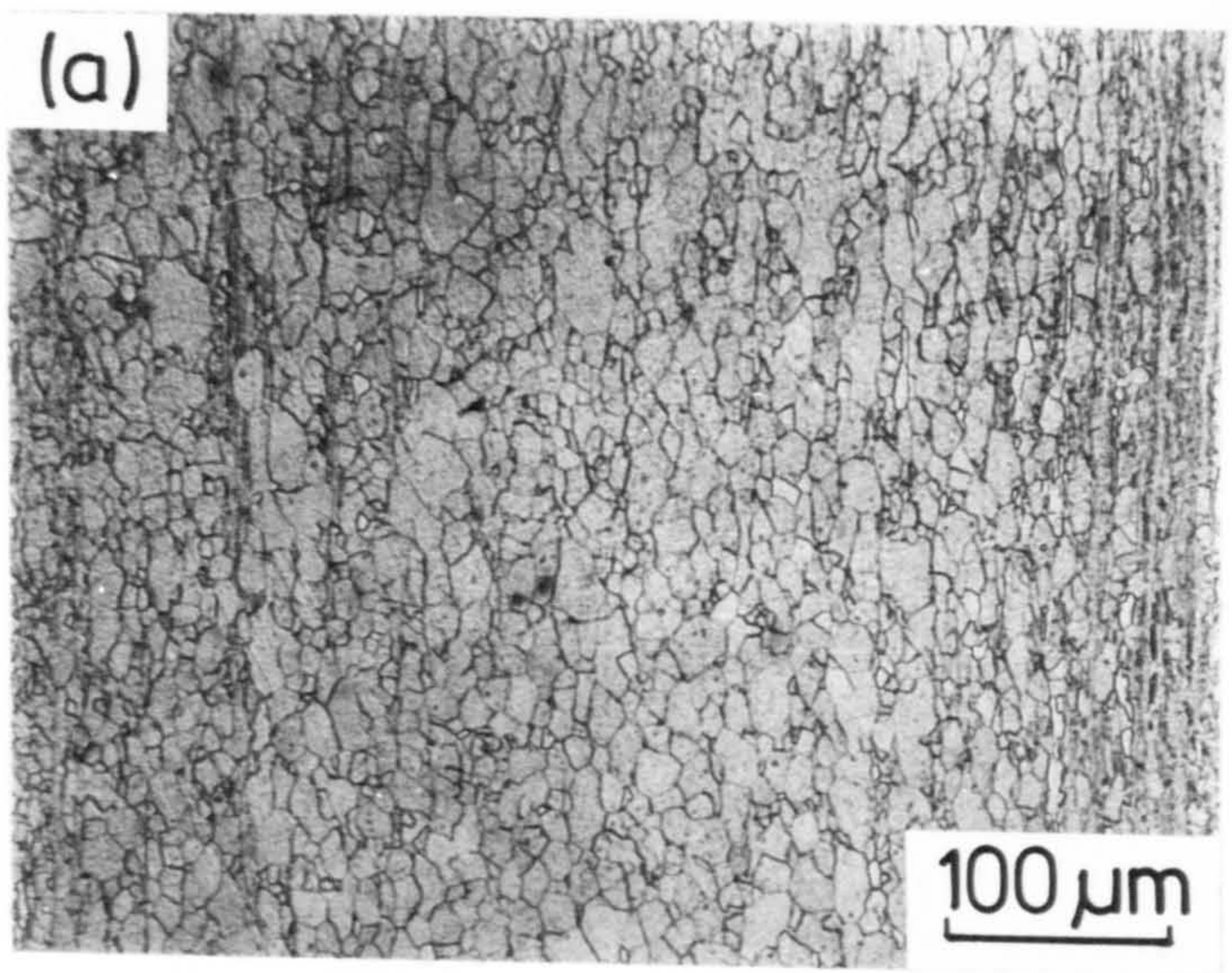
(a)
100 µm

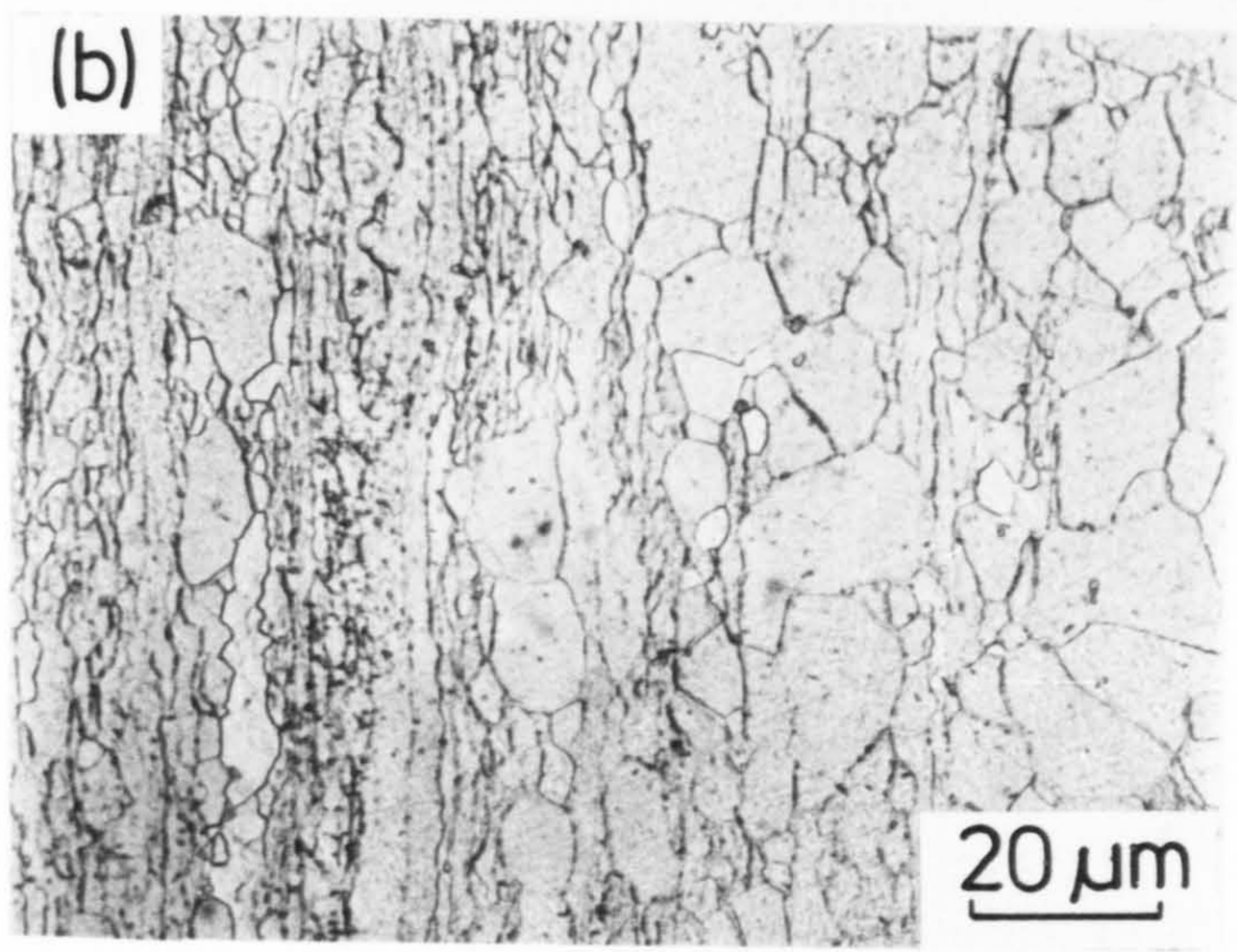
(b)
20 µm

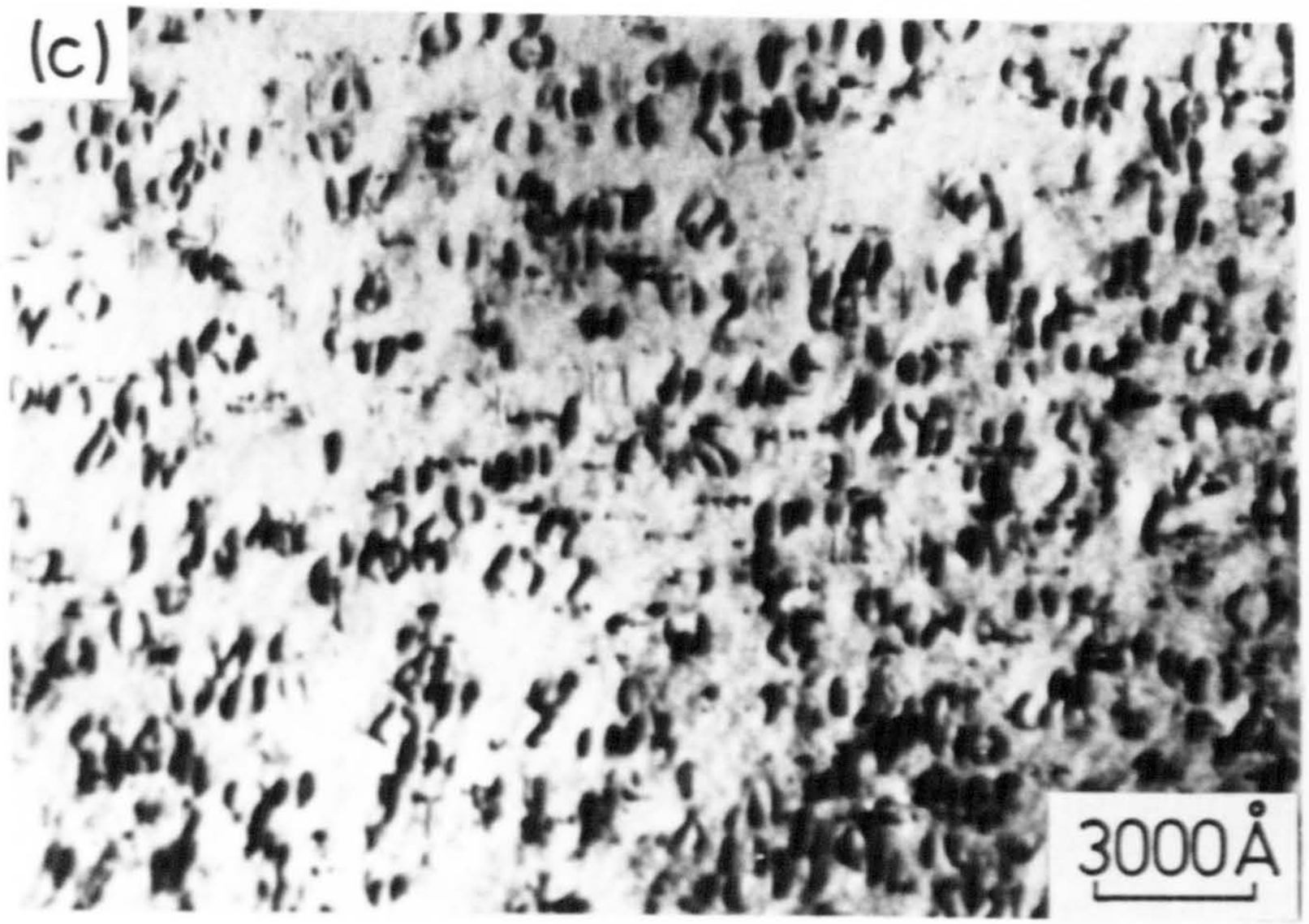
(c)
3000Å

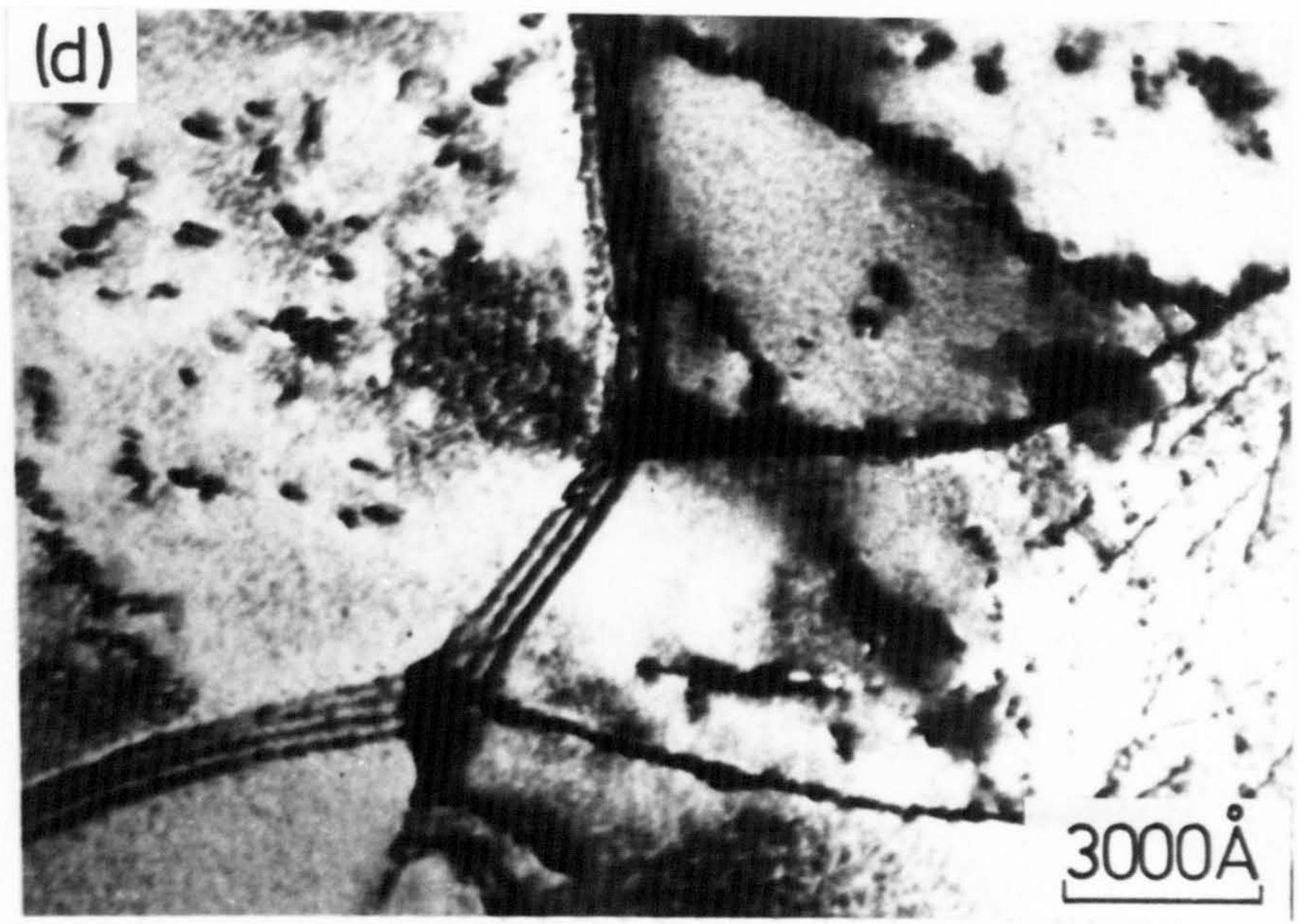
(d)
3000Å

the core. Figure X.12(b) is a higher magnification photomicrograph taken near the specimen surface and shows the gradation in structure. Electron microscopy close to the surface shows the complex nature of the microstructure; in some regions there is a homogeneous dispersion of disc-shaped TiN precipitates as shown in Figure X.12(c), while in other areas there is still evidence of dislocation sub-cells in addition to the precipitate dispersion; see Figure X.12(d). The formation of a homogeneous dispersion of precipitates on aging suggests that homogeneous clustering within the dislocation sub-cells occurs during nitriding in addition to heterogeneous precipitation onto dislocations.

The dislocation arrays in cold-worked and nitrided materials are remarkably stable and since the precipitates are slow to overage, high strengths can be retained even after long times at temperatures up to 800°C. Figure X.13 shows a transmission electron micrograph of a dislocation array in annealed and nitrided Fe-0.15 w/o Ti after aging for 240 h at 800°C and clearly indicates the stabilising effect of the TiN precipitates which decorate the dislocation network.

X.6 General Discussion

The results presented in this chapter show that it is possible to achieve useful properties from nitrided

Figure X.13

Transmission electron micrograph of a dislocation array in Fe-0.15 w/o Ti, annealed then nitrided in $3NH_3$:$97H_2$ at 650°C for 5 h, then hydrogen reduced at 650°C for 5 h and aged at 800°C for 240 h.


0·5µm.

materials by cold-working prior to nitriding. However, it has not been possible, due to the complex nature of the microstructure, to separate the effects of dislocation structure and substitutional-interstitial solute-atom clustering.

HSLA steels for vehicle manufacture and engineering components are gradually being replaced by dual-phase steels since the latter offer advantages through weight reduction and hence possible fuel economy. In Figure X.14 strengths and ductilities obtained in the present investigation, together with additional results obtained at Newcastle for cold-worked and nitrided Fe-Nb alloys (Sakemoto, 1980) are compared with similar properties of commercial HSLA steels and dual-phase steels. On this basis, cold-worked and nitrided alloys might offer a useful extension to the present generation of HSLA steels although it is unlikely that ductility can be improved significantly. One advantage of cold-worked and nitrided materials, however, is in formability. In general, the higher the strength of a material the lower is its formability. However, the interstitial-free starting materials of the present work are soft and can be formed with the greatest ease. The subsequent strengthening is by gaseous nitriding. A further advantage of these "formable and strengthenable" steels is their simple and economical compositions.

Figure X.14

Comparison of the tensile properties of cold-worked and nitrided alloys with commercial low-alloy steels.

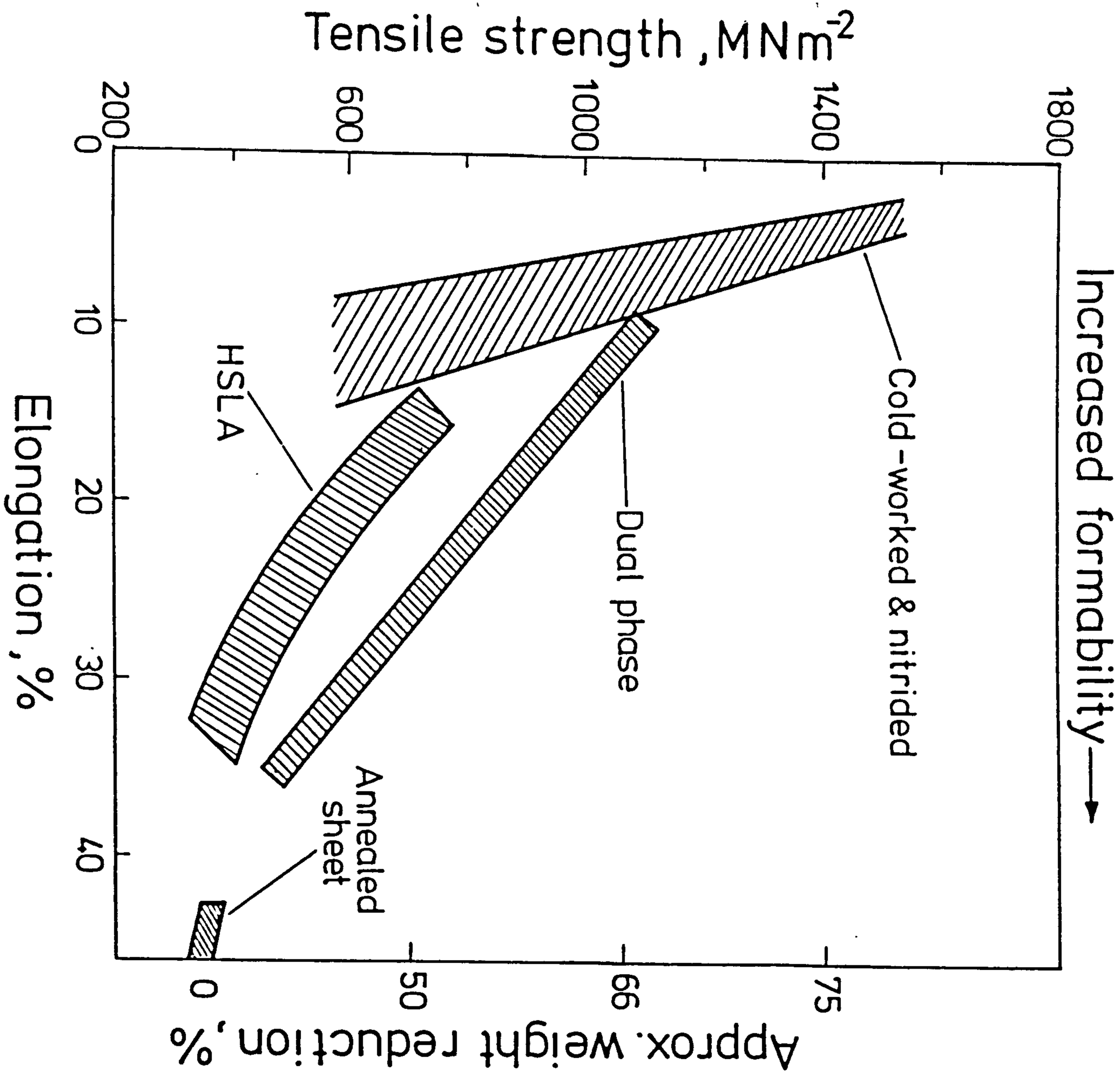
Tensile strength, MNm^{-2}
200
0
600
1000
1400
1800
Increased formability
Elongation, %
10
20
30
40
HSLA
Cold-worked & nitrided
Dual phase
Annealed sheet
Approx. weight reduction, %
0
50
66
75

X.7 Conclusions

(1) Cold-working Fe-Ti alloys prior to nitriding greatly reduces the embrittling effects observed with annealed and nitrided materials. It is possible, however, for cold-worked and nitrided materials to show poor ductility if nitriding is carried out at temperatures too low for limited recrystallisation to take place.

(2) Nitriding stabilises the cold-worked structure by heterogeneous precipitation of TiN or Ti-N clusters and this leads to higher strengths than with annealed and nitrided alloys. It is impossible to predict exactly the increases in strength because of the complex nature of the microstructure.

Chapter XI

CLUSTERING IN A COMMERCIAL STEEL

XI.1 Introduction

A number of experiments have been carried out to test the proposed model for the strengthening of Fe-Ti alloys in a commercial steel. The alloy used was developed by Armco Steel Corporation and is a deep drawing steel. Since strengthening is imparted by nitriding after forming, complex high-strength stampings can be produced which could not otherwise be fabricated from high strength steels; the steel is therefore "formable and strengthenable" (FS).

XI.2 Results and Discussion

Samples of the alloy, which had been either cold-worked 30% or annealed, were nitrided at 650°C in ammonia-hydrogen gas mixtures for 5 h. Selected samples were hydrogen reduced at 500°C after nitriding to remove "excess" nitrogen. The yield strength of the cold-worked and nitrided material is always higher than the corresponding sample which had been annealed prior to nitriding (see Figure XI.1) although both increase with nitriding potential (R). For the annealed and nitrided alloy the lower yield strengths after hydrogen reduction are consistent with the removal of "excess" nitrogen from solid solution. As observed with nitrided

Figure XI.1

Yield strength against nitriding potential (R) for "FS" alloys annealed or cold-worked (30%) prior to nitriding at 650°C for 5 h; selected samples are hydrogen reduced at 500°C for 18 h.

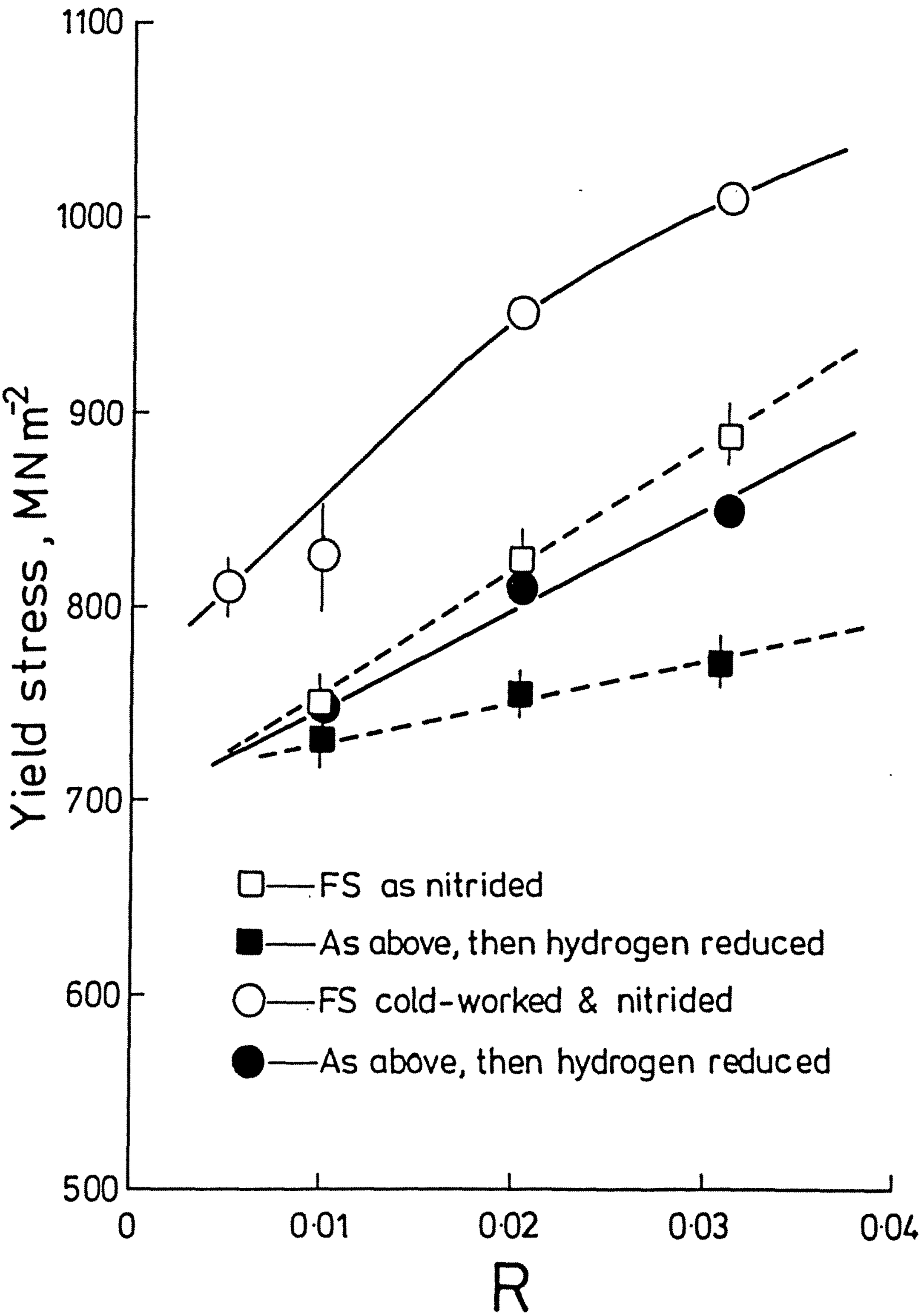
1100
1000
900
800
700
600
500
Yield stress, MN m-2
0
0·01
0·02
0·03
0·04
R
□—FS as nitrided
■—As above, then hydrogen reduced
○—FS cold-worked & nitrided
●—As above, then hydrogen reduced

Fe-Ti alloys in Chapter IX, there is no improvement in ductility on hydrogen reduction (see Figure XI.2(a)) showing that reduced ductility is again a consequence of a fine dispersion of particles in the ferrite matrix. The lattice parameter of annealed and nitrided material is higher than that of pure iron (2.8664 Å) confirming the presence of Ti-N clusters in the "FS" material; see Table XI.1. However, the lattice parameter results do indicate some loss of titanium from solid-solution.

Table XI.1

Lattice parameters of "FS" after nitriding at 650°C for 5 h at different nitriding potentials (R)

R	a, Å	w/o N by X-ray*	Total w/o N
0	2.8667	-	-
0.06	2.8679	0.043	0.070
0.20	2.8684	0.061	0.097
0.31	2.8684	0.061	0.115

*assuming Δa_N = 0.0070 Å per a/o N. This is a measure of the nitrogen in random solid solution and in clusters; the difference between columns 3 and 4 is the nitrogen precipitated as TiN and other nitrides.

Figure XI.2

Variation of (a) uniform elongation and (b) weight gain for "FS" alloys annealed or cold-worked (30%) prior to nitriding at 650°C for 5 h; selected samples are hydrogen reduced at 500°C for 18 h.

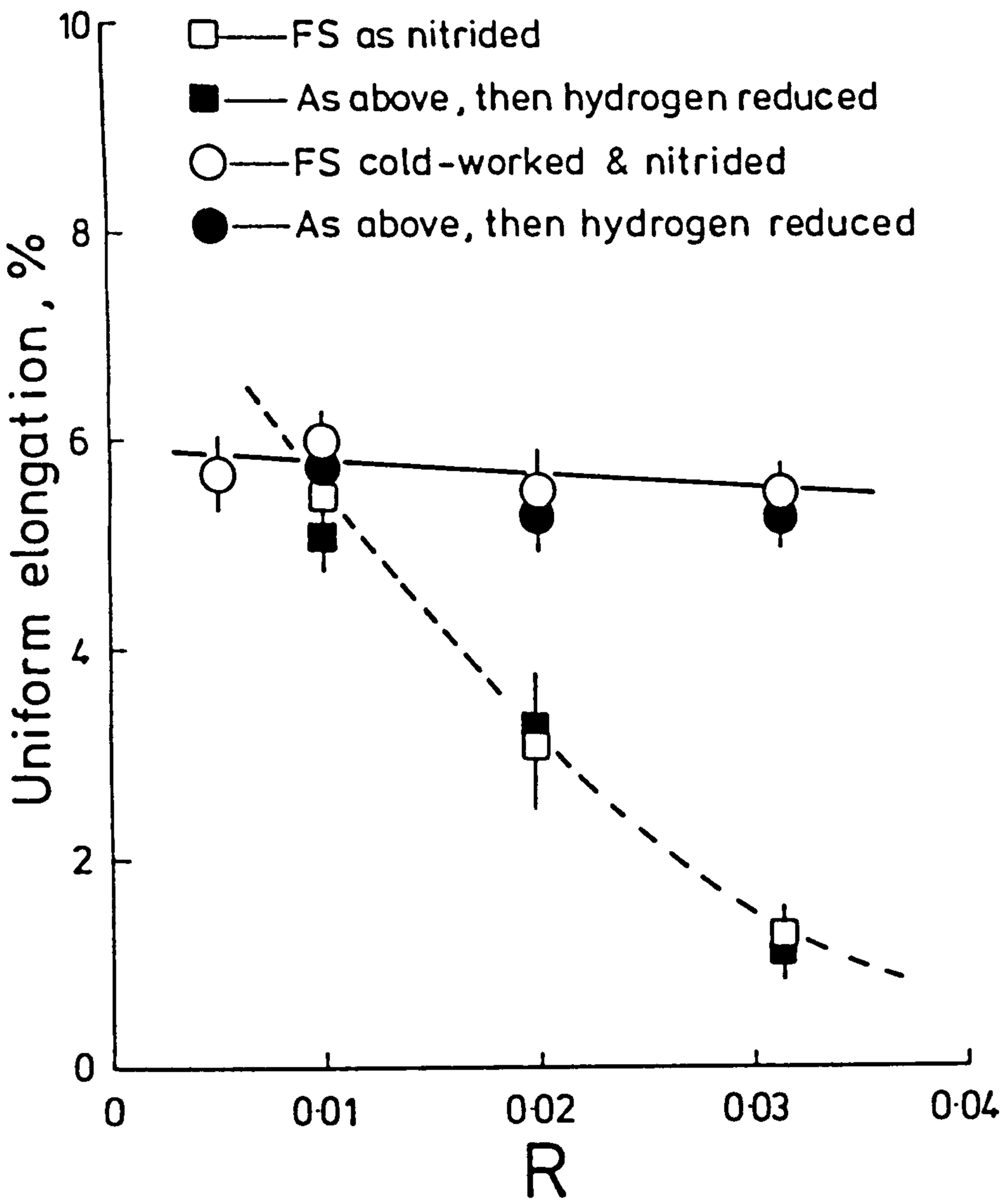
(a)
FS as nitrided
As above, then hydrogen reduced
FS cold-worked & nitrided
As above, then hydrogen reduced
Uniform elongation, %
10
8
6
4
2
0
0
0·01
0·02
0·03
0·04
R

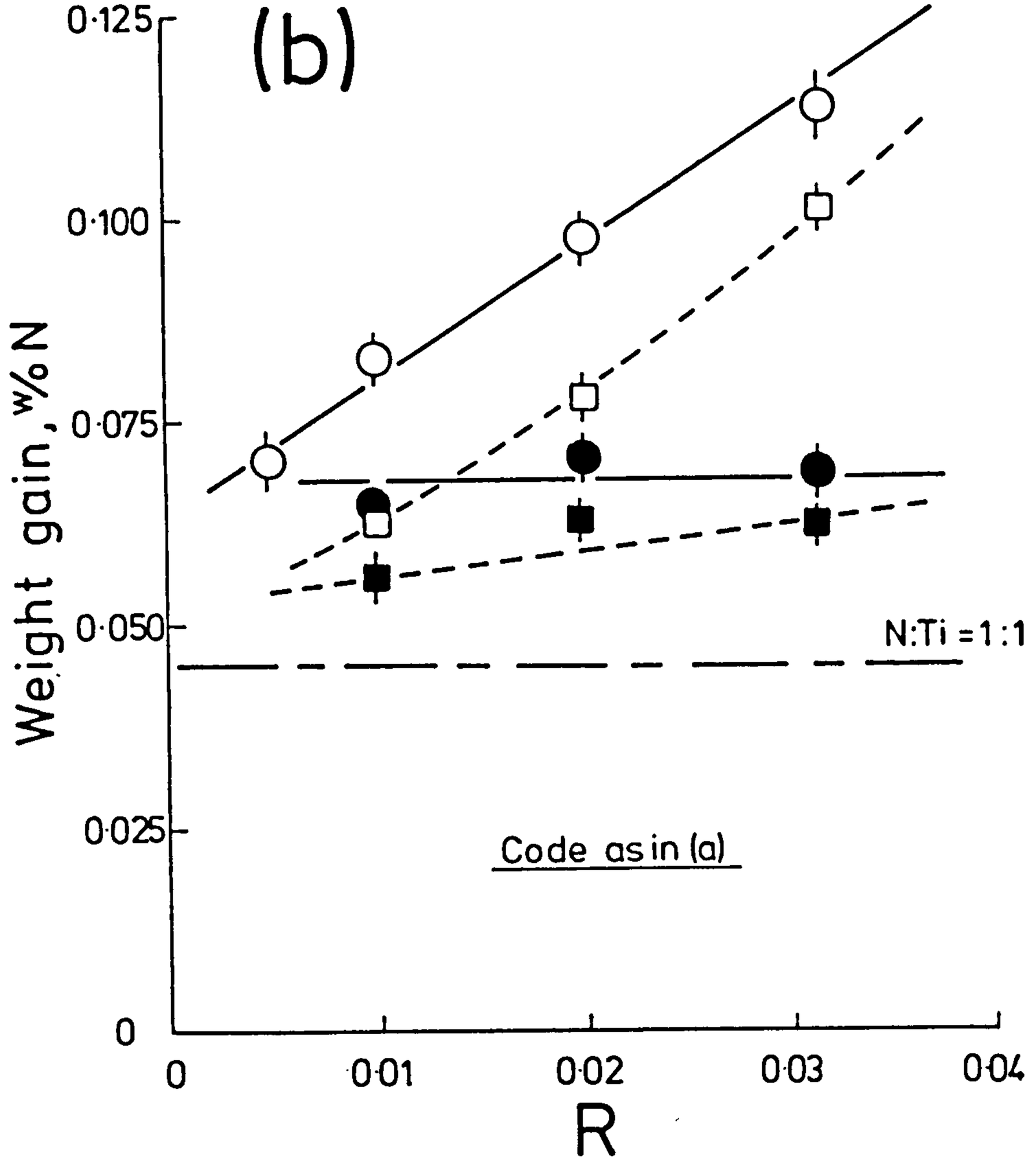
(b)
Weight gain, %N
0·125
0·100
0·075
0·050
0·025
0
N:Ti = 1:1
Code as in (a)
0
0·01
0·02
0·03
0·04
R

The cold-worked material shows the expected increases in strength and improvements in ductility over annealed and nitrided material (see Figures XI.1 and XI.2(a) respectively) although the alloy has been cold-worked only 30% prior to nitriding. The weight gain observed on nitriding cold-worked material is higher than that in the annealed alloy. This feature was not observed in the experimental Fe-0.15 w/o Ti alloy and is a consequence of the 0.05 w/o Al in solid solution in the "FS" alloy. It is generally thought that aluminium nitride cannot precipitate homogeneously in ferrite due to its complex crystal structure (hexagonal) and so must precipitate heterogeneously (Podgurski & Knechtel, 1969). Nitriding to form Ti-N clusters therefore provides a high volume fraction of heterogeneous sites onto which the AlN can precipitate. For this reason, on hydrogen reduction of annealed and nitrided material the weight change does not correspond to a N:Ti atomic ratio of 1:1 as shown in Figure XI.2(b). The slight dependence of weight gain on R is due to different amounts of aluminium nitride precipitating onto Ti-N clusters. Nitriding in $1NH_3:99H_2$ at 650°C for long periods causes the yield strength of the nitrided material to fall slightly as the Ti-N clusters overage, but the alloy continues to pick-up nitrogen (see Table XI.2) showing that aluminium nitride is still precipitating heterogeneously within the material or possibly that aluminium is being incorporated into the Ti-N cluster. The

Table XI.2

Variation in yield strength and weight gain for "FS" nitrided in $1NH_3:99H_2$ at 650°C for the times indicated

time, h	Yield strength, MN/m^2	Weight gain w/o N
5	750	0.063
8.5	750	0.068
18	740	0.072
70	680	0.086
140	-	0.088

final weight gain on nitriding is in reasonable agreement with the removal from solution of all nitride forming elements plus the amount of nitrogen in equilibrium with the ferrite matrix. On nitriding the cold-worked alloy the aluminium nitride precipitates onto dislocations, and as there are sufficient heterogeneous sites to remove all the aluminium from solution the weight gain after hydrogen reduction is independent of R; see Figure XI.2(b).

Scanning electron microscopy of annealed and nitrided material shows a change in fracture behaviour from micro-void coalescence in the as-annealed alloy, Figure XI.3(a), to intergranular and cleavage failure of the as-nitrided material; see Figure XI.3(b). On hydrogen reduction, no changes in fracture behaviour are observed (Figure XI.3(c)) and both as-nitrided and nitrided and hydrogen reduced material show evidence of precipitation at grain boundaries; these grain boundary precipitates can be clearly seen in Figure XI.3(d). The as-cold-worked material fails by micro-void coalescence; Figure XI.4(a). The grain structure after nitriding still shows evidence of the rolling operation, being slightly elongated in the direction of working as shown by Figure XI.4(b). A fractograph of the cold-worked and nitrided alloy showing a mixture of intergranular, cleavage and micro-void coalescence failure modes is shown in Figure XI.4(c) while Figure XI.4(d) shows a greater proportion of micro-void coalescence for the cold-worked nitrided and hydrogen reduced material. These observations are similar to those in nitrided Fe-Ti alloys and indicate that the grain boundary precipitation of a second-phase, which is very detrimental to properties, can be prevented in a commercial alloy by cold-working prior to nitriding.

The "FS" alloy therefore behaves in a similar manner to laboratory-cast Fe-0.15 w/o Ti showing that a simple system can be used as a model for a more complex one. It should be pointed out, however, that the effect of aluminium

Figure XI.3

Scanning electron fractographs of "FS"

(a) un-nitrided.

(b) annealed and nitrided in $2NH_3$:$98H_2$ at $650^{\circ}C$ for 5 h.

(c) as in (b); hydrogen reduced at $500^{\circ}C$ for 18 h.

(d) as in (b).

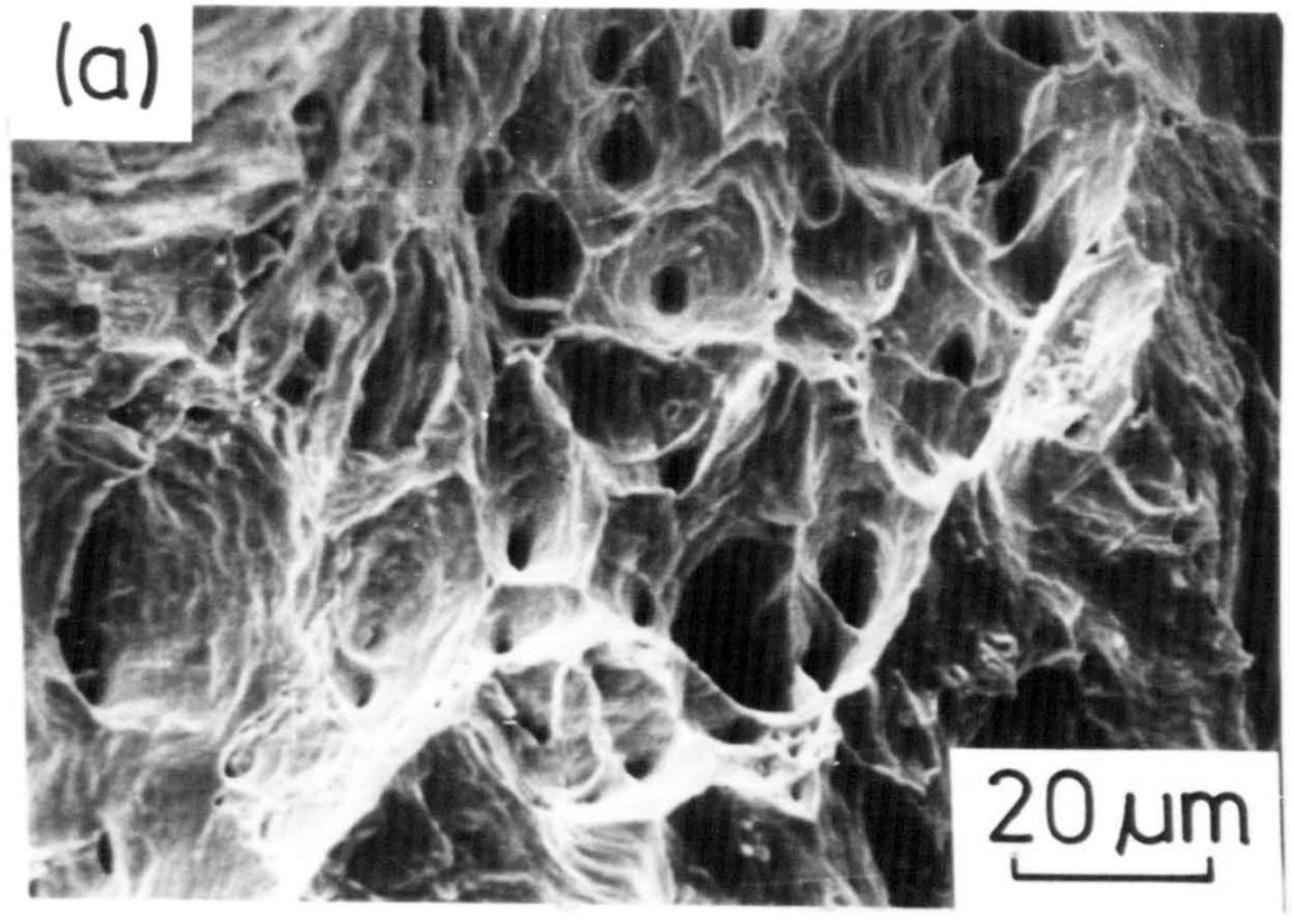
(a)
20 µm

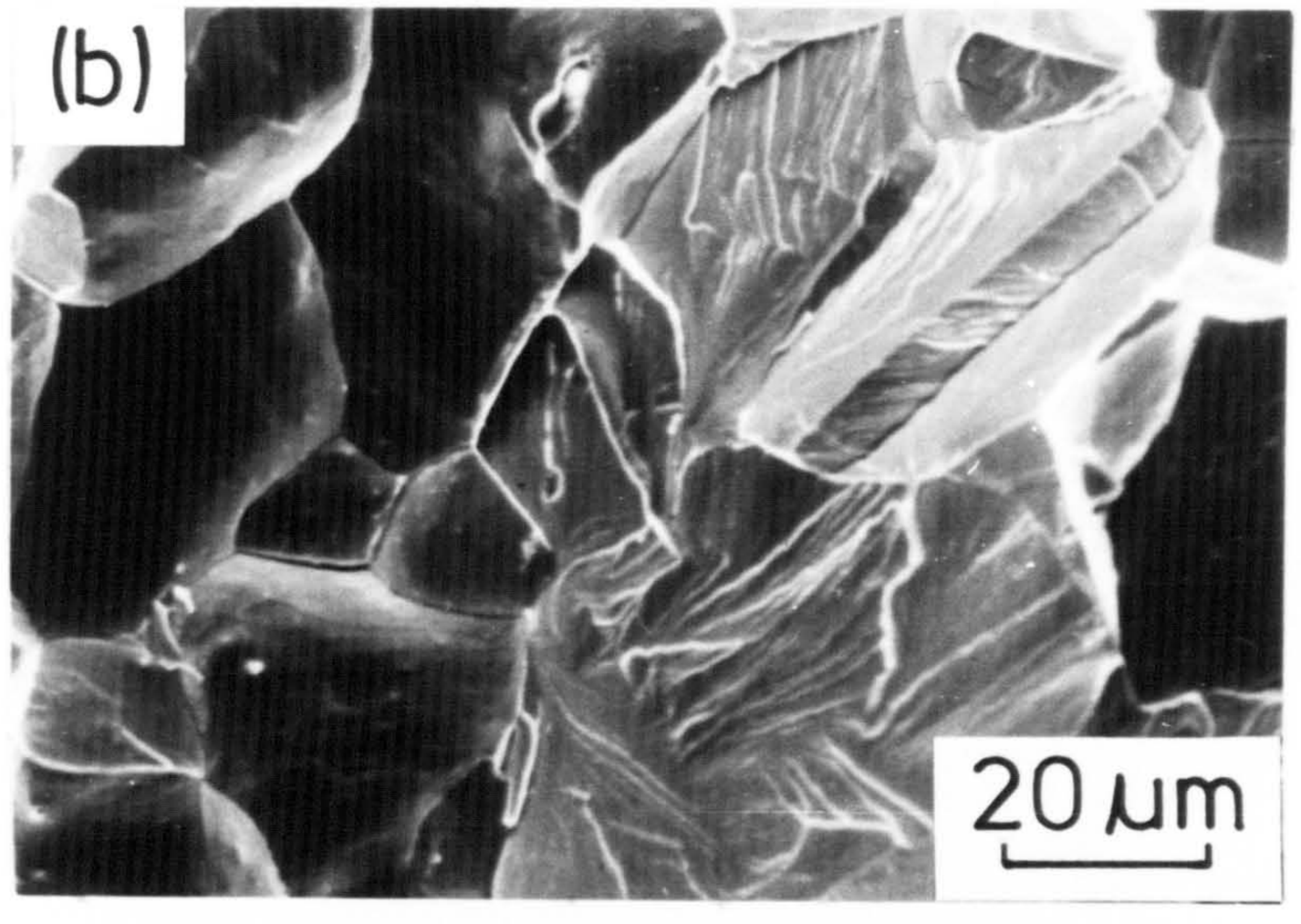
(b)
20 µm

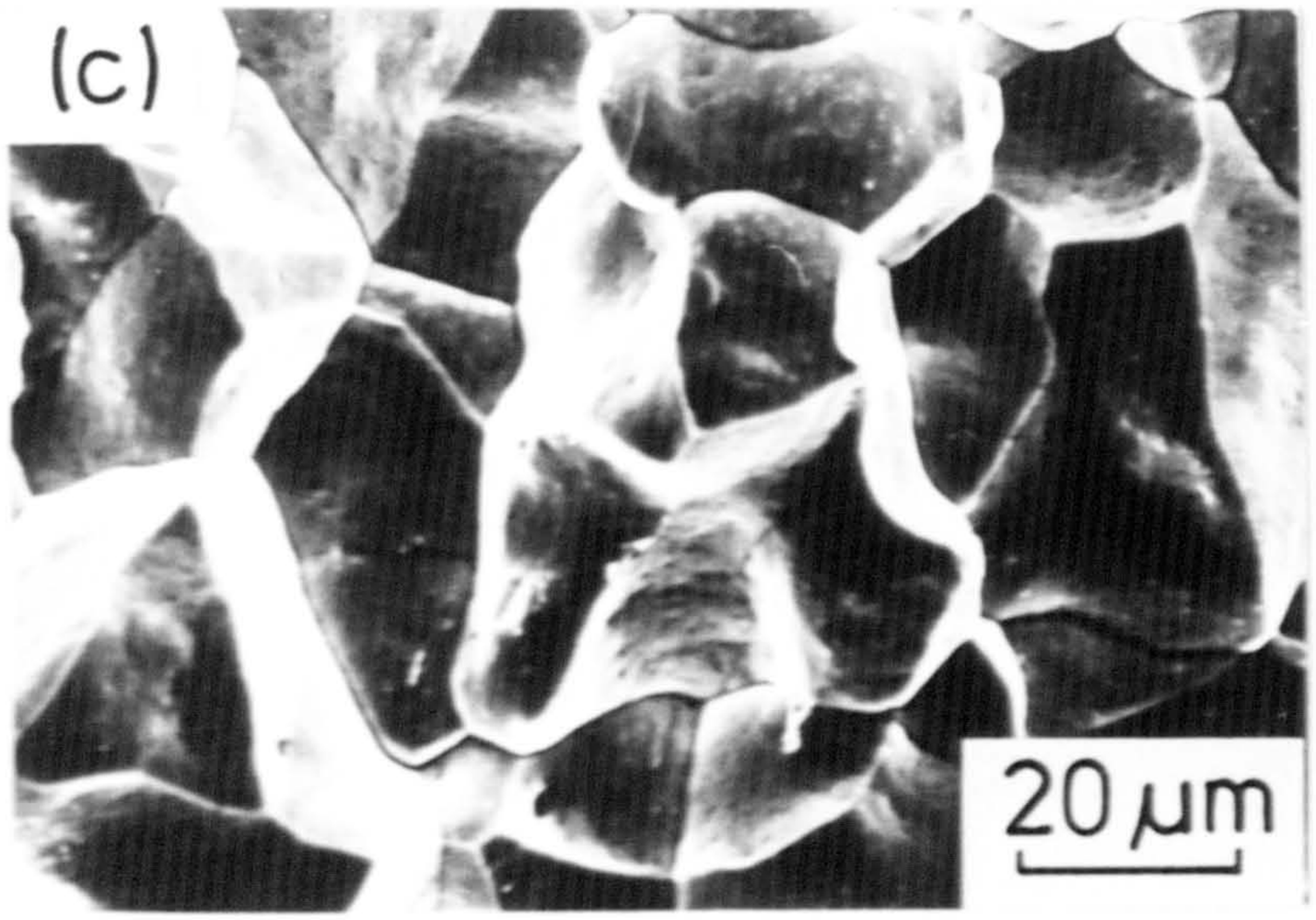
(c)
20 µm

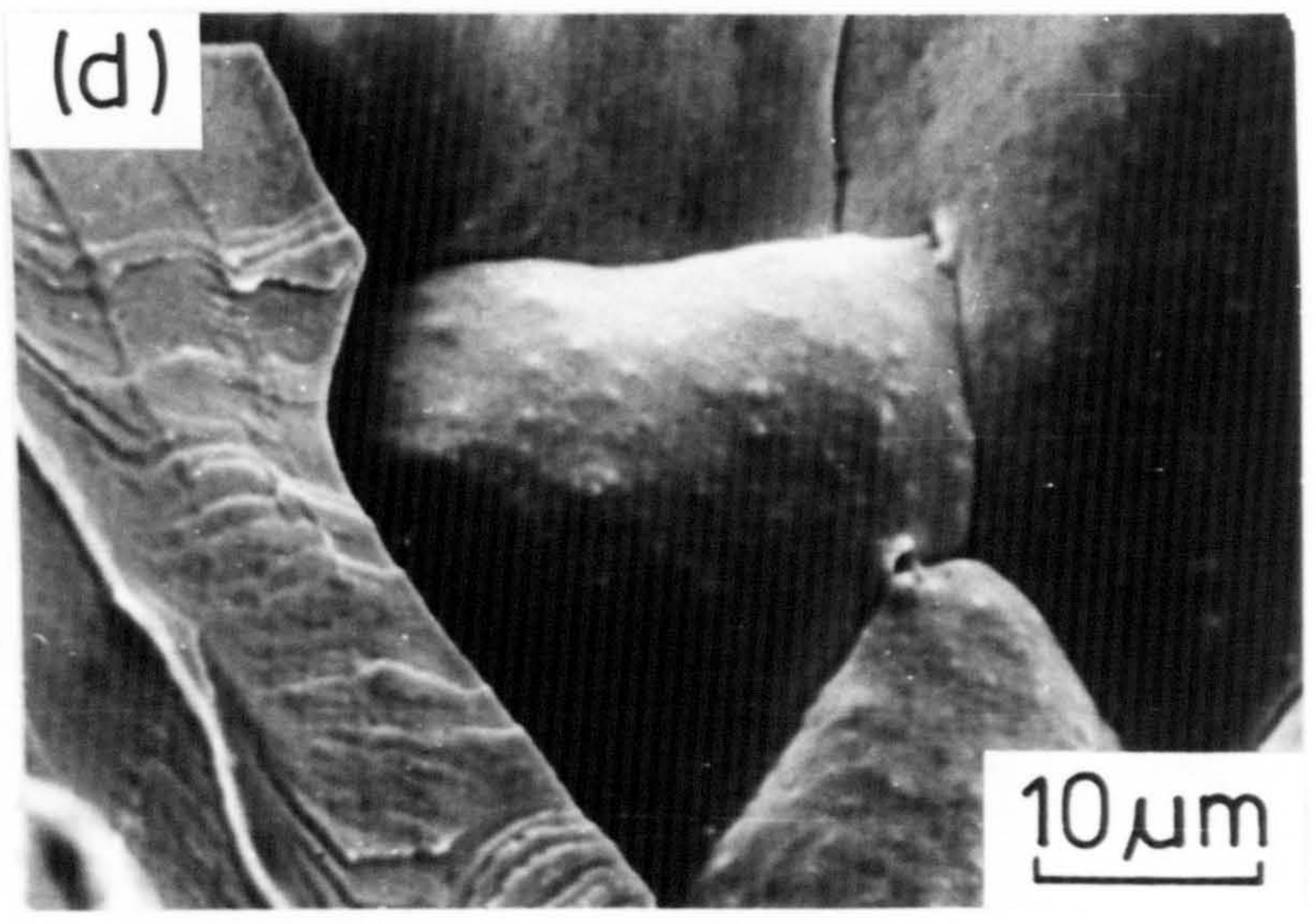
(d)
10 µm

Figure XI.4

Micrographs of cold-worked (30%) FS

(a) scanning electron fractograph of the un-nitrided alloy.

(b) optical micrograph of material nitrided in $3NH_3:97H_2$ at 650°C for 5 h.

(c) scanning electron fractograph of material nitrided in $3NH_3:97H_2$ at 650°C for 5 h.

(d) as in (c); hydrogen reduced at 500°C for 18 h.

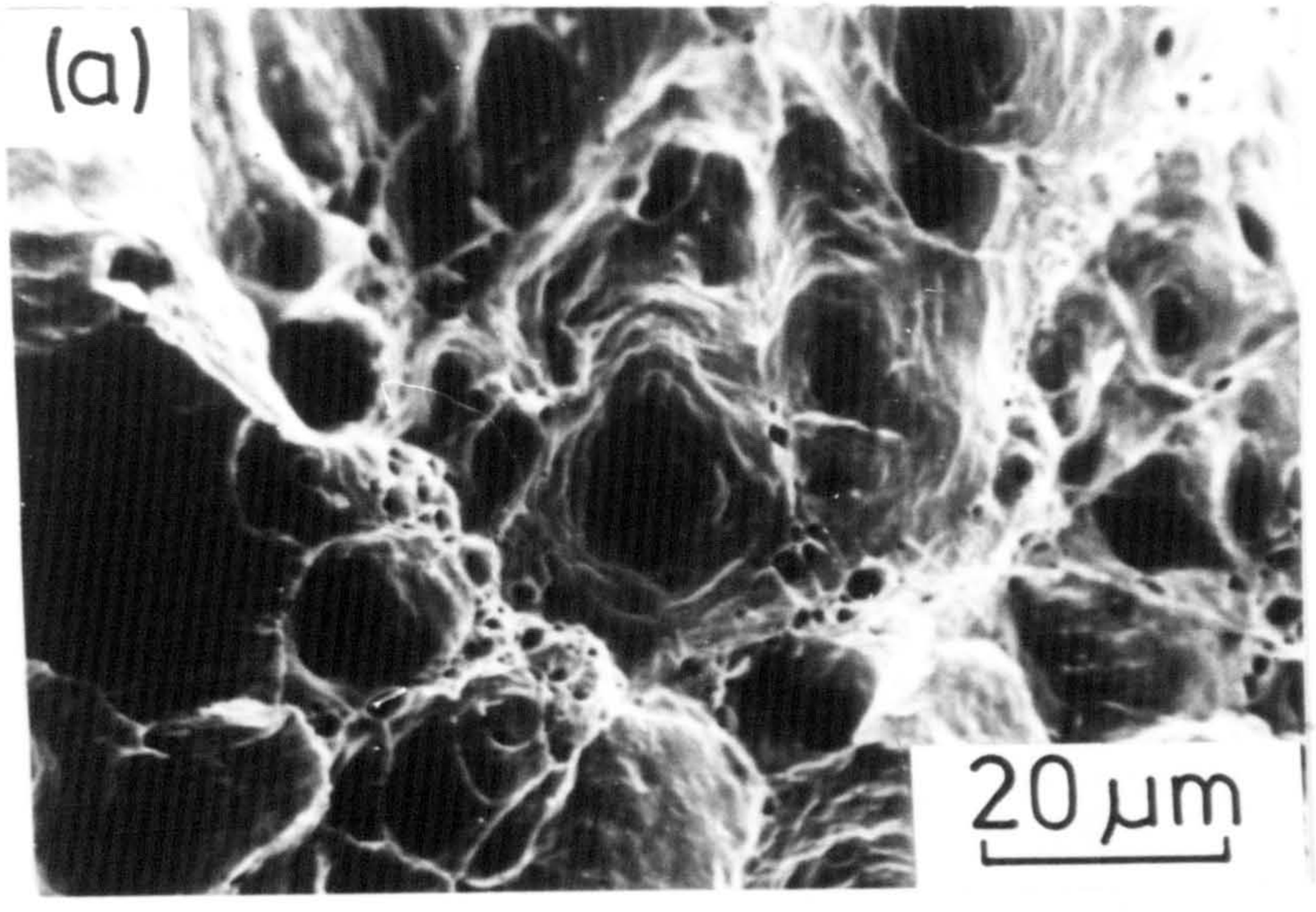
(a)
20 µm

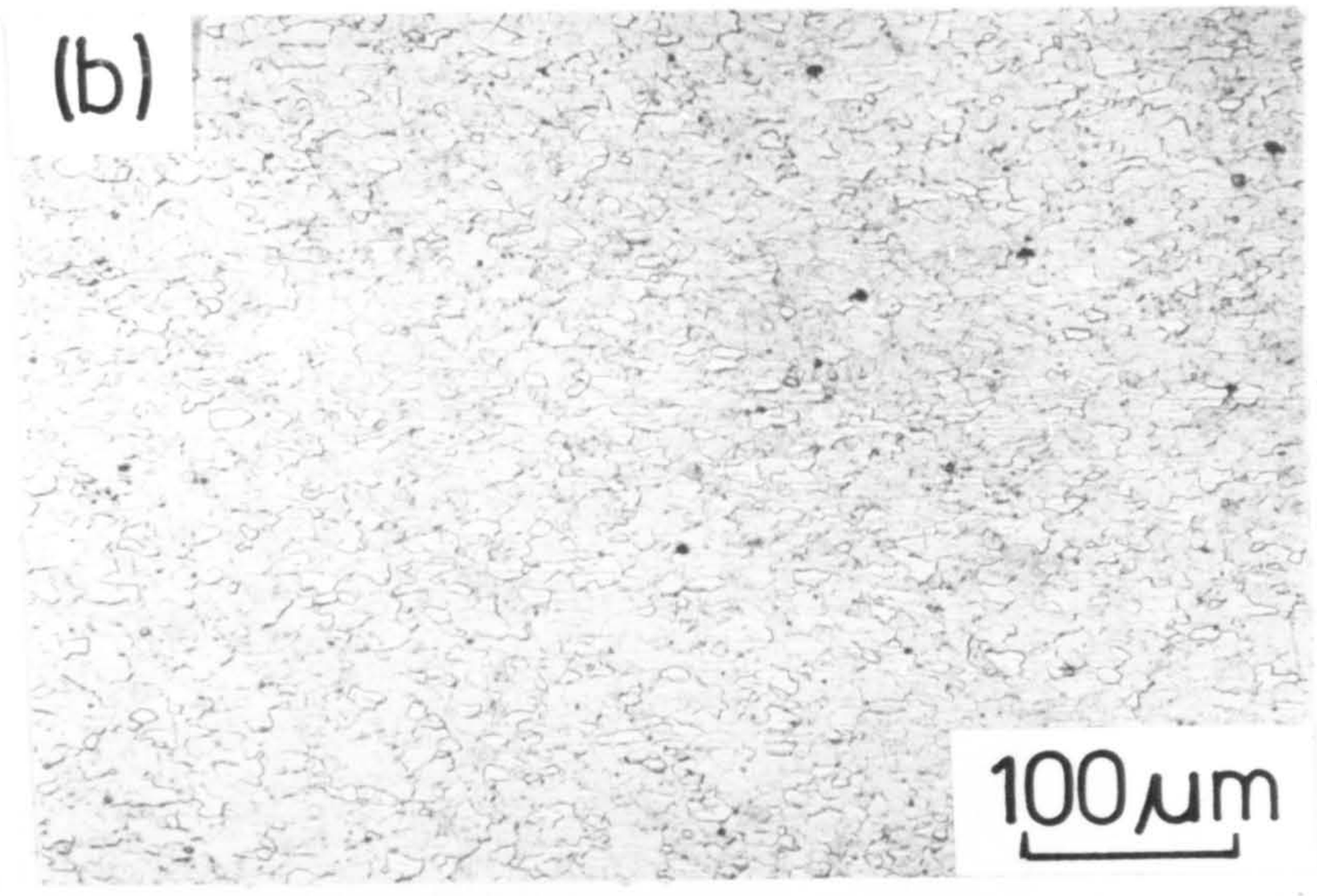
(b)
100 µm

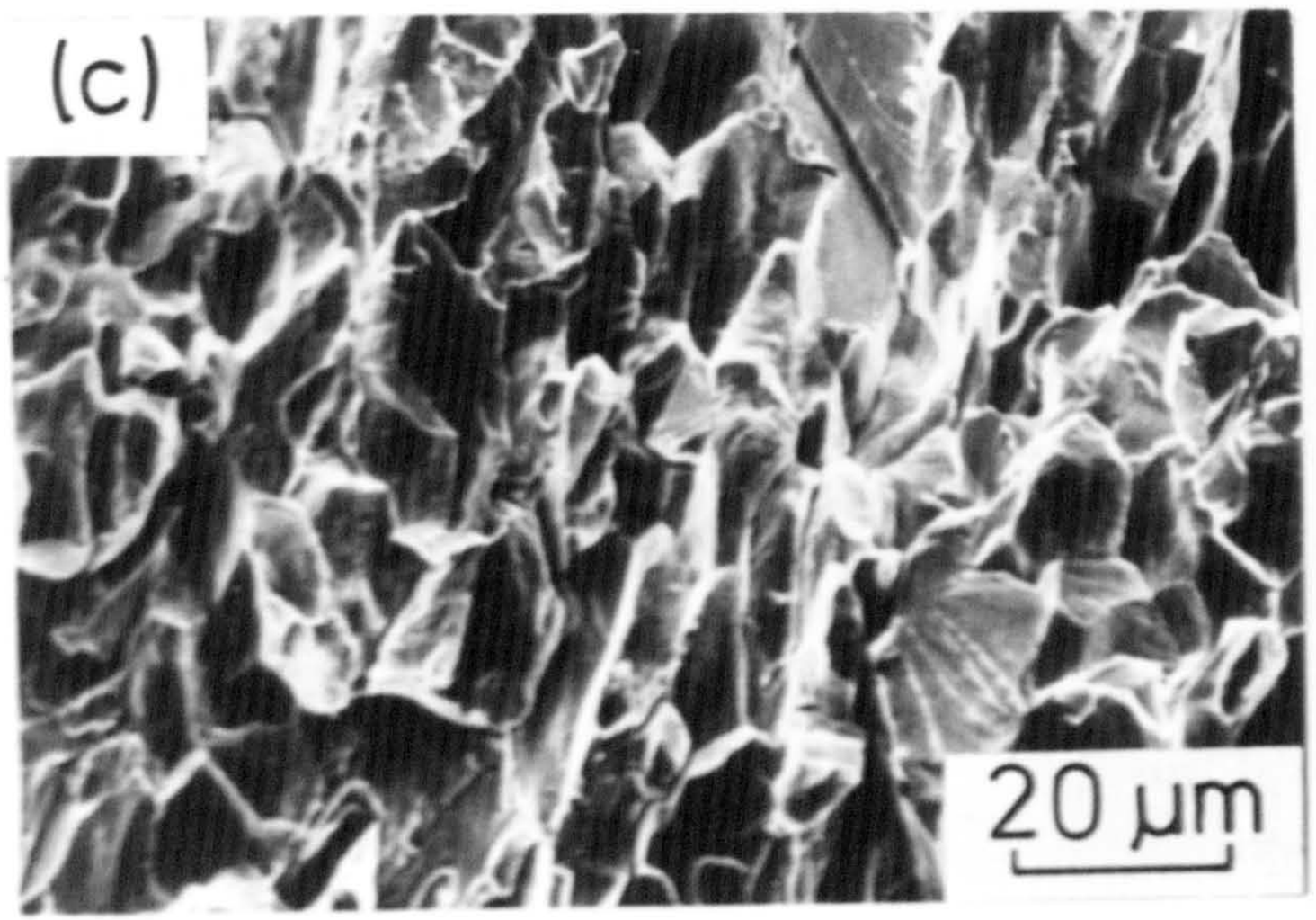
(c)
20 µm

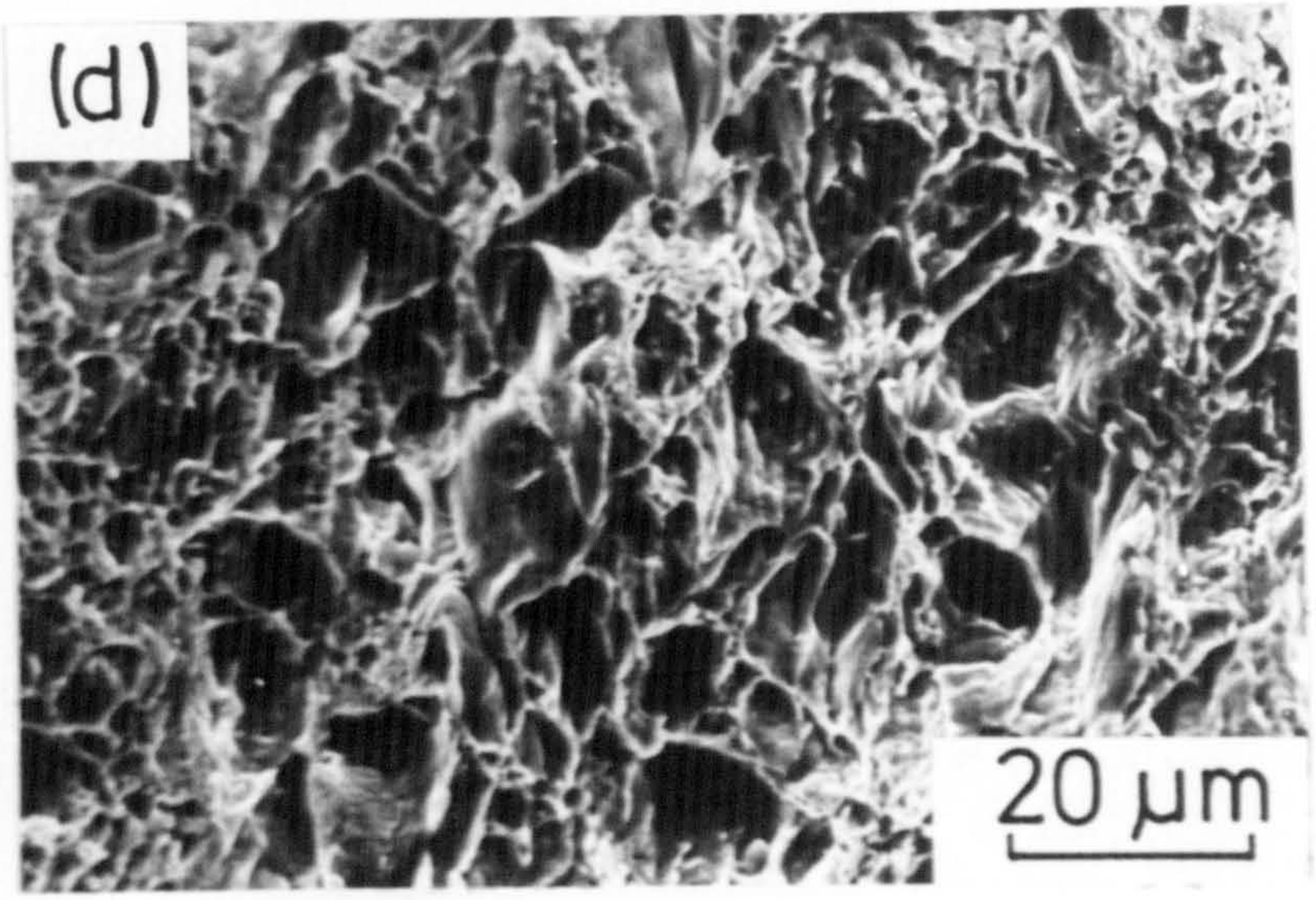
(d)
20 µm

on the nitriding behaviour of "FS" shows that such modelling has limitations.

Chapter XII

GENERAL DISCUSSION

Mixed substitutional-interstitial solute-atom clusters or GP zones formed on nitriding Fe-Ti alloys give a remarkably high strengthening of the ferritic matrix and are the first stage of a transformation sequence which ends with the equilibrium precipitate, TiN. Initially the zone is envisaged as a "defect monolayer" structure in which nitrogen atoms are coordinated by either one, two, three or four titanium atoms. In addition there exist nitrogen atoms octahedrally coordinated by six iron-atoms. Some of these nitrogens are influenced by titanium next-nearest neighbours and give rise to high-temperature relaxations in internal friction experiments. The normal Snoek peak due to nitrogen in ferrite decreases as the titanium concentration in the alloy increases because nitrogen atoms, originally occupying Snoek sites at the nitriding temperature, condense onto the Ti-N zones formed on nitriding. In addition, the average energy of the relaxation processes which characterise the high-temperature peak also increases with titanium concentration. The subsequent rejection of iron from the Ti-N zones, either by aging at high temperatures or by nitriding for long times at temperatures $> 580^{o}C$, causes changes in the distribution of nitrogen atoms between various sites. This aging, at a given titanium concentration, causes an

increase in the number of nitrogens occupying Snoek sites due to a reduction in the number of heterogeneous sites onto which nitrogen atoms can segregate on quenching. Accompanying the increase in the Snoek peak are changes in the high-temperature relaxation peak which moves to higher temperatures with a reduction in height. The modifications in zone composition and structure which occur on aging nitrided Fe-0.18 w/o Ti for short times at 800°C cause significant changes in the strength of the material.

The nitrogen retained in random solid solution in nitrided and quenched Fe-Ti alloys ages at low temperatures, 20°-200°C, giving heterogeneous clustering and subsequent precipitation of nitrogen on existing Ti-N zones formed at the nitriding temperature. The transformations are analogous to those in the quench-aging of nitrogen-ferrite, except that the stabilities of both the "Fe-N" clusters and α''-$Fe_{16}N_2$ precipitates are increased by the very stable Ti-N clusters on which they form.

The formation of Ti-N clusters is accompanied by large increases in strength that are attributed predominantly to an increased resistance to dislocation movement resulting from the creation of new interfaces whenever dislocations cut the substitutional-interstitial zones. In clustered Fe-Ti alloys the increases in hardness are proportional to the square root of the titanium concentration and are strongly temperature dependent, both observations being compatible with a chemical strengthening model. By grain

size analyses it is found that nitriding increases the temperature-dependent component of the friction stress in a similar way to that found by Heslop & Petch (1956) for the Peierls-Nabarro force in Fe-N alloys. It is important to note that the temperature dependence of yield stress in polycrystalline materials measures two effects; (i) the temperature dependence of friction stress and (ii) the Hall-Petch slope. In nitrided Fe-Ti alloys the Hall-Petch slope is strongly temperature dependent as it is in strongly pinned Fe-N alloys thus showing in both materials that unpinning of dislocation sources is the predominant process at yield. In Fe-Ti-N the Hall-Petch slope is greater than in Fe-N alloys, a consequence of the inhomogeneous slip distribution which occurs in nitrided materials with, perhaps, a contribution arising from some residual "chemical bonding" at dislocations causing an increase in the interaction energy. The friction stress of nitrided Fe-Ti alloys is also temperature dependent, due at low temperatures to the Peierls-Nabarro force of body-centred cubic iron, and at high temperatures ($>150^{o}C$) to the thermally activated movement of glide dislocations over the substitutional-interstitial zones.

Aging Ti-N clusters causes a gradual transformation to titanium nitride, with reductions in the friction stress, the Hall-Petch slope, and the temperature dependence of yield stress. Eventually the particles are looped by glide dislocations in an Orowan mechanism that is characterised by an increase in work-hardening rate and a

temperature-independent yield strength.

Although strong, nitrided Fe-Ti alloys are very brittle because in addition to the high volume fraction of small Ti-N clusters within the ferrite grains there is some heterogeneous precipitation of titanium nitride at grain boundaries. By cold-working prior to nitriding, even greater strengths are attained and, because the grain boundaries are replaced by a fine dislocation sub-cell structure, the ductility is much improved. However, even cold-worked and nitrided alloys show poor ductility if nitriding is carried out at temperatures where significant recrystallisation cannot take place. With these limitations, it is suggested that cold-worked and nitrided alloys provide a useful extension to the present generation of HSLA steels and offer advantages in formability. Usually, the higher the strength of a material the lower is its formability, but this does not apply to the present Fe-Ti alloys which, unlike conventional high-strength steels, can be fabricated into complex shapes very easily by cold-forming and subsequently strengthened by gaseous nitriding. They provide a simple model for a new variety of metallic materials - "formable and strengthenable steels".

REFERENCES

Abrahamson, E.P. & Lopata, S.L., 1966, Trans. A.I.M.E., 236, 76.

Armstrong, R., Codd, I., Douthwaite, R.M. & Petch, N.J., 1962, Phil. Mag., 7, 45.

Arrott, A. & Noakes, J.E., 1963, "Iron and its Dilute Solid Solutions". Eds. Spencer, C.W. & Werner, F.E., New York, Wiley Interscience, p. 81.

Ashby, M.F. & Brown, L.M., 1963(a), Phil. Mag., 8, 1083.

Ashby, M.F. & Brown, L.M., 1963(b), Phil. Mag., 8, 1649.

Baird, J.D. & Jamieson, A., 1966, J.I.S.I., 204, 793.

Bergstrom, T. & Roberts, W., 1972, Scand. J. Met., 1, 265.

Boyd, J.D. & Nicholson, R.B., 1971, Acta Met., 19, 1971.

Bozorth, R.M., 1959, "Magnetic Properties of Metals and Alloys", A.S.M.

Brooker, G.R., Norbury, J. & Sutton, A.L., 1957, J.I.S.I., 187, 205.

Brown, G.G. & Whiteman, J.A., 1969, J. Aust. Inst. Metals, 14, 217.

Brown, L.M. & Ham, R.K., 1971, "Strengthening Methods in Crystals". Eds. Kelly, A. & Nicholson, R.B., Elsevier Pub. Co., p. 9.

Chen, F.P.H., 1965, Ph.D. Thesis, Rensselaer Polytechnic Institute, Troy, New York, U.S.A.

Christian, J.W., 1970, Proc. 2nd Int. Conf. on Strength of Metals and Alloys, Amer. Soc. Metals, p. 29.

Cochardt, A.W., Schoek, G. & Wiedersich, H., 1955, Acta Met., 3, 533.

Codd, I. & Petch, N.J., 1960, Phil. Mag., 5, 30.

Cottrell, A.H., 1963, "The Relation between the Structure and Mechanical Properties of Metals", N.P.L., Symposium No. 15, H.M.S.O. (London), p.456.

Cottrell, A.H. & Fisher, R.M., 1963, quoted by Cottrell, A.H., 1963.

Cracknell, A. & Petch, N.J., 1955, Acta Met., 3, 186.

Cuddy, L.J. & Podgurski, H.H., 1977, Met. Trans., 8, 245.

Darken, L.S. & Gurry, R.W., 1945, J. Am. Chem. Soc., 67, 1398.

De Hoff, R.T. & Rhines, F.N., 1968, "Quantitative Microscopy", McGraw-Hill, p. 201.

Dijkstra, L.J., 1947, Philips Res. Rep., 2, 357.

Dijkstra, L.J., 1949, Trans. A.I.M.E., 185, 252.

Dijkstra, L.J. & Sladek, R.J., 1953, Trans. A.I.M.E., 197, 69.

Dingley, D.J. & McLean, D., 1967, Acta Met., 15, 885.

Douthwaite, R.M. & Evans, J.T., 1973, Scripta Met., 7, 1019.

Driver, J.H., Unthank, D.C. & Jack, K.H., 1972, Phil. Mag., 26, 1227.

Duesbery, M.S. & Hirsch, P.B, 1967, "Dislocation Dynamics". Eds. Rosenfield, A.R. et al., McGraw-Hill, p. 57.

Embury, J.D., 1971, "Strengthening Methods in Crystals". Eds. Kelly, A. & Nicholson, R.B., Elsevier Pub. Co., p. 331.

Fast, J.D. & Verrijp, M.B., 1955, J.I.S.I., 180, 337.

Fast, J.D., 1976, "Gases in Metals", Eindhoven, p. 169 & 129.

Ferguson, P., 1981, Ph.D. Thesis, University of Newcastle upon Tyne.

Forman, A.J.E. & Makin, M.J., 1966, Phil. Mag., 14, 911.

Foxall, R.A. & Statham, C.D., 1970, Acta Met., 18, 1147.

Fullman, R.L., 1953, Journal of Metals, 5, 447.

Gyster, A., Lutjering, G. & Gerold, V., 1974, Acta Met., 22, 901.

Hall, E.O., 1951, Proc. Phys. Soc., 648, 747.

Hamano, R. & Tsuya, K., 1979, Scripta Met., 13, 1043.

Henderson, S., 1976, Ph.D. Thesis, University of Newcastle upon Tyne.

Hepworth , M.T., Smith, R.P. & Turkdogen, E.T., 1966, Trans. A.I.M.E., 236, 1278.

Heslop, J. & Petch, N.J., 1956, Phil. Mag., 1, 866.

Hirsch, P.B. & Humphreys, F.J., 1969, "Physics of Strength and Plasticity". Ed. Argon, A.S., M.I.T., p. 189.

Hornbogen, E. & Zum Gahr, K.H., 1975, Metallography, 8, 181.

Jack, D.H., Lidster, P.C., Grieveson, P. & Jack, K.H., 1973, "Inter. Symposium on Metallurgical Chemistry - Applications in Ferrous Metallurgy", I.S.I. (London), p. 374.

Jack, D.H., 1976, Acta Met., 24, 137.

Jack, K.H., 1951(a), Proc. Roy. Soc., A208, 216.

Jack, K.H., 1951(b), ibid., p. 200.

Jack, K.H. & Maxwell, D., 1952(a), J.I.S.I., 170, 254.

Jack, K.H. & Maxwell, D., 1952(b), 10th Annual Pittsburgh Diffraction Conf.

Jack, K.H., 1975, "Heat Treatment '73", The Metals Society (London), p.39.

Jack, K.H., 1978, Proc. 1st Polish Conf. on "Carbides, Nitrides, Borides", Poznan-Kolobrzeg., p. 21.

Jones, D.M., 1976, Ph.D. Thesis, University of Newcastle upon Tyne.

Jones, D.M., Stephenson, A., Hendry, A. & Jack, K.H., 1979, Proc. 5th Int. Conf. on Strength of Metals and Alloys. Eds. Haasen, P. et al., Pergamon Press, p. 737.

Keh, A.S., 1962, "Direct Observations of Lattice Defects in Crystals", Wiley (Interscience), p. 213.

Kelly, A. & Nicholson, R.B., 1963, Prog. in Materials Sci., 10, 151.

Kelly, P.M., 1972, Scripta Met., 6, 647.

Kelly, P.M., 1973, Inter. Met. Reviews, 18, 31.

Kirkwood, D.H., Atasoy, C.E. & Keown, S.R., 1974, Met. Sci., 8, 49.

Kocks, U.F., 1966, Phil. Mag., 13, 541.

Kocks, U.F., 1970, Met. Trans., 1, 1121.

Kocks, U.F., Argon, A.S. & Ashby, M.F., 1975, Prog. Met. Sci., 19, 110.

Krawitz, A. & Sinclair, R., 1975, Phil. Mag., 31, 697.

Krzyminski, H., 1969, Berg u. Huttenmannische Monatschefte, 114, 235.

Laberberg, G. & Josefoson, A., 1955, Acta Met., 3, 236.

Lehrer, E., 1930, A. Electrochem., 36, 383.

Li, J.C.M. & Chou, Y.T., 1970, Met. Trans., 1, 1145.

Low, J.R. & Turkalo, A.M., 1962, Acta Met., 10, 15.

Marcinkowski, M.J. & Fisher, R.M., 1965, Trans. A.I.M.E., 233, 293.

Martin, J.W., 1980, "Micromechanisms in Particle-Hardened Alloys", Cambridge University Press.

Mehl, R.F., Barrett, C.S. & Jerabek, H.S., 1934, Trans. A.I.M.E., 113, 211.

Melander, A. & Persson, P.A., 1978, Acta Met., 26, 267.

Mortimer, B., 1971, Ph.D. Thesis, University of Newcastle upon Tyne.

Nacken, V.M. & Kuhlman, U., 1966, Archiv. Eisenhutten., 37, 235.

Nelson, J.B. & Riley, D.P., 1945, Proc. Phys. Soc., 57, 160.

Ono, K., 1968, J. Appl. Phys., 39, 1803.

Orowan, E., 1948, "Symposium on Internal Stresses in Metals and Alloys", The Institute of Metals (London), p. 451.

Orowan, E., 1954, "Dislocations in Metals". Ed. Cohen, A.I.M.E. (New York), p. 131.

Perovic, V., Purdy, G.R. & Brown, L.M., 1979, Acta Met., 27, 1075.

Petch, N.J., 1953, J.I.S.I., 174, 25.

Phillips, V.A. & Seybolt, A.U., 1968, Trans. A.I.M.E., 242, 2415.

Phillips, V.A. & Tanner, L.E., 1973, Acta Met., 21, 441.

Pipkin, N.J., 1968, Ph.D. Thesis, University of Newcastle upon Tyne.

Podgurski, H.H. & Knechtel, H.E., 1969, Trans. A.I.M.E., 245, 1595.

Podgurski, H.H. & Davis, F.N., 1981, Acta Met., 29, 1.

Pope, M., Jones, D.M. & Jack, K.H., 1975, "Proc. 5th Inter. Conf. on Internal Friction and Ultrasonic Attenuation in Crystalline Solids". Eds. Lenz, D. & Lucke, K., Berlin-Heideberg:.Springer-Verlag, p. 266.

Rachinger, W.A., 1948, J. Sci. Instrum., 25, 254.

Raynor, G.V., 1975, Phil. Mag., 31, 1099.

Ritchie, I.G. & Rawlings, R., 1967, Acta Met., 15, 491.

Roberts, W., 1970, Ph.D. Thesis, University of Newcastle upon Tyne.

Russell, K.C. & Brown, L.M., 1972, Acta Met., 20, 969.

Saada, G., 1960, Acta Met., 8, 200.

Sakamoto, M., 1980, Wolfson Research Group Report, Crystallography Laboratory, University of Newcastle upon Tyne.

Schwartz, D.M. & Ralph, B., 1969, Metal. Sci. J., 3, 216.

Schwerdtfeger, K. & Turkdogen, E.T., 1970, "Techniques for Metals Research", New York Interscience, 4, pt. 1.

Smit, J. & Van Bueren, H.G., 1954, Philips Res. Rep., 9, 460.

Speirs, D.L., 1969, Ph.D. Thesis, University of Newcastle upon Tyne.

Speirs, D.L., Roberts, W., Grieveson, P. & Jack, K.H., 1970, Proc. 2nd Int. Conf. on Strength of Metals and Alloys, Amer. Soc. Metals, p. 601.

Spitzig, W.A., 1981, Acta Met., 29, 1359,

Stephenson, A., 1973(a), Ph.D. Thesis, University of Newcastle upon Tyne.

Stephenson, A., 1973(b), Unpublished work, see Jones, D.M., 1976, Ph.D. Thesis, University of Newcastle upon Tyne.

Sutton, A.L. & Hume-Rothery, W., 1955, Phil. Mag., 46, 1295.

Swartz, J.C., 1969, Acta Met., 17, 1511.

Szabo-Miszenti, G., 1970, Acta Met., 18, 477.

Tabor, D., 1951, "The Hardness of Metals", Clarendon Press, p. 105.

Tanner, L.E., 1966, Phil. Mag., 14, 111.

Taylor, A., 1951, J. Sci. Instr., 28, 200.

Warren, B.E., 1958, Prog. Metal Phys., 8, 147.

Watson, J.D. & Brown, G.G., 1974, Metal Sci. J., 8, 9.

Wert, C.A. & Marx, J., 1953, Acta Met., 1, 113.

Zener, C., 1947, J. Appl. Phys., 18, 1022.

Zener, C., 1948, "Elasticity and Anelasticity in Metals", University of Chicago Press.

Zwell, L. & Wriedt, H.A., 1972, Met. Trans., 3, 593.